ISSN number 0971 - 9709

The Journal of Indian Geophysical Union

VOLUME 23, ISSUE 1 | JANUARY 2019

AN OPEN ACCESS BIMONTHLY JOURNAL OF IGU

EDITORIAL OFFICE

Indian Geophysical Union, NGRI Campus, Uppal Road, Hyderabad- 500 007
Telephone: +91 -40-27012799; 27012734; Telefax:+91-04-27171564
E. mail: jigu1963@gmail.com, website: www.j-igu.in

The Open Access Journal with six issues in a year publishes articles covering
Solid Earth Geosciences; Marine Geosciences; and Atmospheric, Space and Planetary Sciences.

Annual Subscription

Individual ₹ 1000 per issue and Institutional ₹ 5000 for six issues

Payments should be sent by DD drawn in favour of "The Treasurer, Indian Geophysical Union", payable at Hyderabad, Money Transfer/NEFT/RTGS (Inter-Bank Transfer), Treasurer, Indian Geophysical Union, State Bank of India, Habsiguda Branch, Habsiguda, Uppal Road, Hyderabad- 500 007
A/C: 52191021424, IFSC Code: SBIN0020087, MICR Code: 500002318, SWIFT Code: SBININBBHO9.

For correspondence, please contact, Hon. Secretary, Indian Geophysical Union, NGRI Campus, Uppal Road, Hyderabad - 500 007, India; Email: igu123@gmail.com; Ph: 040 27012799, 272012734

ISSN: 0257-7968 (Clarivate Analytics)
ISSN: 0971-9709 (NISCAIR))
Approved as bimonthly ESCI journal by Clarivate Analytics
Cited in Indian Citation Index (ICI), New Delhi
Evaluated by NISCAIR, New Delhi

CONTENTS

J. Ind. Geophys. Union (January 2019)
v.23, no.1, pp: 3-9

Viscoelastic seismic modeling and Q estimation for an attenuating media+

Nimisha Vedanti[1,2]* and Ajay Malkoti[2]

[1]CSIR-National Geophysical Research Institute, Uppal Road, Hyderabad-500007, India
[2]Academy of Scientific and Innovative Research-NGRI, Uppal Road, Hyderabad-500007, India
*Corresponding Author: nimisha@ngri.res.in

ABSTRACT

In seismic modelling experiments, the propagating seismic wave experiences attenuation when real media is simulated. However, for computational ease, we often ignore this effect and model the Earth as either an acoustic or an elastic medium. In this paper, we briefly discuss the importance of considering attenuation in seismic modelling, by using a viscoelastic wave equation. Further we also briefly discuss the effects of attenuation on seismic data and its incorporation in seismic modelling. We find that the attenuation has a large effect on synthetic seismogram, which should be properly addressed in advanced seismic processing and imaging methods.

INTRODUCTION

Attenuation is a property of a medium due to which the energy of a seismic wave can be dissipated in the form of heat and thus leading to a reduction in the wave amplitude. Factors and phenomena responsible for the attenuation can be broadly classified as either extrinsic, or intrinsic. In extrinsic attenuation, redistribution of energy leads to a reduction of amplitudes, while in intrinsic attenuation, the waves suffer energy loss due to conversion of mechanical energy into heat. Commonly observed wave phenomena like geometric spreading, scattering, leaky modes, etc. can be cited as examples of extrinsic attenuation and they do not contribute towards intrinsic attenuation. In general, seismic attenuation is quantified in terms of quality factor (Q), which can be defined as a ratio of stored energy to dispersed energy, as it measures relative energy loss per oscillation cycle of the seismic waves. In ideal scenario, Q is related to the physical state of the rock and it increases with increase in density and velocity.

Since attenuation results in a loss of seismic energy, the recorded seismic traces are required to be compensated for an exact of amount of Q. To achieve this, determination of a precise Q model is required, especially in the high attenuating regions like Deccan Volcanic Province (DVP), where thick basalt sequences cause high attenuation to the propagating seismic waves (Vedanti et al., 2015, 2018). In these areas, data processing using conventional methods may fail because of low signal to noise ratio, especially in the sub-basalt formations. In a synthetic study carried out by Malkoti et al., (2015), it is shown that due to attenuation, amplitudes of the late arrivals or amplitudes from deeper reflectors, are highly diminished in the generated seismogram, which makes processing and interpretation very challenging in sub-basalt layers. In recent past, attempts have been made to apply advanced techniques like full waveform inversion (FWI) to improve the seismic imaging. This technique needs 'complete wave field information' with precise amplitudes to obtain the accurate gradients and thus, it needs a Q structure of the domain. There are several techniques mentioned in the literature for estimation of Q from the acquired seismic data. Most of these techniques are based upon certain data attributes, such as spectral ratio technique which depends mainly on the amplitude, however, the seismic attenuation has a high influence on several other attributes known as the first order effect. Hence, considering the medium as an attenuating media, has its own consequences on Q estimation techniques and it is quite likely to obtain different values of Q from the same data using different methods (Tonn, 1991). To understand this problem of the estimation of Q, we first need to understand the theory of viscoelasticity and the aspects we should consider while incorporating attenuation in a seismic modelling experiment. Thus in this paper, we briefly discuss these aspects of incorporating attenuation in seismic modelling and demonstrate its need by using a simple Earth model.

VISCOELASTIC MODELS

Viscoelasticity is a property of a medium that exhibits both viscous and elastic characteristics when it undergoes deformation. In a pure elastic medium, the process of 'application and removal of the load' follows energy conservation; however, in a viscoelastic material, it involves energy loss. The energy is dissipated during the loading and unloading cycle and thus obtained hysteresis curve area can be used to estimate the attenuation or the quality factor Q. There are several approaches available in literature to model the quality factor, which includes simple damping, frictional models, complex moduli, time dependent moduli etc. (Carcione, 2007; Kjartansson, 1979; Liu et al., 1976; Tal-Ezer et al., 1990). However, in this paper, we preferred to follow more reasonable 'time dependent moduli' approach

+ Invited paper

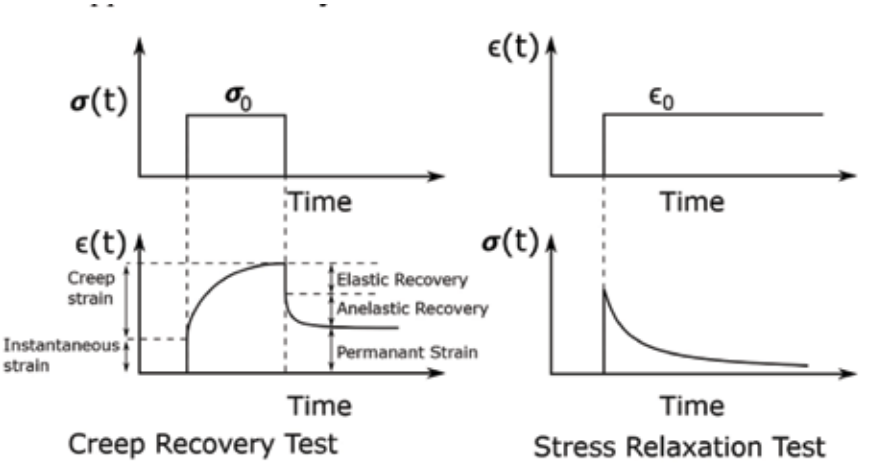

Figure 1. Characteristic functions for an ideal viscoelastic material.

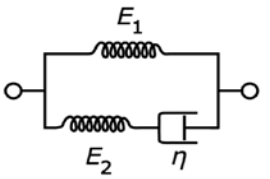

Figure 2. The Zener model with three elements (wiki).

for which it is required to define the basic characteristics of a viscous material.

Ideal viscoelastic material exhibits the characteristics functions (creep and stress-relaxation functions) as shown in Figure 1. These characteristic functions are obtained under the two kinds of tests, where the first test is, "Creep Recovery Test", and the second is "Stress Relaxation Test". In case of the former, a constant stress is applied on the sample for a fixed duration of time and created stress changes are observed over the body. In the latter test, a constant strain/deformation is applied on the body and then the stress variation with time is observed.

Different mechanical models can be defined to describe such a viscoelastic material. In these models, number of parameters may vary from 1 to N depending upon different configurations, which can be used to approximate the rheology of the material by satisfying the above defined tests functions. While doing so, we try to mimic the attenuation by using minimum number of elements to incorporate the correct amount of attenuation, while preserving the characteristics. Thus, we start with a simplest family of models i.e., the 1-element/parameter family that includes single springs or dash pots. In a pure elastic medium, there is no dissipation of energy, so it can be represented with a spring. However, a viscous material can lose the energy and hence it is modeled as a dashpot, which acts like a damper. Stress-strain relation for these two can be written as

$$\text{For spring,} \qquad \sigma = k\epsilon$$

$$\text{For Dashpot,} \qquad \sigma = \eta \frac{d\epsilon}{dt}$$

To represent the Earth more accurately, these two models shall be used in different combinations to form models with higher number of parameters. 1 spring and 1 dashpot model, is called as 2 parameters family. The spring and dashpot components can be arranged either in parallel or in series which are called as Kelvin-Voigt model and Maxwell model, respectively. These arrangements should properly model the characteristics shown in Figure 1. However, the Kelvin-Voigt model cannot model either creep function or stress-relaxation function correctly, which is a disadvantage while Maxwell model only has acceptable stress relaxation function. This limitation led to the inclusion of higher number of parameters such as 3-parameter model e.g., Zener model (Figure 2), also known as Standard Linear Solid (SLS) model, and 4-parameters model e.g., Burger model.

The most useful model to compute the time dependent moduli among these models is a Generalized Standard Linear Solid (GSLS) model for which the general stress-strain relation can be written as:

$$a_0\sigma(t) + \sum_{i=1}^{L} a_i \frac{\partial^i \sigma(t)}{\partial t^i} = b_0\varepsilon(t) + \sum_{i=1}^{L} b_i \frac{\partial^i \varepsilon(t)}{\partial t^i} \qquad (1)$$

Where, a_i, b_i are constants for a linear material. The complex modulus ($M^\star$) for a general viscoelastic material can be calculated by applying the sinusoidal varying

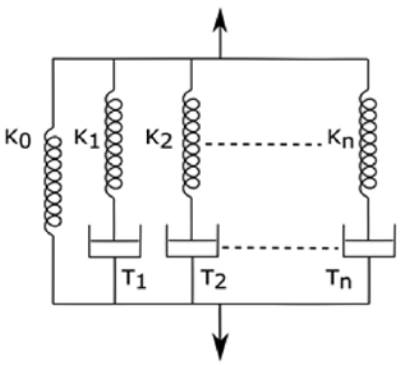

Figure 3. Standard Linear Solid model with Zener elements.

oscillating stress of given frequency, e.g., $\sigma(\omega)=\sigma^0 \exp(i\omega t)$. After certain amount of time the initial effect is negligible and the strain will also be in the form of $\varepsilon(\omega)=\varepsilon^0 \exp(i\omega t)$. The complex modulus of the material is given by Bland (1960); Christensen (2012).

$$M(\omega) = \frac{\sigma^0(\omega)}{\varepsilon^0(\omega)} = \frac{a_0 + \sum_{=1}^{L} a_i\, \omega^i}{b_0 + \sum_{i=1}^{L} b_i\, \omega^i} \tag{2}$$

Thus, the better approach to model time dependent moduli is to assemble many Zener models in parallel, which gives us a "Generalized Zener model" (Figure 3).

Viscoelastic wave formulation

There are many formulations available in literature to define the above mentioned viscoelastic materials in time domain. In this paper, we only discuss the memory variable approach which is based upon a SLS model (Carcione et al., 1988; Liu et al., 1976). As we know that the stress (σ_{ij}) strain (ϵ_{kl}) relationship for a viscoelastic medium can be written in the form of convolution integral as

$$\sigma_{ij} = \dot{\Lambda}(t) \star \varepsilon_{ij}(t)\delta_{ij} + \dot{M} \star \varepsilon_{ij} \tag{3}$$

Where Λ and M are the relaxation functions. A general relaxation function (Ψ) can be modeled with the help of SLS model comprised of L relaxation mechanisms (Carcione, 2007).

$$\psi(t) = M_R \left[1 - \frac{1}{L}\sum_{l=1}^{L}\left(1 - \frac{\tau_\varepsilon^l}{\tau_\sigma^l}\exp\left(-\frac{t}{\tau_\sigma^l}\right)\right)\right] H(t-t') \tag{4}$$

M_R is the relaxed modulus, H(t) is the heavy side function, $\tau^l{}_\sigma$ and $\tau^l{}_\varepsilon$ stress and strain relaxation times, respectively. The stress-strain and memory variable equations can be obtained by substituting the relaxation function (Eq. 4) into Eq. 3. Further, separate relaxation functions should be considered for the P-wave and S-wave. Thus, it will yield following relations:

$$\frac{\partial \sigma_{ij}}{\partial t} = \Lambda\, \dot{\varepsilon}_{k,k}\, \delta_{ij} + 2M\, \dot{\varepsilon}_{i,j} - \frac{1}{L}\sum_{l=1}^{L} r_{ij}^l \tag{5}$$

$$\frac{\partial r_{ij}^l}{\partial t} = -\frac{1}{\tau_\sigma^l} r_{ij}^l + \frac{1}{\tau_\sigma^l}\Lambda^l\, \dot{\varepsilon}_{k,k}\, \delta_{ij} + \frac{1}{\tau_\sigma^l} M^l (\dot{\varepsilon}_{i,j} + \dot{\varepsilon}_{j,i}) \tag{6}$$

Where, we have $\Lambda=\prod-2M$; $\Lambda^l=\prod^l-2M^l$, and $\Lambda_R=\prod_R-2M_R$. To simplify the equations we have assumed that, $\prod=\prod_R(1-\sum^L{}_{(l=1)}\, T_p{}^l)$; $M=M_R(1-\sum^L{}_{(l=1)}\, T_s{}^l)$; $\prod^l=\prod_R T_p{}^l$; and $M^l=M_R\, T_s{}^l$. Here $\prod_R$ and $2M_R$ are relaxed modulus for respective waves functions, $r^l{}_{ij}$, is known as the memory variable, and $T_p{}^l$ and $T_s{}^l$ stands for $\frac{1}{L}\left(1-\frac{\tau_{\varepsilon p}^l}{\tau_\sigma^l}\right)$ and $\frac{1}{L}\left(1-\frac{\tau_{\varepsilon s}^l}{\tau_\sigma^l}\right)$, respectively.

Eq. (5) and (6), along with the continuity equation, forms a complete set of equation for viscoelastic modelling. Thus the complete set of wave equation for 2D viscoelastic wave can be written in expanded form as follows.

$$\rho\frac{\partial v_x}{\partial t} = \frac{\partial \sigma_{xx}}{\partial x} + \frac{\partial \sigma_{xz}}{\partial z} + \rho f_x \tag{7}$$

$$\rho\frac{\partial v_z}{\partial t} = \frac{\partial \sigma_{zx}}{\partial x} + \frac{\partial \sigma_{zz}}{\partial z} + \rho f_z \tag{8}$$

$$\frac{\partial \sigma_{xx}}{\partial t} = (\Lambda + 2M)\, \dot{\varepsilon}_{x,x} + \Lambda\, \dot{\varepsilon}_{z,z} - \frac{1}{L}\sum_{l=1}^{L} r_{xx}^l \tag{9}$$

$$\frac{\partial \sigma_{zz}}{\partial t} = \Lambda\, \dot{\varepsilon}_{x,x} + \Lambda\, \dot{\varepsilon}_{y,y} + (\Lambda + 2M)\, \dot{\varepsilon}_{z,z} - \frac{1}{L}\sum_{l=1}^{L} r_{zz}^l \tag{10}$$

$$\frac{\partial \sigma_{xz}}{\partial t} = M\, \dot{\varepsilon}_{x,z} + M\, \dot{\varepsilon}_{z,x} - \frac{1}{L}\sum_{l=1}^{L} r_{xz}^l \tag{11}$$

$$\frac{\partial r_{xx}^l}{\partial t} = -\frac{1}{\tau_\sigma^l} r_{xx}^l + \frac{1}{\tau_\sigma^l}(\Lambda^l + 2M^l)\, \dot{\varepsilon}_{x,x} + \frac{1}{\tau_\sigma^l}\Lambda^l\, \dot{\varepsilon}_{z,z} \tag{12}$$

$$\frac{\partial r_{zz}^l}{\partial t} = -\frac{1}{\tau_\sigma^l} r_{xx}^l + \frac{1}{\tau_\sigma^l}\Lambda^l\, \dot{\varepsilon}_{x,x} + \frac{1}{\tau_\sigma^l}(\Lambda^l + 2M^l)\, \dot{\varepsilon}_{z,z} \tag{13}$$

$$\frac{\partial r_{xz}^l}{\partial t} = -\frac{1}{\tau_\sigma^l} r_{xz}^l + \frac{1}{\tau_\sigma^l} M(\dot{\varepsilon}_{x,z} + \dot{\varepsilon}_{z,x}) \tag{14}$$

The relaxation times can be determined by minimizing the error between $Q(\omega)$ and given Q_0 (Blanch et al., 1995):

$$\phi = \int_{\omega_1}^{\omega_2} \left[Q^{-1}(\omega, \tau_\sigma^l, \tau_\varepsilon^l) - Q_0^{-1}(\omega)\right]^2 d\omega \tag{15}$$

where, $Q(\omega) = \frac{\mathrm{Re}[M^c(\omega)]}{\mathrm{Im}[M^c(\omega)]}$; $M^c(\omega) = \mathcal{F}\{\partial_t[\psi(t)]\}$ and $\tau^l{}_\sigma = \frac{1}{\omega_l}$ is the stress relaxation time.

These equations can be solved using the finite difference method. Here we use a synthetic data set to demonstrate the importance of the method.

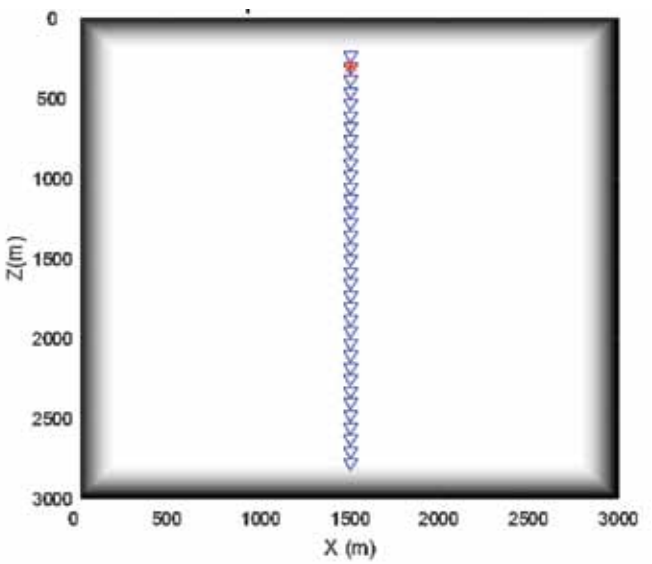

Figure 4. Arrangement of source (in red asterisk) and receiver (blue triangles) along with absorbing boundaries (along edges) as used in simulation.

Measurement of attenuation

In general attenuation measurements are carried out using the amplitude information from the seismic data. Thus, in this paper we only discuss the amplitude based spectral ratio technique, for Q estimation. The data used in this study was generated by designing a synthetic Vertical Seismic Profiling (VSP) survey. The VSP geometry used is shown in Figure 4, where we have laid the receivers vertically and placed the source at the top for the seismic wave simulation.

Spectral ratio technique

This method is very common among the geophysicists and has many variants. The fundamental principle of this method is to compare the spectral characteristics of the seismogram while assuming that the amplitude of a wave can be described by the following relationship:

$$A(\omega) = G(t)R(t)A_0(\omega)\exp\left(-\frac{\omega t}{2Q}\right) \quad (16)$$

where, A_0 is the initial amplitude of the wave which has reduced to A after travelling for time t in the given medium of attenuation characterized by Q. G and R represent the reduction in amplitude due to geometric spreading and reflectivity, respectively. Assuming two receivers placed some distance apart records the amplitude $A_1(\omega)$ and $A_2(\omega)$ respectively at time t_1 and t_2 respectively. We obtain

$$\ln\left(\frac{A_{2(\omega)}}{A_1(\omega)}\right) = -\frac{\omega\Delta t}{2Q} \quad (17)$$

Where, $\Delta t = t_2 - t_1$. When we plot the logarithm of amplitude ratio with the frequency, it represents the equation of straight line with a slope as equal to $\frac{\Delta t\,\pi}{Q}$, which can be in turn utilized to estimate the attenuation Q.

First order effect of attenuations

When a medium offers attenuation to seismic waves, certain phenomena come into play which can be understood as the first order effect of attenuation. Here, we describe the most important ones and their mitigation.

1. *Frequency dependence of* Q: The attenuation experienced by a seismic wave is dependent on the frequency and attenuation mechanism. In a seismic modelling experiment, it's advised to assume constant attenuation over the seismic frequency range (McDonal et al., 1958).
2. *Frequency dependence of the reflectivity*: Attenuation causes the reflectivity of the interfaces to become frequency dependent and thus can affect the attenuation estimation. Hence one must constrain the experiments to include only/nearly normal incident rays. It can be achieved using VSP geometry.
3. *Velocity dispersion causing the travel time difference (drift)*: As mentioned earlier, attenuation causes different frequencies to be attenuated differently. The higher frequencies attenuate faster in comparison to lower frequencies. This causes changes in seismic wavelet and it gets broader with depth. It also causes shifting of the peak amplitude and thus the events experiences a drift. This effect can be corrected or compensated by providing the appropriate time shift or by matching with well log.

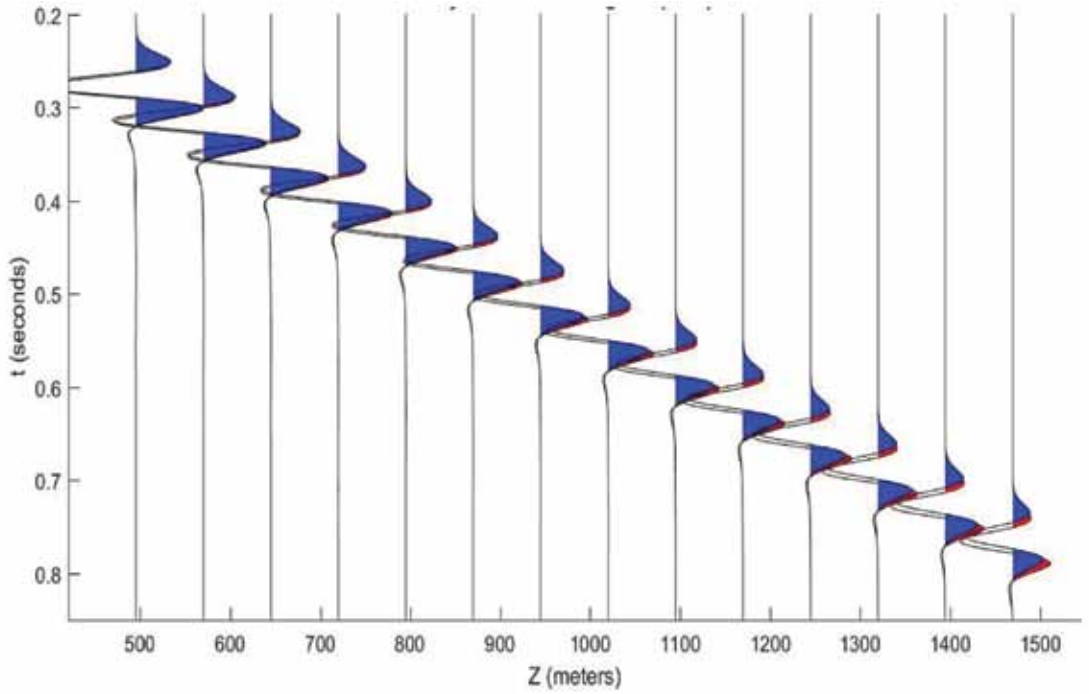

Figure 5. A zoomed section of the VSP gather generated using elastic wave formulation (in red color) and viscoelastic formulations (in blue color).

Table 1. List of parameters used in seismic simulation carried out for a viscoelastic media.

Parameter	*Value*
Model physical parameters	
Velocity, V_p	2000 ms^{-1}
Velocity, V_s	1700 ms^{-1}
Density, ρ	1900 kgm^{-3}
Quality factor, Q	70
Source Parmeters	
Source signature	Ricker
Central frequency, f_0	15Hz
Zero time offset/shift, f_0	0.07sec
Total time length, T	1sec
Simulation parameters	
Model size (x,z)	3km x 3km
Grid spacing, Δh	5m
Time step, Δt	0.1msec
Absorbing boundary nodes	40

Numerical Simulation of Seismic Wave Propagation in Viscoelastic media

Following the above mention concepts, we carried out a synthetic VSP modelling for the elastic as well as viscoelastic medium. The outputs of these simulations are compared in Figure 5. Some of the important parameters for the model and for the simulation are shown in the Table 1, along with their corresponding values. It can be seen that the receivers are arranged vertically as in VSP geometry (Figure 4). The simulation parameters, i.e. time step (*dt)* was taken according to stability condition and to minimize the grid dispersion, more than 6 grids/wavelength were used. To suppress the edge reflections, damping type absorbing boundaries (Cerjan et al., 1985) were applied on all the sides. The synthetic VSP seismogram generated by using viscoelastic formulation, considering attenuation in the media, is used for Q estimation. The results generated after taking care of all the above mentioned effects are shown in Figure 5.

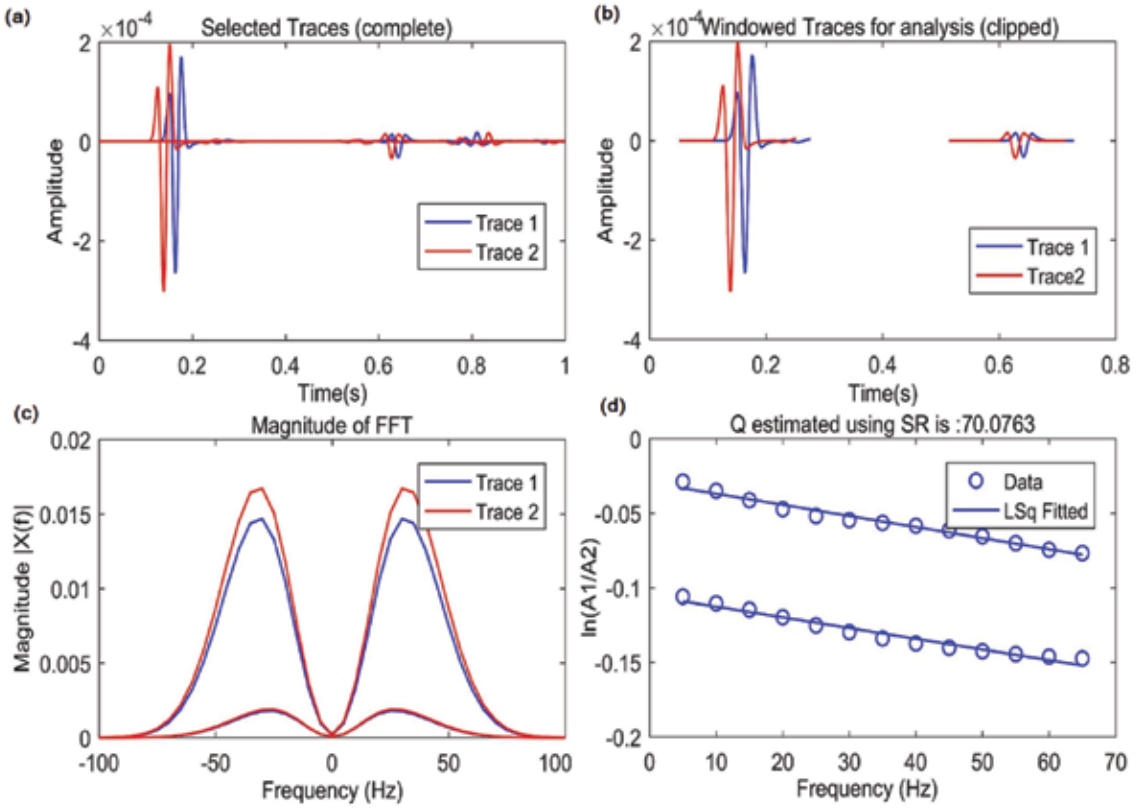

Figure 6. An example of attenuation estimation using spectral ratio. The complete traces selected for the estimation, (a) The clipped part used for the estimation at two places, (b) Fourier spectrum of the given clipped traces, (c) The least square fitting for the determination of slope to estimate Q, (d) Here 'Trace 1 refers' to elastic VSP trace and Trace 2 refers to viscoelastic VSP trace.

We have also used a two layered model and generated a VSP record for this model. Source and simulation parameters were same as for homogeneous. We have chosen two nearby locations to picked events (down going and upcoming) and computed the attenuation for down going as well as upcoming wave. Figure 6 demonstrates the key steps involved in attenuation measurement using the Spectral Ratio method for a two layer case. The steps are namely- selection of traces, clipping the waveform part, Fourier Transform of the clipped part, and estimation of attenuation using the slope of linear fit. For the seismic wave simulation, we have used the 'FDwave' package developed by Malkoti et al. (2018a, 2018b).

RESULTS

The Figure 5 shows a very simple experiment using homogeneous model to demonstrate the difference between the elastic and viscoelastic seismogram. The difference due to the first order effects is very prominent for late phases. This type of mismatch, if not taken care of, can lead to the erroneous results. In Figure 6, we have shown a successful application of this method for Q estimation. As we can see in this figure that considering the first order effects of attenuation and following the prescribed solutions, we can estimate the value of attenuation quite precisely.

CONCLUSIONS

In this paper we have discussed the behavior of an attenuating media and how to model it, using the theory of viscoelasticity, we have shown that the seismic attenuation has a large effect on synthetic seismogram, which was generated for a synthetic VSP survey. Further, we demonstrate an application of Spectral ratio technique to estimate precise value of Q using the synthetic seismic data. We have also discussed the first order effects of attenuation, which should be considered while incorporating seismic attenuation in the seismic modelling experiment. Further, details on the theory and seismic wave simulation algorithm being used are available in Carcione et al. (1988) and Malkoti et al. (2018a, 2018b) respectively.

Compliance with Ethical Standards

The authors declare that they have no conflict of interest and adhere to copyright norms

REFERENCES

Blanch, J., Robertsson, J. and Symes, W., 1995. Modeling of a constant Q: Methodology and algorithm for an efficient and optimally inexpensive viscoelastic technique. Geophysics 60, 176–184. https://doi.org/10.1190/1.1443744

Bland, D.R., 1960. The theory of linear viscoelasticity. Pergamon Press, Oxford; New York.

Carcione, J.M., 2007. Wave Fields in Real Media: Wave propagation in anisotropic, Anelastic, Porous and Electromagnetic Media. Elsevier.

Carcione, J.M., Kosloff, D. and Kosloff, R., 1988. Wave propagation simulation in a linear viscoelastic medium. Geophys. J. Int. 95, 597–611.

Cerjan, C., Kosloff, D., Kosloff, R. and Reshef, M., 1985. A nonreflecting boundary condition for discrete acoustic and elastic wave equations. Geophysics, 50, 705–708. https://doi.org/10.1190/1.1441945

Christensen, R., 2012. Theory of Viscoelasticity: An Introduction. Elsevier.

Kjartansson, E., 1979. Constant Q-wave propagation and attenuation. J. Geophys. Res.: Solid Earth, 84, 4737–4748. https://doi.org/10.1029/JB084iB09p04737

Liu, H.-P., Anderson, D.L. and Kanamori, H., 1976. Velocity dispersion due to anelasticity; implications for seismology and mantle composition. Geophys. J. Int., 47, 41–58.

Malkoti, A., Vedanti, N., Kunagu, P. and Tiwari, R., 2015. Modeling viscoelastic seismic wave propagation in Deccan flood basalt, western India, in: SEG Technical Program Expanded Abstracts 2015, SEG Technical Program Expanded Abstracts. Society of Exploration Geophysicists, 3764–3768. https://doi.org/10.1190/segam2015-5898555.1

Malkoti, A., Vedanti, N. and Tiwari, R.K., 2018a. An algorithm for fast elastic wave simulation using a vectorized finite difference operator. Computers & Geosciences 116, 23–31.

Malkoti, A., Vedanti, N. and Tiwari, R.K., 2018b. Viscoelastic modeling with a vectorized finite difference operator. Computers and Geosciences (submitted).

McDonal, F., Angona, F., Mills, R., Sengbush, R., Van Nostrand, R. and White, J., 1958. Attenuation of shear and compressional waves in pierre shale. Geophysics, 23, 421–439. https://doi.org/10.1190/1.1438489

Tal-Ezer, H., Carcione, J. and Kosloff, D., 1990. An accurate and efficient scheme for wave propagation in linear viscoelastic media. Geophysics, 55, 1366–1379. https://doi.org/10.1190/1.1442784

Tonn, R., 1991. The determination of the seismic quality factor Q from VSP data: a comparison of different computational methods. Geophys. Prosp., 39, 1–27.

Vedanti, N., Lakshmi, K., Dutta, S., Malkoti, A. and Pandey, O.P., 2015. Investigation of Petrophysical Properties and Ultrasonic P-and S-Wave attenuation in Deccan Flood Basalts, India, in: 2015 SEG Annual Meeting. Society of Exploration Geophysicists.

Vedanti, N., Malkoti, A., Pandey, O.P. and Shrivastava, J.P., 2018. Ultrasonic P- and S-Wave Attenuation and Petrophysical Properties of Deccan Flood Basalts, India, as Revealed by Borehole Studies. Pure and Appl. Geophys., 175, 2905–2930. https://doi.org/10.1007/s00024-018-1817-x

Received on: 30.11.18; Revised on: 7.12.18; Accepted on: 14.12.18

J. Ind. Geophys. Union (January 2019)
v.23, no.1, pp: 10-27

Characterising the source rocks in petroleum systems using organic and stable isotope geochemistry: An overview+

Devleena Mani
Centre for Earth, Ocean and Atmospheric Sciences (CEOAS),
University of Hyderabad (UoH), Hyderabad- 500046, India
Email: dtiwarisp@uohyd.ac.in

ABSTRACT
Geochemical investigations for correlating the petroleum (oil and gas) with source rocks and that with petroleum itself, which can be produced from a similar or dissimilar source rock, is important for the assessment of generation potential of a prolific or potential petroleum system. Analytical advancements have synergized the hydrocarbon exploration methods, with exploration geochemistry becoming increasingly an integral part of source rock characterization. Geochemical studies investigate the presence and properties of hydrocarbons trapped in geological formations, or the potential to generate such hydrocarbons and provide source rocks properties, by measuring the compositional changes associated with hydrocarbon generation, migration, accumulation and production. These are critical for proper and efficient management of the hydrocarbon assets at all stages. The source rocks and the petroleum are primarily characterized utilizing the organic geochemical and stable isotope techniques. Organic geochemistry deciphers the source, depositional environment and thermal maturity of sedimentary organic matter from which the hydrocarbons are generated and the stable isotopes of carbon, nitrogen and hydrogen describe the paleo productivity, origin, evolution and correlation of organic matter with generated or in situ hydrocarbon components. The paper presents an overview of the stable isotopic and organic geochemical properties of shales from Damodar Valley basin of India in the light of its gas generation potential.

Key words: Source rocks; organic matter; kerogen; isotopes; biomarkers; thermal maturity; Damodar Valley; Permian; Shale Gas

INTRODUCTION

The unifying concept of petroleum system encompasses a combination of essential elements (source, reservoir, seal, and overburden rocks) and essential processes (basin and trap formation, deposition of source and reservoir rocks and generation-migration-accumulation of hydrocarbons) (Magoon and Dow, 1994). The geologic time when essential elements and processes are correctly placed is critical. Formation of an effective petroleum system is realized only when the organic matter preserved in a source rock, is converted into petroleum (oil and natural gas) and accumulated in a trap, following which there are reasonable chances of its exploitation. A petroleum system investigation includes the identification, naming, determining the level of certainty, and mapping the geographic, stratigraphic, and temporal extent of a petroleum system (Magoon and Dow, 1994; Kenneth et al., 2012).

Geochemical investigations for correlating the petroleum with source rocks and that with petroleum itself is important for the evaluating the generation potential of a prolific or potential play. Advancement in high resolution mass spectrometers for the determination of trace levels of compound specific organic components and their isotope ratios have synergized the hydrocarbon exploration methods, with exploration geochemistry becoming an increasingly integral part of it. Geochemical studies investigate the presence and properties of hydrocarbons trapped in geological formations or the potential to generate such hydrocarbons by providing highly specific information about the characteristics of a petroleum system from just a few rock, oil or gas samples (Eden and Mungo, 2013). It involves the chemical analysis of source rocks and measures the compositional changes associated with hydrocarbon generation, migration, accumulation and production, which are critical to proper and efficient management of the hydrocarbon assets at all stages (Eden and Mungo, 2013). The source rocks and the petroleum are primarily characterized using the organic geochemical and stable isotope techniques. Organic geochemistry deciphers the source, depositional environment and thermal maturity of sedimentary organic matter from which the hydrocarbons are generated and the stable isotopes of carbon, nitrogen and hydrogen describe the paleo productivity, origin, evolution and correlation of organic matter with generated hydrocarbon components (Mani et al., 2011).

This paper presents an overview on characterising the source rocks in petroleum and shale gas/oil systems, using organic and stable isotope geochemistry, with a case study describing the potential of gas generation from Permian shales of the Damodar Valley basin. The origin, evolution, qualitative and quantitative properties of sedimentary organic matter and its thermal decomposition kinetics, all of which are critical for resource assessment, are discussed in light of the Permian shales from Jharia sub-basin, which might be potential source rock for natural gas generation.

+ Invited paper

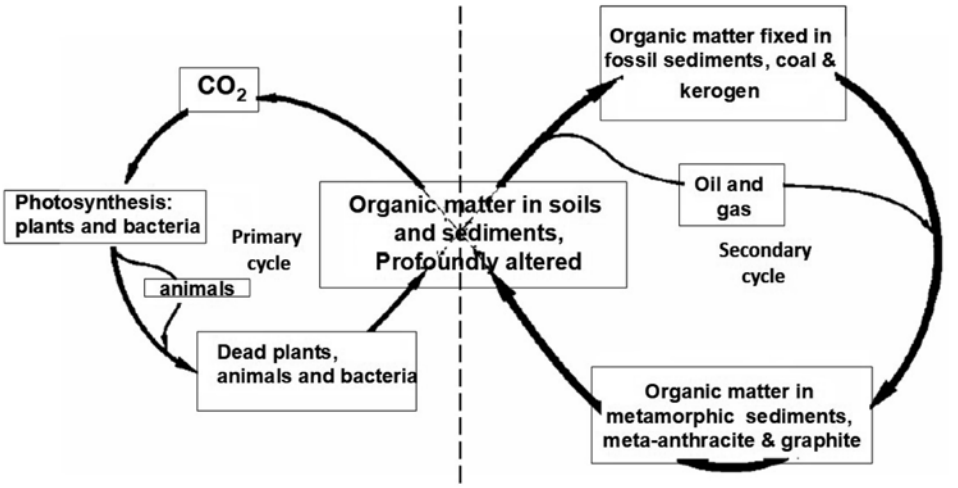

Figure 1. The organic carbon cycle (modified after Tissot and Welte, 1984).

ORGANIC MATTER – FROM SOURCE ROCKS TO TRAPS

Synthesis of organic matter

It is evident that organic matter in sediments upon exposure to subsurface temperature and pressure, transforms into hydrocarbons. The mass production of organic matter is achieved by universal process of photosynthesis, wherein autotrophic green plants, blue green algae and photosynthetic bacteria convert solar energy into chemical energy, utilizing the CO_2 and H_2O from the ambient environment to fix the carbon in the form of polysaccharide - glucose ($C_6H_{12}O_6$) with the release of free oxygen and water.

$$6CO_2 + 12\,H_2O \xrightarrow{h\nu} C_6H_{12}O_6 + 6O_2 + 6H_2O$$

Oxygenation of primitive reducing atmosphere of early Earth supported the evolution of diverse lifeforms and is considered an important event in timeline of photosynthesis. Though the exact timing of the 'great oxidation event' is being constrained narrowly by present day research, the earliest evolution of free oxygen and production of organic matter has been reported to be much older than 2.5 - 3 billion years. Nearly 75 million petagrams (Pg) of carbon are distributed within various reservoirs of the Earth's crust, biosphere, and ocean (Petsch, 2014). Most of the carbon on Earth is concentrated in sedimentary rocks, a large part (~ 82%) of it in the form of inorganic carbonates and remaining (~18%) as organic carbon. A dynamic equilibrium between the oxidised (e.g. CO_2; HCO_3^-) and reduced ($C_6H_{12}O_6$; CH_4) forms of carbon is manifested in the global carbon cycling, which involves sequence of processes through which carbon compounds move from one carbon reservoir or sink to another.

Organic Carbon cycle

The atmospheric, hydrospheric and terrestrial reservoirs of carbon are in constant exchange with each other. Carbonates get precipitated in the aquatic reservoirs in the form carbonate sediments such as calcites. Dissolution of sedimentary carbonates produces carbonate and bicarbonate ions and carbon dioxide, which are in equilibrium in the surrounding waters.

$$CO_2(aq) + H_2O \rightleftharpoons H_2CO_3$$
$$H_2CO_3 \rightleftharpoons H^+ + HCO_3^-$$
$$HCO_3^- \rightleftharpoons H^+ + CO_3^{2-}$$
$$Ca^{2+} + CO_3^{2-} \rightleftharpoons CaCO_3$$

The terrestrial plants form the organic matter directly from the atmospheric reservoir by photosynthesis, while marine plants synthesize it from the dissolved CO_2 in the hydrosphere. Terrestrial and marine organic matter is largely destroyed by oxidation, and CO_2 is returned for recirculation in the system. The cycling of organic carbon is illustrated in the organic carbon cycle (Figure 1), which consists two sub-cycles, a primary and a secondary one.

The primary cycle is smaller with a lower turnover and shorter half-life of days to couple of years, whereas the secondary cycle has a larger turnover and half-life of millions of years. The two cycles are interconnected by a tiny leak of 0.01-0.1% of total organic carbon, which represents the oxidation of sedimentary organic matter to carbon dioxide (Tissot and Welte, 1984). For petroleum formation, the secondary cycle is significant. Once the organic matter completes the second cycle during formation of a sedimentary basin, upon increasing burial it is subjected to diagenetic and catagenetic reactions, which lead to formation of petroleum.

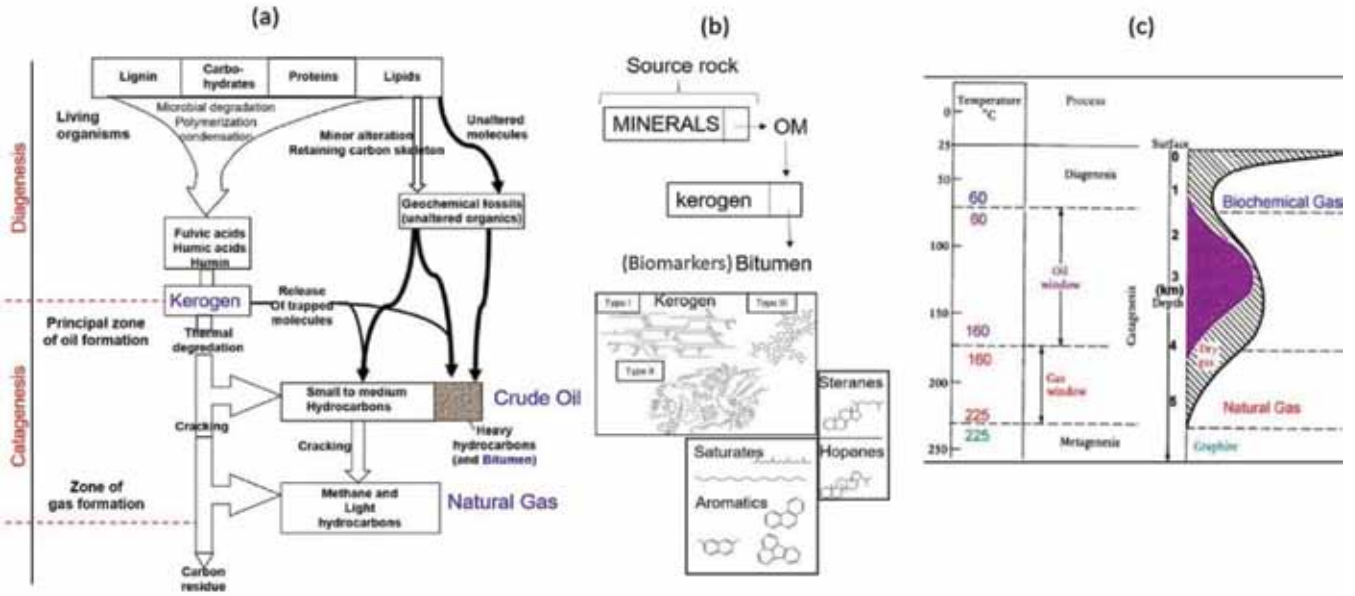

Figure 2. Thermal transformation of organic matter in source rock to petroleum and natural gas (modified after Hunt, 1996; Tissot and Welte, 1984).

Preservation of organic carbon in sediments

The long-term fate of organic matter in sediments is mainly governed by tectonic activities. Phases of subsidence and increasing burial, or uplift and erosion define whether the organic content is preserved and thermally evolved into petroleum, or is eroded and oxidized back to carbon dioxide (Tissot and Welte, 1984). The average preservation rate of organic carbon is estimated to be less than 0.l%, and is controlled by the geological and geochemical conditions of sedimentation. Higher organic productivity, nutrient supply (brought by rivers, upwelling currents, and water mixing), low oxygen content of associated water column and sediments (less than 0.2 mL/L water), restricted water circulation, lack of bioturbation, very fine-grained sediment particles (<2 μm), and an optimum sedimentation rate favour the preservation of organic matter in the sediments. The upper limit of the preservation rate of organic carbon, to be found in certain oxygen-deficient environments such as Black Sea, favourable for deposition of source rock-type sediments, is about 4% (Peters et al., 2005).

Thermal transformation of organic carbon

About 10 - 20% of petroleum is formed from the hydrocarbons, mainly lipids which has been synthesized naturally by the earlier living organisms. It constitutes carbon homologs, (≥ C15+ compounds) that have identifiable biological and chemical structure or 'biomarkers' (Hunt, 1996). These are soluble in organic solvents and constitute the bitumen part of organic matter. The carbon skeleton in biomarker compounds gets only minimal or slightly altered during the digenetic processes, thus providing useful information on paleo-events of its deposition and preservation. The second major source of petroleum is kerogen, which constitutes about 80–90% of hydrocarbons, and involves the conversion of the proteins, lipids, and carbohydrates of living organisms into organic matter of sedimentary rocks. Consecutive burial of organic matter at different depths in the subsurface causes various chemical and physical transformations in it, ultimately leading to the formation of liquid and gaseous hydrocarbons, through the stages of diagenesis, catagenesis, and metagenesis (Figure 2) (Hunt, 1996). Diagenesis occurs in recent sediments at shallow depths, where the temperatures are less than 60°C. The bio-polymers like carbohydrates and proteins transform into geo-polymers, or kerogen. Increased sedimentation leads to burial of previously deposited beds and exposure of sediments to subsurface conditions of increasing temperature (T~50 –150°C) and pressure (P~300 –1000 bars). Overburdened sedimentary column and tectonic activities govern the subsurface P–T conditions. Thermal degradation of kerogen results in the formation of petroleum, condensates, and wet gases. At still higher temperature (150°–200°C), organic matter is cracked to dry gas. Metamorphism is the last stage of evolution of sediments in the subsurface (Hunt, 1996).

Besides the prevailing depositional conditions and environment, the accumulation and preservation of organic matter also depends upon the sediment grain size. Clay type sediments adhere maximum organic material, followed by the carbonate matrices. As a result, amongst the sedimentary rocks, fine grained shales have the highest percentage of organic carbon, only seconded by

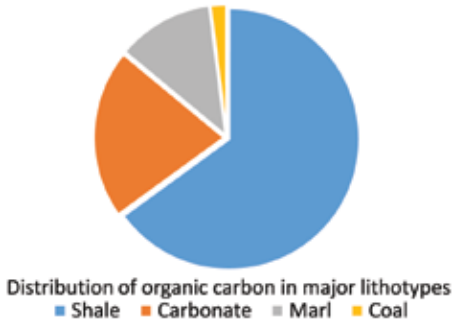

Figure 3. Distribution of organic carbon in different sedimentary rocks.

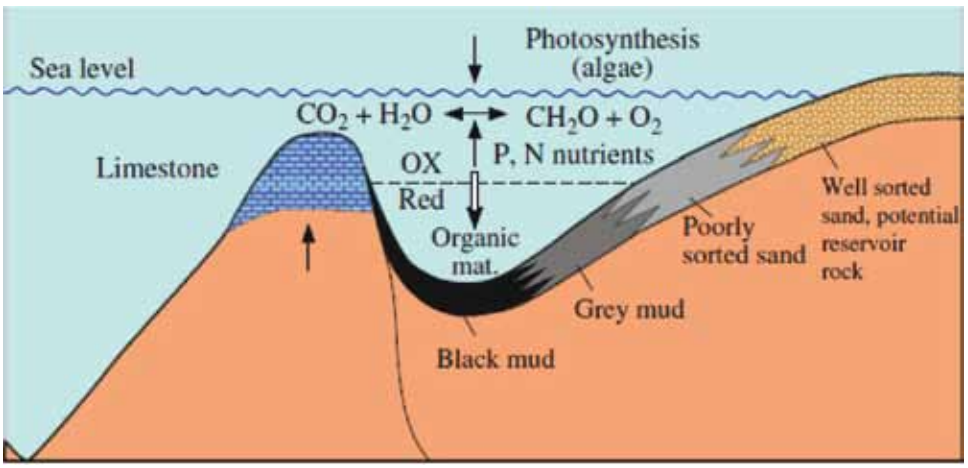

Figure 4. Depositional environment for potential source rock (after Bjørlykke, 2015).

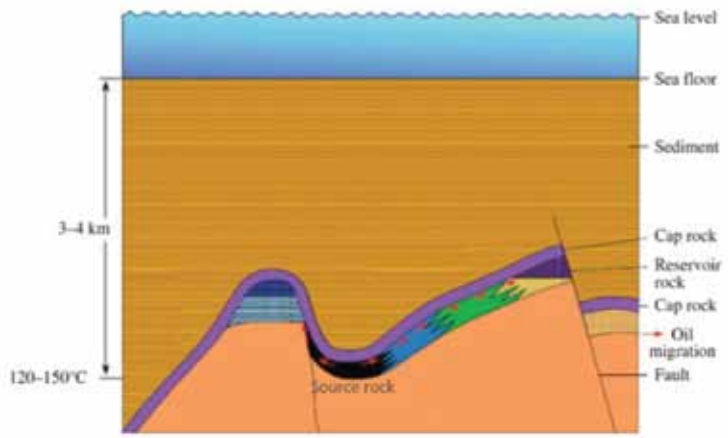

Figure 5. Schematic of essential elements of petroleum system (after Bjørlykke, 2015).

the carbonate rocks (Figure 3). The similar hydrodynamic behaviour of the organic matter tends to get deposited preferentially with fine-grained mud. Unlike sand, fine grained mud more readily excludes oxygen-rich water below the sediment-water interface, thereby enhancing anoxia when it develops. Oxygen deficit environment is essentially important for the preservation of organic matter.

Source, reservoir and trap rocks

The organic matter in sedimentary rocks, with increasing temperature and time, transforms into petroleum and natural gas. The black-grey colour of sedimentary rocks is primarily due to the presence of organic matter in it. It is well known that shale is the most abundant sedimentary

Table 1. Sources and types of kerogen with variable oil and gas generation potential

Depositional environment	Kerogen Type	Maceral Type	Origin	Hydrocarbon potential
Aquatic	I	alginite	algal bodies	+ Oil
		amorphous organic matter	structureless debris of algal bodies	
	II		structureless, planktonic material, primarily of marine origin	
Terrestrial		exinite	skins of spores and pollen, cuticle of leaves, herbaceous plants	
	III	vitrinite	fibrous and woody plant fragments and structureless colloidal humic matter	Gas and some oil
	IV	inertinite	oxidized, recycled woody debris	none -

rock, and black shales containing 1-3% of total organic carbon (TOC) and as high as 20% form important petroleum source rocks in the world. Some depositional controls favourable for good source rocks include major marine transgressions, warm equable climate, and anoxia (Figure 4).

The generated hydrocarbons, after being expelled from source rocks migrate upward and laterally along faults and fractures until a trap is encountered. The density variations in natural gas and petroleum leads to formation of free gas cap on the top of the trap, oil reservoir in the middle and salt water at the bottom. In the trap, the reservoir rock is overlain by an impermeable caprock or seal (Figure 5).

Because of migration, the physical and chemical properties of petroleum formed deep in the basin and where it ends in the trap are different both vertically and horizontally.

SOURCE ROCK CHARACTERIZATION

Organic Geochemistry

Organic geochemistry provides analytical data for identification and mapping of petroleum source rocks. The maps generated from the organic geochemical data indicates the quantity, quality and thermal maturity of organic matter in a source rock and is important in determining the stratigraphic and geographic extent of a pod of active source rock in a petroleum system (Peter and Cassa, 1994). These characteristics of active source rocks lead to the determination of the amount of oil and gas available for traps and significantly assist in reducing the exploration risk. Carbon compounds manifest themselves on Earth in inorganic or oxidised forms, such as carbonates or carbon dioxide etc. and organic or reduced forms such as methane, carbohydrates which are produced by living organisms. Kerogen is the dispersed, amorphous, macromolecular organic matter. It is the precursor geo-polymer from which most of the hydrocarbons are generated in a source rock, with minor contribution from the bitumen, which is derived mainly from the lipid and fat content of once existing organisms. Thus, the source rocks are, in general, characterised by the organic richness, type and thermal maturity of the kerogen and the bituminous biomarkers present in it. Organic richness is characterised by the total organic carbon content, expressed in weight percent (% TOC). Higher the TOC, greater is the hydrocarbon generation potential. A TOC < 0.5% is considered to have poor generation potential, whereas that between 3-4% is considered very good to excellent.

Kerogen

The type or quality of organic matter is dependent upon the source of organic components and its environment of preservation, thus resulting in different kerogen types with varying capacity for oil and gas generation. Kerogen is classified under Type I, II, III and IV based on their Carbon (C), hydrogen (H) and oxygen (O) content (Van Krevelen, 1961). Type I and II have generated most of the world's oil. Type I is generated predominantly in lacustrine/marine depositional setting and is derived mainly from algal lipids (Table I). It contains several long aliphatic chains and the H/C ratio is originally high (H/C >1.5) (Tissot and Welte, 1984; Peters et al., 2005). Type-II kerogen contains aliphatic chains and more number of aromatic and naphthenic rings compared to Type I. The range of hydrocarbon compounds generated and the oil and gas potential of Type-II kerogen are lower (H/C= 1.2 to 1.5) than Type I kerogen. Type-III kerogen has low H/C range (H/C= 0.7 to 1.0). It generates primarily gas, condensates and some waxes and contains mainly condensed poly-aromatics and oxygenated

Table 2. Thermal maturity and oil and gas generation potential (after Tissot and Welte, 1984)

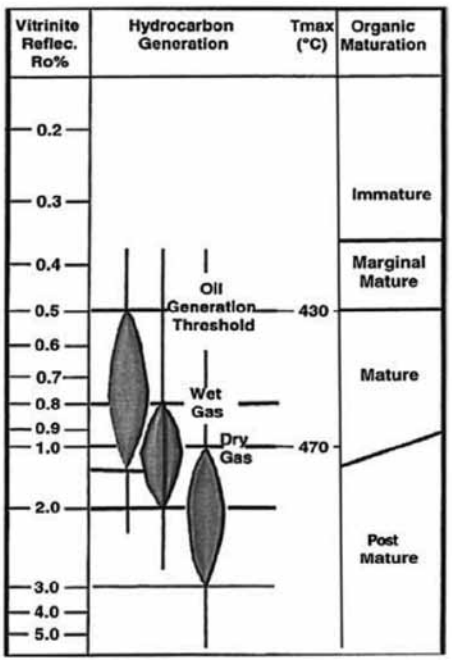

Table 3. Selected biomarkers along with their source and depositional environments

Hydrocarbon Biomarkers	Proxy information
n-Alkanes	
Long chain *n*-alkanes with predominance maxima at *n*-C_{27}, *n*-C_{29} and *n*-C_{31}	Terrigenous plant source
n-alkanes with *n*-C_{15}n, *n*-C_{17} and *n*-C_{19} predominance	Marine algae/ lacustrine source
Carbon Preference Index (CPI)	Thermal Maturity
Acyclic Isoprenoids	
Pristane (Pr) Phytane(Ph) ratios	
Pr/Ph < 2	Marine, fresh water and brackish water *(Reducing Environ)*
Pr/Ph < 2-4	Fluvio-marine and coastal swamp *(Oxic to suboxic)*
Pr/Ph up to 10	Peat swamp *(Oxic environment)*
Unusual distributions of n-alkanes and cyclohexylalkanes	Characteristic of *Gloeocapsomorpha prisca* found in early Paleozoic samples
Steranes	
C_{27} and C_{28} steranes	Algal source
C_{29} steranes	Higher plants
C_{30} steranes	Marine phytoplankton
Hopanes	
C_{35} homohopanes	Anoxic Depositional Environment
28,30-bisnorhopane	High in certain reducing environments
30-norhopanes	Carbonate Source Rock
Botryococcane	Lacustrine depositional settings
C35 homohopane	Degree of oxicity of marine sediments
Gammacerane	Stratified Column
Oleanane	Characteristic of angiosperms (flowering plants) found only in Tertiary and Upper Cretaceous rocks and oils
Dinosterane	Marine dinoflagellates, possibly distinguishing Mesozoic and Tertiary from Paleozoic source input
24-n-Propylcholestane	Marker for marine algae extending from at least the Devonian to the present.

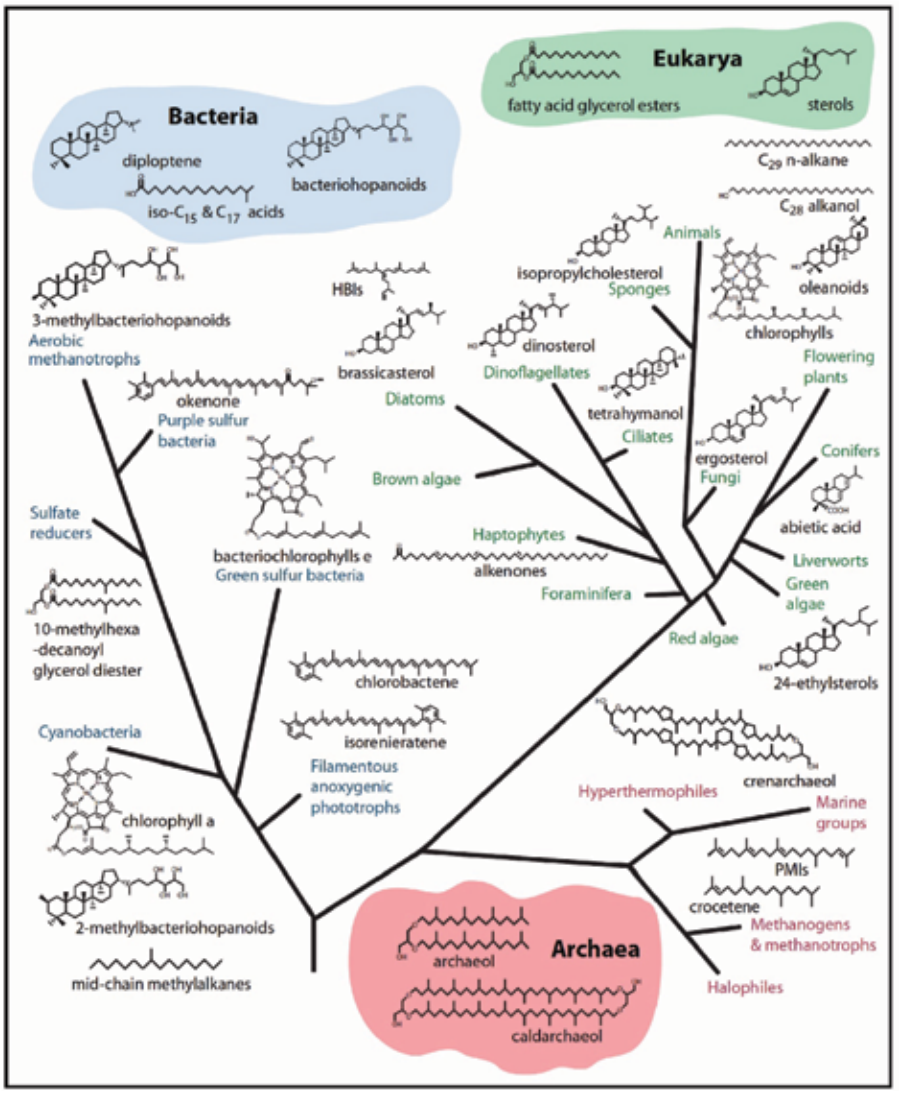

Figure 6. Biomarker tree of life showing the three domains of life (after Briggs and Summons, 2014)

functional groups, with minor aliphatic chains. The organic matter is mostly derived from terrestrial higher plants. Type IV kerogen is inert and generates only small amount of methane and CO_2 (Hunt, 1996).

Various thermal maturity parameters such as vitrinite reflectance, conodont index, Rock Eval Tmax etc. indicate the extent of heat experienced by the source rocks. High subsurface temperatures (60°- 200°C) eventually lead to the cooking and transformation of organic matter into the oil and gas (Table 2). Depending upon the thermal exposure, the rocks are categorised as immature, with no ability to generate petroleum in present condition; mature, in oil or gas condensate zone or post-mature, largely in gas generating window (Peter and Cassa, 1994).

Geochemical logs prepared from organic richness, type and thermal maturity of kerogen, help in identifying a potential, effective, and spent petroleum source rock, the thermal maturation gradient, including immature, mature, and post-mature zones, and in situ and migrated petroleum shows (Peters and Cassa, 1994).

Biomarkers

Biological markers or biomarkers are complex organic compounds composed of carbon, hydrogen, and other elements occurring in sediments, rocks, and crude oils. These compounds originate from formerly living organisms and show little or no change in structure from their parent organic molecules in living organisms. Biomarkers are important because select lipids and their hydrocarbon remnants derived from earlier organisms carry a high degree of taxonomic specificity, which allows the reconstruction of past organismic diversity from the sedimentary inventory of fossil biomarkers (Figure 6, Table 3). Biomarkers help in deciphering the source, depositional environment and thermal maturity of the organic matter and are particularly used in source rock to oil and oil to oil correlation studies.

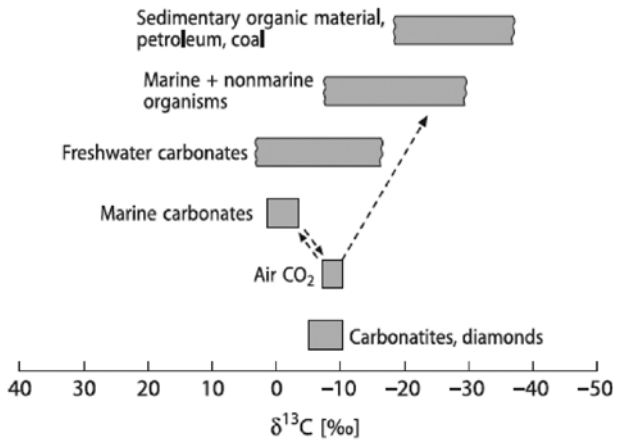

Figure 7. Range of carbon isotope values in different reservoirs (after Schidlowski, 1987)

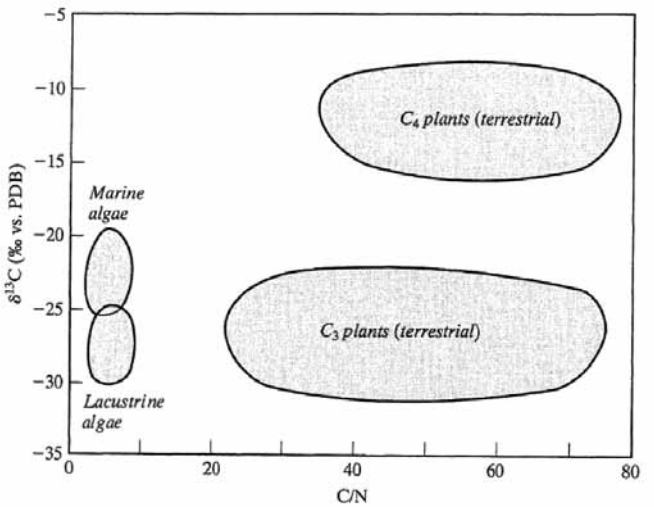

Figure 8. Carbon and nitrogen isotope ranges for organic matter sourced from different biological mass (after Sharp, 2007)

Stable isotope geochemistry

Isotopes of carbon, hydrogen, nitrogen and oxygen have been used to study diverse aspects of organic matter burial, productivity, storage and cycling on the Earth. The isotopic variations documented in the sedimentary shales and carbonates, provide information on the productivity, gross carbon storage and development of prolific source rocks in sedimentary basins. As a result of kinetic isotope effects, the transformation of inorganic carbon into living matter entails a marked bias in favour of light isotopes (^{12}C), with heavy species (^{13}C) retained in the inorganic reservoir (Schidlowski, 1987). This isotopic discrimination leads to the preferential accumulation of ^{12}C in all forms of biogenic (reduced) carbon as compared with the inorganic (oxidized) carbon pool of surficial environment, mainly in form of the atmospheric carbon dioxide and dissolved marine carbonate (Schidlowski, 1987). When the biogenic materials and carbonates are incorporated in newly formed sediments, the kinetic isotope effect, associated with the autotrophic carbon fixation, is propagated from the surficial exchange reservoir into the rock section of the carbon cycle (Schidlowski, 1987). Over geological time, this effect has ultimately brought about a conspicuous isotope disproportionation of Earth's primordial carbon into a light and heavy crustal carbon reservoir (Figure 7).

The hydrocarbon components generated from different organic matter types differ in isotopic compositions due to the characteristic parent source material (Figure 8). Depending upon the different enzymatic process used for carbon fixation in photosynthesis, there may even be different isotopic values for terrestrially derived organic matter, in addition to the variability of marine and lacustrine organic signatures. Plants using C3 Calvin cycle show less efficient carbon fixation and observe large ^{13}C depletions compared to plants adopting C4 cycle (Figure 9).

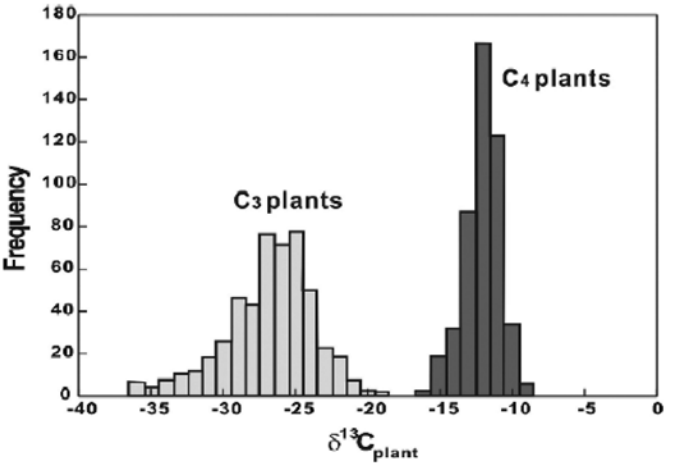

Figure 9. Carbon isotope values of C_3 and C_4 plants (after Sharp, 2007)

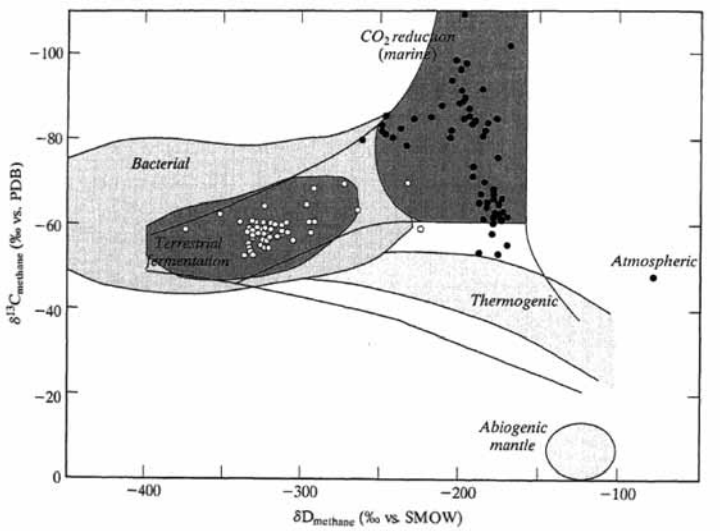

Figure 10. Schematic showing varying sources of methane (After Hoefs, 1996)

The isotopic variations provide significant information on the origin and correlation of petroleum and natural gas. The gas systems originating from a respective source of organic matter have been classified into two distinct types, namely biogenic (or microbial) and thermogenic (Figure 10). There can also be mixtures of the two gas types. Occurrence of thermogenic gas in the subsurface establishes the possibility or presence of a source rock and provides information on the elements of the petroleum or gas system, which otherwise lacks in biogenically produced gases.

Organic Petrology

Organic petrology comprises of the visual examination of organic matter under microscope and is useful for the characterization of the source rocks. The study of macerals or organic constituents in sedimentary rocks, such as coal, petroleum source-rocks and oil shales (with abundant organic matter) and limestone, sandstone and shale (with minor dispersed organic matter), provide important information about kerogen type, its thermal maturity level, and the hydrocarbon generation potential. Reflectance measurements and overall observations of organic matter (OM) under the microscope with white and UV light in oil immersion or dry environment, allow identification of maceral composition of source rocks and understanding of interplay between OM and minerals for in-depth evaluation of source rock potential in conventional and unconventional exploration and production.

There are three major maceral groups, liptinite, vitrinite and inertinite (Table 4). The liptinite group is derived from the resinous and waxy parts of plants, the vitrinite group from coalified woody tissue, and the inertinite group is derived from charred and biochemically altered plant cell wall material.

Table 4. Macerals classification and sources (after Kentuky.edu, 2018)

Macerals		Origin
Group	Maceral	
Vitrinite	Telinite	Plant cell walls (with visible structure)
	Collotelinite	Plant cell walls (gelified, structureless)
	Vitrodetrinite	Small particles of plant attritus (worn-down particles of plant humus)
	Collodetrinite	Mottled peat groundmass (originally attritus [worn-down particles])
	Corpogelinite	Primary and secondary cell infillings from humic gels
	Gelinite	Amorphous humic matter in crack fillings
Liptinite	Sporinite	Outer cell walls of plant spores and pollen
	Cutinite	Outer coatings (cuticles) of leaves, roots, stems
	Suberinite	Degraded (suberinized) cell walls of cork in bark and roots
	Resinite	Plant resins, balsams, latexes, fats, and waxes
	Alginite	Algae
	Bituminite	Amorphous fluorescent material of either algal or bacterial origin
	Exsudatinite	Secondary crack-filling material formed from maturation after oil generation
	Fluorinite	Secondary crack-filling material formed from maturation after oil generation
	Liptodetrinite	Fragments or degradation residues of liptinites
Inertinite	Fusinite	Carbonized (fusinized) plant cell walls (from fires and other processes)
	Semifusinite	Partly humified and dehydrated plant tissues
	Funginite	Fungal spores and other fungal tissues
	Secretinite	Possible oxidation product of resins
	Macrinite	Dehydrated small, clumped (flocculated) peat matrix substances
	Inertodetrinite	Tiny, carbonized (fusinized) inertinite precursors
	Micrinite	Secondary coalification residues of liptinitic substances

Liptinitic organic matter generates more of the oil compared to the vitrinite, which is gas prone. The intertinite is generally comprises the recycled organic matter with no oil or gas generative property (Table 1).

Kerogen Kinetics

The petroleum evaluation in a sedimentary basin involves a quantitative approach, taking into account the amount of oil and gas generated by primary cracking of kerogen when temperature increases through time (Tissot and Espitalie 1984). The degradation of kerogen into hydrocarbons is described by a series of n parallel chemical reactions, each of which obey a first order kinetics, characterized by Arrhenius Law.

$$\frac{dXi}{dt} = -ki.Xi \quad \text{.....1}$$

1. $\frac{dXi}{dt}$ = hydrocarbon generation rate
   Xi= residual petroleum potential
   t=time (sec)

where ki is

$$ki = A\exp(-\frac{Ei}{RT}) \quad \text{..... 2}$$

2. A= Arrhenius constant; s^{-1}
   Ei =activation energy; kcal/mole
   R = molar gas constant; 0.00199 kcal/mole
   T = absolute temperature in degree Kelvin
   ki =rate constant for a reaction i

Combining Eq. 1 and 2,

$$\frac{dXi}{dt} = A\exp(-Ei/RT).Xi$$

Xi = The residual petroleum potential

$$Q = \sum_{i=1}^{n}(Xio - Xi)$$

where, Xio is the value of Xi at $t=0$

The activation energy and associated kinetic parameters are integrated with the burial and thermal history of the basin which are used in basin modelling studies to predict the amount and timing of generated hydrocarbons as function of time and temperature (Tissot and Espitalie, 1984).

ANALYTICAL METHODOLOGY

A range of geochemical analyses, comprising of organic and isotopic composition determination, are performed to determine the properties of source rocks. Kerogen, being insoluble in organic solvents is generally studied using petrological and pyrolysis methods. The biomarkers are studied using solvent extraction and chromatographic techniques. The kinetic parameters of thermal decomposition of kerogen are then combined with geological data for deciphering comprehensive maturity models for hydrocarbon generation and expulsion in sedimentary basins.

Rock Eval Pyrolysis

Rock Eval pyrolysis is a routinely used technique for source rock characterization. It involves thermal cracking of sedimentary organic matter in accordance with a programmed temperature pattern in an open system pyrolyzer to estimate the petroleum generation potential of the source rocks. The process occurs in two ovens, pyrolysis and oxidation (combustion), respectively of the Rock Eval

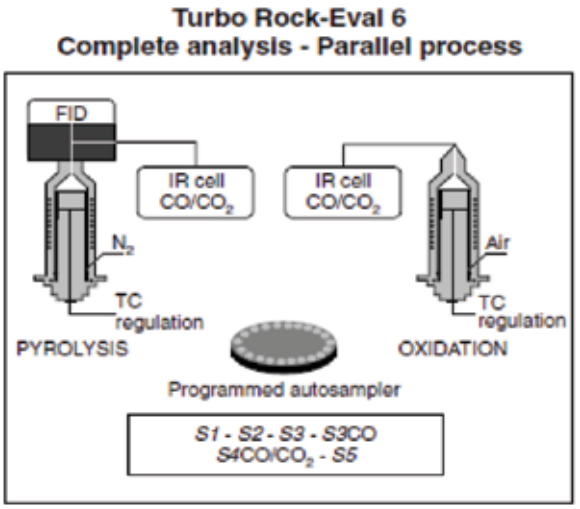

Figure 11. Schematic of Rock Eval 6 Pyrolyzer (after Behar et al., 2001)

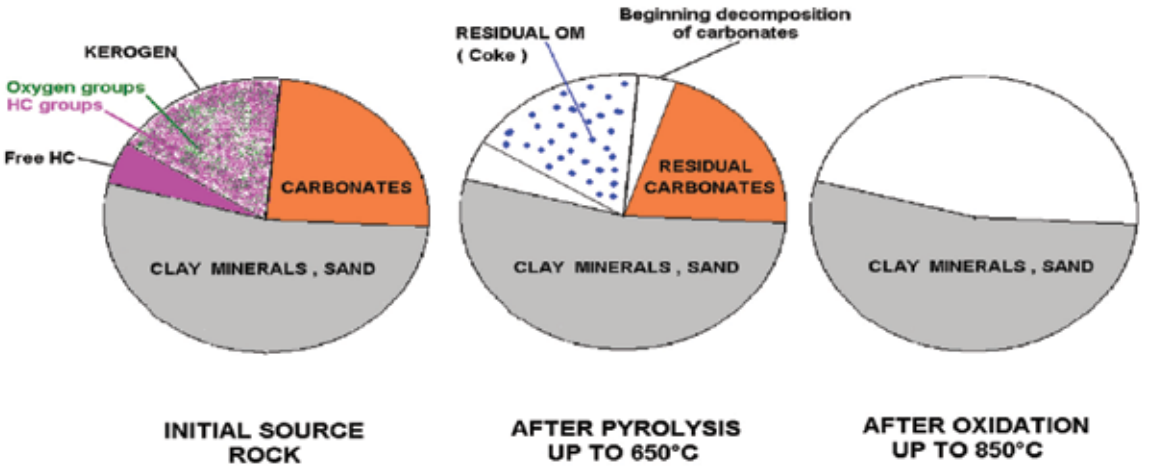

Figure 12. Evolution of a typical source rock during pyrolysis and oxidation in a rock eval pyrolyser (after Tissot and Espitalie, 1984)

pyrolyzer (Figure 11). The pyrolyzed hydrocarbons, both the thermo-labile ones (given by peak S1) and those obtained during the cracking of organic matter (given by peak S2), are detected by a flame ionization detector (FID). The residual rock, recovered after pyrolysis, is combusted in oxidation oven up to 850°C. The CO and CO_2 released during pyrolysis and oxidation processes are monitored online by an infrared cell. This enables the determination of organic and mineral carbon content of samples, defined as the TOC and MinC, respectively. The Tmax value is a thermal maturity parameter. It corresponds to the temperature at which the maximum amounts of hydrocarbons are released from the thermal degradation of kerogen, i.e., the temperature at which S2 peak reaches its maximum.

Among the other calculated parameters of Rock Eval, the hydrocarbon potential or HI is defined by 100 × S2/TOC. The OI is defined as 100 × S3/TOC, where S3 is the CO_2 released during the pyrolysis. These indices help in establishing the kerogen type and its maturity (Behar et al., 2001; Espitalié et al., 1987; Peters and Cassa, 1994; Mani et al, 2014). Figure 12 depicts the evolution of a typical source rock during pyrolysis and oxidation in a rock eval pyrolyser.

Depending upon the type of kerogen, the hydrocarbon generation capacity is different. Higher H/C ratios have greater possibility of generating oil. Thus, Type I kerogen is oil prone and generates significant amount of petroleum. With decrease of hydrogen content, and/or increase of O/C ratios, more and more gas prone behaviour of source rocks is exhibited (Figure 13)

Gas chromatography–mass spectrometry (GC-MS)

The composition and concentration of volatile gases and the biomarkers components in a source rock are determined using Gas chromatography. The gas chromatography–mass spectrometry (GC–MS) is a separation technique (GC),

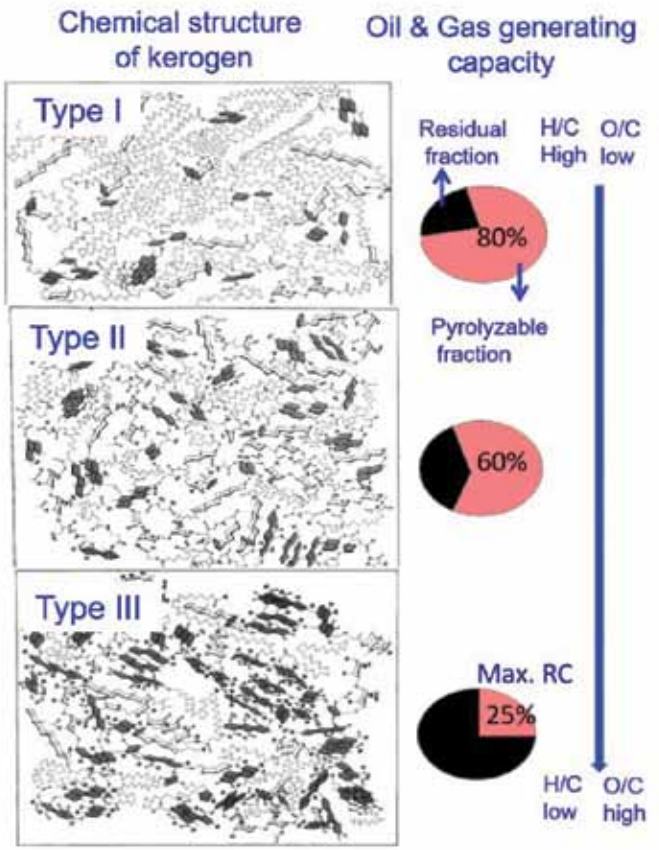

Figure 13. Chemical structure and hydrocarbon generating capacity of kerogen (after Vandenbroucke, 2003)

coupled with analytical power of mass spectrometre (MS). It is used to detect compounds using the relative gas chromatographic retention times and elution patterns of components of a mixture in combination with the mass spectral fragmentation patterns, which is the characteristic of a compound's chemical structures (Sneddon et al., 2007). A typical GC–MS system performs the following functions: (1) separation of individual compounds in a mixture by gas chromatography; (2) transfer of separated components to the ionizing chamber; (3) ionization; (4) mass analysis; (5) detection of the ions by an electron multiplier; and (6) data acquisition, processing, and display by a computer system (Figure 14).

As the individual organic compounds elute from the GC column, they enter the MS. During ionization, they are bombarded by a stream of electrons leading to the fragmentation into ions. The mass of the fragment, divided by its charge is the mass to charge ratio (*m/z*). Almost always, the charge is +1, and *m/z* ratio represents the molecular weight of the fragment. In general, MS are configured with magnetic sector or quadrupole type mass analyzers. A quadrupole GC–MS has a group of four electromagnets that focus each fragment through a slit into the detector. These are programmed to direct only certain fragments, one at a time (scan), until the complete range of *m/z* is recovered. This produces a mass spectrum, which is a graph of the signal intensity (relative abundance) versus the *m/z* ratios (essentially the molecular weight). Each compound has a unique fingerprint, and the software is equipped with a library of spectra for unknown compounds (Sneddon et al., 2007).

The homologous series of saturated and aromatic fractions are identified by characteristic masses of the fragmented ion and their retention times in the chromatographic column e.g. alkanes by $m/z = 57$; steranes by $m/z = 271$; hopanes by $m/z = 191$ etc. The individual compounds or their isomers in a series are identified by the characteristic fragmentation pattern of the molecular ions, its retention time, and use of respective biomarker standards and/or published mass spectra.

Isotope ratio mass spectrometry (IRMS)

Isotope ratio mass spectrometry (IRMS) has been widely used to determine the ratio of stable isotopes of several low molecular weight elements such as carbon ($^{13}C/^{12}C$) and oxygen ($^{18}O/^{16}O$) in geological samples. Stable isotopes provide important information on the origin and source of hydrocarbon gases and in oil to oil and oil to source rock correlation studies. Such studies are performed using

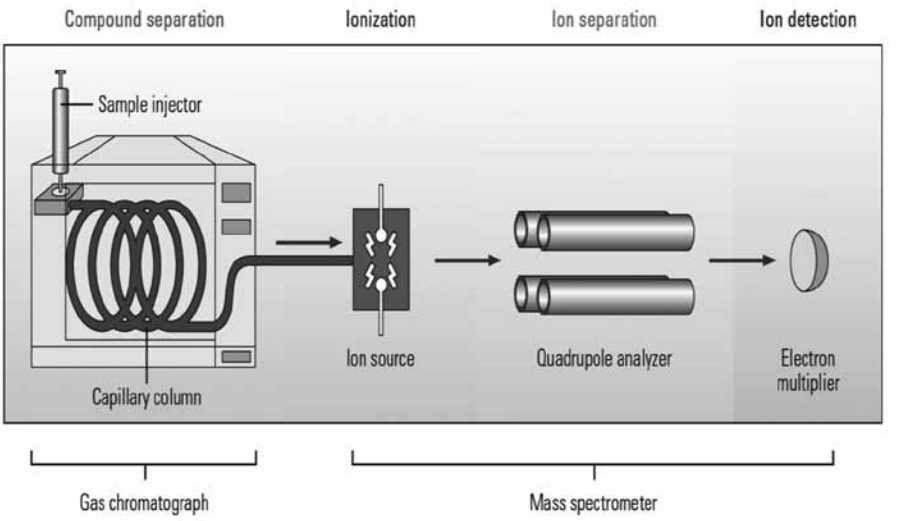

Figure 14. Components of a Gas Chromatograph-Mass Spectrometer.

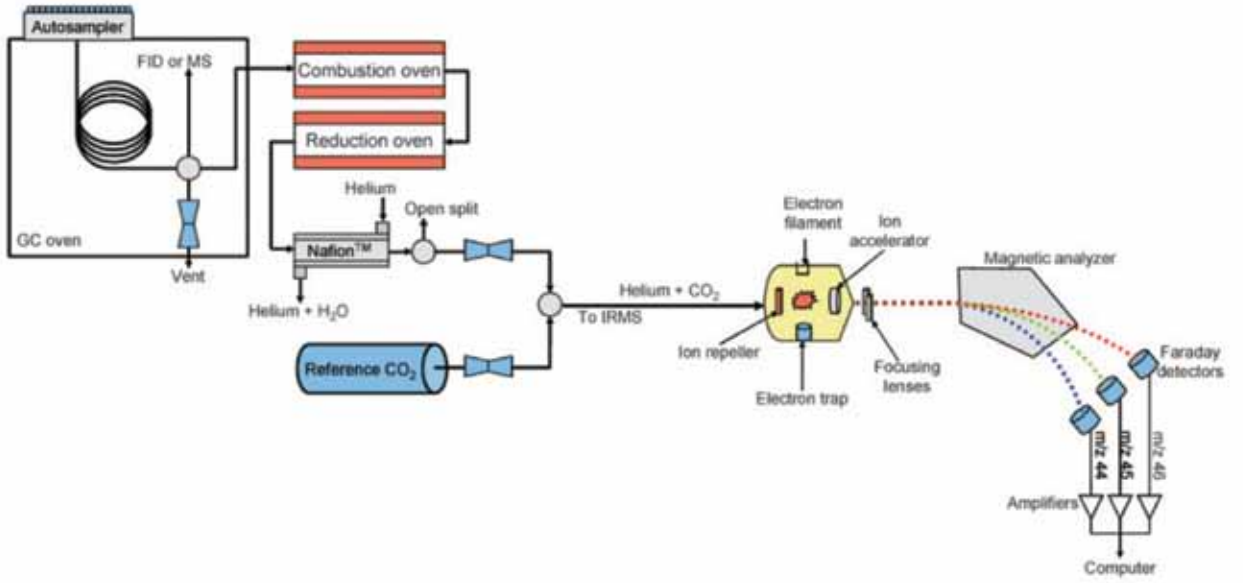

Figure 15. A schematic of Gas Chromatograph-Combustion-Isotope Ratio Mass Spectrometer (GC-C-IRMS)

hyphenated techniques, which include the separation power of a gas chromatograph coupled to the mass spectrometer, along with the introduction of a sample combustion interface into the gas chromatograph-IRMS (Platzner, 1997). Broadly, a mass spectrometer comprises of the (1) ion source for the fragmentation of the sample molecule into ions and (2) mass analyzer for separating and detecting the ion beam according to the mass of the respective ions (Figure 15). In GC–C–IRMS, the separated products of the sample mixture, carried in the stream of helium, are eluted at the output of the gas chromatograph and passed through an oxidation/reduction reactor and then are introduced into the ion source of mass spectrometer for the ratio determination. An open split-coupling device ensures that only a part of the sample/reference gas containing carrier gas is fed into the ion source, thus reducing the volume constraints and sample size. Continuous Flow-IRMS is a standard term used for the IRMS instruments, that are coupled online to preparation lines or instruments.

This includes the (1) Gas Chromatography–Combustion–IRMS (GC–C–IRMS), used for the compound specific isotope ratio determination of individual hydrocarbon components, (2) Gas Bench–IRMS (GB–IRMS), used for the C and O isotope ratio determinations on carbonates, and (3) Elemental Analyzer–IRMS (EA–IRMS), for the determination of bulk isotopic compositions of the coexisting organic matter.

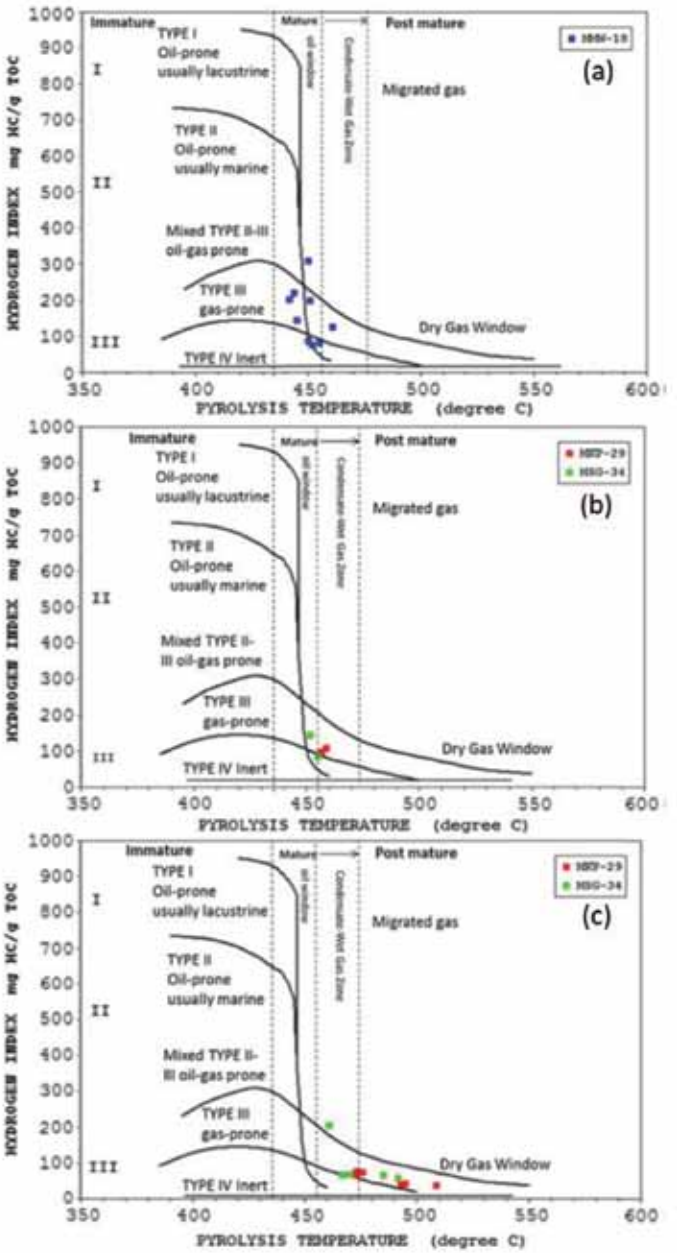

Figure 16. Kerogen type and thermal maturity of shales from Raniganj formation (MMW-18 borewell, represented in blue) (Figure a). Barren Measure formation (MKP-29 borewell represented in red and MSG-34 borewell represented in green) (Figure b); and Barakar Formation (MKP-29 borewell represented in red and MSG-34 borewell represented in green) (Figure c) of Damodar valley (Mani et al., 2015)

CASE STUDY

Gas generation potential of Permian shales in Damodar Valley basin

Jharia sub-basin, Damodar Valley:

Organic matter rich and thermally mature Permian shales are widely distributed in the Gondwana basins of Indian sub-continent. Gas shows have been reported in the wells drilled in the Raniganj area of Damodar Valley, which forms an important coal repository among the Indian Gondwana basins (Padhy and Das, 2013). Barakar and Raniganj are the main coal-bearing formations in the basin, and a marine/lacustrine succession that got deposited between these continental depositions resulted in the coal-devoid Barren Measure formation (Chandra, 1992). Thermal maturity of the coals surrounding the Barren Measure shale formation suggests it to be within the gas window (Padhy and Das, 2013), making it a potential shale gas target.

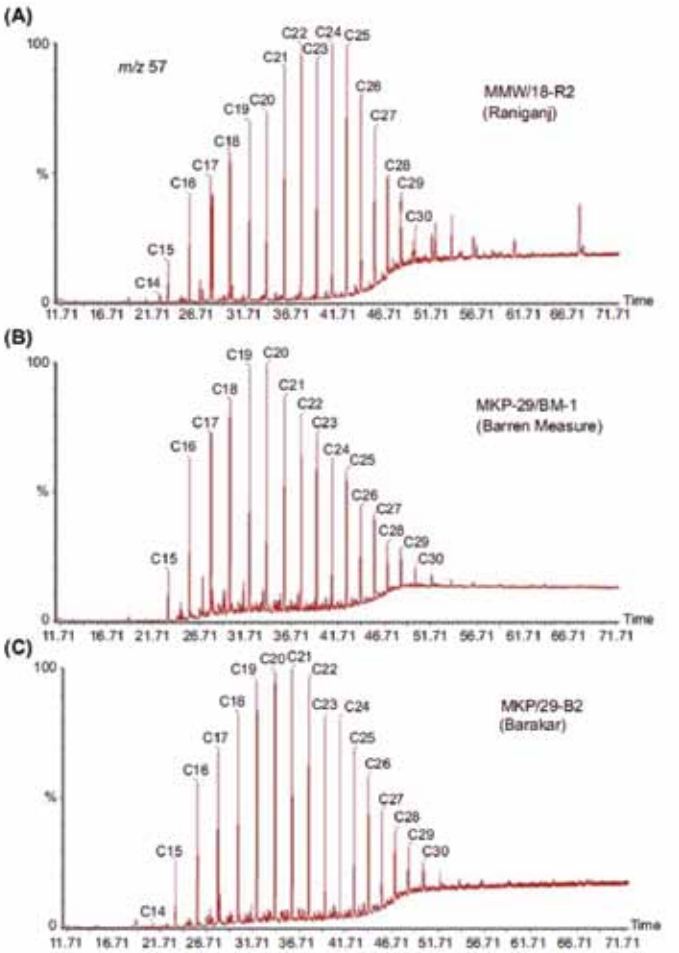

Figure 17. Saturated hydrocarbons (*n*C13 to *n*C30) in organic extracts of shales from Damodar Valley Basin (Mani et al., 2017)

The Permian shales from the Jharia sub-basin of Damodar Valley were studied for their organic matter properties, to infer the gas generation potential (Mani et al., 2015, 2017). Rock Eval pyrolysis of the shales showed excellent organic richness with TOC content ranging between 2.86% and 23.09%. Organic matter is characterized by Type II/III and Type III kerogen, and the thermal maturities span between the mature (oil window-gas condensate) and post-mature (dry gas) zone for hydrocarbon generation. The Raniganj and Barren Measure shales are in the late oil generation window, and the Barakar shales show post-mature stage for oil (Figure 16).

The bulk and compound specific carbon isotope ratios of hydrocarbon gases from the flash combustion and thermal desorption studies, respectively, of these shales indicate a thermogenic gas from the terrestrial organic matter, except for Barren Measure, where a lacustrine/marine source has been inferred (Mani et al., 2015). The isotopic compositions vary in a narrow range and are nearly similar for most of the studied samples (−40.4 to −44.8‰). The exposure of organic matter to high subsurface temperatures has not enriched or altered the $\delta^{13}C$ values significantly (Mani et al., 2015).

The organic matter in the shales was extracted and the aliphatic and aromatic biomarker constituents in it were studied using GC-MS (Mani et al., 2017). The total organic extract contains high proportion of saturated hydrocarbons in the range *n*C13 to *n*C30 and acyclic isoprenoids in all the samples (Figure 17).

The aromatic fractions in the organic extracts of the Raniganj, Barren Measure, and Barakar shale, in general, contain naphthalene, phenanthrene, biphenyl, and their alkylated derivatives, along with a low abundance of dibenzothiophene and its homologs. The ratio obtained by dividing the sum of odd carbon-numbered alkanes to the sum of even carbon-numbered alkanes has been defined by carbon preference index (CPI) (Didyk et al., 1978). It gives information on the maturity of the organic matter. The CPI of Damodar basin shales range from 0.9 to 1.1, which indicates no even or odd carbon preference and suggests the organic-rich sediments to be thermally mature. This is also corroborated by the unimodal peak

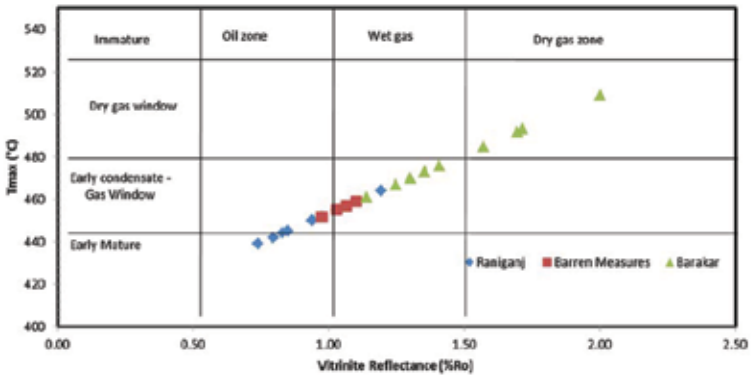

Figure 18. Thermal maturity of Permian shales from Damodar Valley Basin using Vitrinite reflectance and Rock Eval Tmax plot (Mani et al., 2015)

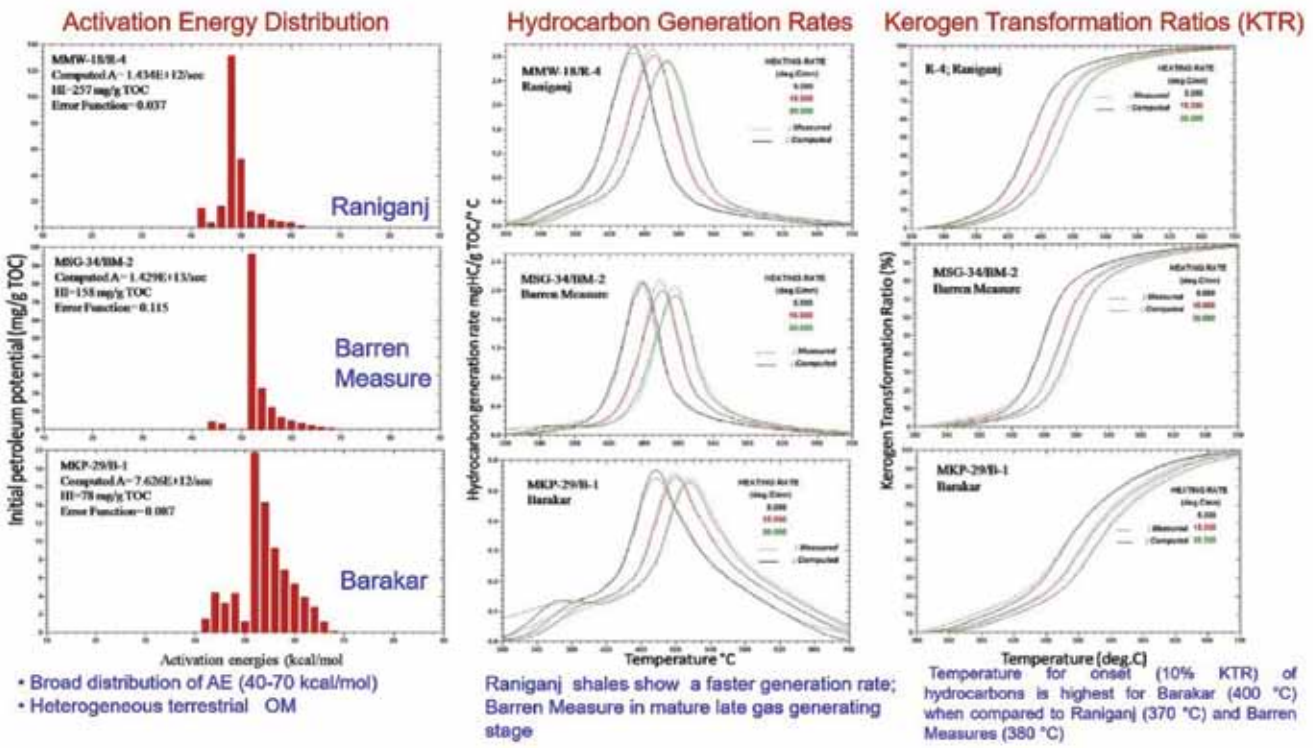

Figure 19. Kinetic parameters of Hydrocarbon generation obtained from the pyrolysis of shales from Damodar Valley Basin (Mani et al., 2015).

distribution of the n-alkanes. The differences of pristine to phytane (Pr/Ph) ratios, which indicate the oxygenation conditions during the deposition of the Damodar Valley shales, suggest that these shales were deposited in fluvio-marine and coastal swamp depositional environment under oxic to sub-oxic conditions. The ratios of α/β isomers in aromatic biomarkers are maturity dependent and their concentrations are useful in the calculation of temperature-sensitive maturity parameters. Such isomeric ratios, expressed in form of indices such as Methylphenanthrene indices (MPI-1), dimethylnaphthalene ratios (DNR-1 and DNR-2), and trimethylnaphthalene ratio (TNR-1) are high in Jharia shales, suggesting a mature to highly mature state of kerogen. The high maturity of the shales is also supported by the Tmax parameter of Rock Eval pyrolysis. Vitrinite and inertinite are the dominant macerals in the Jharia shales. Liptinite occurs sparsely (Mani et al., 2015). The Raniganj and Barren Measure shales show vitrinite and inertinite macerals, with lesser occurrence of liptinite. The random reflectance (Rr%) varies between 0.99 and 1.22 for Raniganj shales and 1.1–1.41 for the Barren Measure. The Barakar shales consist mainly of vitrinite and inertinite with a random reflectance ranging between 1.11 and 2.0.

Further, the mineral matrix is characterized by abundant clay minerals with siderite and pyrite. The kinetic parameters obtained during pyrolysis studies indicate that Raniganj has lower activation energies (ΔE = 42–62 kcal/mol) in comparison to Barren Measure and Barakar (ΔE = 44–68 kcal/mol) (Figure 19, Mani et al., 2015). Temperature for onset (10%), middle (50%), and end (90%) of kerogen transformation is least for the Raniganj shales (Mani et al., 2015). It is followed by the Barren Measure and Barakar shales.

Thus, the organic geochemical and stable isotopic studies carried out on the Permian Gondwana shales from Jharia sub-basin of Damodar Valley, in particular, those from the Barren Measure formation, demonstrate excellent properties of a potential shale gas system (Mani et al., 2015). These shales possess abundant organic matter in highly mature stage for generation of gaseous hydrocarbons. Integration of organic geochemical, stable isotope, mineralogical and petrological data with the stratigraphic extent, thickness and structural features such as faults and fractures associated with the shale horizons is important for the shale gas exploratory studies in the basin.

SUMMARY

Source rock characterization using geochemical logs and maps is necessary in a sedimentary basin analysis with the objective of identifying the pod of active or potential source rock. A source rock can be described as potential (could generate oil), effective (generated or currently generating oil), or spent (generated oil). A spent source rock can still generate gas. The pod of active source rock contributes hydrocarbons to the petroleum system. Source rock assessments include determination of its richness, kerogen type, thermal maturity, product generated, time, and provenance or depositional environment. The organic richness of the source rock organic can be poor, fair, good, very good, or excellent and the kerogen can be described as type I, II, III, or IV, based on petrological and geochemical analyses. The source rocks can be immature, mature, and postmature, based on parameters like vitrinite reflectance, Tmax, and thermal alteration index. Geochemical logs of closely spaced Rock-Eval pyrolysis and TOC, vitrinite reflectance, lithology, and related data are indispensable tools in the sedimentary basin evaluation process. Useful geochemical logs require adherence to systematic sampling and proper procedures for sample preparation, analysis, and interpretation. The logs generated from such datasets aid in identify petroleum source rocks (as potential, effective, or spent), the thermal maturation gradient (including immature, mature, and postmature zones), and in situ and migrated petroleum shows. These rapid and inexpensive screening methods generate libraries of geochemical logs that progressively reduce the risk associated with petroleum exploration as the study region becomes more thoroughly sampled. Logs from various locations can be used to map the pod of active source rock, regional variations in organic facies, and the volume of generated petroleum. This information can be used as input to refine mathematical basin models. As hydrocarbons have become more difficult to discover and recover, the ever more precise forms of analysis to differentiate between a viable prospect and a dry hole can be provided essentially by exploration geochemistry.

ACKNOWLEDGEMENTS

The contents of this paper form part of the invited lecture delivered by the author upon conferment of Indian Geophysical Union - Krishnan Gold Medal – 2017. The author is extremely thankful to the IGU for the award and acknowledges CSIR-NGRI, particularly, the petroleum geochemistry group, for the support towards the research.

Compliance with Ethical Standards

The author declare that she has no conflict of interest and adhere to copyright norms

REFERENCES

Bjørlykke, K., 2015. Introduction to Petroleum Geology Chapter 1 In: K. Bjørlykke (ed.), Petroleum Geoscience: from sedimentary environments to Rock Physics, DOI 10.1007/978-3-642-34132-8_1, # Springer-Verlag Berlin Heidelberg.

Briggs, D. and Roger E. Summons, 2014. Ancient biomolecules: Their origins, fossilization, and role in revealing the history of life. BioEssays 36(5).

Behar, F., Beaumont, V., Penteado, H.L. and De, B., 2001. Rock-Eval 6 technology: performances and developments oil & gas science and technology. Rev. IFP, 56 (2), 111–134.

Chandra, D., 1992. Jharia Coalfield. Mineral resources of India 5. Geological Society of India, Bangalore, pp. 149.

Didyk, B.M., Simoniet, B.R.T., Brassell, S.C. and Eglington, G., 1978. Organic geochemical indicators of paleoenvironmental conditions of sedimentation. Nature, 272, 216–222.

Eden, H. and Mungo, D., 2013. Geochemistry-the dark horse upstream. Geo Expro 10(1), 22-25.

Espitalie, J., Marquis, F. and Sage, L., 1987. Organic geochemistry of the Paris Basin. In: Brooks, J., Glennie, K. (Eds.), Petroleum Geology of North West Europe. Graham and Totman, London, 71–86. http://www.uky.edu/KGS/coal/coal-macerals.php#

Hunt, J.M., 1996. Petroleum Geology and Geochemistry. W. H. Freeman and Company, San Francisco, p. 617.

Mani, Devleena, Patil, D.J. and Dayal, A.M., 2011. Stable carbon isotope geochemistry of near surface adsorbed alkane gases in Saurashtra basin**.** Chem. Geol., 280(1-2), 144–153.

Mani, Devleena, Dayal, A.M., Patil, D.J., Mateen Hafiz, Naveen Hakoo and Bhat, G.M., 2014. Gas potentiality of Proterozoic and Phanerozoic shales from NW Himalaya, India: Inferences from new pyrolysis data, Int. J. Coal Geol., 128-129, 81-95,

Mani, Devleena, Patil, D.J., Dayal, A.M. and Prasad, B.N., 2015. Thermal maturity, source-rock potential and kinetics of hydrocarbon generation in Permian shales of Damodar Valley basin, Eastern India, Marine and Petrol. Geol., 66, 1056-1072.

Mani, Devleena, Kalpana, M.S., Patil, D.J. and Dayal, A.M., 2017. Organic matter in gas shales: Origin, evolution and characterization. Chapter in Shale Gas: Exploration, Environmental and Economic impacts, 3, 25-52.

Magoon, L.B. and Dow, W.G., 1994. The petroleum system: From source to trap: AAPG Memoir 60, 655 pp.

Padhy, P.K. and Das, S.K., 2013. Shale oil and gas plays: Indian sedimentary basins. Geohorizons, 18(1), 20-25.

Peters, K.E., Walters, C.C. and Moldowan, J.M., 2005. The Biomarker Guide: Biomarkers and isotopes in the environment and human history, 1, Cambridge Press, pp. 1115.

Peters, K.E. and Cassa, M.R., 1994. Applied source rock geochemistry. In: Magoon, L.B., Dow, W.G. (Eds.), The Petroleum system from source to trap, AAPG Memoirs, 60, 93-120.

Peters, Kenneth E., David J. Curry, and Marek Kacewicz, 2012. An overview of basin and petroleum system modeling: Definitions and concepts, in Peters, Kenneth E., David J. Curry, and Marek Kacewicz, eds., Basin modeling: New horizons in research and applications: AAPG Hedberg Series no. 4, p. 1-16.

Petsch, S.T., 2014. Weathering of Organic Carbon, Treatise on Geochemistry, 217-238. doi 10.1016/B978-0-08-095975-7.01013-5.

Schidlowski, M., 1987. Application of stable Carbon isotopes to early biochemical evolution on Earth. Annual Rev. Earth Planet. Sci., 15, 47-72.

Sharp, Z., 2017. Principles of stable isotope geochemistry, 2nd Edition doi 10.5072/FK2GB24S9F

Sneddon, J., Masuram, S. and Richert, J.C., 2007. Gas chromatography-mass spectrometry-basic principles, instrumentation and selected applications for detection of organic compounds. Anal. Lett. 40:6, 1003–1012. http://dx.doi.org/10.1080/00032710701300648.

Tissot, B.P. and Welte, D.H., 1984. Petroleum formation and occurrence. A new approach to Oil and Gas, 2nd Edition, Springer Verlag.

Vandenbroucke, M., 2003. Oil and gas science and technology – Rev. IFP, 58(2), 243-269.

Van Krevelen, D.W., 1961. Coal typology-Chemistry-Physics-constitution. Elsevier, Amsterdam.

Received on: 30.11.18; Revised on: 12.12.18; Accepted on: 16.12.18

J. Ind. Geophys. Union (January 2019)
v.23, no.1, pp: 28-40

Delineation of the Trap and sub-trappean sediments in Kutch, Deccan syneclise and Bengal basins-An analysis

A.S.N. Murty[1]*, A.S.S.S.R.S. Prasad[2], and Kalachand Sain[2]

[1]*19-104/4, Kalyanpuri, Uppal, Hyderabad-500 039, India
[2]CSIR-National Geophysical Research Institute, Uppal Road, Hyderabad, India
*Corresponding Author: asnngri@gmail.com

ABSTRACT

Conventional seismic reflection data are not well suited for imaging sub-trappean sediments. In this paper, we report on seismic imaging investigations that used large-offset refraction and wide-angle reflection data from three regions of India, namely, the Kutch basin, the Deccan syneclise, and the Bengal basin. We use travel time modeling of refracted and reflected phases to derive the basement configuration, including the Trap and subtrappean sediment thickness. Some of the record sections show sharp amplitude decays (attenuation) of the refracted phase from the high velocity Traps and travel time delays between the Trap and basement refracted phases, which can be diagnostic of the presence of a low-velocity zone (LVZ) consisting of sediments beneath basalt. We identify reflected phases from the top and bottom of the LVZ. Analysis of the refracted and reflected phases suggests that the relative thickness of the overlying high-velocity and underlying low- velocity sediments, play a major role in the seismic data quality. The sediment thickness also affects the magnitudes of the attenuation, the travel time delay, and the strength of the reflection. In the Kutch area, we find that the Deccan Traps are thin (about 100-800 m), and sub-trappean Mesozoic sediments are about 2 km thick. In the Deccan syneclise, the Traps are relatively thin in the north and Tertiary and sub-trappean Mesozoic sediments are thick in the southwest. Towards the east, the Trap and subtrappean Mesozoic sediments are about 1 km thick. Further east, near the Satpura basin, the Deccan Traps are about 1 km thick, and sub-trappean Gondwana sediments are quite thin (100-400 m). Similarly, in the west Bengal basin, the Rajmahal Traps are about 1 km thick, while the subtrappean Gondwana sediments are 1.8 km thick near Palashi. These results provide crucial information needed for more detailed hydrocarbon exploration in sub-trappean sediments.

Key Words: Seismic refraction, 2-D Travel time inversion, Mesozoic sediments, Deccan Traps, Saurashtra.

INTRODUCTION

Deccan volcanic rocks (Upper Cretaceous) cover large areas in western and central India (Kutch, Deccan syneclise (Figure 1a, b), whereas Rajmahal Volcanic rocks (Upper Jurassic-Lower Cretaceous) cover the eastern part (Bengal basin) (Figure 1c). Outcrops of Mesozoic and Gondwana sediments are present in the adjoining areas of Kutch, the western and eastern parts of Deccan syneclise, and in the west Bengal basin (Prasad et al., 2010, Murty et al., 2008, Kaila, 1988; Kaila et al., 1985, 1981, Mall et al., 2002). A significant amount of these sediments is reported to underlie the volcanic rocks (Traps) (NGRI, 1998, 2004, Murty et al., 2008, Mall et al., 2002)). The oil industry has been engaged in exploring Trap-covered regions for geologic and tectonic studies and hydrocarbon potential because Mesozoic sediments are source rocks for more than 50% of hydrocarbon reserves worldwide (Bois et al., 1982). Seismic imaging in the Trap-covered regions is a complex problem. Conventional seismic reflection methods have not been successful because of reverberations between high-velocity volcanic and low-velocity rocks. Large impedance contrasts within the volcanic sequences, caused by interbeds, breccia and vesicles, contaminate the primary reflections of interest with multiples and scattered noise in this range (Catchings and Mooney, 1988; Pujol et al. 1989, Jarchow et al., 1994; Sain et al., 2002). Subtrappean sediments form a low-velocity zone (LVZ) in seismic data sections because a high-velocity Trap layer is underlain by lower velocity sediments. Seismic refraction studies that used large energy sources can provide high-amplitude reflections from subtrappean interfaces at wide angles, where the noise is less dominant (Catchings and Mooney, 1988; Jarchow et al. 1994, Sain and Kaila 1996). Also, in certain favourable geological conditions, a high-velocity Trap layer that is underlain by low-velocity sediments causes seismic attenuation and travel time delays in the refracted first-arrivals; the magnitudes of the attenuation and delays being a function of the relative thickness of the two layers and their velocities (Catchings and Mooney, 1988; Tewari et al., 1995). Attenuation and travel time delays in the refracted phases and wide-angle reflected phases from top of the LVZ and basement, are indicative of low-velocity sediments beneath high-velocity volcanic rocks. Therefore, seismic refraction and wide-angle reflection data sets can be effectively used to constrain the subsurface velocity structure in Trap covered regions (Tewari et al., 1995; Fruehn et al., 2001; Murty et al., 2008; 2010; 2011).

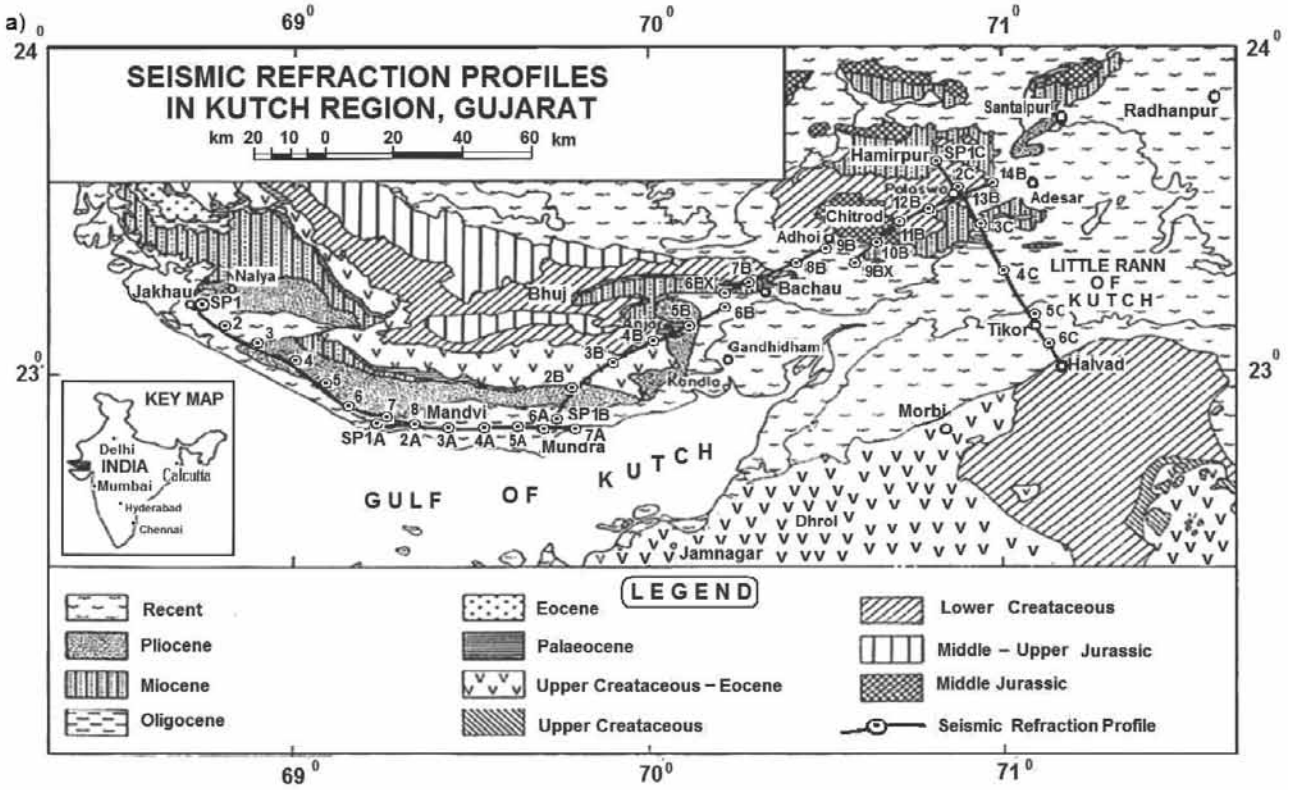
a)
SEISMIC REFRACTION PROFILES
IN KUTCH REGION, GUJARAT
km 20 10 0 20 40 60 km
KEY MAP
Delhi
INDIA
Calcutta
Mumbai
Hyderabad
Chennai
Santalpur
Radhanpur
Hamirpur
Adesar
Chitrod
Adhoi
Bachau
Nalya
Jakhau
Bhuj
LITTLE RANN OF KUTCH
Tikor
Halvad
Gandhidham
Kandla
Mandvi
Mundra
Morbi
Dhrol
Jamnagar
GULF OF KUTCH
LEGEND
Recent
Pliocene
Miocene
Oligocene
Eocene
Palaeocene
Upper Creataceous – Eocene
Upper Creataceous
Lower Creataceous
Middle – Upper Jurassic
Middle Jurassic
Seismic Refraction Profile

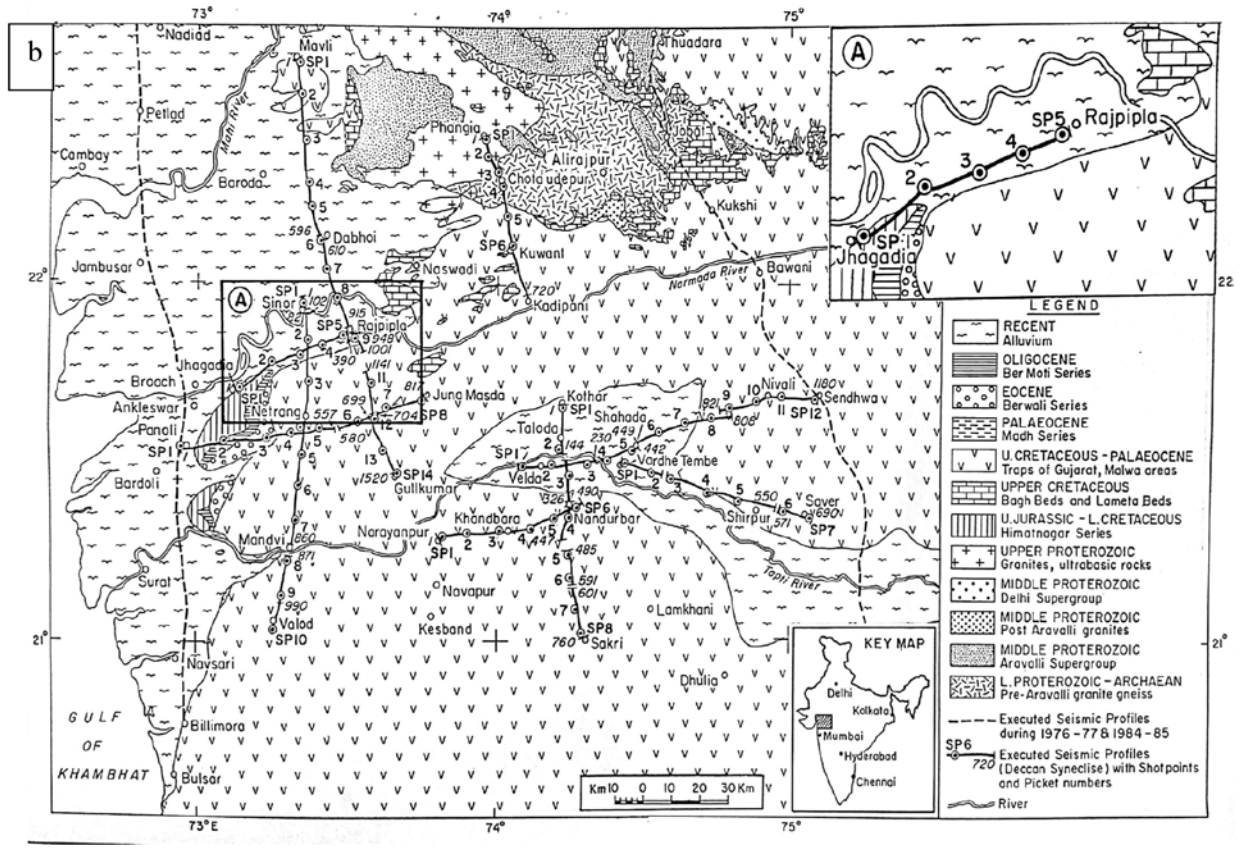
b
Nadiad
Mavli
Petlad
Cambay
Baroda
Dabhoi
Jambusar
Broach
Ankleswar
Panoli
Bardoli
Surat
Navsari
Billimora
Bulsar
GULF OF KHAMBHAT
Thuadara
Phangia
Alirajpur
Chotaudepur
Kukshi
Kuwant
Naswadi
Kadipani
Bawani
Narmada River
Jung Masda
Kothar
Shahada
Taloda
Vardhe Tembe
Nivali
Sendhwa
Velda
Gullkumar
Narayanpur
Khandbara
Nandurbar
Shirpur
Saver
Navapur
Kesband
Lamkhani
Sakri
Dhulia
Tapti River
Rajpipla
Jhagadia
LEGEND
RECENT
Alluvium
OLIGOCENE
Ber Moti Series
EOCENE
Berwali Series
PALAEOCENE
Madh Series
U.CRETACEOUS - PALAEOCENE
Traps of Gujarat, Malwa areas
UPPER CRETACEOUS
Bagh Beds and Lameta Beds
U.JURASSIC - L.CRETACEOUS
Himatnagar Series
UPPER PROTEROZOIC
Granites, ultrabasic rocks
MIDDLE PROTEROZOIC
Delhi Supergroup
MIDDLE PROTEROZOIC
Post Aravalli granites
MIDDLE PROTEROZOIC
Aravalli Supergroup
L.PROTEROZOIC - ARCHAEAN
Pre-Aravalli granite gneiss
Executed Seismic Profiles during 1976 - 77 & 1984 - 85
Executed Seismic Profiles (Deccan Syneclise) with Shotpoints and Picket numbers
River
KEY MAP
Delhi
Kolkata
Mumbai
Hyderabad
Chennai
Km 10 0 10 20 30 Km

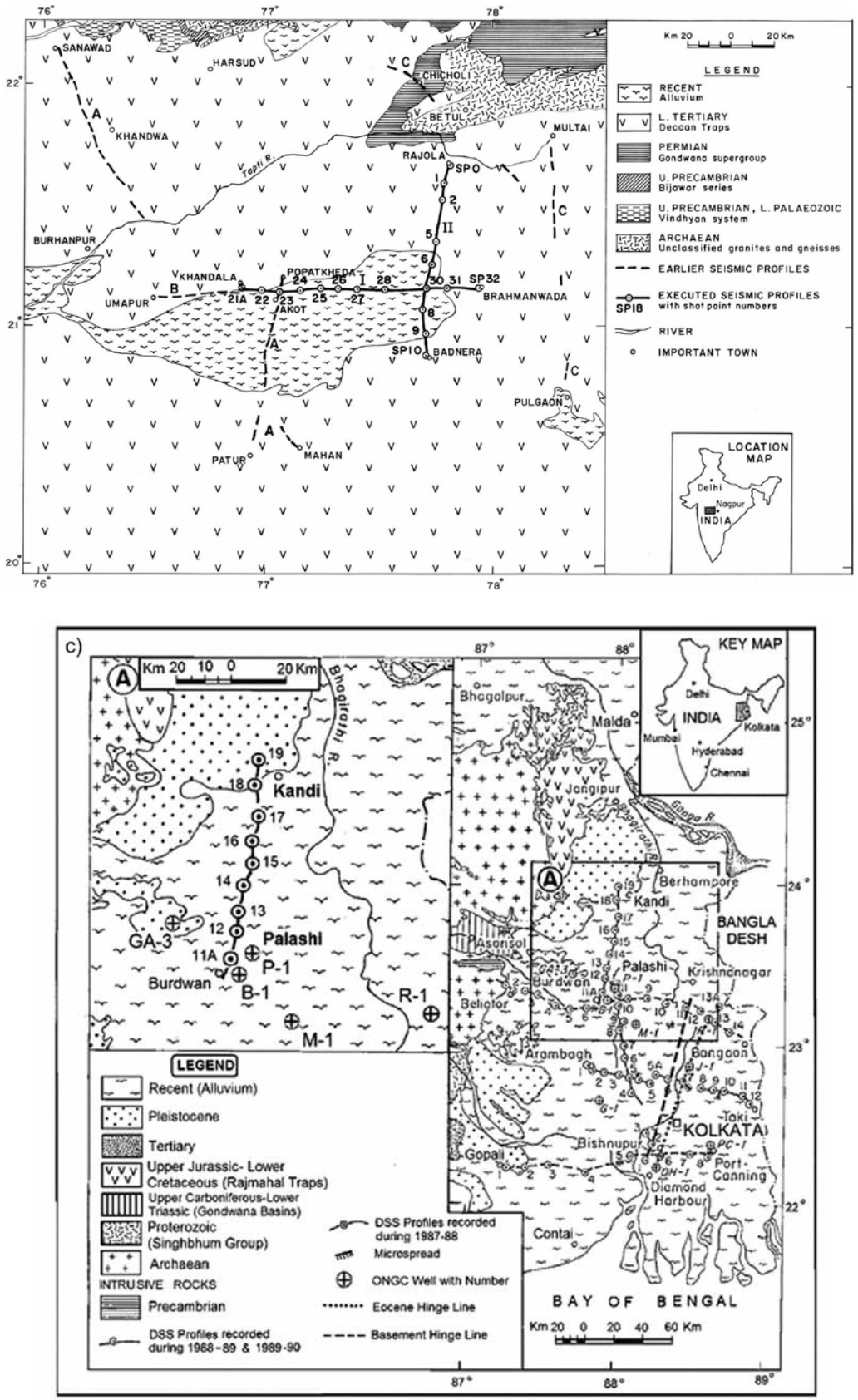

Figure 1. Location of the seismic profiles in (a) Kutch area, (b) Deccan Synclise and (c) West Bengal basin (after Rajendra Prasad et al., 2010, Murty et al., 2011a, 2011b, Murty et al., 2008).

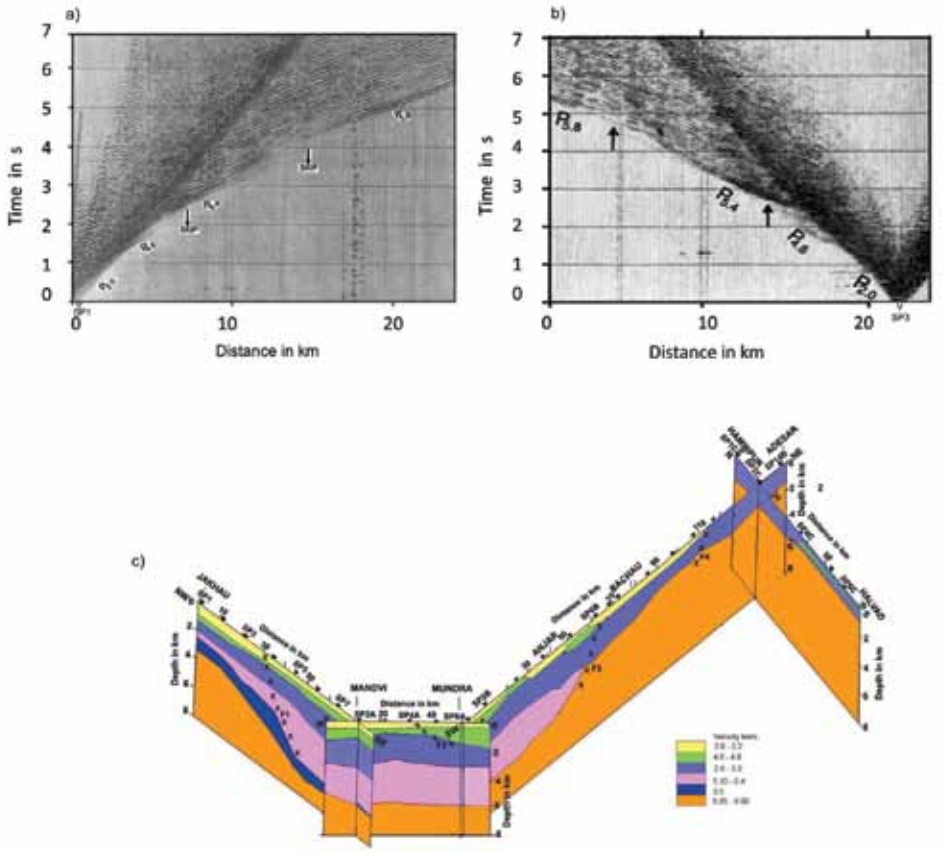

Figure 2. Record sections of reversing shot points (a) SP1 and (b) SP3 in the Kutch on-land basin plotted with distance (km) vs. time (s). $P_{2.0}$, $P_{4.6}$, $P_{5.4}$ and $P_{5.8}$ are first-arrival refracted phases. Amplitude decay in the Trap refracted phase ($P_{4.6}$) and the time skip between $P_{4.6}$ and $P_{5.8}$, indicate the presence of a low-velocity zone, (c) Shallow crustal velocity model along the four segments (Jakhau-Mandvi, Mandvi-Mundra, Mundra-Adesar and Hamirpur-Halvad) in the Kutch basin (after Rajendra Prasad et al., 2010).

Deep Seismic Sounding (DSS) studies in the Cambay-Narmada-Tapti region (Kaila et al., 1981, Sridhar and Tewari, 2001) indicate the presence of subtrappean Mesozoic sediments in grabens, separated by a horst. Similar studies in the eastern part of Deccan syneclise (Kaila, 1986, Mall et al., 2002), indicate the presence of Gondwana sediments beneath the Traps. Integrated geophysical studies were carried out by the National Geophysical Research Institute (NGRI) in Kutch (NGRI, 2000), the western part of Deccan syneclise (NGRI, 2004), which delineated Mesozoic sediments. The integrated studies in the eastern part of the Deccan syneclise (NGRI, 2009) between the Satpura basin (NE) and Godavari Gondwana (SE) graben in central India, also delineated Gondwana sediments beneath the Traps. Kaila et al. (1992) and Murty et al. (2008) further delineated subtrapppean Gondwana sediments beneath the Rajmahal Traps in west Bengal basin. In the present study, we analyze the seismic refraction and wide-angle reflection data sets of Kutch, the Deccan syneclise and the Bengal basins, primarily to delineate thickness variations of the Trap and subtrappean sediments.

SEISMIC DATA ANALYSIS

In all seismic record sections displayed in this paper, we use the term P_i as the P-wave refraction through layer i and P^i as the P-wave reflections from top of layer i.

Kutch basin: Using two DFS-V seismic acquisition systems, seismic refraction data were acquired (NGRI, 2000) along the Jakhau-Mandvi (NW-SE), Mandvi-Mundra (W-E), Mundra-Adesar (SW-NE) and Hamirpur-Halvad (N-S) profiles, which totalled 355 km in length (Figure 1a). All the shots were recorded to an offset of 48 km, with a shot interval of 8-12 km, and a receiver interval of 100 m, using 4-ms sampling interval. Data were recorded simultaneously in (a) analog form on photographic paper, and (b) digital form (SEG B) on magnetic tapes. First-arrival refraction data were picked from monitor records and travel time curves were prepared. Shot gathers of two reciprocal shot points (SP1 and 3) along the Jakhau-Mandvi profile is shown in figure 2a, b. Based on the slopes of the travel time curves, we identify four refracted phases $P_{2.0}$, $P_{4.6}$, $P_{5.4}$ and $P_{5.8}$. The direct wave ($P_{2.0}$) with a velocity

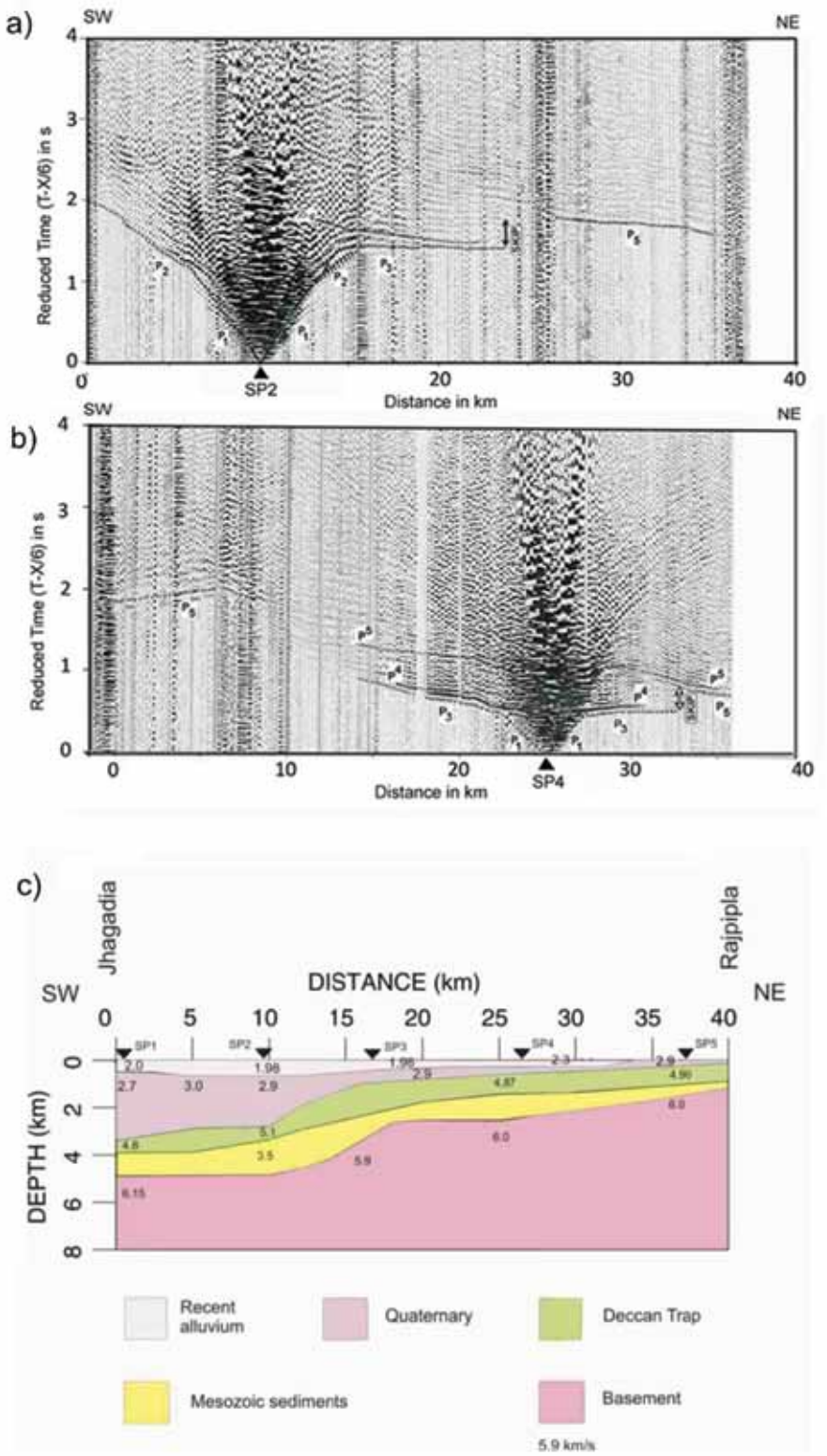

Figure 3. Record sections for shot points (a) SP2 and (b) SP4 from the western Deccan syncline, along the Jhagadia-Rajpipla (SW-NE) profile. P_1, P_2, P_3 and P_5 are first-arrival refracted phases. Amplitude decay in the Trap refracted phase (P_3) and time skip between P_3 and P_5 indicate the presence of a low-velocity zone. P^4 and P^5 are wide-angle reflected phases from the top and bottom of the low-velocity zone (c) Shallow crustal velocity model along Jhagadia-Rajpipla profile (after Murty et al., 2011a).

2.0 kms^{-1} propagates within the alluvium (Tertiary) layer that is observed at the surface. The velocities of the second, third, and fourth phases are 4.6, 5.4, and 5.8 kms^{-1}, respectively. These velocities are characteristic of Deccan Trap, limestone, and granitic basement rocks, respectively, in this region (Kaila et al., 1981). Shot gathers indicate amplitude decay in the $P_{4.6}$ and $P_{5.4}$ refracted phases and time skip between refracted phases $P_{4.6}$ - $P_{5.4}$ and $P_{5.4}$ - $P_{5.8}$ indicating the presence of low-velocity zones (LVZ) between $P_{4.6}$ and $P_{5.4}$ and $P_{5.4}$ and $P_{5.8}$. The low-velocity zones might be responsible for the decay of energy from the overlying high-velocity layer and the delay in arrival time of the refracted from the deeper high-velocity layer (Greenhalgh, 1977). The Trap refracted segment $P_{4.6}$ is short, indicating that the Deccan Trap layer is thin in this region. We observe the magnitudes of the amplitude decay and time skips to be a function of the relative thickness of both high- and low-velocity layers. Considering the prominent amplitude decay and time skips in the first-arrival refraction data, two LVZs are interpreted between $P_{4.6}$ and $P_{5.4}$ (Late Mesozoic) and $P_{5.4}$ and $P_{5.8}$ (Early Mesozoic) respectively along the Jakhau-Mandvi profile.

Deccan Syneclise

Seismic refraction studies were carried out along nine profiles, covering a total length of 700 km in the western part of Deccan syneclise (NGRI, 2004), and four profiles covering a total length of 600 km in the eastern part (NGRI, 2009) (Figure 1b). The data were recorded using RF Telemetry systems with a 100-m receiver interval, 8-10 km shot interval and 2 ms sampling interval. The data were recorded in SEG-D and converted to SEG-Y format. Record sections were generated from the SEG-Y data plotting the traces at their straight distance positions and band pass filtering (5-20 Hz); the traces were normalized and plotted in a reduced-time scale with a reduction velocity 6.0 km s^{-1}. Record sections of two shot points (SP2 and SP4) along the Jhagadia-Rajpipla profile (Figure 3a,b), two shot points (SP3 and SP4) along the Kothar-Sakri profile (Figure 4 a,b), in the western part, and two shot points (SP22, SP23) along the Khandala- Brahmanwada profile (Figure 5 a,b) in the eastern part of Deccan syneclise, are displayed. We picked refracted and reflected travel times from phases identified with pick uncertainties ranging between 20 to 100 ms, depending on the pick quality and S/N ratio. We used refraction data to derive an initial model, and computed reflected times from the model to pick a more reliable phase of the reflection band consisting two cycles. Reciprocal times of the identified phases were checked for every pair of shot points.

The record section of SP 2 (Figure 3a) along the Jhagadia-Rajpipla profile of the western Deccan Syncline, shows four first-arrival refracted phases P_1, P_2, P_3, P_5. From the velocities of the phases (1.95-2.0, 2.7-2.9 km s^{-1}) and the surface geology, P_1 and P_2 represent phases from the Tertiary (Recent and Quaternary respectively) sediments. The velocities of P_3 and P_5 are 5.1 and 6.15 kms^{-1} – a characteristic of Deccan Traps and granitic basement, respectively. There exists an amplitude decay at 14 km offset from SP2 NE and also a time skip between the two refracted phases (P_3 and P_5), indicating the presence of a low-velocity zone (LVZ) beneath the trap layer. The same phenomena of attenuation and travel time delay is observed in SP 4 (Figure 3b). Record sections for shot points 2 and 3 also show a wide-angle reflected phase (P^4), just above first-arrival refracted phase (P_3). The strong reflected phase immediately after the first-arrival; Trap refracted phase indicates the existence of a large velocity contrast. An apparent travel time delay and amplitude decay in the high-velocity refracted phase and the presence of a strong reflected phase just above the refracted phase (due to large velocity contrast), strengthens our argument for a LVZ beneath the Trap cover. We interpret this reflected phase as arising from the top of the LVZ. Similarly, we interpret another reflected phase (P^5) seen from SP 4, but we lack reversed coverage for that phase. We interpret P^5as a wide-angle reflected phase from the bottom of the LVZ. We observed the Trap refracted phase (P_3) from SP2, occurs at ~ 5 km offset from shot point 2 NE (SP 2, Figure 3a), whereas the refracted phase (P_2) observed as far as 10 km towards the SW does not include a high-velocity refracted (P_3) phase. This indicates that the high-velocity Trap layer is deeper in the SW direction. Based on the above observations and on the exposures of Mesozoic sediments near Rajpipla, we infer that a low-velocity layer corresponding to Mesozoic sediments lies between the basement and the Deccan Traps.

The reversing shot points (SP3 and SP4) along the Kothar-Sakri (N-S) profile (Figure 4a,b) are located east of the Jhagadia-Rajpipla profile, in the western part of the Deccan syneclise. The first two phases (P_1 and P_2) with apparent velocities of 4.5-4.7 km s^{-1} and 5.0-5.2 km s^{-1}, respectively, may represent two flows of Deccan Traps, and the third phase (P_3) with an apparent velocity 6.0 km s^{-1}, may correspond to the basement. (P_2) extends to large offsets, indicating that the Deccan Trap layer is thick in this part of the profile. We observe amplitude decay in the Trap refracted phase (P_2) and a travel time delay between the Trap and basement refracted phases (P_2 and P_3 in SP 4). Record sections show a reflected phase, which we designate as P^2 just above the Trap refracted phase (P_2); we interpret P^2 as a reflection from the top of the LVZ. We interpret another reflected phase (P^3) as a reflection from the bottom of the LVZ. P^3 is relatively weak, probably due to attenuation of the seismic wave that propagates through thick Trap and LVZ layers.

Shot gathers from reversing shot points (SP 22 and 23) along the Khandala-Brahmnawada profile in the eastern

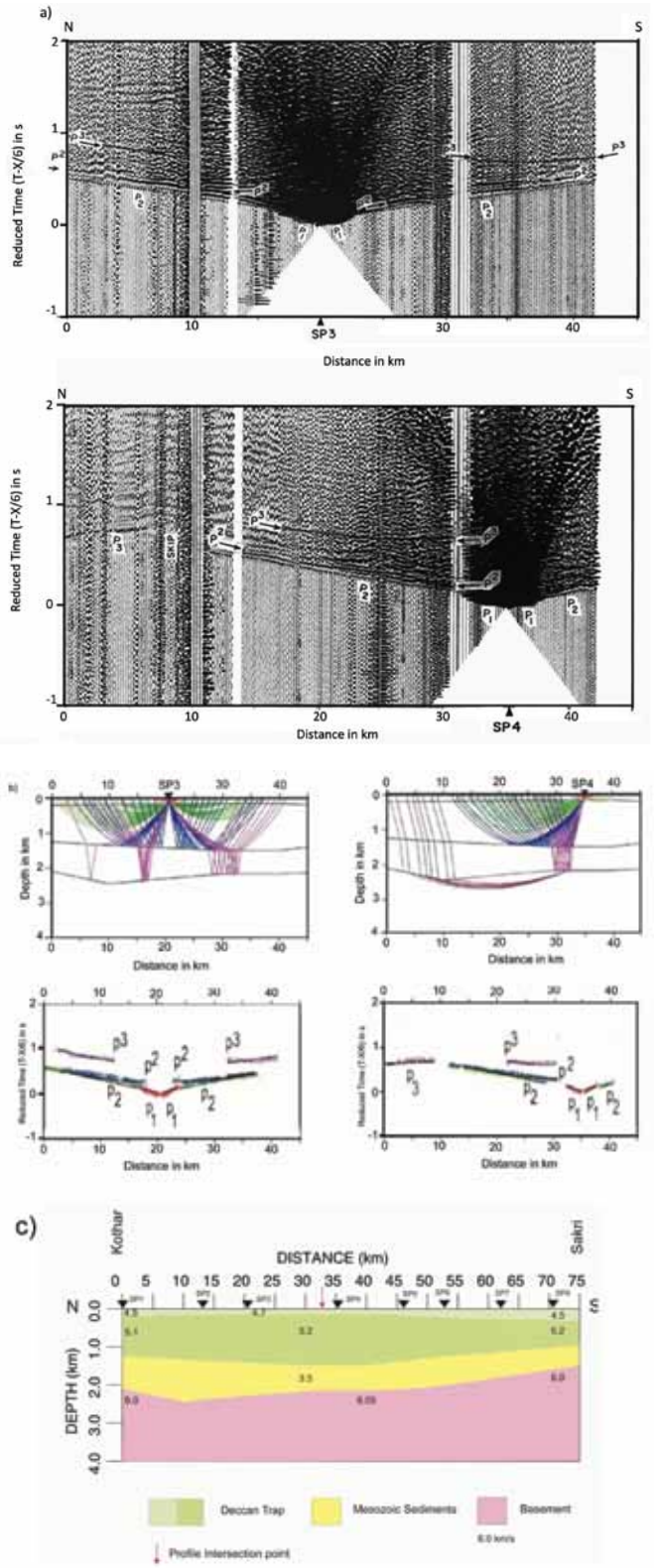

Figure 4. Record sections of shot points (a) SP3 and SP4 in western Deccan syneclise, along Kothar-Sakri (N-S) profile. P_1, P_2, and P_3 are first arrival refracted phases. Amplitude decay in Trap refracted phase (P_2) and time skip between P_2 and P_3 indicate presence of low velocity zone. P^2 and P^3 are wide-angle reflection phases from top and bottom of the low velocity zone, (b) corresponding ray diagrams and travel time fit for SP3 and SP4, (c) shallow crustal velocity model along Kothar-Sakri profile (after Murty et al., 2010).

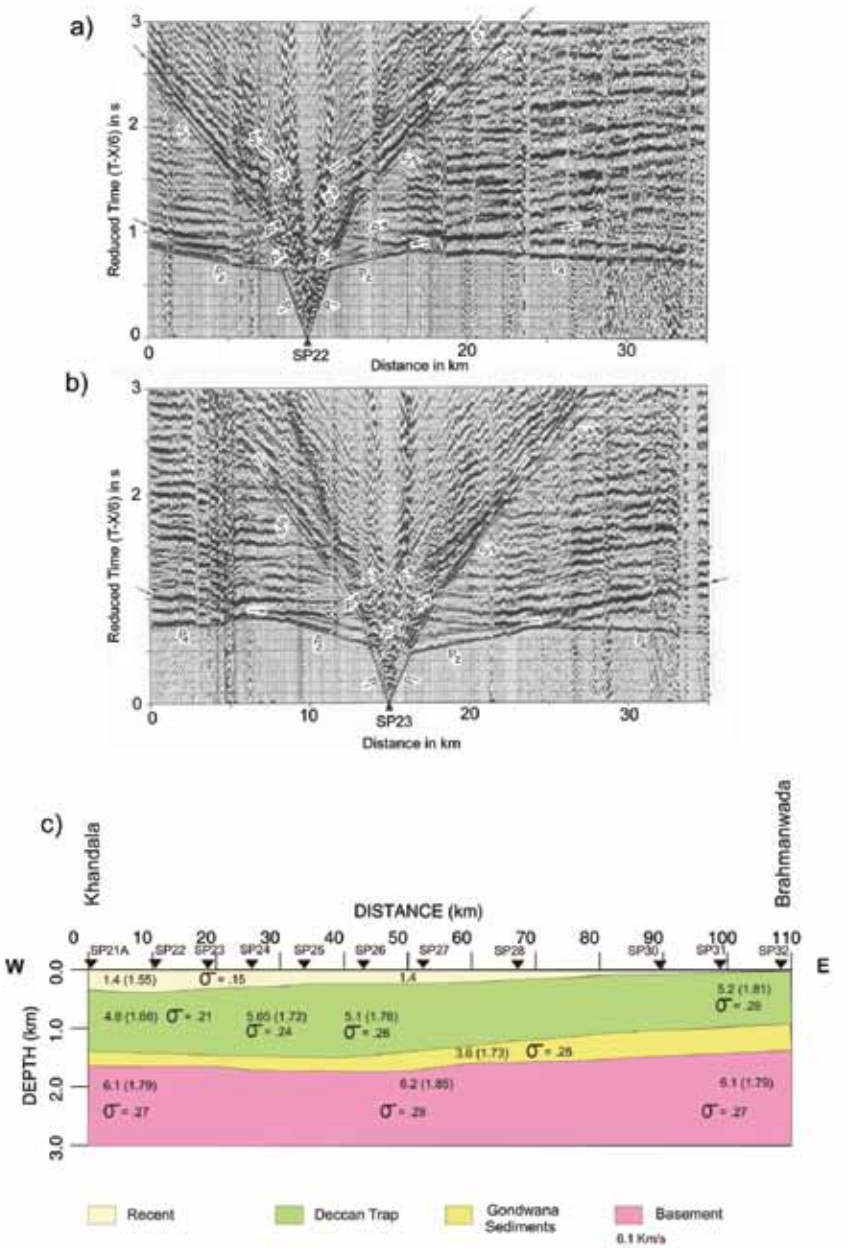

Figure 5. Record sections of shot points (a) SP22 and (b) SP23 in eastern Deccan Syneclise, along Khandala-Brahmanwada profile. P_1, P_2 and P_4 are first-arrival refracted phases. P^3 and P^4 are wide-angle reflected phases from the top and bottom of the low-velocity zone. S_2 and S_4 are S-wave refracted phases. S^3 and S^4 are wide-angle reflected phases from the top and bottom of the low-velocity zone, (c) Shallow crustal velocity model along Khandala-Brahmanwada profile (σ-Poisson's ratio) (after Murty et al., 2011b).

part of Deccan syneclise (Figure 5a, b), show there are three refracted phases (P_1, P_2, P_3) with velocities 1.4, 4.9-5.2, and 6.0-6.2 km s^{-1} that correspond to alluvium, Deccan Traps, and granitic basement, respectively (Figure 5a,b). Attenuation of the high-velocity Trap refracted phase and a travel time delay between the Trap (P_2) and basement refracted (P_4) phases, are not seen from these shot points, whereas the same are clearly observed from the shot points at large offsets along this profile. There is a reflected phase (P^3) that follows the P_2 refracted phase, which likely results from a LVZ beneath the Traps, which results in a large velocity contrast. There is a strong reflection (designated as P^4) in the 10-15 km distance range. Considering the attenuation and travel time delay between the refracted phases (P_2 and P_4) at larger offsets, we interpret the wide-angle reflected phases (P^3 and P^4) from SPs 22 and 23 as

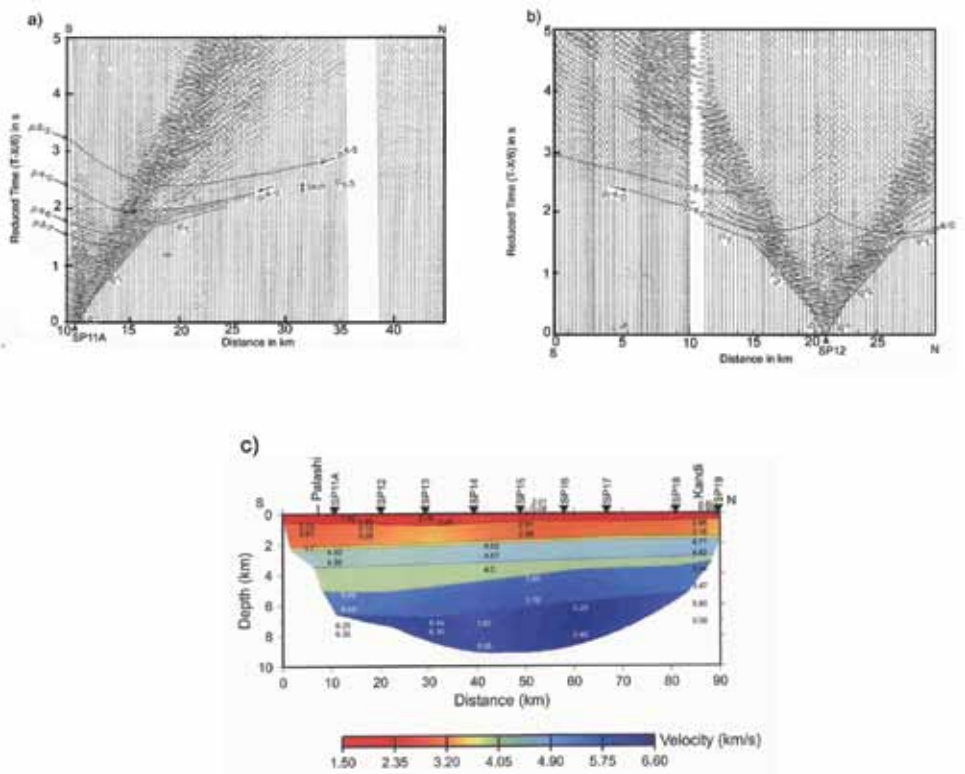

Figure 6. Record sections of reversing shot points (a) SP11A and (b) SP12 in the West Bengal basin, along the Palashi-Kandi (N-S) profile. P_1, P_2, P_T and $P_{5.3}$ are first-arrival refracted phases. Amplitude decay in the Trap refracted phase (P_T) and traveltime delays between P_T and $P_{5.3}$ are indicative of a low-velocity zone. $P^{4.0}$ and $P^{5.3}$ are wide-angle reflected phases from top and bottom of the low-velocity zone. (c) Shallow crustal velocity model along Palashi-Kandi profile is shown at the bottom (after Murty et al., 2008).

reflected phases from the top of a LVZ and basement. The reflected phase (P^4) is strong, with a high-amplitude phase that infers a large velocity contrast. We do not observe significant energy loss associated with the reflected wave propagating between basement and the overlying layer, which is also indicative of a thin LVZ. In general, we have noticed that the strength of the reflection phase from the bottom of the low velocity zone, varies considerably based on the thickness of the high-velocity trap and low-velocity sediment layers. In the case of large trap and sub-trappean sediment thickness (Figure 4c), reflection phase is weak and in the case of thin trap and sub-trappean sediments (Figure 5c) the reflection phase emerges strong and the data quality is better.

West Bengal basin

Record sections from reversing shot (SP11A and SP12) along the Palashi-Kandi (N-S) profile in the west Bengal basin are shown in figure 6a, b. The profile was acquired during 1989-90, using a DFS-V seismic system with 80 m receiver intervals, ~10 km shot intervals, and a 4-ms sampling rate. All shots were recorded with up to 80 km offset. To show the reflected phases clearly, we use low-gain data at near offsets. We picked travel times of the first-arrival refracted and reflected phases from the monitor records. We observe three refracted phases (P_1, P_2 and P_T) in the near offset. Our interpreted refracted phases correlate well with data obtained by the Oil and Natural Gas Corporation (ONGC) in a drilled well at Palashi. We infer the refracted phases (P_1 and P_2) to correlate with Tertiary sediments, and the refracted phase (P_T) to correlate with the Rajmahal Traps. We observe an amplitude decay in the Trap refracted phase (P_T) and travel time delay between the Trap refracted phase and $P_{5.3,}$ as seen in the seismic record from SP 11A. We also observe a strong reflected phase ($P^{4.0}$) just above the Trap refracted phase and another reflected phase ($P^{5.3}$). Amplitude decays, travel time delays, and strong reflections are indicative of a low-velocity zone between the Trap and $P_{5.3}$ layer. We interpret the two reflected phases ($P^{4.0}$ and $P^{5.3}$) to be reflections from the top and bottom of a low-velocity zone. Low-velocity Gondwana sediments, observed in the nearby Palashi well, are likely to comprise our observed LVZ.

MODELLING RESULTS

Shallow crustal velocity models were derived from first-arrival refraction and wide-angle reflection data for Kutch, the Deccan syneclise, and the west Bengal basins (Murty et al., 2008, 2010, 2011a,b ;Prasad et al., 2010), using the travel time inversion method of Zelt and Smith (1992) and the ray tracing program, Rayamp-PC (1987). In the Kutch basin, we infer a five-layer model (Figure 2c) that overlies granitic basement between SP 1 to 6, and a four-layer above-basement model between Jakhau-Mandvi profile-I (Rajendra Prasad et al., 2010). The first layer is unconsolidated Tertiary sediments, which are varying between 0.8 to 0.5 km in thickness from the NE to SW (velocity of 2.0 kms^{-1}). We interpret the second layer to be Deccan Traps, with a velocity of 4.6 km s^{-1}. The Trap is thin (0.2 km) between SP 1 and 5 and increases in thickness to 0.7-0.9 km between SP 6 and 8. We interpret about 1 km of Mesozoic sediments (3.1 kms^{-1}) to underlie the Traps near SP1, increasing in thickness to about 2 km near SP8. The third layer is underlain by a 0.4-km-thick high-velocity layer (5.4 km s^{-1}) at SP 1 that increases in thickness to about 2.5 km between SP 5 and 8. Between the high-velocity (5.4 km s^{-1}) layer and basement (5.9 km s^{-1}), we interpret another low-velocity layer (3.5 km s^{-1}). Basement is at 3.2 km near Jakhau, deepening to about 6.5 in km near Mandvi.

Murty et al. (2011a) interpreted four layers above basement along the Jhagadia-Rajpipla profile in western part of Deccan syneclise (Figure 3c). All the layers, including the basement, are deepest below shot point 1 (near Jhagadia in the southwest) and are shallowest towards northeast, near Rajpipla. Near-surface sediments range in velocity between 1.95-2.3 km s^{-1} and ranges in thickness from about 300 m near Jhagadia to 700 m near SP 2; this layer gradually thins towards the northeast and pinches out near shot point 5. We interpret ~ 2.9 km of Quaternary sediments (2.7-3.05 km s^{-1}) to underlie the near-surface recent sediments beneath SP 1 near Jhagadia. The Quaternary sediments layer rapidly decreases in thickness between SP 2 and SP 3 and is only about 150 m thick near Rajpipla. Deccan Traps (4.8-5.1 km s^{-1}) are about 1 km thick near SP 3, thinning to 500 m to the northeast and southwest. The top of the Trap layer dips steeply between shot points 2 and 3, resulting in a thickened deposit of Mesozoic sediments overlying the Trap layer southwest of SP 2, near Jhagadia. The Mesozoic sediments vary in thickness from about 1 km near Jhagadia (at SP 1) to 1.7 km near SP 2. The depth of basement (5.9-6.15 km s^{-1}) decreases from 4.6 km near shot point 2 to 2.6 km near SP 3 and further thins down to about 1.2 km near Rajpipla. Murthy et al. (2010) interpret three layers above basement (Figure 4c) along the Kothar-Sakri profile in western part of Deccan synclise They interpret the first two layers (4.5-4.7 and 5.1-5.2 km s^{-1}), with layer thickness 0.15-0.30 km and 0.65-1.35 km respectively, as various flows of the Deccan Traps. The total Trap thickness is 1-1.50 km. The underlying low-velocity Mesozoic sediments (3.5 km s^{-1}) are 0.55-1.1 km thick along the profile, and basement (6.0 km s^{-1}) varies in depth from 1.5-2.45 km, dipping towards north. Murty et al. (2011b) modelled three layers above basement along Khandala-Brahmanwada profile (Figure 5c) in the eastern part of Deccan syneclise. The first layer (1.4 km s^{-1}) represents alluvium, which is about 350 m thick at SP21A (near Khandala) that gradually thins towards the east before surfacing near Brahmanwada. The second layer (4.8-5.2 km s^{-1}) corresponds to Deccan Traps, with an average thickness of 1 km along the profile which is underlain by a thin layer (250-400 m) of Gondwana sediments (3.6 km s^{-1}). Basement (6.1-6.2 km s^{-1}) is about 1.6 km deep in the NW near SP 0, decreasing to 1.35 km near Brahmanwada.

Murty et al. (2008) also modelled six layers above basement along the Palashi-Kandi profile (Figure 6c) in the west Bengal basin. The first two layers (1.9-2.1and 2.8-3.1 kms^{-1}) correlate with alluvium and shale which are 0.3-0.75 km and 1.0-1.7 km thick, respectively. The third layer corresponds to Sylhet limestone (3.7 kms^{-1}) and is only a few hundred meters thick and is underlain by a ~ 1-km-thick layer of Rajmahal Traps (4.5-4.7 kms^{-1}). About 1.8 km of Gondwana sediments (4.0 kms^{-1}) underlies the Rajmahal Traps near Palashi, shallowing to about 400 m near Kandi. Murty et al. (2008) interpret Sighbhum group of Meta volcanic rocks (5.4-5.6 kms^{-1}) to underlie the Gondwana sediments and overlie the crystalline basement (5.8-6.25 kms^{-1}), which varies in depth between 4.9 to 6.8 km, dipping towards the south.

DISCUSSION AND CONCLUSIONS

The velocity models derived along various seismic profiles in the Kutch area, the Deccan syneclise, and the west Bengal basin, delineate variations in the Traps and sub-trappean sediments and the basement depth. In the Kutch basin, Recent/Tertiary sediments overlie the Trap along the Jakhau-Mandvi profile. Shot records show near-surface refracted arrivals are followed by a shadow zone (travel time delay), a higher velocity layer, and a second shadow zone before the basement refraction. We correlated well data with our refraction/reflection data and interpreted the shallow crust along the Jakhau-Mandvi profile as Mesozoic sediments. We interpret high-velocity layer between the two low-velocity layers as limestone within Mesozoic sediments. From the derived velocity models along the four segments (Figure 2c), we infer a sedimentary graben between faults F1 and F3. The model shows that basement is 3.3 km deep near Jakhau, increasing to 6.7 km depth at Mandvi. Overlying the basement are five layers, with velocities of 2.0, 4.6, 3.1, 5.4, 3.5 kms^{-1}, which

we interpret as Tertiary sediments, Traps, Late Mesozoic sediments, Mesozoic limestone, and Early Mesozoic sediments, respectively. The model changes toward the northeast. The Traps are almost absent in the north, consisting of an older Mesozoic sequence. The basement shallows to about 3 km from Bachau north-eastward, and the limestone layer discontinues. Across the Little Rann, sediments (2.8 kms^{-1}) overlie the shallow (2 km) basement. The thick Mesozoic sediments in the southern Kutch basin are likely an extension of the thick Mesozoic rocks inferred in north-western Saurashtra, across the Gulf of Kutch.

The velocity models for the western part of Deccan syneclise (Murty et al., 2011a, 2010) are shown in figures 3c and 4c. The Mesozoic sediments in western India occupy a large portion of Rajasthan, Gujarat, and Madhya Pradesh, and the sediments are mostly of marine origin; thus, they are important to the oil industry. On the south-eastern margin of the Cambay basin and the western part of the Deccan syneclise near Rajpipla, a 600-m-thick section of the Cretaceous Bagh beds (Mesozoic) is exposed. Poddar (1964) suggested the presence of suitable facies and favourable prospects for hydrocarbon-bearing Mesozoic sediments below the Deccan Traps towards the Ankleswar oil field. From these considerations and the presence of a relatively thin trap, the thick (~1.7 km) Mesozoic sediments near SP 2 of the Jhagadia-Rajpipla profile (Figure 3c) are significant. Deep seismic sounding studies (DSS) across the Narmada-Son lineament revealed Deccan Traps and subtrappean sediments in the Naramada-Tapti region (Kaila, 1988; Sridhar and Tewari, 2001). The area in the western part of the Deccan syneclise lies between two DSS profiles, the Mehmadabad-Billimora profile in Cambay basin and the Thuadara-Sindad profile to the east. Along the Thuadara-Sindad profile, the Trap thickness is about 900 m, and south of Sendhwa (up to Tapti river), Mesozoic sediments are approximately 1.9 km thick. Sridher and Tewari (2001) observe evidence for a graben between the Narmada and Tapti rivers. Within the graben, basement is 5.0-5.5 km deep between Sendhwa and the Tapti river and contains 1.0-2.8 km Mesozoic sediments beneath the thick (2.0-2.7 km) Trap cover. From the present study of profiles in the western part of the Deccan syneclise, Tertiary and subtrappean sediments are relatively thick in the southwest (Figure 3c). Further east (Figure 4c), the Trap and subtrappean sediments are about 1 km thick. On the basis of isopach contour maps of the Mesozoic sediments in the Narmada-Tapti region, Kaila (1988) hypotheses a Mesozoic basin in the Narmada-Tapti area that formed within a Mesozoic sea. Seismic profiles in the western part of the Deccan syneclise show evidence for a Mesozoic basin in the region.

In the eastern part of the Deccan syneclise, Deccan Traps are about 1 km thick, and subtrappean Gondwana sediments vary in thickness from 100-400 m (Figure 5c). Seismic profiles in the eastern part of Deccan syneclise (Murty et al., 2011b, Kaila, 1988, Kaila and Koteswara Rao, 1985, Mall et al., 2002) indicate a large variation in the thickness of the Deccan Traps in the E-W direction. The variation in the thickness of the Traps arises from the presence of volcanic plugs. Although Gondwana sediments outcrop north of the seismic profile, these sediments are relatively thin in the area of the Satpura horst. A Bouguer gravity low in the area suggests that the Godavari Gondwana graben and the Tapti-Purna fault extend northward of Nagpur. This Tapti-Purna fault is believed to bound the Satpura graben (Mishra, 1992). The entire region of the eastern Deccan syneclise, combined with the Gondwana rocks of the Wardha coal field, constitutes the elongated Godavari Gondwana basin, which extends towards the Satpura basin. Such a linear extension of Gondwana sediments might have resulted from some deep-seated tectonics, such as lithospheric upwelling associated with a plume or a hot spot trace (Curray and Munasinghe, 1991), which, in turn, gave rise to the extensional tectonics that produced the rift valleys in this region.

Seismic profiles in the West Bengal basin (Kaila et al., 1996. Murty et al., 2008) delineate the Traps and subtrappean Gondwana sediments. The Rajmahal Traps are about 1.0 km thick, and Gondwana sediments are about 1.8 km thick in the south near Palashi but decreases to 0.4 km northward near Kandi (Figure 6c). Wells in the west Bengal basin show a large variation in velocity of the Eocene limestone formation, varying from 5.8 km s^{-1} at the Diamond Harbour (0.9 km thick) to 3.2 km s^{-1} (0.2 km thick) at the Palashi -1 well (Kaila et al., 1996). The limestone formation was not found further north in the Purnea well, where basement is shallow near Jangipur and Malda (Chowdhury and Datta, 1973). We suggest that the shallow basement might have limited the northward extension of the early Tertiary Seas towards Purnea and acted as an effective structural barrier to the deposition of Sylhet limestone in the Early Tertiary. According to Chowdhury and Datta (1973) the basement high, while acting as a structural barrier in the early Tertiary period, did not interrupt the continuity of the Gondwanas from south to north. We infer that there was continuous deposition of the Gondwanas from south to north in local basement depressions at the initial stage of the break-up of Gondwana land during the Permocarboniferous period.

ACKNOWLEDGEMENTS

We thank Director, CSIR-NGRI for permission to publish the work and all the CSS crew members for recording the seismic data. We thank the reviewers for their valuable suggestions.

REFERENCES

Bois, C., Bouch, P. and Pelet, R., 1982. Global geologic history and distribution of hydrocarbon reserves, AAPG Bulletin, 66, 1248-1270.

Chowdhury, S.K. and Datta, A.N. 1973. Bouguer gravity and its geologic evolution in the western part of the Bengal basin and adjoining area, India, Geophys. 38, 691-700.

Curray, J.R. and Munasinghe, T., 1991. Origin of Rajmahal Traps and the 85^0 E ridge: preliminary reconstruction of the trace of the Crozet hot spot. Geology, 19, 1237-1240.

Fruehn, Juergen, Moritz M. Fliendner and Robert S. White, 2001. Integrated wide-angle and near – vertical sub salt study using large-aperture seismic data from the Faeroe-Shetland region, Geophys, 66(5), 1340-1348.

Greenhalgh, S.A., 1977. Comments on "The hidden layer problem in seismic refraction work", Geophys. Prospect., 25, 179-181.

Jarchow, C.M., Catchings, R.D. and Lutter, W.J., 1994. Large explosive source, wide-recording aperture, seismic profiling on the Columbia Plateau, Washington, Geophysics, 59, 259-271.

Kaila, K.L. and Koteswara Rao, P., 1985. Crustal structure along Khajuriakalan-Pulgaon profile across the Narmada-Son lineament from Deep Seismic Soundings, I: Deep Seismic Soundings and Tectonics, Editors: K.L. Kaila and H.C. Tewari, AEG publication, India, 43-59.

Kaila, K.L., 1986. Tectonic framework of Narmada-Son lineament-a continental rift system in central India from deep seismic soundings. In: Barazanki, M. and Brown, I. (Eds.), Reflection seismology: a global perspective, Geodyn. Ser., 13, AGU Washington DC, 133-150.

Kaila, K.L., 1988. Mapping of the thickness of the Deccan Trap flows in India from deep seismic sounding studies and inferences about a hidden Mesozoic basin in Narmada-Tapti region. Geol. Soc. India, Mem. No. 10, 91-116.

Kaila, K.L., Krishna, V.G. and Mall, D.M., 1981. Crustal structure along Mehmadabad-Billimora profile in the Cambay basin, India from Deep Seismic Soundings. Tectonophysics, v. 76, pp: 99-130.

Kaila, K.L., Reddy, P.R., Dixit, M.M., and Koteswara Rao, P., 1985. Crustal structure across Narmada-Son Lineament, central India from Deep Seismic Soundings, J. Geol. Soc. India, 26 465-480.

Kaila, K.L, Reddy, P.R., Mall, D.M., Venkateswarlu, N., Krishna, V.G. and Prasad, A.S.S.S. R.S., 1992. Crustal structure of the west Bengal basin, India from deep seismic sounding investigations, J. Int., 111, 45-66.

Kaila, K.L., Murty, P.R.K., N. Madha Rao, I.B.P. Rao, P.K. Rao, A.R. Sridher, A.S.N. Murty, V.Vijay Rao, and B.R. Prasad., 1996. Structure of the crystalline basement in the west Bengal basin, India, as determined from DSS studies, Geophys, J., Int.,124, 175-188.

Mall, D.M., Sarkar, D. and Reddy, P.R., 2002. Seismic signature of Sub-Trappean Gondwana Basin in Central India. Gondwana Research, 5(3), 613-618.

Mishra, D.C., 1992. Mid continental gravity 'High' of central India and the Gondwana tectonics, Tectonophysics, 212, 153-161.

Murty, A.S.N., Kalachand Sain and Rajendra Prasad, B., 2008. Velocity structure of the West-Bengal sedimentary basin, India along the Palashi-Kandi profile using a travel-time inversion of wide-angle seismic data and gravity modeling-An update. Pure and Applied Geophysics, 165, 1733-1750.

Murty, A.S.N., Prasad, B.R., Koteswara Rao, P., Raju and S., Sateesh, T., 2010. Delineation of Subtrappean Mesozoic Sediments in Deccan Syneclise, India, Using Travel time Inversion of Seismic Refraction and Wide-angle Reflection Data. PAGEOPH, 167, 233-251.

Murty, A.S.N, Rao, P.K., M.M. Dixit, G. Kesava Rao, M.S. Reddy, B. Rajendra Prasad and D. Sarkar., 2011a. Basement configuration of the Jhagadia-Rajpipla profile in the western part of Deccan syneclise, India from travel-time inversion of seismic refraction and wide-angle reflection data, India. Journal of Asian Earth Sciences, 40, 40-51.

Murty, A.S.N, M.M. Dixit, B. Mandal, S. Raju, Sanjay Kumar, P. Karupanan, K. Anitha and D.Sarkar., 2011b. Extension of Godavari Gondwana sediments underneath Trap covered region of Satpura basin as evidenced from seismic studies in Deccan Syneclise, India. Journal of Asian Earth Sciences, 42, 1232-1242.

NGRI Technical Report, 1998. Integrated geophysical studies for hydrocarbon exploration, Saurashtra, India. NGRI Technical Report No. NGRI-98-Exp-237.

NGRI Technical Report, 2000. Integrated geophysical studies in Kutch on land to delineate subsurface sedimentary basins structure and Basement configuration-Seismic refraction results, NGRI Technical Report No. NGRI-2000-Exp-281.

NGRI Technical Report, 2004. Integrated geophysical studies for hydrocarbon exploration, Deccan Syneclise, India. NGRI Technical Report No. NGRI-2003-Exp-404.

NGRI Technical Report, 2009. Integrated Geophysical studies for hydrocarbon exploration in eastern part of the Deccan Syneclise, central India. NGRI Technical Report No. NGRI-2009-Exp-679_Volume II.

Poddar, M., 1964. Mesozoic of western India-their geology and possibilities. In: 22^{nd} Int. Geol. Cong., New Delhi, Sect.1-part1. Geology of Petroleum, 126-143.

Pujol, J., Fuller, B.N., and Smithson, S.B., 1989. Interpretation of a vertical seismic profile conducted in the Columbia Plateau basalts. Geophysics, 54, 1258-1266.

Rajendra Prasad, B., Venkateswarlu, N., Prasad, A.S.S.S.R.S., Murty, A.S.N. and Sateesh, T., 2010. Basement configuration of on-land Kutch basin from seismic refraction studies and modeling of first arrival travel time skips, Journal of Asian Earth Sciences, 39, 460-469.

Rayamp-PC, 1987. 2 D Ray tracing\Synthetic seismogram. Version 2.1, Geophys, Laboratory, Mc-Gill University.

Sain, K., and Kaila, K.L., 1996. Interpretation of first arrival traveltimes in seismic refraction work. Pure Appl. Geophys., 147, 181-194.

Sain, K., Zelt, C.A. and Reddy, P.R., 2002. Imaging of subvolcanic Mesozoics in the Saurashtra peninsula of India using travel time inversion of wide-angle seismic data, Geophys., J. Int. 150, 820- 826.

Sridhar, A.R. and Tewari, H.C., 2001. Existence of a sedimentary graben in the western part of Narmada zone: Seismic evidence. Joul. Geodynamics, 31, 19-31.

Tewari, H.C., Dixit, M.M., and Murty, P.R.K., 1995. Use of traveltime skips in refraction analysis to delineate velocity inversion. Geophys. Prospect., 43, 793-804.

Zelt, C.A., and Smith, R.B., 1992. Seismic travel time inversion for 2-D crustal velocity structure. Geophys. J. Int., 108, 16-34.

Received on: 13.11.18; Revised on: 21.11.18; Accepted on: 25.12.18

J. Ind. Geophys. Union (January 2019)
v.23, no.1, pp: 41-54

Dimensionality and directionality analysis of the magnetotelluric data along the coastal part of western Saurashtra, Gujarat

K. Dilip Singh*, Kapil Mohan, and Mehul Nagar
Institute of Seismological Research, Raysan, Gandhinagar-382009 (Gujarat)
Also at Gujarat University, Navrangpura, Ahmedabad, Gujarat, 380009.
* Corresponding Author: ds200705@gmail.com

ABSTRACT
The Magnetotelluric (MT) data from 14 MT stations along a NW-SE profile, having a length of 40 km, is processed for a period range of 0.01-100s along the coastal part of north-western Saurashtra, India to estimate the dimensionality of the MT data, using three different approaches, that is, Phase Tensor (PT) technique, WALDIM code, Swift's and Bahr's Skew technique. The Swift's and Bahr's skew result suggests 1D structure for low periods (0.01-1 s) and 2D structure for high periods (1-100 s), except for some sites which show a 3D subsurface structure for high periods (1-100 s). The results generated through PT and WALDIM code are consistent with those from Swift's and Bahr's skew technique. The strike estimated through Phase Tensor (PT), Groom-Bailey (GB) and Becken and Burkhardt (BB) technique for broad period 0.01-100s suggest NNE-SSW regional strike direction, which is well correlated with the Delhi-Aravalli tectonic trend. From the 1D inverse model, the Quaternary and Tertiary sediments are found up to the depth of 300-400m followed by Deccan Trap. A conductive zone (having resistivity <20 Ohm-m) in the central part of the profile near Okha Rann is also observed which suggests the presence of a fault.

Keywords: Magnetotellurics, Dimensionality, Strike, Galvanic distortion, Western Saurashtra coast, Gujarat

INTRODUCTION

Gujarat state is divided into three regions namely, Mainland Gujarat, Kachchh and Saurashtra on the basis of seismotectonics and geomorphology of the region (Yadav et al., 2008). The Saurashtra region comes under two seismic zones (IV and III) on the seismic zoning map of India (BIS, 2002). The major portion of the Saurashtra peninsula is covered by Arabian Sea water. The interior of the Saurashtra is either covered by Deccan Traps or Quaternary deposits due to which no clear faults have been identified. Various geophysical studies have been carried out in the Saurashtra region for regional as well as local tectonic interpretation. From Gravity and Magnetic method, Mishra et al. (2001) delineated major structural trends using satellite data: (i) NE-SW Precambrian Aravalli trend, observed in entire Saurashtra but dominating in the SE part of Saurashtra. (ii) ENE-WSW to E-W trend, which represents the Precambrian Son-Narmada lineament trend in southern Saurashtra. (iii) The NW-SE trend, parallel to the west coast of Saurashtra, visible over the entire Saurashtra peninsula. (iv) N-S to NNE-SSW trend dominating in the eastern part of Saurashtra close to the Cambay basin. In central northern part of Saurashtra a Magnetotelluric survey with 607 stations was carried out in grid by Sharma et al. (2004), which identified near-surface structural features: (i) a near N-S trending fault/fracture passing through Amreli to Chotila and (ii) a near NW-SE trending fault passing through west of Lalpur. Subbarao et al. (2012) recorded magneto-variational fields by an array of magnetometers covering whole Saurashtra region and inferred the presence of two prominent conductivity anomalies: (i) the first elongated anomaly coinciding with the horst and graben offshore structures of Saurashtra and Kachchh, and (ii) the second anomaly is found over the Saurashtra depression that correlates well with the low-magnetization anomaly extending in the NW-SE direction towards Cambay basin. From Deep Resistivity Sounding (DRS) data, Singh et al. (2004) generated a geo-electrical section of Navibandar-Rajkot-Dhrangadhra and observed the resistivity of sediments less than 60 ohm-m, traps of 100-600 ohm-m and basement of >1000 ohm-m. The presence of the number of hidden volcanic plugs in the area of Porbandar-Navibandar, Kutiyana, Junagadh and, Rajula region are observed in which some plugs are not exposed at the surface and could be an extension of Girnar, Barda and Alech hills at depth. Patro et al., 2015 have acquired a N-S profile across the center of the Saurashtra and correlated the velocity model from the seismic study with the resistivity model generated from MT data and observed that velocity of different layers increases with increase in resistivity of the different layers. From MT data analysis the resistivity of 120 ohm-m, 20 ohm-m and >1000 ohm-m were found for Deccan trap, Mesozoic sediments, and basement rock respectively.

In a nutshell, most of the geophysical study has been conducted in the Southern and central part of the Saurashtra. The NW Saurashtra has not been covered with geophysical survey. Therefore, the MT survey was planned in the NW part of Saurashtra to understand the dimensionality, directionality and the conductivity variations in the subsurface. Total 14 MT stations have

Table 1. Lithostratigraphy of Neogene-Quaternary deposits of Saurashtra region (Bhatt, 2000 and Pandey et al., 2007)

Stratigraphic Unit	Lithology	Age
Holocene Deposits	Beach and dune sands Tidal clays, alluvium	Holocene
Unconformity		
Chaya Formation	Calc-rudite, Calc-arenites	Late Pleistocene to Holocene
	Coral reef limestone Off-white colored bioclastic limestone & conglomerate	Middle to Late Pleistocene
Unconformity		
Dwarka Formation	Recrystallized fossiliferous limestone and sandy Limestone	Lower Pliocene
	Sandy clays and sandstones	Upper Miocene
	Bioclastic and coralline limestone with few dolomitic bands	Middle Miocene
Disconformity		
Gaj Formation	Yellow and brown fossiliferous limestone	Lower to Middle Miocene
Deccan Trap	Basalt and other derivatives covered at places by laterite and bauxite	Upper Cretaceous to Eocene

been acquired. The MT data of 13 stations were used for further analysis and one station is rejected due to presence of high-level noise in the data. The dimensionality analysis has been carried out using Swift skew (Swift, 1967); Bahr skew (Bahr, 1988, 1991); Phase Tensor Analysis (PTA) (Caldwell, 2004), WALDIM decomposition technique (Marti et al., 2009). The strike analysis has been carried out using Multisite Multifrequency tensor decomposition (McNeice and Jones, 2001; Becken and Burkhardt, 2004).

GEOLOGY AND TECTONICS

The Saurashtra region is a horst structure (Biswas, 1982), bounded by the Cambay Rift Basin (CRB) in the east, West Coast Fault (WCF) in the west, extension of Son Narmada Fault in the south and North Kathiawar Fault (NKF) in the north (Figure 2). Major geological and tectonic events of the Saurashtra region are narrowed to Mesozoic and Cenozoic era and associated with (i) break-up of Africa from the Indian block containing Madagascar and Seychelles, (ii) later breakup of Madagascar from India due to Marion hotspot activity, and (iii) break-up of the Seychelles plateau from India followed by eruption of Deccan volcanism related to interaction of Reunion hotspot activity (Subbarao et al., 2012). The region has observed various tectonic activities such as deviational forces causing inter-continental splitting, different phases of rifting, re-activation of the ancient fault zones and Deccan volcanism due to reunion plume activity. Major continental part is covered with the Deccan trap. The coastal plains fringing the trappean highland comprise Cenozoic cover consisting of Tertiary and Quaternary sediments (Biswas, 1987). The Tertiary exposures are patchy in occurrence and mostly belong to Dwarka Formation (Bhatt, 2000) (Figure 1). A thin cover of Neogene and Quaternary sediments occurs at the top surface (Table 1).

Magnetotelluic data and processing

Magnetotelluric (MT) data at 14 stations are acquired along the NW-SE traverse of ~40 km with ~3 km station spacing. The MT data acquisition system ADU-07e of M/s Metronix, Gmbh, Germany was deployed. The data was measured for five components, using induction coils (MFS-06) for three orthogonal channels of magnetic field variation (Hx, Hy, and Hz) and Pb-$PbCl_2$ electrode dipoles (80m dipole length) for orthogonal electric field variations (Ex and Ey). The MT data were recorded for about 48 hours over a broad period range. The time series data were processed using a software package Mapros to estimate the apparent resistivity and phase curves (Figure 3).

METHODOLOGY

In MT method, the horizontal Electric fields (**E**) and the horizontal magnetic fields (**B**) are linked through a

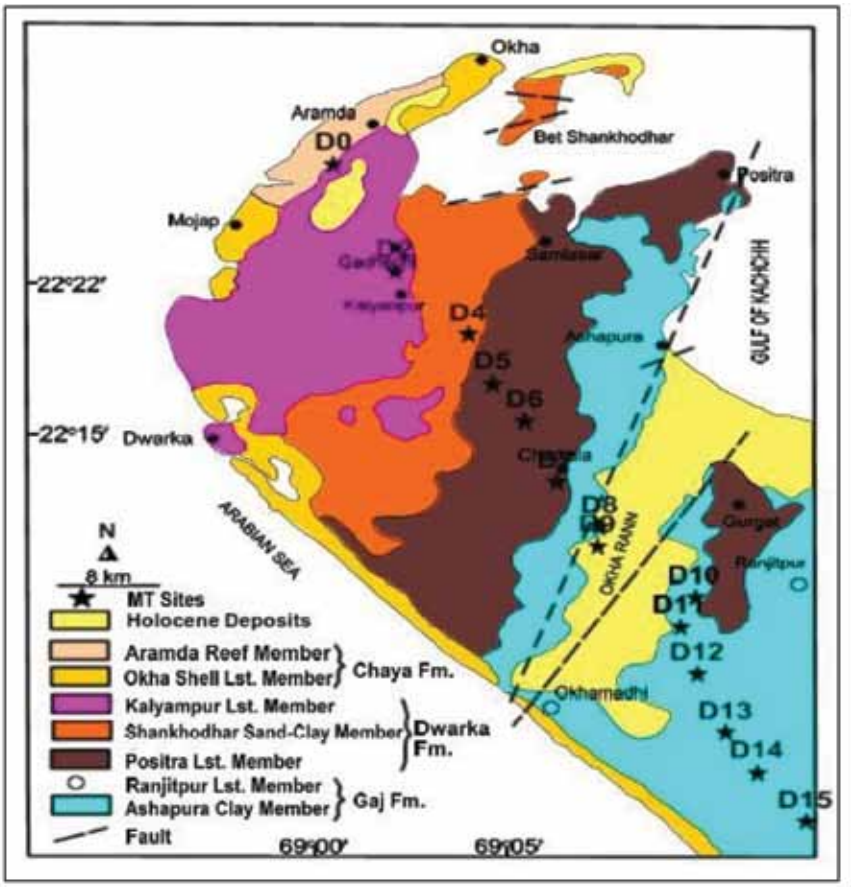

Figure 1. Geological Map of the study area of the Saurashtra region (Gujarat), along with Magnetotelluric Stations marked in black star symbol (modified after Bhatt, 2000).

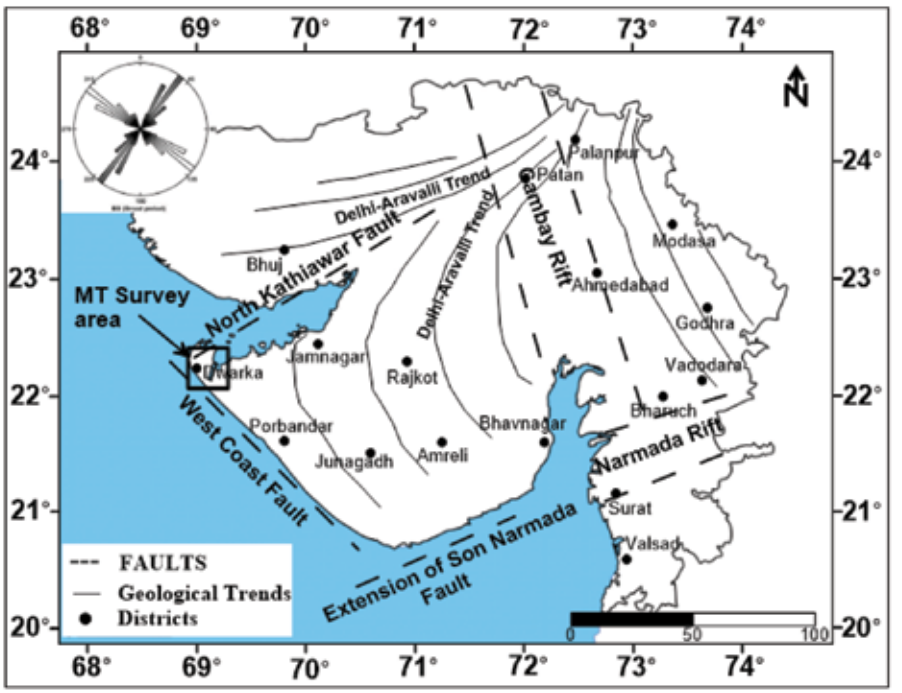

Figure 2. Tectonic Precambrian trend (after Biswas, 2005) along with regional strike direction estimated through BB technique.

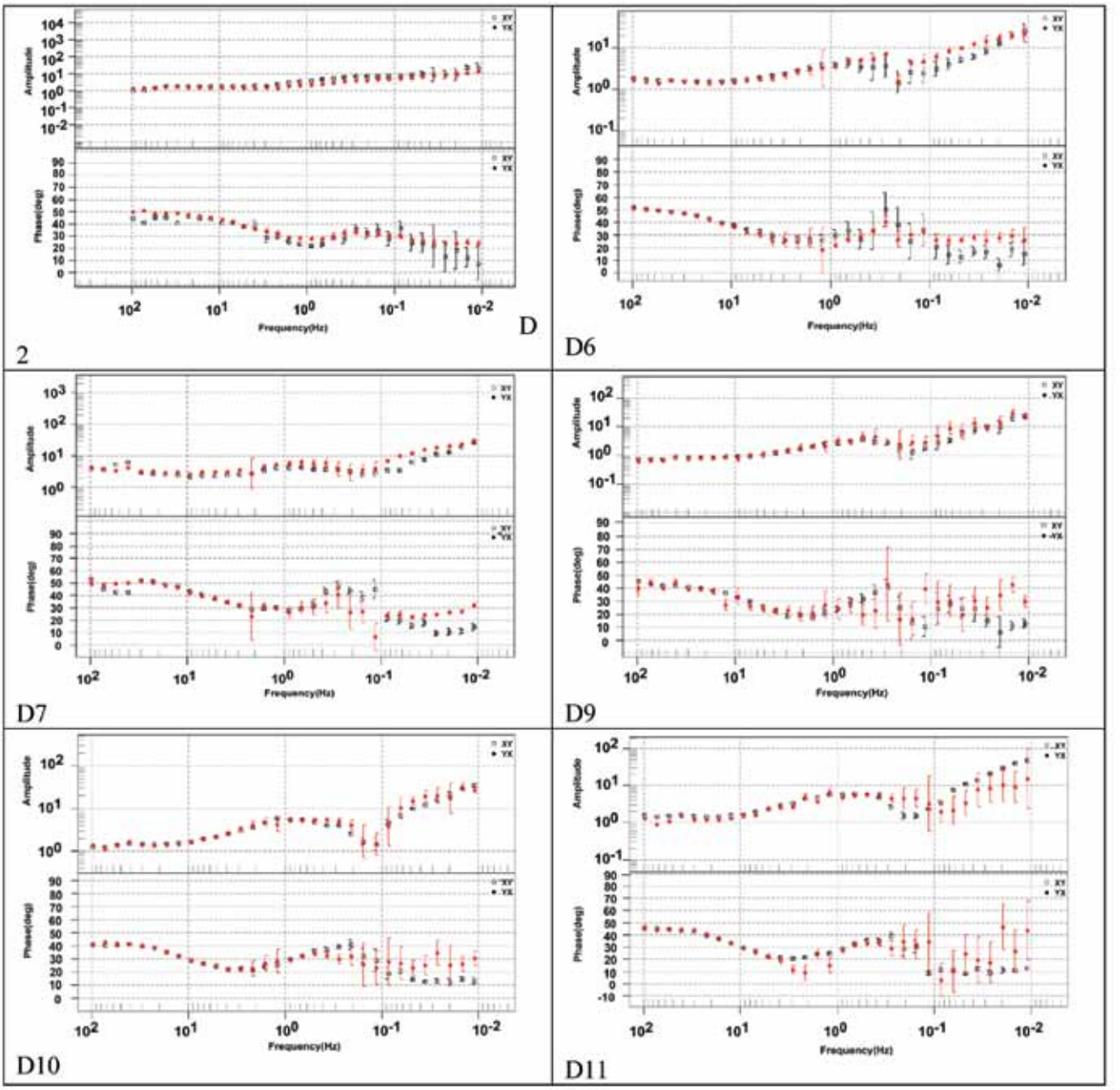

Figure 3. Computed apparent resistivity and Phase Vs. Frequency curves after time-series processing.

complex impedance tensor **Z** (Bahr, 1988) in the frequency domain:

$$E = Z.B$$

$$Z = \begin{pmatrix} Z_{xx} & Z_{xy} \\ Z_{yx} & Z_{yy} \end{pmatrix}$$

Swift skew

Swift's skew indicates the dimensionality of the subsurface structure (Swift, 1967). This is independent of rotation of the tensor matrix and the values ranges generally from 0 to 0.5 (Vozoff, 1972). The values are less than 0.2 for 1-D and 2-D structures (Swift, 1967). Higher skew values indicate the more complex structure of the site. In some cases, apparent resistivity and phase may be well-behaved but skew will show a high value if 3-D inhomogeneity is present (Berdichevsky, 1999). Skew measures impedance components differences to find out the deviation from 2-D structures (Swift, 1967). The diagonal terms are influenced strongly by noise. Consider the modified impedances.

$$S_1 = Z_{xx} + Z_{yy},$$
$$S_2 = Z_{xy} + Z_{yx},$$
$$D_1 = Z_{xx} - Z_{yy},$$
$$D_2 = Z_{xy} - Z_{yx}$$

Where, S1 and D1 are rotationally invariant.

Further, Swift's skew is defined as,

$$K = \left|\frac{S_1}{D_2}\right|$$

Bahr skew

Bahr's skew (BS) is a measure of the local 3-D distortion of regional 2-D fields based on impedance phase, rather than on impedance magnitudes that is the conventional definition of skew (Vozoff, 1972). For BS greater than 0.3 the data considered as 3-D (Bahr, 1991). The Bahr's skew is given as:

$$\eta = \frac{\left(\left[D1, S2\right] - \left[S1, D2\right]\right)^{1/2}}{|D_2|}$$

Where, D_1, D_2, S_1 and S_2 are derived in above equations.

Extended Groom and Bailey decomposition

Extended Groom and Bailey decomposition method (McNeice and Jones, 2001) has been used to find the most consistent 2-D parameters over a different frequency band. Extended GB decomposition (McNeice and Jones, 2001) utilizes all the physical constraints implicit to the Groom Bailey decomposition model (Groom and Bailey, 1989) which imposed simultaneously on all dataset and a global minimum misfit solution achieved to estimate a regional geo-electrical strike in presence of galvanic 3-D distortions. This decomposition technique shows shear and twist values. If the values are above +/-45 for shear and twist, the data is 3D in nature.

Phase tensor analysis

The invariant parameters lambda and beta determine the dimensionality of regional impedance tensor (Bibby et al., 2005 & Caldwell et al., 2004). Bibby (2005) distinguished 1-D, 2-D and 3-D structures on the values of lambda and beta. In case of 1-D structure, the lambda as well as beta will be zero, for 2-D structure lambda become non-zero, while the beta become zero and for 3-D structure both beta as well as lambda become non-zero. The criterion provided by the phase tensor parameters is necessary but not sufficient for determining the dimensionality of the regional conductivity structure (Bibby et al., 2005). The dimensionality evaluated using phase tensor gives the best result by considering the MT sites from different locations collectively. It has become common practice to combine the problem of determining the strike direction with distortion removal. The phase tensor provides the better solution for dimensionality and the strike direction. The Phase Tensor is defined as,

$$\phi = X^{-1} \quad Y$$
$$\phi = \left(DX_R\right)^{-1}\left(DY_R\right)$$
$$\phi = X_R^{-1} D^{-1} DY_R$$
$$\phi = X_R^{-1} Y_R = \phi_R$$

Where, Φ & ΦR are measured and regional phase tensors, D is distortion tensor, X and Y are real & imaginary parts of the measured impedance tensor, XR and YR are real and imaginary parts of regional impedance tensor.

The following equations derive the formulae of Lambda and Beta:

$$\phi = \begin{bmatrix} X_{22}Y_{11} - X_{12}Y_{21} & X_{22}Y_{12} - X_{12}Y_{22} \\ X_{11}Y_{21} - X_{21}Y_{11} & X_{11}Y_{22} - X_{21}Y_{12} \end{bmatrix} \Big/ \det(X)$$
$$\phi = \begin{bmatrix} \phi_{11} & \phi_{12} \\ \phi_{21} & \phi_{22} \end{bmatrix}$$

Where, det(X) = $X_{11}X_{22} - X_{21}X_{12}$

The simplest algebraic representations of the tensor invariants are the trace

$$tr(\phi) = \phi_{11} + \phi_{22}$$

The skew is:

$$sk(\phi) = \phi_{12} - \phi_{21}$$

and the determinant of the matrix is:

$$\det(\phi) = \phi_{11}\phi_{22} - \phi_{12}\phi_{21}$$

The first order function of all the invariants is:

$$\phi_1 = \frac{tr(\phi)}{2}$$
$$\phi_2 = \left[\det(\phi)\right]^{1/2}$$

and

$$\phi_3 = \frac{sk(\phi)}{2}$$
$$\phi_{\min} = \left(\phi_1^2 + \phi_3^2\right)^{1/2} - \left(\phi_1^2 + \phi_3^2 - \phi_2^2\right)^{1/2}$$
$$\phi_{\max} = \left(\phi_1^2 + \phi_3^2\right)^{1/2} + \left(\phi_1^2 + \phi_3^2 - \phi_2^2\right)^{1/2}$$
$$Ellipticity(\lambda) = \frac{(\phi_{\max} - \phi_{\min})}{(\phi_{\max} + \phi_{\min})}$$
$$Skew(\beta) = \frac{1}{2}\tan^{-1}\left(\frac{\phi_3}{\phi_1}\right)$$

Therefore, PT ellipses can be plotted by obtaining values from Ellipticity (λ) and Skew angle (β).

Table 2. Estimated PT ellipse parameters for different periods at each site.

Periods	PT Ellipse Parameters	D2	D4	D5	D6	D7	D8	D9	D10	D11	D12	D13	D14	D15
0.1s	Beta	0.0	1.9	-1.9	-0.1	4.2	-0.7	-7.3	-0.6	1.6	0.4	2.7	0.2	0.4
	Phimin	0.8	0.7	0.7	0.7	0.9	1.1	0.6	0.5	0.5	0.5	0.5	0.4	0.4
	phimax	0.9	0.8	0.8	0.8	0.9	1.1	0.7	0.6	0.6	0.6	0.5	0.5	0.4
1s	Beta	2.1	-1.7	-2.9	-0.3	-3.5	4.6	-2.3	1.4	1.2	0.8	-5.1	3.0	5.6
	Phimin	0.4	0.5	0.5	0.4	0.5	0.6	0.4	0.5	0.5	0.6	0.5	0.5	0.6
	phimax	0.5	0.5	0.8	0.6	0.5	0.6	0.5	0.6	0.5	0.7	0.7	0.8	0.8
10s	Beta	-6.0	7.2	-42	-15	3.7	2.4	-5.4	6.5	41	-32	-0.9	-40	41
	Phimin	0.4	0.4	0.5	0.2	0.2	0.3	0.2	0.2	-0.1	-0.0	0.3	0.0	0.3
	phimax	0.8	0.8	0.9	0.7	0.8	0.8	1.3	1.3	0.8	0.2	1.2	0.7	0.9
100s	Beta	5.8	3.8	26	-17	5.2	7.0	5.7	7.6	2.4	-27	-1.8	-32	4.0
	Phimin	0.1	0.3	0.3	0.2	0.2	-0.2	0.2	0.2	0.2	0.2	0.1	0.4	0.5
	phimax	0.5	0.5	2.9	0.6	0.9	0.5	0.7	0.8	2.8	0.8	0.7	1.1	1.1

Induction Arrows

Induction arrows are vector representations of the complex ratios of vertical to horizontal magnetic field components (Naidu, 2012). It determines the presence or absence of lateral variations in conductivity (Jupp and Vozoff, 1976). In a 2-D Earth, induction arrow is associated only with the E-polarization. Thus, insulator conductor boundaries extending through a 2-D Earth gives rise to induction arrows that orient perpendicular to them and their magnitude indicate the intensities of anomalous current concentrations (Wiese, 1962). The vectors point towards the anomalous internal concentrations of current (Simpson and Bahr, 2005) called Parkinson convention, whereas the vector points away from the internal current concentrations are called Wise convention

WALDIM Technique

WALDIM, a FORTRAN code is used to perform the dimensionality analysis of Dwarka MT data. This code is based on Weaver et al. (2000) criteria. WALDIM technique allows categorizing the dimensionality into bands of periods for each site, in order to have a more stable estimate of the dimensionality. For particular site and their frequency, the code figures the type of dimensionality structure, as well as, strike direction and distortion parameters, including errors. This method of averaging over period bands differs from that used in the Strike Decomposition code, with the main difference that, whereas Strike Decomposition code provides least-squares fit to data from a given period band, however WALDIM averages the separate results within the band. Weaver et al. (2000) presented a dimensionality study based on sets of rotationally invariant scalars computed from the observed MT impedance tensor. The set of eight invariants (i.e. seven independent (I1, I2, I3, I4, I5, I6, I7) and a dependent one (Q)) known as WAL invariants, defined in a way that the invariants represent a Mohr circle diagram. The I1 and I2 are non-dimensional and normalized to unity, their vanishing has a physical interpretation, specifically related to the geoelectric dimensionality. Based on these WAL invariants, Marti et al. (2009) developed a code for dimensionality analysis known as WALDIM. This provides a robust description of the subsurface dimensionality, as well as the parameters necessary for data correction prior to model.

RESULTS AND DISCUSSIONS

To obtain dimensionality information of the regional subsurface structure the Swift's skew and Bahr's skew are computed for a period range of 0.01-100 s, at all stations (Figure 4). The Swift's skew values have been found less than 0.2° at majority stations for period range 0.01-100 s, which suggests the 1D and 2D nature of the structure, but at some stations the Swift's skew plot shows higher value (i.e. > 0.2°) for period range 10-100s, indicating the 3D subsurface structure. The Bahr's skew plot shows a value less than 0.3° for period range of 0.01-100s, which suggests the structure, is 1D and 2D, but at some sites, the value rises above 0.3° for period range 10-100s, indicating the structure is 3D. Patro et al., (2005), Tao et al., (2010), Naidu et al., (2011), Hubert, (2012), Barcelona et al., (2013), Oskooi et al., (2013) and Pranata et al., (2017) have also applied these techniques in the past.

Phase tensor ellipse calculated for the four different periods (0.1, 1, 10 and 100 sec) are presented in Figure 5. As stated earlier, Bibby, (2005) distinguished 1D, 2D and 3D structures based on lambda and beta values. Referring to the criteria given by Bibby (2005), the calculated phase tensor ellipses for 0.1sec and 1sec are close to circular, which indicates the 1D subsurface structure. The ellipses

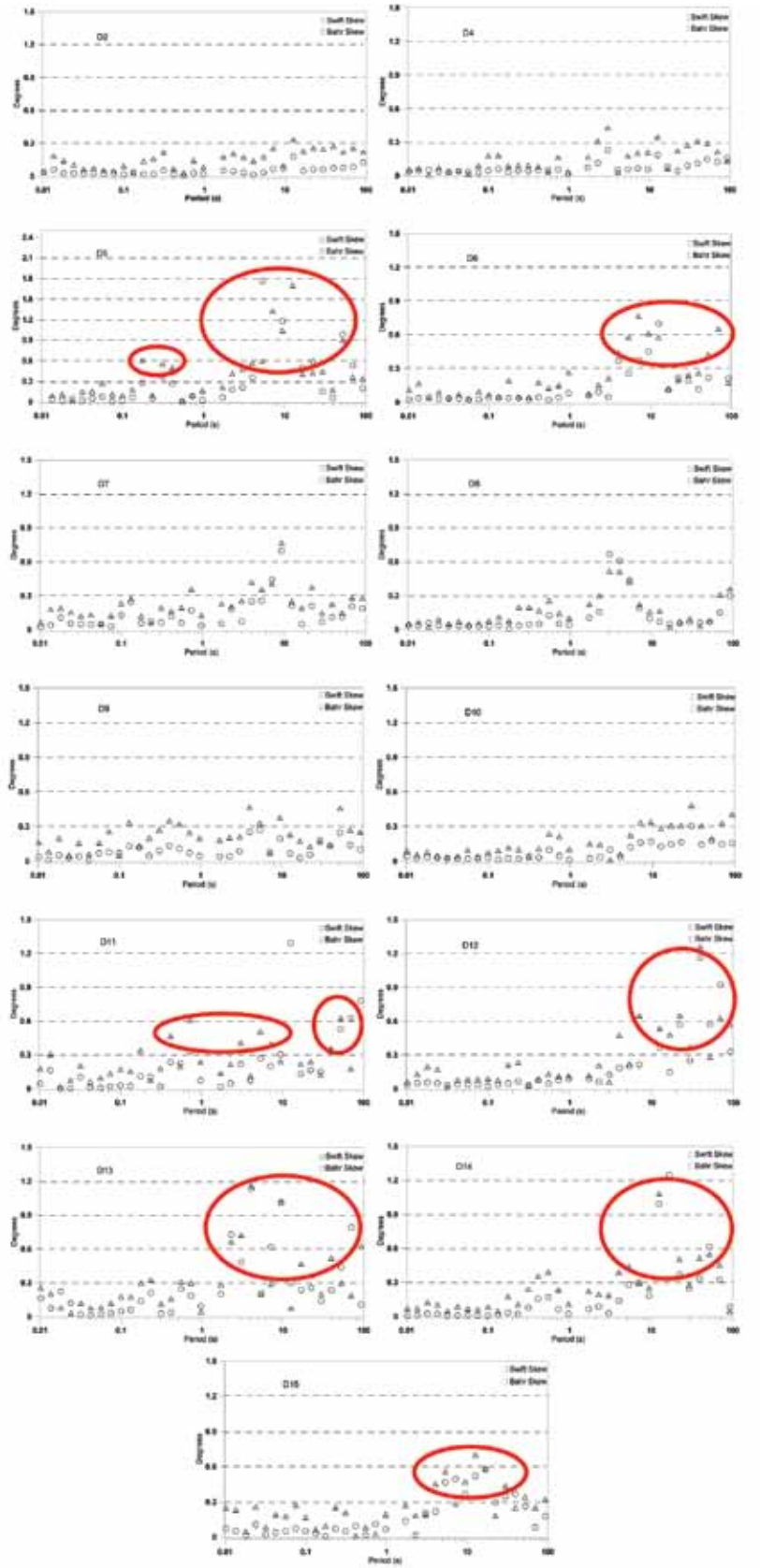

Figure 4. Swift's and Bahr's skew plots showing 3D effects (data points marked with red circles) for periods greater than 1 sec.

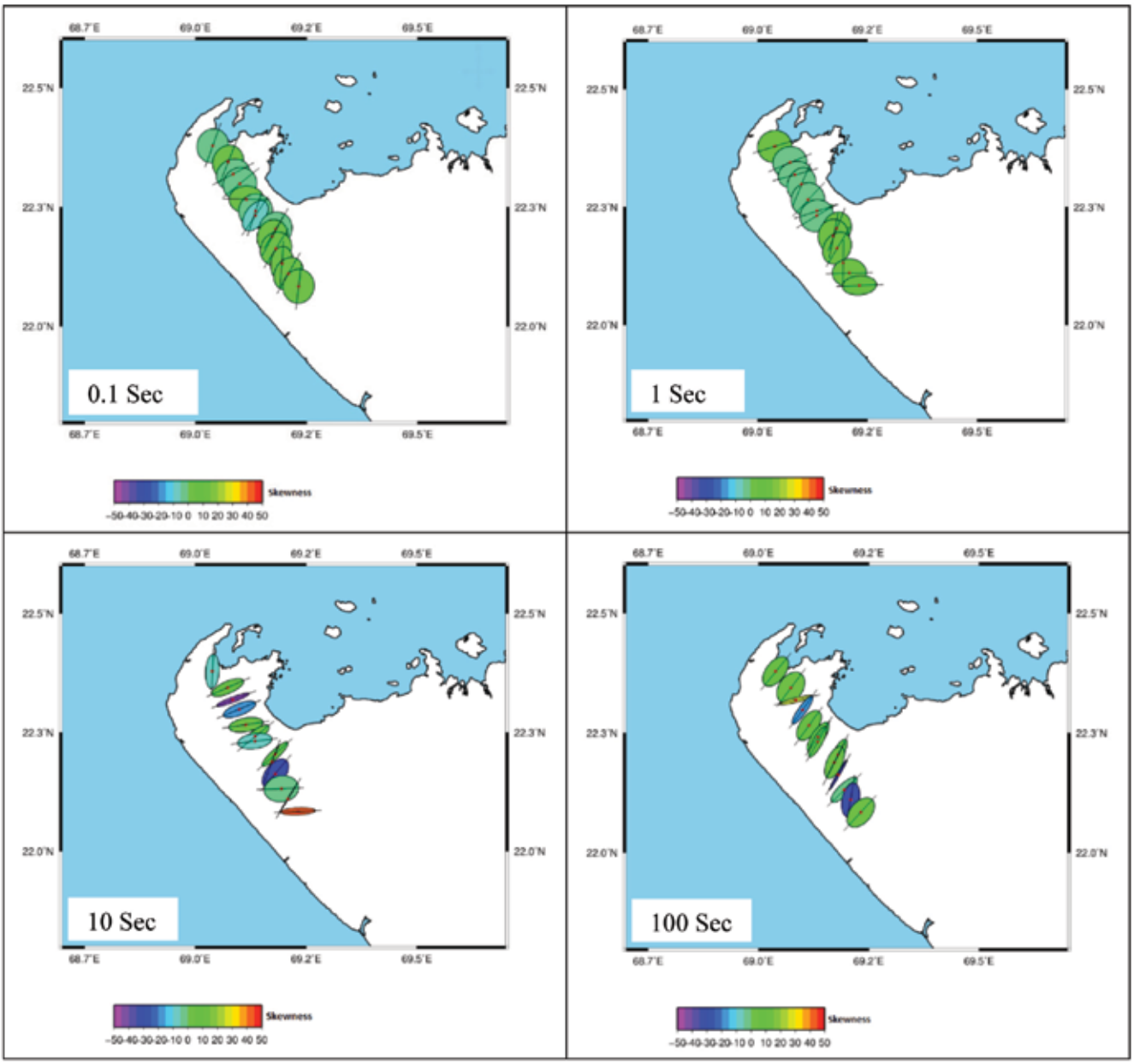

Figure 5. Phase Tensor Ellipse plots along the MT profile for four different periods (0.1, 1, 10 and 100 Secs).

at 10secs and 100secs are elongated, suggesting the 2D structure. At some stations, the plot shows high skew values which indicate 3D subsurface structure. The major axes of the ellipses are aligned mainly in NNE-SSW direction, which is consistent with the structural trend shown in Figure 2. The estimated values of major axes, minor axes and beta are mentioned in Table-2. Heise et al., (2008), Tao et al., (2010), Selway et al., (2012), Booker, 2014, Febriani et al., (2017) and Pranata et al., 2017 employed the phase tensor technique in their study to estimate the dimension of the subsurface structure.

According to Jones and Groom (1993), the proper selection of strike angle is important as it represents the structure in the model calculated from MT data and if the strike angle chosen is incorrect, it will lead to erroneous model. The choice of strike angle can be done by geological/tectonic trends of the region. There are several ways to estimate strike direction. In the present study, strike direction for broad period as well as various period bands is estimated through Phase Tensor (PT), Groom-Bailey (GB) and Becken and Burkhardt (BB) techniques (Figure 6). The NNE-SSW strike direction has been estimated in the

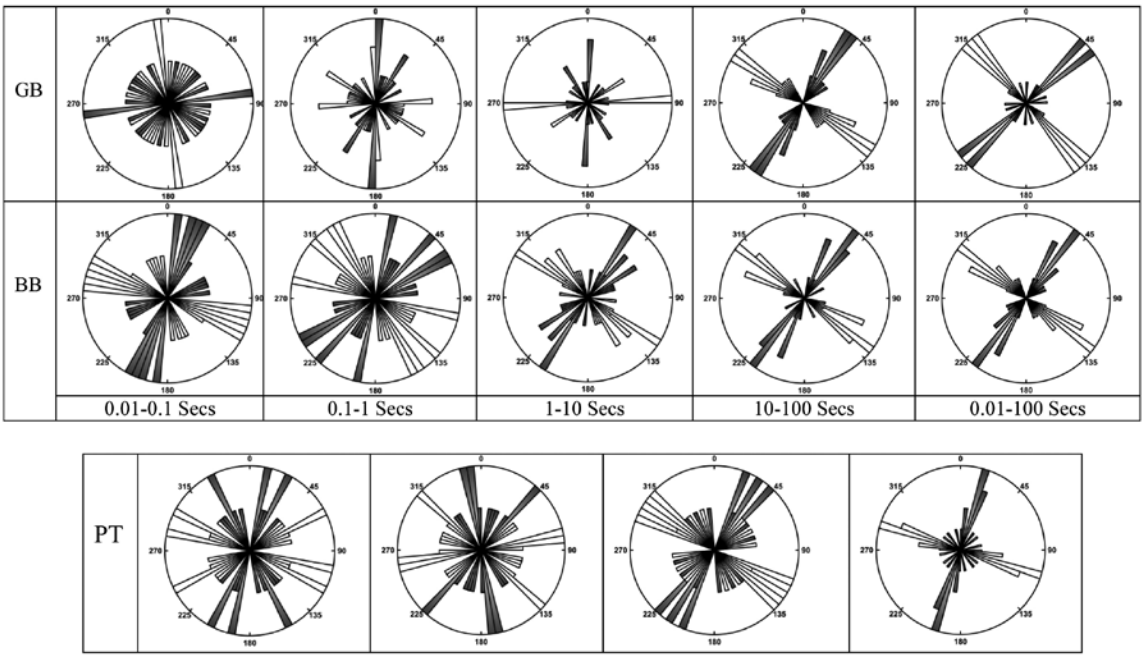

Figure 6. Rose diagram plot of regional strike direction for broad period through Groom-Bailey Decomposition (GBD), Becken and Burkhardt Decomposition (BBD) and phase tensor (PT) techniques.

Table 3. Strike values estimated for broad period range through three techniques (GB, BB and PT)

Sites	GB (0.01-100s)	BB (0.01-100s)	PT(100s)
D2	54.7	37.8	18.55
D4	73.1	36.6	08.00
D5	40.4	57.3	16.08
D6	39.5	27.1	16.56
D7	43.6	35.5	21.91
D8	51.9	38.0	-14.24
D9	0.00	30.1	20.15
D10	42.6	28.5	21.29
D11	34.8	48.3	16.82
D12	43.6	20.6	01.75
D13	54.7	45.5	08.57
D14	45.5	27.0	-39.25
D15	51.3	67.0	37.73

area, which is in good agreement with the tectonic trend (Figure 2). The regional strike values are given in Table 3 for broad period range estimated through GB, BB and PT technique. Earlier, Patro et al. (2005) (BB technique); Naidu et al., 2011 (GB technique) and Barcelona et al., 2013 (GB technique), adopted these techniques in their study for the estimation of regional strike direction.

The dimensionality analysis has been conducted using WAL rotational invariants criteria the WALDIM code (Marti et al., 2009). The WALDIM code estimates the dimensionality in to period bands at each site. For each site the dimensionality of the band is the most occurring dimensionality response of the data in the band, if there occurs more than one dimensionality type in the band, priority is given to the lowest dimensionality. The dimensionality in the lower periods (0.0102 – 0.8286 sec) has been found 1D, except stations D12, D13, D14 and D15 (showing 3D and undetermined). The undetermined dimensionality is caused due to presence of error bars of the invariants Marti et al., 2009, while for higher periods (1.1110 – 90.4510 sec), it shows 3D/2D and 3D dimensionality at all stations (Table-4). Several researchers

Table 4. Dimensionality Analysis using WALDIM technique.

Sites	bands	Tmin.	Tmax.	Dimensionality	Sites	bands	Tmin.	Tmax.	Dimensionality
D2	1	0.0102	0.0793	1D		4	11.6078	90.4510	3D
	2	0.1063	0.8286	1D	D10	1	0.0102	0.0793	1D
	3	1.1110	8.6570	3D/2D		2	0.1063	0.8286	1D
	4	11.6078	90.4510	3D		3	1.1110	8.6570	3D
D4	1	0.0102	0.0793	1D		4	11.6078	90.4510	3D
	2	0.1063	0.8286	1D	D11	1	0.0102	0.0793	1D
	3	1.1110	8.6570	3D		2	0.1063	0.8286	1D
	4	11.6078	90.4510	3D		3	1.1110	8.6570	3D
D5	1	0.0102	0.0793	1D		4	11.6078	90.4510	UNDETERMINED
	2	0.1063	0.8286	1D	D12	1	0.0102	0.0793	1D
	3	1.1110	8.6570	UNDETERMINED		2	0.1063	0.8286	3D
	4	11.6078	90.4510	3D		3	1.1110	8.6570	3D
D6	1	0.0102	0.0793	1D		4	11.6078	90.4510	3D
	2	0.1063	0.8286	1D	D13	1	0.0102	0.0793	3D
	3	1.1110	8.6570	UNDETERMINED		2	0.1063	0.8286	3D
	4	11.6078	90.4510	3D		3	1.1110	8.6570	UNDETERMINED
D7	1	0.0102	0.0793	1D		4	11.6078	90.4510	UNDETERMINED
	2	0.1063	0.8286	3D	D14	1	0.0102	0.0793	1D
	3	1.1110	8.6570	1D		2	0.1063	0.8286	3D
	4	11.6078	90.4510	3D		3	1.1110	8.6570	3D
D8	1	0.0102	0.0793	1D		4	11.6078	90.4510	3D
	2	0.1063	0.8286	1D	D15	1	0.0102	0.0793	1D
	3	1.1110	8.6570	3D		2	0.1063	0.8286	3D
	4	11.6078	90.4510	3D/2D		3	1.1110	8.6570	UNDETERMINED
D9	1	0.0102	0.0793	1D		4	11.6078	90.4510	3D
	2	0.1063	0.8286	3D					
	3	1.1110	8.6570	UNDETERMINED					

have used this technique in their study for dimensionality analysis (Marti et al., 2010; Tao et al., 2010; Barcelona et al., 2013; Marti et al., 2016 and Kashkouli et al., 2016.

The purpose of distortion decomposition is to separate local and regional parameters as much as possible under the assumption that the regional structure is at most 2D and the local structures cause only galvanic scattering of the electric fields (Groom and Bailey, 1989). According to groom and bailey (1989), a family of unit vectors of an electric field is given by a vector on the x-axis which is deflected clockwise by an angle $\tan^{-1} e$, and a vector along the y-axis which is deflected in counter-clockwise direction with the same angle. Therefore, distortion parameter shear is estimated by a shear angle. Similarly, for estimation of twist angle, the electric field vectors rotate through a clockwise angle $\tan^{-1} t$. RMS Error is a factor which indicates whether the MT data fits the distortion model with the acceptable value of RMS error or not. In Figure 7, the distortion parameters are calculated for various period bands as well as the broad period band. The maximum shear angle value observed for the period band 10-100s is 15.99°. Similarly, for twist angle, the maximum value observed for the period band 10-100s is 12.76°. Thus, for periods greater than 10s higher shear and twist values were observed, which could be the reason for the 3D structure shown in swift and Bahr skew results. However, the values of shear and twist angle for the broad period band is below +/-45°, which suggests a 2D structure. Thus, the distortion model fits the data with an acceptable average RMS error value of ~2°.

According to Simpson and Bahr (2005), induction arrows can be used to demarcate the presence or absence of lateral variations in conductivity, as these vertical magnetic fields are caused by lateral conductivity gradients. Induction arrows eliminate the 90° ambiguity cases, which helps in proper choice of regional strike direction. The induction arrow for the period band of 0.01 to 100sec is given in Figure 8. Westward and eastward pointing arrows, respectively

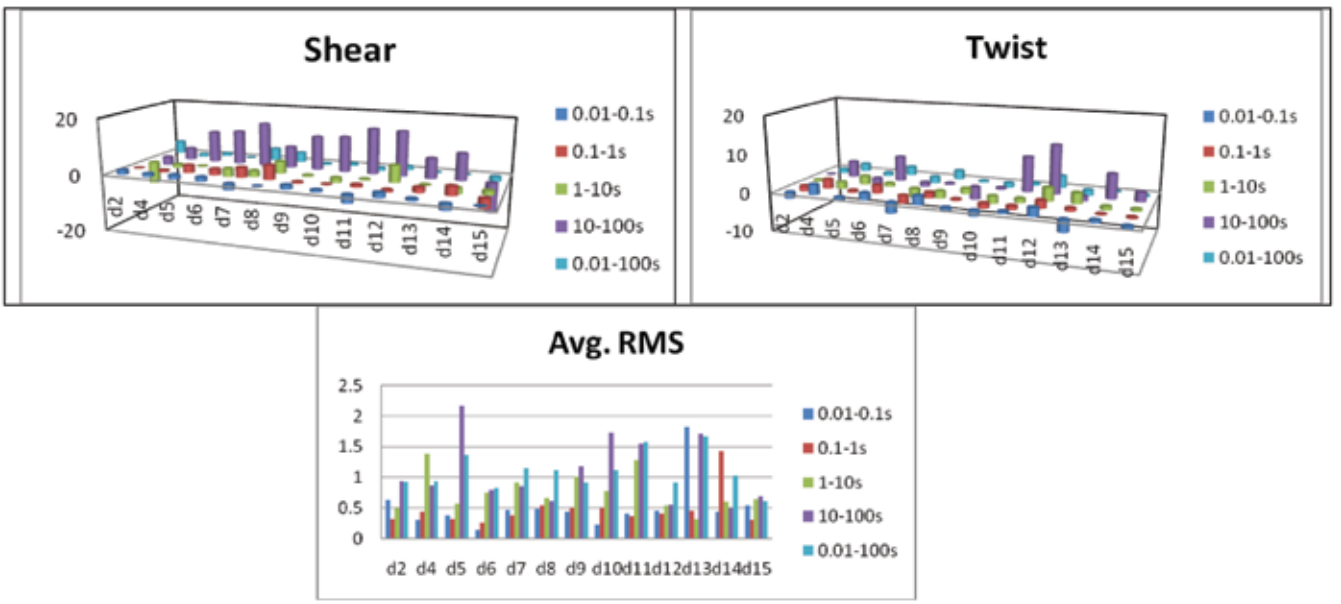

Figure 7. Distortion parameters plotted through GBD technique for various period bands as well as broad period band.

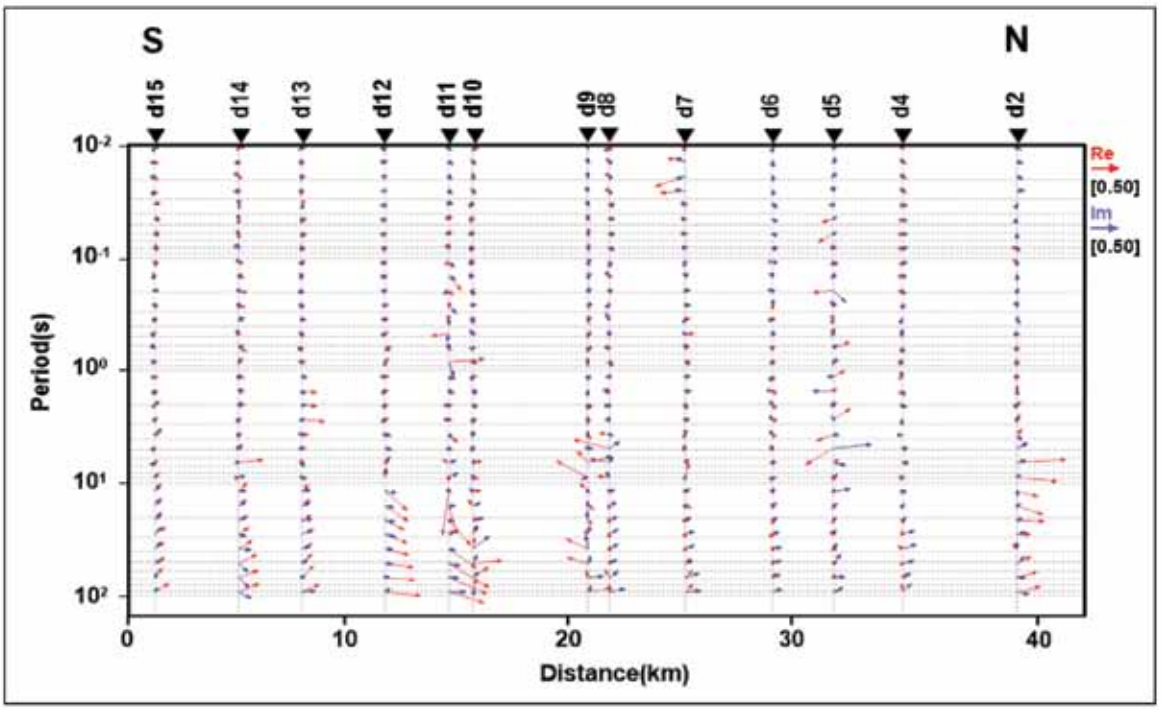

Figure 8. Induction arrow plot for broad period at each MT station.

indicate a zone of low resistivity that trends parallel to the strike direction (real arrows are oriented perpendicular to the electric strike). As expected, the real induction arrows point towards the conductive zone, present between the stations d9 and d10. Due to low resistive zone, the orientation of real induction arrows changes from east to west at station d9, also at station d2 the real induction arrows pointing towards the east, indicating a conductive zone. At increasing distance from the conductor the length of the arrows decreases. A sub-parallel alignment of the real arrows to their imaginary parts is another indication for a two-dimensional geometry (Rothe et al., 2004), which is observed at high periods (Figure 8).

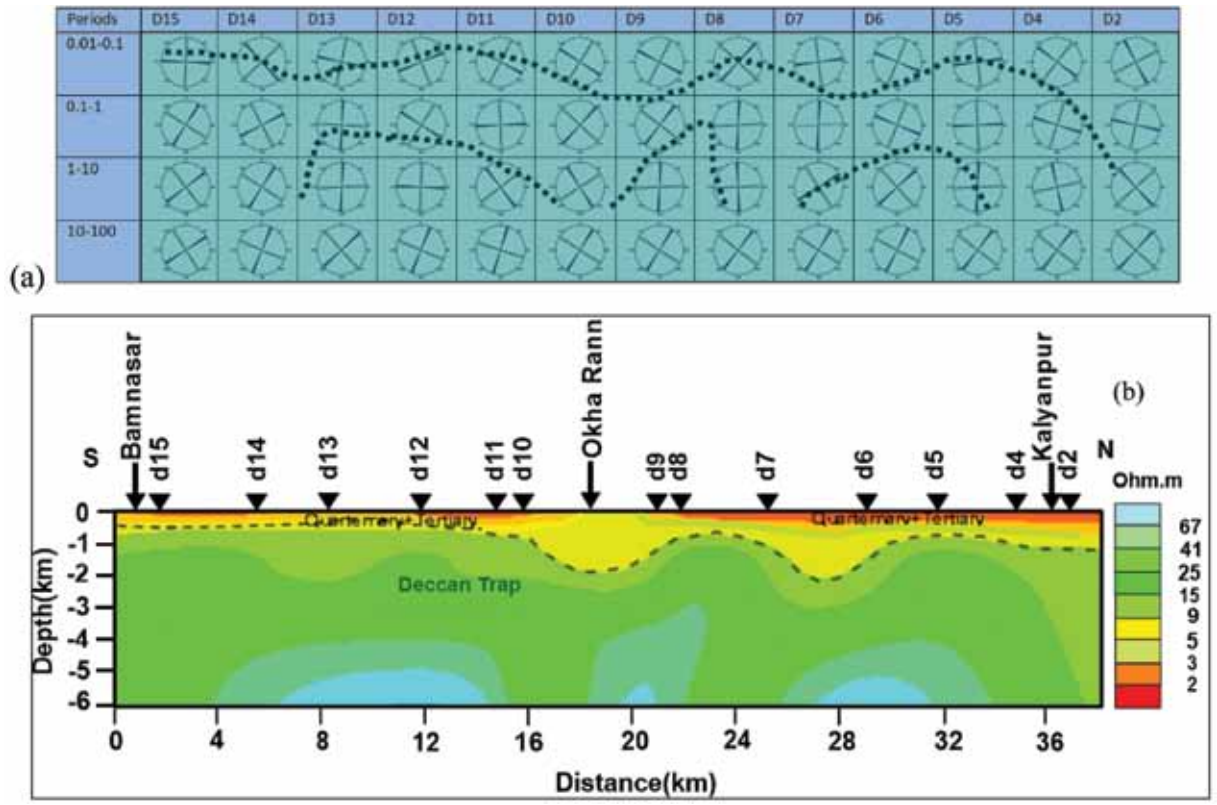

Figure 9. Correlation of (a) the estimated strike direction for various period bands at each site with (b) the 1D resistivity section generated from Occam's 1D inversion.

Correlation of strike with 1D model

A 1D smooth modeling approach is adopted for delineation of subsurface resistivity structure subjected to Occam's linearized scheme. The dimensionality analysis suggested 1D nature of data up to the 1s period. Therefore, 1D Occam inverse model up to 6 km depth is shown in Figure 9(b). The inverted model gave a resistivity value of <10 Ohm-m for Quaternary and Tertiary sediments and ~20 - 60 Ohm-m for Trap layer. The thickness of sediments is observed about 500m deep in the Southern part of the profile and increases to ~2km in the central part of the profile near Okha rann (Figure 9(b)). The thickness of sediments reduces to ~1km in the Northern part of the profile. The strike trend matches well with the 1D resistivity model. The NS strike direction is observed at station D5, D8 and D13 and also the undulations are clearly seen at the boundary of Quaternary-Tertiary sediments and Deccan trap in the 1D resistivity model (Figure 9(b)).

CONCLUSION

In the present study, the Dimensionality and Directionality analysis have been computed using Phase Tensor Analysis (PTA) technique, WALDIM Fortran code, Swift's and Bahr's Skew technique, Groom-Bailey (GB) and Becken and Burkhardt (BB) technique. Dimensionality parameters Swift skew and Bahr skew plots show 2D subsurface structure except some stations showing values greater than 0.3° for higher periods, which indicates the 3D subsurface structure. Because of heterogeneity present in the area, the skewness values are not same for all MT stations and for all period bands. The Phase Tensor analysis for all MT stations at four different bands shows moderate skewness values, except some stations which shows high skewness values suggesting the subsurface structure is more than 2D, the WALDIM results are consistent with Phase Tensor analysis results. The distortion model generated from the Groom and Bailey decomposition technique fits the data with RMS error value of ~2.0. Regional strike estimated through three techniques (PT, GB, and BB) suggests a NNE-SSW direction, consistent with the Delhi-Aravalli trend. From 1D resistivity model, the undulations are found at the boundary of Quaternary-Tertiary sediments and Deccan trap in the central and Northern part of the profile, which indicates the presence of faults.

ACKNOWLEDGEMENTS

We thank Director General and Director for their permission to publish the present work. This work is supported by

Gujarat Pavitra Yatradham Vikas Board (GPYVB). We are thankful to Prof. Alan G Jones and Prof. Becken and Burkhardt for providing strike decomposition codes.

Compliance with Ethical Standards

The authors declare that they have no conflict of interest and adhere to copyright norms.

REFERENCES

Bahr, K., 1988. Interpretation of the magnetotelluric impedance tensor: Regional induction and local telluric distortion, J. Geophys, 62, 119-127.

Bahr, K., 1991. Geological Noise in Magnetotelluric Data: A Classification of Distortion Types. Phys. Earth and Planet. Int.. 66, 24-38.

Barcelona et al., 2013. The potentials of audiomagnetotellurics in the study of geothermal fields: A case study from the northern segment of the La Candelaria Range, Northwestern Argentina. J. Appl. Geophys., 88, 83-93.

Becken, M. and Burkhardt, H., 2004. An Ellipticity criterion in Magnetotelluric tensor analysis. Geophys. J. Int., 159, 69-82

Berdichevsky, M.N., 1999. Marginal notes on magnetotellurics. Surv. Geophys., 20, 341-375.

Bhatt, N., 2000. Lithostratigraphy of neogene-quaternary deposits of Dwarka-Okha area, Gujarat. J. Geol. Soc. India. 55, 139-148.

Bibby, H.M., Caldwell, T.G. and Brown, C., 2005. Determinable and non-determinable parameters of Galvanic distortion in magnetotellurics. Geophys. J. Int., 163, 915-930.

Biswas, S.K., 1982. Rift basins in western margin of India and their hydrocarbon prospects with special reference to Kutch basin. Am. Assn. Petroleum Geol. Bull., 66, 307-327.

Biswas, S.K., 1987. Regional tectonic frame work, structure and evolution of the western marginal basins of India. Tectonophysics. 135, 307-327

Biswas, S.K., 2005. A review of structure and tectonics of Kutch basin, Western India, with special reference to earthquakes. Curr. Sci., 88(10), 1592-1600

Booker, 2014. The magnetotelluric phase tensor: A critical review. Surv. Geophys, 35, 7-40.

Caldwell, T.G., Bibby, H.M. and Brown, C., 2004. The Magnetotelluric phase tensor, Geophys. J. Int., 158, 457-469.

Febriani et al., 2017. The Magnetotelluric phase tensor analysis of the Sembalun Propak area, West Nusa Tenggara, Indonesia. J. Phys., conference series. 817: 012072

Groom, R.W. and Bailey, R.C., 1989. Decomposition of the Magnetotelluric impedance tensor in the presence of local three-dimensional galvanic distortion. J. Geophys. Res., 94, 1913-1925.

Heise et al., 2008. Three-dimensional modelling of Magnetotelluric data from the Rotokawa geothermal field, Taupo Volcanic Zone, New Zealand. Geophys. J. Int., 173, 740-750.

Hubert, 2012. From 2D to 3D models of electrical conductivity based upon Magnetotelluric data: Experiences from two case studies. Digital comprehensive summaries of Uppsala dissertations from the faculty of Science and Technology. 890:55

Jones and Groom, 1993. Strike-angle determination from the Magnetotelluric impedance tensor in the presence of noise and local distortion: rotate at your peril. Geophys. J. Int., 113, 524-534.

Jupp, D.L.B. and Vozoff, K., 1976. Stable iterative methods for the inversion of geophysical data. Geophysical J. Royal Astron. Soc., 42, 957-976.

Kashkouli et al., 2016. Dimensionality analysis of the subsurface structures in Magnetotellurics using different methods (a case study: oil field in Southwest of Iran). J. Mining. Environ, 7, 119-126.

Marti, A., Queralt, P. and Ledo, J., 2009. WALDIM: A code for the dimensionality analysis of magnetotelluric data using the rotational invariants of the magnetotelluric tensor. Comput. Geosci., 35:2295-2303

Marti et al., 2010. Dimensionality imprint of electrical anisotropy in Magnetotelluric responses. Phys. Earth planet. Int., 182(3-4), pp.139.

Marti et al., 2016. Magnetotelluric characterization of the Alhama de Murcia Fault (Eastern Betics) preliminary results. Near surface Geoscience. Conference and Exhibition.

McNeice, G.W. and Jones, A.G., 2001. Multisite, multifrequency tensor decomposition of magnetotelluric data. Conf. paper in Geophysics. 66, 158-173.

Mishra et al., 2001. Major lineaments and gravity-magnetic trends in Saurashtra, India. Curr. Sci., 80(8).

Naidu et al., 2011. Electrical signatures of the Earth's crust in central India as inferred from Magnetotelluric study. Earth Planets and Space. 63, 1175-1182.

Naidu, G.D., 2012. Deep Crustal Structure of the Son-Narmada-Tapti Lineament, Central India, Springer Thesis, DOI: 10.1007/978-3-642-28442-7_2.

Oskooi et al., 2013. Investigation of electrical resistivity and geological structures on the hot springs in Markazi province of Iran using Magnetotelluric method. Boll. Geof. Teor. Appl., 54, 245-256.

Patro et al., 2005. Electrical Imaging of Narmada-Son lineament zone, Central India from Magnetotellurics. Phys. Earth Planet. Int., 148, 215-232.

Patro et al., 2015. Sub-basalt sediment imaging-The efficacy of Magnetotellurics. J. Appl. Geophys., 121, 106-115.

Pandey, D.K., Bahadur, T. and Mathur, U.B., 2007. Stratigraphic distribution and depositional environment of the chaya formation along the Northwestern Coast of Saurashtra Peninsula, Western India. J. Geol. Soc. India. 69(6), 1215-1231.

Pranata et al., 2017. Magnetotelluric Data Analysis using Swift Skew, Bahr Skew, Polar Diagram and Phase Tensor: A Case Study in Yellowstone, US. A Physical and Computational Science. 54(3), 311-317.

Rothe et al., 2004. Correlation of electrical conductivity and structural damage at a major strike-slip fault in Northern Chile. J. Geophys. Res., 109.

Selway et al., 2012. A simple 2D explanation for the negative phases in TE Magnetotelluric data. Geophysical J. Int., 188, 945-958.

Sharma et al., 2004. Delineation of electrical structure beneath Saurashtra peninsula using MT studies. 5th Conference and Exposition on Petroleum Geophysics, Hyderabad, India. 79-80.

Singh, S.B. et al., 2004. Delineation of Basaltic covered sediments in the Saurashtra region using Deep Resistivity Sounding studies. 5th Conference and Exposition on petroleum geophysics, Hyderabad. 69-74.

Simpson, F. and Bahr, K., 2005. Practical Magnetotellurics. Cambridge University Press, Cambridge, 270 pp.

Subbarao, P.B.V., Singh, A.K. and Rao, C.K., 2012. Regional conductance map of Saurashtra and surrounding regions. Curr. Sci., 103(2).

Swift, C.M., 1967. A magnetotelluric investigation of an electrical conductivity anomaly in the South Western of United States. Ph.D. Thesis. Massachusetts Institute of Technology.

Tao et al., 2010. Refined processing and two-dimensional inversion of Magnetotelluric data I: Impedance tensor decomposition and analysis of structural dimensionality. Chinese J. Geophys., 53, 6

Vozoff, K., 1972. The magnetotelluric method in the exploration of sedimentary basins. Geophys., 37, 98-141.

Weaver, J.T., Agarwal, A.K. and Lilley, F.E.M., 2000. Characterization of the Magnetotelluric in terms of its invariants. Geophys.J. Int., 141, 321-336.

Wiese, H., 1962. Geomagnetische... Teil II: Die streichrichtung der Untergrundstrukturen des elektrischen Widerstandes, erschlossen aus geomagnetischen variationen. Geo□.s Pura et Appl. 52, 83-103.

Yadav et al., 2008. Probabilistic assessment of earthquake hazard in Gujarat and adjoining regions. Pure Appl. Geophys., 165, 1813-1833.

Received on: 14.6.18; Revised on: 21.9.18; Accepted on: 1.10.18

J. Ind. Geophys. Union (January 2019)
v.23, no.1, pp: 55-68

Performance evaluation of different interpretation techniques of vertical electrical sounding data

P. Venkateswara Rao[1], M. Subrahmanyam[1]* and D. Ratnakar[2]

*[1]Department of Geophysics, Andhra University, Visakhapatnam-530003, India
[2]CSIR-National Geophysical Research Institute, Uppal Road- Hyderabad.
*Corresponding Author: smangalampalli@rediffmail.com.

ABSTRACT

Numerous interpretation techniques are available in the literature to interpret Vertical Electrical Sounding (VES) data and thus it becomes very difficult to choose one of them. A performance analysis of each method and its comparison with other techniques would aid the geophysicists to choose a better technique. An attempt has been made here to evaluate the performance and comparison of a few widely used interpretation techniques. The computer oriented interpretation techniques RESIST, IRESAN and IPI2Win have been subjected to rigorous analysis using input model parameters. These techniques are applied to interpret the theoretical three and five layered earth models generated for various combinations of resistivities and thicknesses and the output results are analyzed for their accuracy for all the three techniques. The analysis of their performance reveals that IPI2Win technique yields comparatively better results with minimum errors in the output of the interpreted parameters.

Key words: Vertical electrical sounding, Inversion algorithm, Percentage error, RMS error.

INTRODUCTION

The electrical method is one of the important geophysical methods in exploring the subsurface materials, particularly in shallow layers. The VES curves are usually interpreted using curve-matching procedures with the help of theoretical curves (Compagnie Generale de Geophysique, 1963; Flathe, 1963; Orellana and Mooney, 1966; Rijkswaterstaat, 1969) in conjunction with the auxiliary-point method of partial curve matching (Kalenov, 1957; Orellana and Mooney, 1966; Zohdy, 1965). Numerous techniques are available in literature for interpreting the VES data based on curve matching, inversion algorithm, forward algorithm and modeling to obtain the true resistivity and thickness of different layers. The utility of the master curves to interpret field data from various geological settings is rather restricted in the sense that the standard curves are available only for a limited number of layers of given resistivities and thicknesses. Quite often, it is found that the observed VES curve does not match with any of the available standard curves. In case of 5 or more number of layers, no standard curves are available for direct matching. In fact, even the experienced interpreter may find it difficult to obtain satisfactory curve matches, when he uses the auxiliary-point method for geoelectrical sections containing layers with small effective-relative resistances or small effective-relative conductance (Flathe, 1963; Zohdy and Jackson, 1973; Zohdy, 1974, Zohdy, 1975). The availability of inexpensive micro and personal computers has now made it possible to develop and implement algorithms, which can provide very efficient and accurate interpretation of VES data. Different computer programs like RESIST, IRESAN, Winsev, 1X1D, Zhond and IPI2 Win to interpret the resistivity sounding data are available based on different algorithms. In this study an attempt has been made to evaluate the performance of three most widely used techniques via IRESAN, RESIST and IPI2Win inversion algorithms for performance evaluation study. The percent errors in each parameter (ρ_1, ρ_2, $\rho_{3...}$, h_1, $h_{2....}$) for each technique, when applied to different models, are calculated.

WIDELY USED TECHNIQUES

Iterative Inversion

In this scheme, an initially guessed model is successively improved until the RMS (Root Mean Square) error is minimized to an acceptable level and the parameters remain stable (i.e., in successive iterations there is no improvement in the parameters), with respect to changes in the model. One of the simple ways to achieve this is provided by the Gauss method (Kowalik and Osborne, 1968), which requires accurate values of the partial derivatives of the model data with respect to their parameters. In this method, theoretical curves are computed from the initial guess model and matched with the observed values, which are improved iteratively until a best fit is achieved in the inversion process.

IRESAN

This program is developed by Das and Verma (1977), based on the steps of forward and inversion algorithms. While the theory for forward computation is largely reproduced from their work, the formulation for the inversion is based on the work by Jupp and Vozoff (1975).

The computation of vertical electrical resistivity curves in the forward algorithm is based on theory of digital linear filters. The inversion algorithm is structured around a modified version of the program, developed by Jupp and Vozoff (1975). The numerical scheme is based on a modified Gauss-Newton-Marquardt method to solve a system of non-linear equations. Using a variety of stabilization methods, the solution is obtained by the Singular Value Decomposition (SVD) of Jacobean matrix of partial derivatives with respect to parameters.

RESIST:

This program was developed by Vander Velpen and Sporry (1993) to process data obtained with Wenner, Schlumberger and Dipole-Dipole array, which is built around three main procedures:

(i) Smoothing of noisy field data, accurate computation of apparent resistivity models and inversion of resistivity data on an iterative procedure, which includes a priori information of the model parameters, without generating convergence problems.

(ii) Data smoothing (single point correction, curve branch shifting, and eccentricity correction for Schlumberger configuration) is done on the screen. For the computation of apparent resistivity model curves, the linear filter was used.

(iii) The inversion of resistivity data is based on the "Marquardts-Levenberg" technique (Marquardt, 1963). To overcome the convergence problem in using a priori information of model parameters, the Marquardts-Levenberg inversion algorithm was modified, considering a probabilistic treatment of the field observations and the model parameters. This modification allows the program to quickly reach a solution.

IPI2Win

This is free download software with copy right to Bobachev et al., 1990-2002, Moscow State University, Geophysical faculty, Department of geophysics and distributed by Geo Scan-M Ltd, Moscow, Russia. (http://geophys.geol.msu.ru/ipi2win.htm). IPI2Win is designed for automated and interactive semi-automated interpretation of vertical electrical sounding and/or induced polarization data obtained with any of the most popular arrays used in the electrical prospecting and can be run on any computer with Windows 95/98 NT operating system.

The program pays special attention to the user-friendly interactive interpretation. Due to handy controls, the interpreter can choose one from a set of equivalent solutions, which fits well with both the geophysical data (i.e., best fitting error) and geological data (i.e., geologically sensible resistivity cross-section).

INTERPRETATION OF SOUNDING DATA

IPI2Win is capable of solving electrical resistivity 1D forward and inverse problems for a variety of commonly used arrays for the cross-sections with resistivity contrast within the range of 0.0001 to 10000 ohm-m. The forward problem is solved using the linear filtering. In comparison, the inverse problem is solved using a variant of the Newton algorithm of the least number of layers or the regularized fitting minimizing algorithm using Tikhonov's approach to solve incorrect problems. Priory information on layers depths and resistivities can be used for regularizing the process of the fitting error minimizing. The IPI2Win approach involving interactive semi-automated interpretation is preferable, since it considers both the effectiveness and the geological sense into consideration. Some of these, being rather of descriptive than quantitative nature, can hardly be introduced as formal parameters into the interpreting model. In this case, the interpreter's experience and geological erudition may occur to be of even greater importance, than the calculation accuracy. The best fitting two-layered model is automatically suggested for the initial interpreting model of the present sounding point. Model editing involves altering the quantity of layers (from 2 up to 30) by means of splitting or joining them and changing the properties of the layers on the screen. The layer properties can be edited at the desired cell of the table in the model window. The theoretical curve will be redrawn for the present values of the model parameters.

The inversion techniques may yield several models that converge to a reasonable solution, with least RMS error. The model that fits the observed curve may not be the correct solution, keeping in view of the principle of equivalence. Hence, a detailed study is necessary and the models that fit the observed data is also to be analyzed in terms of its priority to the real model (actual lithology). In this article we have attempted all these analyses.

METHODOLOGY

To test the performance of these three techniques, theoretical curves have been generated with Schlumberger array and subjected to interpretation. Schlumberger array is widely used for conducting Vertical Electrical Sounding surveys to explore the subsurface. Hence, the theoretical Vertical Electrical Sounding curves with Schlumberger array have been generated over three and five layer subsurface models for different combinations of resistivities and thicknesses. Six models for A, H and Q and eight models for K-type have been used for generating theoretical VES curves. Two models of HKH and KHA of five layers were also interpreted in this study (Figure 1).

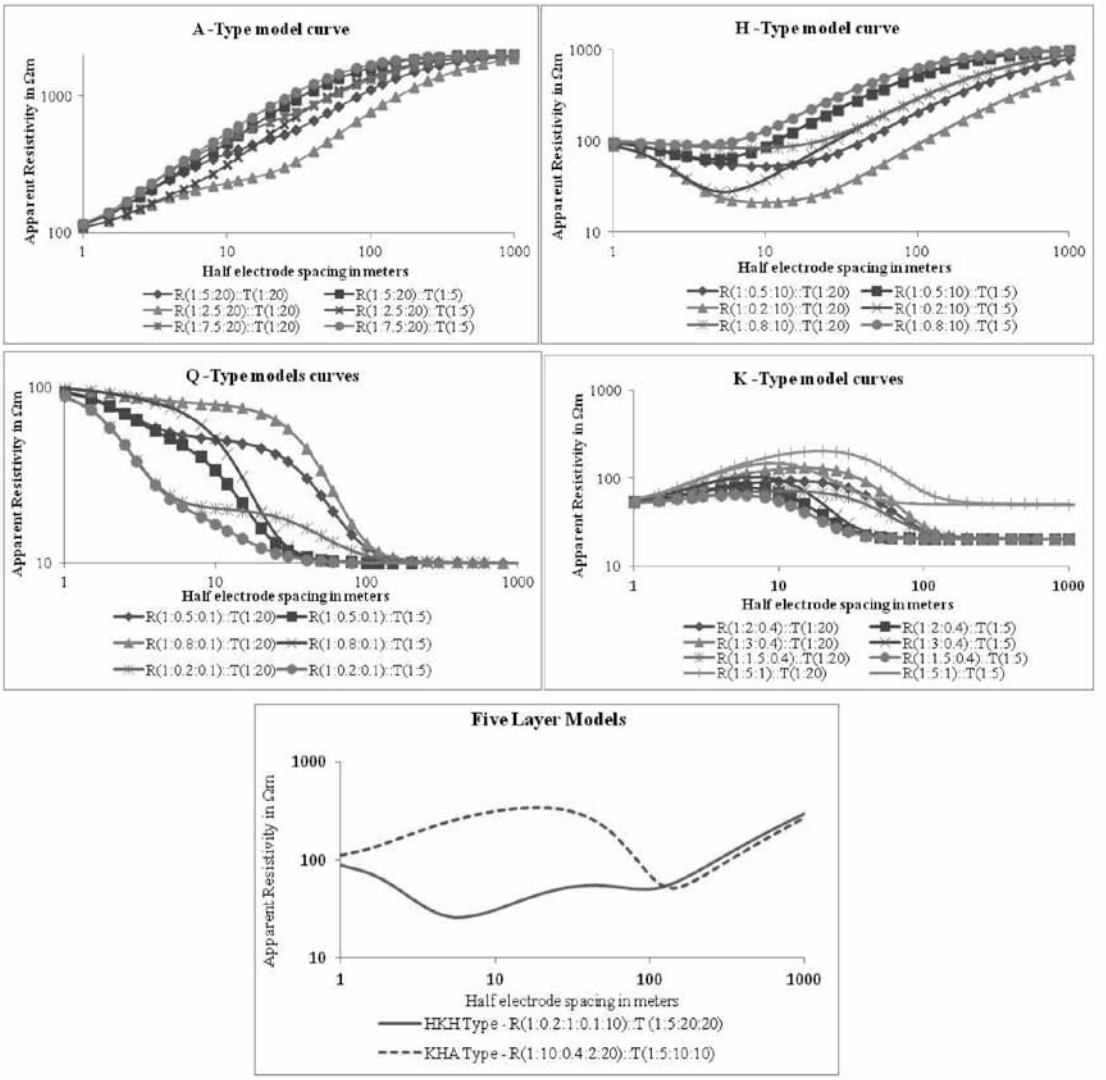

Figure 1. Three and five layer models for interpretation.

All the three interpretation algorithms used in this study require initial guess model (Figure 2). The input theoretical model is updated by optimization technique, till a best fit between theoretical and observed (minimum RMS error) is achieved. To analyze the performance, errors (0, ±5%, ±10%, ±20%, ±30%, ±40% and ±50%) have been added to the theoretical parameters (resistivity and thickness) of the model and are given as input initial guess values for the techniques. It means that the error of the input model is known so that final output values can be compared for its accuracy. The convergence criteria (RMS error) for each technique are noted. The output parameters are compared with the actual parameters of the model curve. Errors and percent errors are computed as the difference between the theoretical and interpreted values. Thus, the percent errors are computed for all the error ranges introduced to the input models in all the parameters, such as resistivities and thicknesses for the three interpretation techniques.

RESULTS AND ANALYSIS

A-type curves

Six models of A-type theoretical curves, generated for different combinations of resistivities (ρ_i) and thicknesses (h_i): ρ_1: ρ_2: ρ_3 and h_1:h_2 respectively are (1) 1:2.5:20 and 1:5 (2) 1:2.5:20 and 1:20 (3) 1:5:20 and 1:5 (4) 1:5:20 and 1:20 (5) 1:7.5:20 and 1:5 (6) 1:7.5:20 and 1:20. These theoretical VES curves are interpreted using RESIST, IRESAN and IPI2Win inputting the initial guess models with errors of 0, ±5%, ±10%, ±20%, ±30%, ±40% and ±50% added to the actual values. The output parameters corresponding to RMS error minimum are considered. The

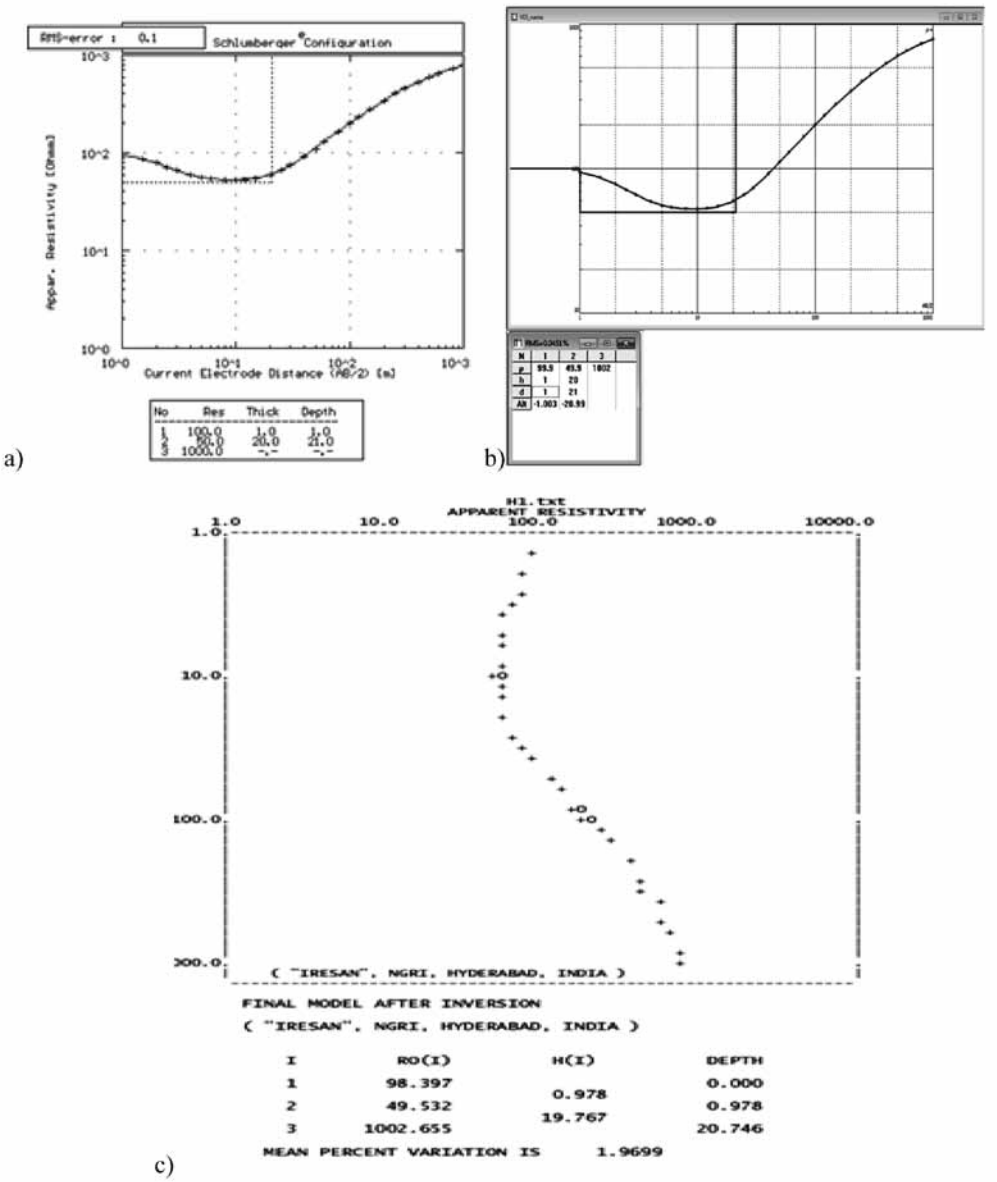

Figure 2. Interpretation of VES curve over a three layered sub surface model by the three software programs (a) RESIST (b) IPI2 Win and (c) IRESAN.

difference between the actual theoretical parameters of the ρ_1, ρ_2, ρ_3, h_1 and h_2 and output values of ρ_1, ρ_2, ρ_3, h_1 and h_2 are computed and percent errors are calculated. The plots (Figure 3, A1 to A6) show -0.8 to 0.5 percent error in all the parameters (ρ_1, ρ_2, ρ_3, h_1 and h_2) in the case of IPI2Win and the RMS error is also less than 0.05%. On the other hand, IRESAN also yields reasonable results with percent errors less than 1 % in all the parameters with the exception of a few cases (for resistivity ratios 1:5:20 and 1:7.5:20) where percent errors is around 5% in first layer resistivity and thicknesses. This is true for all the ranges of error in the initial input models. In the case of RESIST program, though the convergence criteria (minimum RMS error) is achieved, the output values of the parameters are in large errors (maximum of $\pm$50% particularly in first and second layers parameters), when the initial guess model is away ($>\pm$30%) from the actual model. It can also be observed from all the plots of Figure 3, that in certain cases (when the thickness of second layer is more (1:20), the percent error in the output is small ($<$1.5%) for the over estimates (5%, 10%, 20%, 30%, 40% and 50%) of the initial input parameters. And for underestimates (-5%, -10%, -20%, -30%, -40% and -50%), the error percentage in the output increases with the increase of error in the input for all the parameters However, it can be confidently said, if the initial guess model is close to actual model (0, $\pm$5%), the

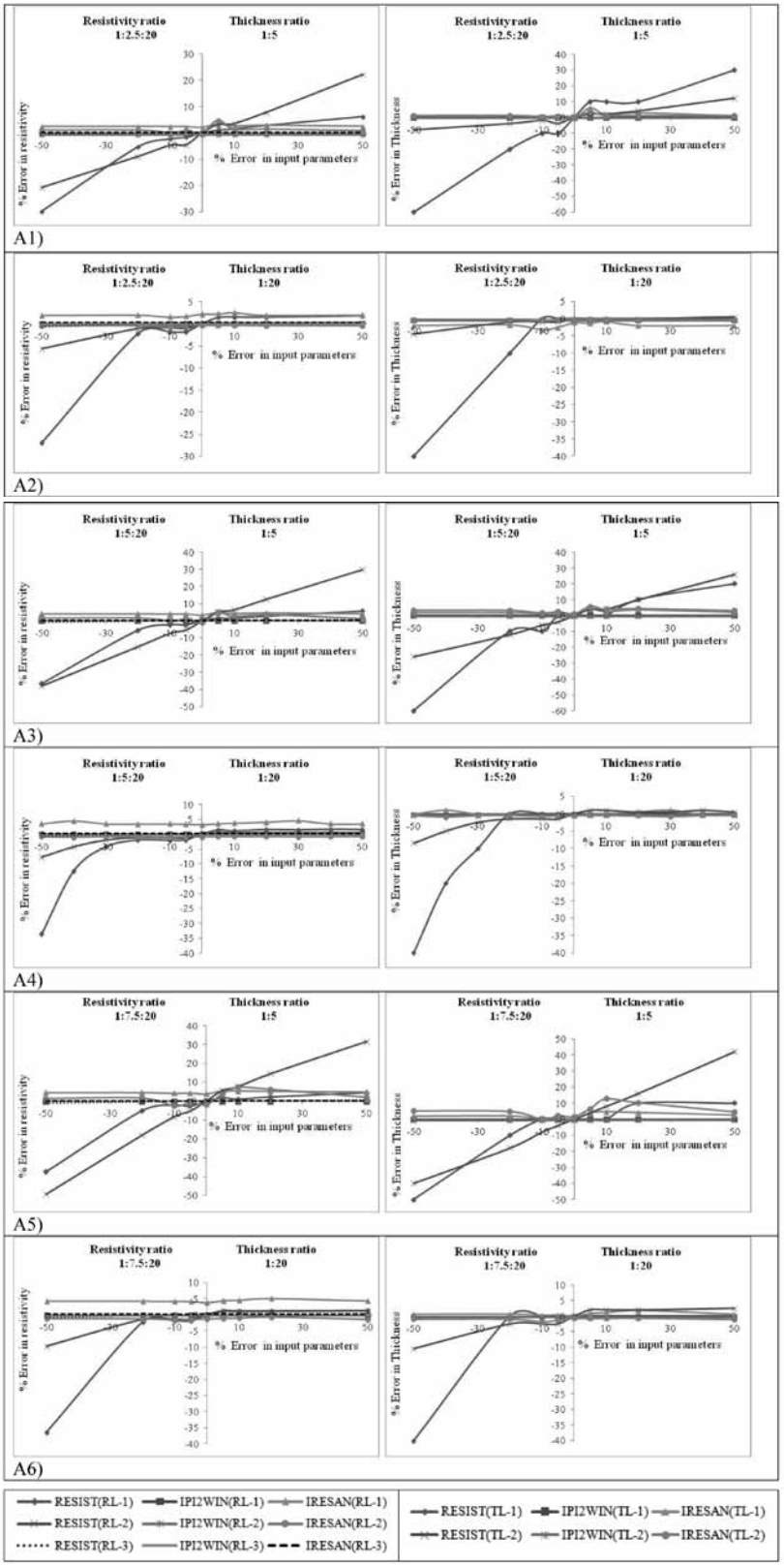

Figure 3. Percentage error plots (A1 to A6) from three computer programs (IPI2Win, RESIST and IRESAN) of A- type model curve with different resistivity and thickness ratios. RL-1, RL-2 and RL-3 are percentage errors in resistivities of layers-1, 2 and 3and TL-1, TL-2 are percentage errors in thicknesses of layers-1 and 2.

percent error in output is very less (<±10%), whereas in the case of IRESAN program, the percent error in output values is constant for all the subsurface parameters and for all the ranges of percent errors in the input models. In all the cases of models considered, the IPI2Win yields better results and percent error in output values is less than ± 0.5% whatever may be the percent deviation of the input model from the actual one. The RMS error is also less than 0.05% for IPI2Win, less than1% for RESIST and less than 2% for IRESAN (Appendix).

H-type curves

Theoretical curves in H-type have been generated for six models of subsurface for different combinations of resistivities (ρ_i) and thicknesses (h_i). The models for (ρ_1: ρ_2: ρ_3 and h_1: h_2) are (1) 1:0.2:10; 1:5 (2) 1:0.2:10; 1:20 (3) 1:0.5:10; 1:5 (4) 1:0.5:10; 1:20 (5) 1:0.8:10; 1:5 (6) 1:0.8:10; 1:20. Same procedure is followed as in the above case. The percent error plots of IPI2Win results (Figure 4, H1 to H6) show ±1 percent in all the parameters (ρ_1, ρ_2, ρ_3, h_1 and h_2) and the RMS error is also less than 0.102%.

In the case of IRESAN program, these plots show that the percentage errors are less than ±2% for most of the layer parameters and for all input error ranges. However, in certain cases of large errors (>±10%) in the initial model, the error in the output values is around ±5%. In the case of resistivity ratio of 1:0.2:10 and thickness ratio 1:5, the percent error is ±15% (Figure 4, H1 and H5) in second layer resistivity and thickness though the RMS error is less than 3% (Appendix). It is observed from the plots (Figure 4, H1 to H6) that the percentage errors are constant for of all parameters. In certain cases, if the initial guess model is close to actual model (0, ±5%), the percent error in output is very less (<±2%). It is noticed from the plots (Figure 4, H6), the output percentage error from IRESAN program is fluctuating if the resistivity contrast between first and second layers is less (1:0.8) and thickness of the second layer is more (1:20).

In the case of RESIST program, the output values reveal percentage errors less than one for all the error ranges of input values, but with the exception of the case where resistivity contrast between first and second layers is very less (1:0.8:10) (Figure 4, H5 and H6). In this case also, the percent error in first layer is less than ±5%, that too for large errors (±50%) of input model. RMS error is 0.4%. If the resistivity contrast is more between first and second layers and for large errors in input model, the output values are constant with percentage error ranging from -4.5 to 2.5. However, it can be confidently said, if the initial guess model is close to actual model (0, ±5%), the percent error in output is very less (<±0.5%). The maximum RMS error values for all the interpreted H-type curves for RESIST, IRESAN and IPI2Win are less than 0.1%, 2.85% and 0.1% respectively (Appendix).

K-type curves

K-type theoretical curves have been generated for eight models of subsurface for different combinations of resistivities (ρ_i) and thicknesses (h_i). The models for (ρ_1: ρ_2: ρ_3 and h_1: h_2) are (1) 1:1.5:0.4; 1:5 (2) 1:1.5:0.4; 1:20 (3) 1:2:0.4; 1:5 (4) 1:2:0.4; 1:20 (5) 1:3:0.4; 1:5 (6) 1:3:0.4; 1:20 (7) 1:5:1; 1:5 (8) 1:5:1; 1:20. The percent error plots for IPI2Win results (Figure 5) show zero percent in all the parameters (ρ_1, ρ_2, ρ_3, h_1 and h_2) for most of the models and in a few cases (Figure 5, K4 and K6), the percent error is less than ±0.5% in resistivity and thickness values for third layer. The RMS error is very less and never greater than 0.4% in any case.

IRESAN also yields reasonable results with percent errors less than ±2% in most of the cases (Figure 5). If the thickness of the second layer is large (1:20) and resistivity contrast between first and second layers is also high (1:5:1), then an error of less than 5% is observed in the results of first layer resistivity and second layer thickness (Figure 5, K8). For all the eight models and for all the parameters considered have the same percent error in the output irrespective of the magnitude of error in the input model. The RMS error (Appendix) is less than one for all the model curves considered with the exception of K7 (Figure 5, K7) model for which RMS error is around 4.4%. In the case of RESIST program, it can be observed from figures 5, that K1 to K8, the percent error in the output is dependent on the input model error. For underestimates, if the error is large (-50%) in input, output error (-50%) is also large. For over estimates of input, the error percentage in output is less than 5% in all the parameters for the entire input model with the exception one case (1:1.5:0.4). In this case (1:1.5:0.4), the percent error in output increases (up to 20%) with increase of error in input. This may be due to small contrast in the resistivity values of first and second layers.

The RMS error values are in the range 0.1%-1.1%; 0.4%-6.1%; and 0.09% – 0.4% respectively for RESIST, IRESAN and IPI2Win algorithms (Appendix).

Q-type curves

Q-type theoretical curves generated for six models for (ρ_1: ρ_2: ρ_3 and h_1: h_2) are (1) 1:0.2:0.1; 1:5 (2) 1:0.2:0.1; 1:20 (3) 1:0.5:0.1; 1:5 (4) 1:0.5:0.1; 1:20 (5) 1:0.8:0.1; 1:5 (6) 1:0.8:0.1; 1:20. All the three techniques have been applied for obtaining the true values of resistivities and techniques. The percent error plots of output results with IPI2Win algorithm (Figure 6, Q1 to Q6) show -1.5 to 1 percent variation in all the parameters (ρ_1, ρ_2, ρ_3, h_1 and h_2) with the exception in a few cases where percent errors is around 4% in the thickness of second layer. The RMS error (Appendix) is also less than 0.42%.

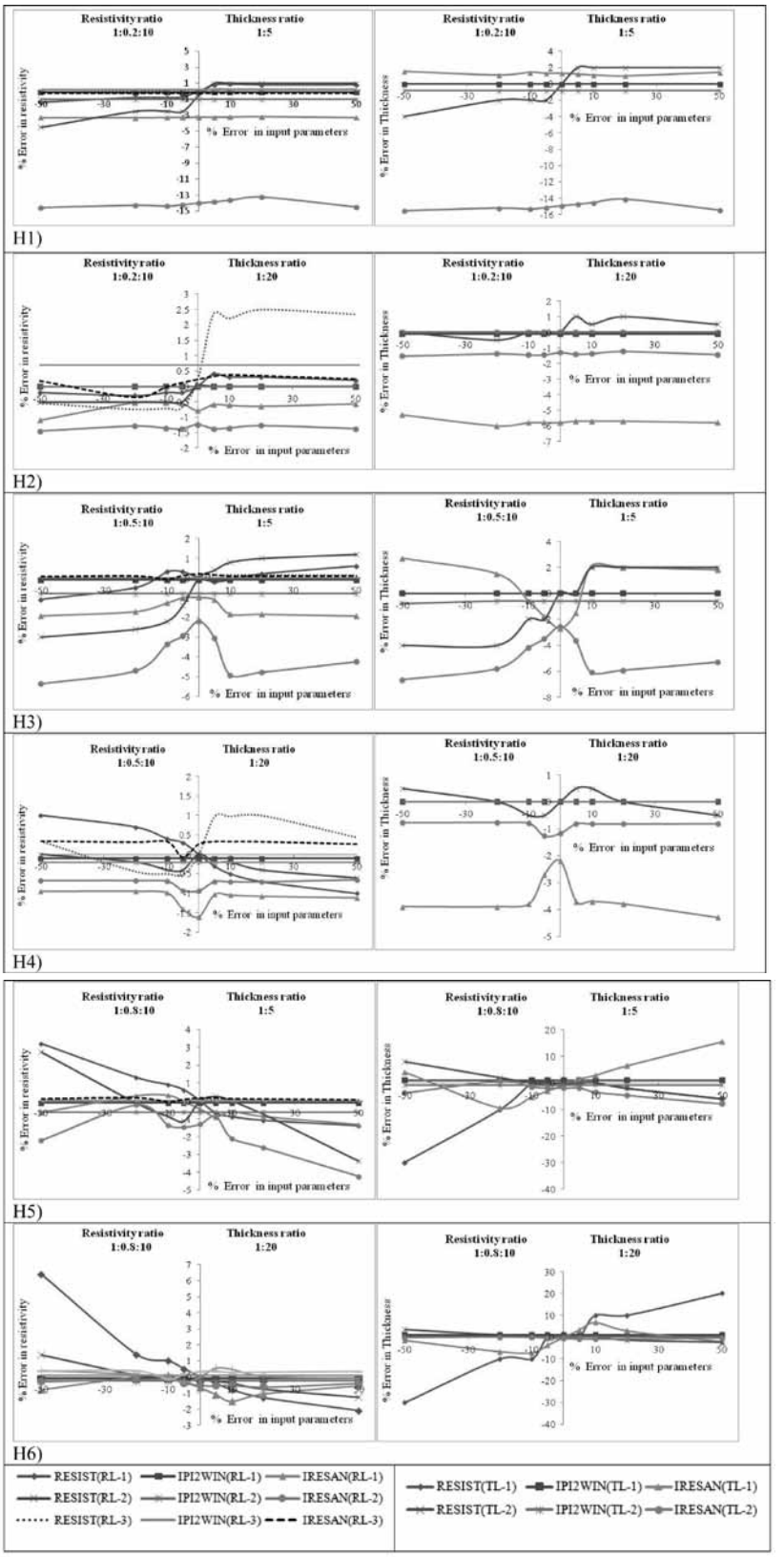

Figure 4. Percentage error plots (H1 to H6) from three computer programs (IPI2Win, RESIST and IRESAN) of H- type model curve with different resistivity and thickness ratios. RL-1, RL-2 and RL-3 are percentage errors in resistivities of layers-1, 2 and 3and TL-1, TL-2 are percentage errors in thicknesses of layers-1 and 2.

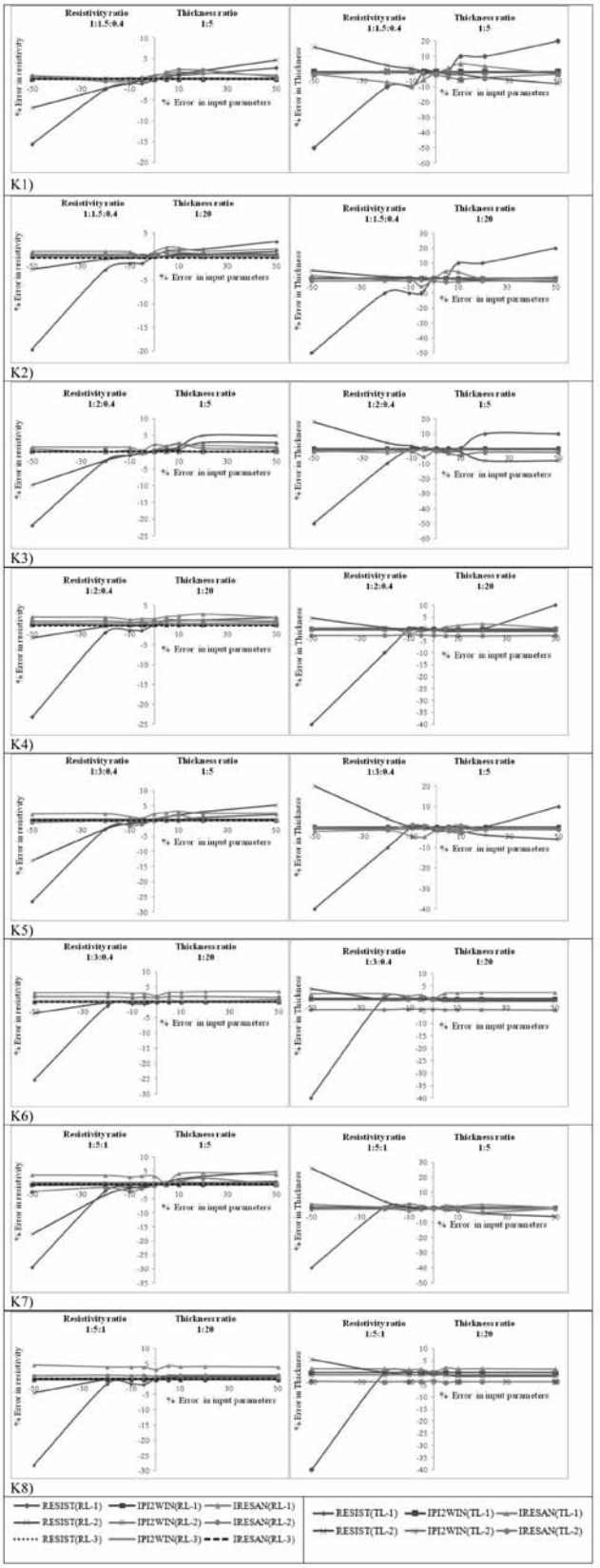

Figure 5. Percentage error plots (K1 to K8) from three computer programs (IPI2Win, RESIST and IRESAN) of K- type model curve with different resistivity and thickness ratios. RL-1, RL-2 and RL-3 are percentage errors in resistivities of layers-1, 2 and 3 and TL-1, TL-2 are percentage errors in thicknesses of layers-1 and 2.

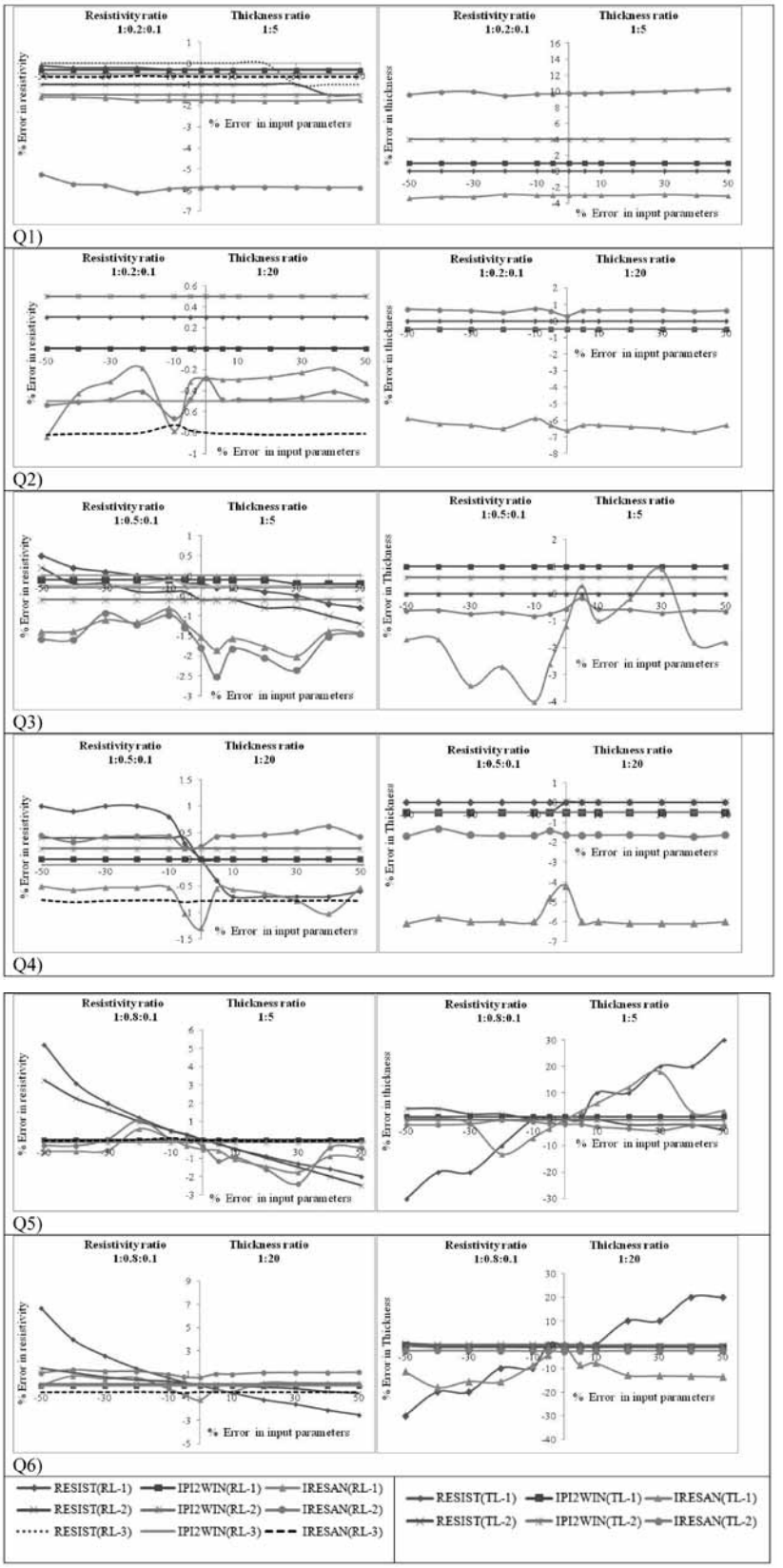

Figure 6. Percentage error plots (Q1 to Q6) from three computer programs (IPI2Win, RESIST and IRESAN) of Q- type model curve with different resistivity and thickness ratios. RL-1, RL-2 and RL-3 are percentage errors in resistivities of layers-1, 2 and 3 and TL-1, TL-2 are percentage errors in thicknesses of layers-1 and 2.

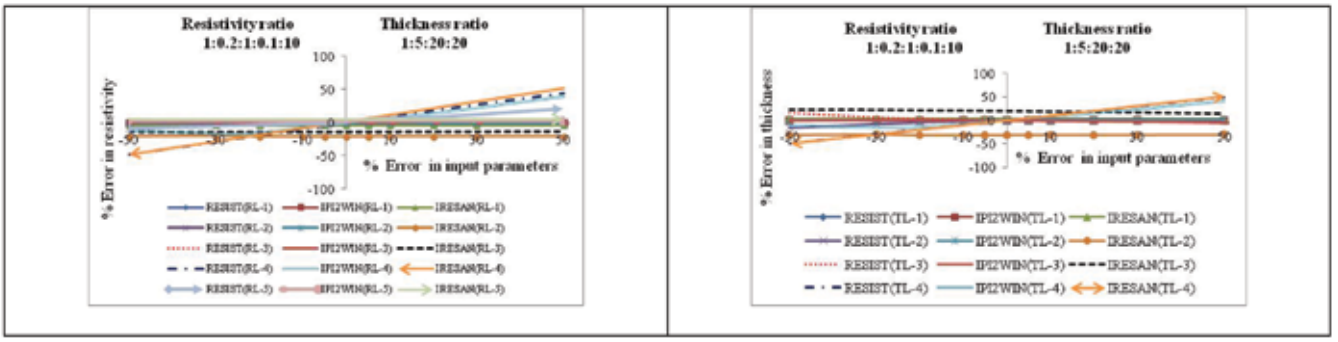

Figure 7(a). Percentage error plots from three computer programs (IPI2Win, RESIST and IRESAN) of HKH- type model curve with different resistivity and thickness ratios. RL-1, RL-2, RL-3, RL-4 and RL-5 are percentage errors in resistivities of layer-1, 2, 3, 4 and 5 and TL-1, TL-2, TL-3, TL-4 are percentage errors in thicknesses of layer-1, 2, 3 and 4.

IRESAN yields reasonable results with almost constant errors varying from -10% to 10% except in the case where the resistivity contrast between first and second layers is 1:0.8 and second layer thickness is 5 times the first one. The percentage error in the output values of the thickness of layer 1 is in large error ($\pm$16%) that too when the initial guess model is away (>$\pm$20%) from the actual model. This indicates uncertainty of the program for the guess parameters with low resistivity/thickness contrasts for input model. In the case of RESIST program, the percent error in most of the output parameters is less than $\pm$3% and never more than 5% with exception of Q5 and Q6 models (Figure 6, Q5 and Q6). In these cases also, the percent error in the output model for the first layer thickness is in proportion to the error in the input model (maximum of $\pm$30%). The RMS error values for RESIST, IRESAN and IPI2Win are respectively in the ranges 0.1% – 0.4%; 0.62% – 6.2%; and 0.18% – 0.42% (Appendix).

Five layer cases

Theoretical VES curves have been generated over five layer subsurface models. The two resistivity and thickness ratios considered for these models are (ρ_1: ρ_2: ρ_3: ρ_4: ρ_5 and h_1: h_2: h_3: h_4) are (1) 1.0:0.2:1.0:0.1:10; 1:5:20:20 and (2) 1.0:10.0:0.4:2.0:20; 1:5:10:10. The two model curves have been interpreted using all the three interpretation algorithms after adding errors to the parameters of input model.

Analysis of HKH type curve (1.0:0.2:1.0:0.1:10; 1:5:20:20) for different error ranges in input models, the percent errors in the output parameters of all the three techniques have been computed and plotted (Figure 7a). The percent error in resistivities for IPI2Win is almost zero or around $\pm$1% for all the layer parameter except layer 4 where percent error increases with increasing error in input model. This may be due to large resistivity contrast (0.1:10) between layer 4 and 5. The percent error in thickness is also zero in case of thickness of layers 1, 2 and 3. In the case of the layer 4, the percent error is around -15% for underestimates of input models. In the case of overestimates of input model percent error in the output increases. The percent is as large as around 40% when input model is in 50% error. In the case of IRESAN algorithm, the percent error in the output of resistivity parameters varies in the range of 4% to 20% for all the layers except for overestimates in resistivity of the layer 4, where the percent error increases to $\pm$40% with increase of error in input model. The percent error varies between 5% and 30% in case of thickness for the layers 1, 2, 3 and 5, where as the percent error increases for thickness of the layer 4 with increase of error in input model. The analysis of RESIST algorithm shows that for overestimates of error in input model, the percent error in output values is less than 5% and for underestimates of error in input model, the percent error in output of resistivity values increases with the increase of error in input. But for resistivity values of layer 4 and 5, the percent in output increases with increase in the error of input model. The same inference is true in case of output of thickness parameters.

In analysis of KHA (1:10:0.4: 2:20; 1:5:10:10) (Figure 7b), IPI2Win algorithm shows (Figure 7b) a percent error in resistivity values of around $\pm$1% in layers 1, 2, 3 and 5 and for all the error ranges of the input models. In the case of the layer 4, the percent error in the output is zero for all the ranges of error in input models. But when input model error is more than 30%, the percent error in the output substantially increases to very high values (~2500%). This may be due to large contrast (1:10:0.4:2:20) in the resistivities between 2nd, 3rd and 4th layers. In the case of thickness, the percent error in output values is in the range -0.2% to 28% for the entire range of input error models, with exception of layer 4, where the error percent is high around 50% for all the input error models.

In case of IRESAN, the percent error is around $\pm$5% for all input error models in resistivity values of layers 1, 2 and 5 (Figure 7b). In case of layer 3 and 4, the percent error varies with error in input model. The same analysis is true in thickness parameter also, except for layers 3 and 4 which vary with percent errors in input models.

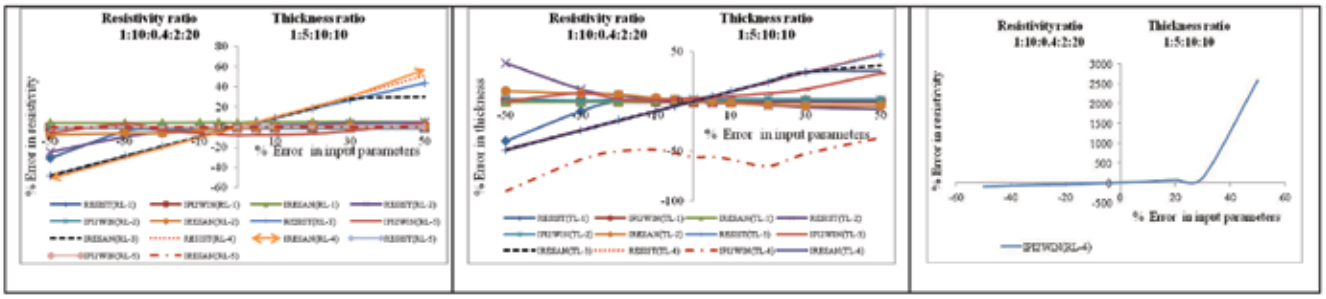

Figure 7(b). Percentage error plots from three computer programs (IPI2Win, RESIST and IRESAN) of KHA- type model curve with different resistivity and thickness ratios. RL-1, RL-2, RL-3, RL-4 and RL-5 are percentage errors in resistivities of layers-1, 2, 3, 4 and 5and TL-1, TL-2, TL-3, TL-4 are percentage errors in thicknesses of layer-1, 2, 3 and 4.

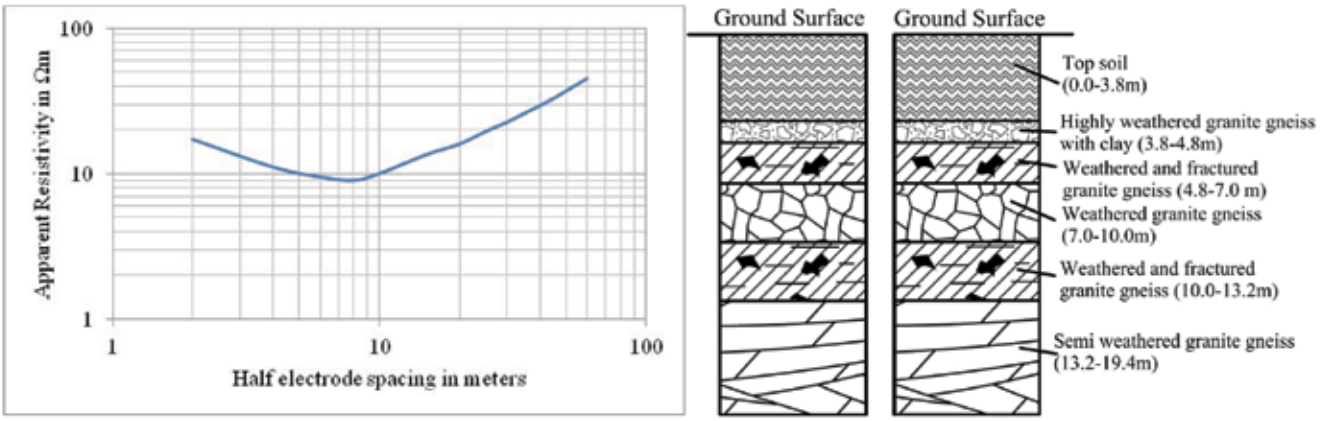

Figure 8. VES data curve carried out at Jaddangi village and the lithology of the drilled well near sounding point. Interpreted results of the three programs are given table 1.

The analysis of RESIST algorithm yields less error (<5%) in the output of resistivity of layers 1, 2 and 5 for all the input error models with the exception of -50% for which the error in output is around -30%. In case of layer 3 and 4 with increase of error in input model, there is an increase in error in output values. The percent error in thickness for layer 1 and 2 is less than $\pm$5% for overestimates in input error. For underestimates in input error of more than -30%, the output percent error is large (<$\pm$40). In case of layers 3 and 4, the percent error increases with increasing error in input models.

EXAMPLES

Two field curves from different locations corresponding to different lithologies were interpreted with all the three techniques.

Example 1

A sounding carried out at Jaddangi village (17.4801^{0}N, 82.1545^{0}E) in East Godavari district covered by granite gneiss, was compared with the lithology of a drilled well at a distance of 196 m is taken for reference for comparing interpreted results (Figure 8). The sounding curve is subjected to interpretation by the three programs using two initial guess models. From a comparison of the results (Table 1), it is observed that in spite of the large deviations in the two initial models, the final output values of resistivities and thicknesses for all the three layers for both the initial models are consistent in the case of IPI2Win algorithm and differ in the case of RESIST and IRESAN particularly with respect to the parameters of the layers 2 and 3.

Example-2

The Vertical Electrical Sounding data has been taken from the published work (Kedareswarudu et al., 2006) over Borra caves, Visakhapatnam district (Figure 9). The actual measured depth to the bottom of cave from surface is approximately 2.5 meters. The results of interpretation using three different algorithms and with two initial guess models with large deviations are shown in table 2. The interpreted results of IPI2Win show more or less same values in output layer resistivities and thicknesses though there is deviation in the two input models (Table 2). On the other hand, the interpreted results of RESIST and IRESAN show differences in the output parameters for the two input

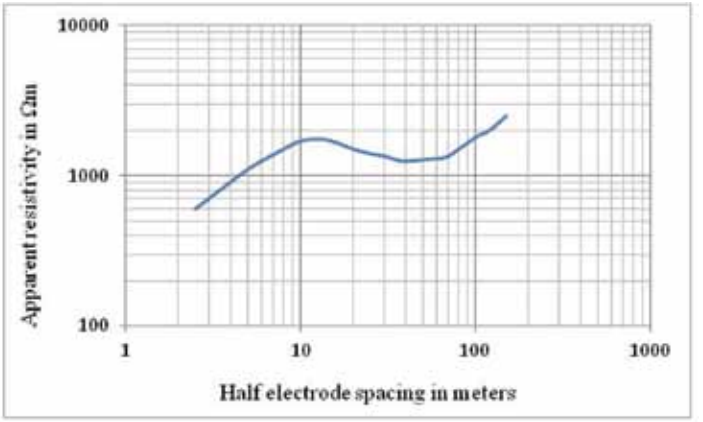

Figure 9. VES data curve carried out at Borra caves area. Interpreted results of the three programs are given table 2.

Table 1. Results and comparison of three inversion algorithms for the above sounding data carried out at Jaddangi (L-1, 2, 3 and 4 are layer numbers). VES curve is shown in figure 7. R=Resistivity, T=Thickness.

Guess Model	Guess model values			RESIST		IRESAN		IPI2Win	
		R (Ωm)	T (m)	R (Ωm)	T (m)	R (Ωm)	T (m)	R (Ωm)	T (m)
1	L-1	20	2	19	1.9	20.47	1.557	21.1	1.32
	L-2	5	5	5.6	4.4	4.94	3.085	6.95	5.48
	L-3	25	10	26.2	9.7	21.24	13.19	28.3	14
	L-4	300	-	303.4	-	663.55	-	2530	-
2	L-1	30	2	22.5	1.3	21.304	1.33	21.2	1.32
	L-2	10	10	8.2	7.7	6.547	5.754	6.98	5.56
	L-3	40	20	47.3	17.2	42.788	15.59	28.7	13.6
	L-4	500	-	517.5	-	619.84	-	1408	-

Table 2. Results and comparison of three inversion algorithms for the sounding data carried out at Borra Caves (L-1, 2, 3 and 4 are layer numbers). VES curve is shown in figure 8. R=Resistivity, T=Thickness

Guess model	Guess model values			RESIST		IRESAN		IPI2Win	
		R (Ωm)	T (m)	R (Ωm)	T (m)	R (Ωm)	T (m)	R (Ωm)	T (m)
1	L-1	100	1	169.5	0.6	162.92	0.577	333	1.25
	L-2	5000	5	4766.9	4.9	9072.186	2.576	16739	1.39
	L-3	500	5	252.7	9.8	227.175	8.909	139	4.85
	L-4	10000	-	7166.3	-	7455.228	-	4903	-
2	L-1	300	0.5	205.8	0.7	204.981	0.728	333	1.25
	L-2	10000	2.5	9284.7	2.4	9508.493	2.452	16668	1.39
	L-3	200	10	238.1	8.4	225.709	8.832	154	5.37
	L-4	5000	-	5217.5	-	7315.92	-	4906	-

models. The measured depth to the bottom (~ 2.5 m) of cavern (revealed by high resistivity value is due to cavity) is in agreement with the results of IPI2Win (first and second layer thickness is 1.25+1.39= 2.64 meters).

CONCLUSIONS

From the analysis of all percent error plots of all the parameters, it is observed that IPI2Win yields less error irrespective of the magnitude of percent error in the input model. However, IRESAN and RESIST methods also yielded good results in certain cases of models and in some parameters only and showed large errors in other parameters. All the three algorithms are very effective, when the input models are close to the actual ones. Choosing of an initial model very close to actual model (unknown) is very difficult. RESIST and IRESAN algorithms reveal that the contrast in resistivities and

thickness between the subsurface layers plays a significant role in the interpreted results. If the contrast in the parameters (Resistivity/Thickness) of the model is large and also when the input model is in large error, the output parameters are in large errors. This analysis is true for all the cases of VES curves of the entire subsurface models. The IPI2Win algorithm yields better interpreted results even though the input model deviates largely from the actual model. The RMS error is never greater than 0.2% (Appendix) and much less in the case of five layer models. The RMS error is comparatively large for IRESAN software and is less than 5% (Appendix). RESIST software shows an RMS error around 0.1% for most of the models and in a few cases converges to a high value and never more than 0.9% (Appendix).

In cases of A and K type model curves (figures 3 and 5), RESIST algorithm software yields large percent errors, if the input model parameters are in large under estimates, whereas if the input parameters are in large over estimates, the percent errors in output are not much. For H and Q type curves (figures 4 and 6), this method showed errors which are in proportion to the deviation of the input model in the output. From the above study, it is inferred that the IPI2Win results are more reliable showing consistent output, in spite of large deviations in the initial guess models.

ACKNOWLEDGEMENT

Mr.P.Venkateswara Rao acknowledges the financial support from UGC-Rajiv Gandhi National Fellowship, New Delhi-110001. The authors express their sincere thanks to the reviewers particularly to Dr.M.R.K.Prabhakara Rao, who has critically evaluated the manuscript. His suggestions and comments helped the authors in revising the script thoroughly.

Compliance with Ethical Standards

The authors declare that they have no conflict of interest and adhere to copyright norms.

REFERENCES

Bobachev, A.A., Modin, I.N. and Shevnin, V.A., 1990-2002. Moscow State University, Geophysical faculty, Department of Geophysics developed IPI2Win with copyright to authors and distributed by Geo Scan-M Ltd, Moscow, Russia. (http://geophys.geol.msu.ru/ipi2win.htm)

Compagnie Generale de Geophysique, 1963. Master curves for electrical sounding 2nd revised edition. The Hague, European Assoc. Explor. Geophysicists.

Das, U.C. and Verma, S.K., 1977. A generalized program to compute type curves for resistivity sounding using digital linear filters, UNDP/CSIR Monograph, October, 1977.

Flathe, H., 1963. Five-layer master curves for the hydro geological interpretation of geoelectric resistivity measurements above a two-storey aquifer. Geophys. Prosp, 11, 471-508.

Jupp, D.L.B. and Vozoff, K., 1975. Stable iterative methods for the inversion of geophysical data, Geophys. J.R. Astr. Soc., 42, 957-976.

Kalenov, E.N., 1957. Interpretation of vertical electrical sounding curves. Moscow, Gostoptekhizdat, 471p. [in Russian].

Kedareswarudu, U., Ramesh, Y. and Lakshmipathi Raju, A., 2006. Results of electrical resistivity investigations on Borra caves, Visakhapatnam, Andhra Pradesh. J. Indian Acad. Sci., 49, 53-58.

Kowalik, J. and Osborne, M.R., 1968. Methods of unconstrained optimization problems, Elseveir (USA). 13, 148p.

Marquardt, D.W., 1963. An algorithm for Least-squares estimation of nonlinear parameters. J. Soc. Industrial and Appl. Math. 11, 431-441.

Orellana, E. and Mooney, H.M., 1966. Master tables and curves for vertical electrical sounding over layered structures: Madrid, Interciencia, 150 p.

Rijkswaterstaat, 1969. Standard graphs for resistivity prospecting: The Hague, European Assoc. Explor. Geophysicists. Netherlands.

Vander Velpen, B.P.A. and Sporry, R.J., 1993. RESIST. A computer program to process resistivity sounding data on PC compatibles. Computers and Geosciences, 19, 691-703.

Zohdy, A.A.R., 1965. The auxiliary point method of electrical sounding interpretation, and its relationship to the Dar Zarrouk parameters, Geophysics, 30, 644-660.

Zohdy, A.A.R., 1974. Use of Dar Zarrouk curves in the interpretation of vertical electrical sounding data: U.S. Geol. Survey Bull. 1313-D, 41 p.

Zohdy, A.A.R., 1975. Automatic Interpretation of Schlumberger Sounding Curves, Using Modified Dar Zarrouk Functions: U.S. Geol. Survey Bull. 1313-E, 48 p.

Zohdy, A.A.R. and Jackson, D.B., 1973. Recognition of natural brine by electrical soundings near the Salt Fork of the Brazos River, Kent and Stonewall Counties, Texas: U.S. Geol. Survey Prof. Paper 809-A, 14 p.

Received on: 17.8.18; Revised on: 24.10.18; Accepted on: 29.10.18

APPENDIX

Table 1. RMS error values of three algorithms for different percentage errors in input models.

Model	% Error	RMS error value			Model	% Error	RMS error value			Model	% Error	RMS error value			Model	% Error	RMS error value		
		RESIST	IRESAN	IPI2WIN			RESIST	IRESAN	IPI2WIN			RESIST	IRESAN	IPI2WIN			RESIST	IRESAN	IPI2WIN
A1	0	0	1.7441	0.0456	H1	0	0.1	1.9692	0.0451	K1	0	0.1	4.3881	0.141	K8	0	0.1	1.0442	0.19
	5	0.1	1.7438	0.0456		5	0.1	1.9639	0.0451		5	0.1	4.3878	0.141		5	0.1	1.0573	0.19
	10	0.1	1.744	0.0456		10	0.1	1.9639	0.0451		10	0.1	4.3882	0.141		10	0.1	1.0466	0.19
	20	0.1	1.7458	0.0456		20	0.1	1.964	0.0451		20	0.1	4.3896	0.141		20	0.1	1.0545	0.19
	30	0.1	1.7446	0.0456		30	0.1	1.9646	0.0451		30	0.1	4.3891	0.141		30	0.1	1.0515	0.19
	40	0.1	1.744	0.0456		40	0.1	1.9667	0.0451		40	0.1	4.3883	0.141		40	0.1	1.0472	0.19
	50	0.1	1.7438	0.0456		50	0.1	1.9667	0.0451		50	0.1	4.3878	0.141		50	0.1	1.0437	0.19
	-5	0.1	1.7438	0.0456		-5	0.1	1.9681	0.0451		-5	0.1	4.3881	0.141		-5	0.1	1.0452	0.19
	-10	0.1	1.7443	0.0456		-10	0.1	1.9639	0.0451		-10	0.1	4.3892	0.141		-10	0.1	1.051	0.19
	-20	0.1	1.7437	0.0456		-20	0.1	1.9639	0.0451		-20	0.1	4.3878	0.141		-20	0.1	1.0445	0.19
	-30	0.2	1.7437	0.0456		-30	0.1	1.9639	0.0451		-30	0.1	4.3878	0.141		-30	0.1	1.0461	0.19
	-40	0.6	1.7438	0.0456		-40	0.1	1.9639	0.0451		-40	0.4	4.3879	0.141		-40	0.1	1.0495	0.19
	-50	1.2	1.7438	0.0456		-50	0.1	1.9639	0.0451		-50	1	4.3879	0.141		-50	0.1	1.056	0.19
A2	0	0	1.395	0.0385	H2	0	0.1	1.8514	0.0506	K2	0	0.1	0.645	0.245	Q1	0	0.1	4.3253	0.181
	5	0.1	1.3966	0.0385		5	0.1	1.8431	0.0506		5	0.1	0.649	0.245		5	0.1	4.3221	0.181
	10	0.1	1.3906	0.0385		10	0.1	1.8337	0.0506		10	0.1	0.6639	0.245		10	0.1	4.3221	0.181
	20	0.2	1.394	0.0385		20	0.1	1.834	0.0506		20	0.2	0.6456	0.245		20	0.1	4.3223	0.181
	30	0.2	1.3936	0.0385		30	0.1	1.8356	0.0506		30	0.2	0.6615	0.245		30	0.1	4.3229	0.181
	40	0.3	1.3924	0.0385		40	0.1	1.8362	0.0506		40	0.2	0.6463	0.245		40	0.1	4.3247	0.181
	50	0.5	1.3918	0.0385		50	0.1	1.8379	0.0506		50	0.2	0.6623	0.245		50	0.1	4.3221	0.181
	-5	0.1	1.3907	0.0385		-5	0.1	1.8444	0.0506		-5	0.1	0.6617	0.245		-5	0.1	4.3239	0.181
	-10	0.1	1.3928	0.0385		-10	0.1	1.8421	0.0506		-10	0.1	0.6444	0.245		-10	0.1	4.3221	0.181
	-20	0.3	1.3902	0.0385		-20	0.1	1.834	0.0506		-20	0.2	0.6494	0.245		-20	0.1	4.3221	0.181
	-30	0.3	1.3912	0.0385		-30	0.1	1.8341	0.0506		-30	0.2	0.6464	0.245		-30	0.1	4.3221	0.181
	-40	0.5	1.3902	0.0385		-40	0.1	1.8337	0.0506		-40	0.4	0.6449	0.245		-40	0.1	4.3237	0.181
	-50	0.9	1.3902	0.0385		-50	0.1	1.8334	0.0506		-50	0.8	0.6438	0.245		-50	0.1	4.3221	0.181
A3	0	0.1	1.8501	0.0472	H3	0	0	2.8451	0.102	K3	0	0.1	6.0862	0.235	Q2	0	0.1	0.8828	0.209
	5	0.1	1.85	0.0472		5	0.1	2.8439	0.102		5	0.1	6.0839	0.235		5	0.1	0.8945	0.209
	10	0.1	1.8514	0.0472		10	0.1	2.844	0.102		10	0.1	6.084	0.235		10	0.1	0.8832	0.209
	20	0.1	1.8495	0.0472		20	0.1	2.8452	0.102		20	0.1	6.0842	0.235		20	0.1	0.8874	0.209
	30	0.1	1.8495	0.0472		30	0.1	2.8447	0.102		30	0.1	6.0851	0.235		30	0.1	0.9005	0.209
	40	0.1	1.8497	0.0472		40	0.1	2.8433	0.102		40	0.1	6.0855	0.235		40	0.1	0.8822	0.209
	50	0.1	1.8498	0.0472		50	0.1	2.8438	0.102		50	0.1	6.086	0.235		50	0.1	0.883	0.209
	-5	0.1	1.8498	0.0472		-5	0.1	2.8439	0.102		-5	0.1	6.0841	0.235		-5	0.1	0.8842	0.209
	-10	0.1	1.852	0.0472		-10	0.1	2.844	0.102		-10	0.1	6.0846	0.235		-10	0.1	0.9006	0.209
	-20	0.1	1.8495	0.0472		-20	0.1	2.8462	0.102		-20	0.1	6.0839	0.235		-20	0.1	0.8842	0.209
	-30	0.1	1.8511	0.0472		-30	0.1	2.8464	0.102		-30	0.3	6.084	0.235		-30	0.1	0.8894	0.209
	-40	0.5	1.8495	0.0472		-40	0.1	2.8458	0.102		-40	0.6	6.0839	0.235		-40	0.1	0.8821	0.209
	-50	1	1.8495	0.0472		-50	0.1	2.8464	0.102		-50	1.1	6.0839	0.235		-50	0.1	0.8822	0.209
A4	0	0.1	1.5362	0.0402	H4	0	0.1	2.5527	0.0654	K4	0	0.2	0.8934	0.368	Q3	0	0.1	6.2329	0.254
	5	0.1	1.5476	0.0402		5	0.1	2.5533	0.0654		5	0.2	0.8954	0.368		5	0.1	6.2261	0.254
	10	0.1	1.5356	0.0402		10	0.1	2.5542	0.0654		10	0.2	0.9022	0.368		10	0.1	6.2266	0.254
	20	0.2	1.5424	0.0402		20	0.1	2.5565	0.0654		20	0.2	0.8934	0.368		20	0.1	6.2253	0.254
	30	0.2	1.5413	0.0402		30	0.1	2.5526	0.0654		30	0.2	0.8934	0.368		30	0.2	6.2253	0.254
	40	0.3	1.5355	0.0402		40	0.1	2.5517	0.0654		40	0.2	0.8935	0.368		40	0.2	6.2254	0.254
	50	0.5	1.5355	0.0402		50	0.1	2.5517	0.0654		50	0.2	0.8937	0.368		50	0.2	6.2255	0.254
	-5	0.1	1.5353	0.0402		-5	0.1	2.5521	0.0655		-5	0.2	0.9136	0.368		-5	0.1	6.229	0.254
	-10	0.1	1.5377	0.0402		-10	0.1	2.5518	0.0654		-10	0.2	0.9095	0.368		-10	0.1	6.2259	0.254
	-20	0.2	1.5351	0.0402		-20	0.1	2.5536	0.0655		-20	0.2	0.895	0.368		-20	0.1	6.226	0.254
	-30	0.2	1.5371	0.0402		-30	0.1	2.5523	0.0654		-30	0.3	0.8956	0.368		-30	0.2	6.2259	0.254
	-40	0.5	1.535	0.0402		-40	0.1	2.552	0.0654		-40	0.5	0.8963	0.368		-40	0.3	6.2275	0.254
	-50	0.8	1.5351	0.0402		-50	0.2	2.5516	0.0654		-50	0.9	0.8974	0.368		-50	0.4	6.2254	0.254
A5	0	0	1.5999	0.0471	H5	0	0.1	1.8246	0.0398	K5	0	0.1	3.304	0.0931	Q4	0	0.2	0.6509	0.42
	5	0.1	1.5988	0.0471		5	0.1	1.8292	0.0398		5	0.1	3.3093	0.0931		5	0.2	0.6674	0.42
	10	0.1	1.5995	0.0471		10	0.1	1.8403	0.0398		10	0.1	3.3077	0.0931		10	0.2	0.6564	0.42
	20	0.1	1.6049	0.0471		20	0.1	1.8278	0.0398		20	0.1	3.304	0.0931		20	0.2	0.6753	0.42
	30	0.1	1.5991	0.0471		30	0.1	1.8261	0.0398		30	0.1	3.3046	0.0931		30	0.2	0.7057	0.42
	40	0.1	1.6036	0.0471		40	0.1	1.8253	0.0398		40	0.1	3.3055	0.0931		40	0.2	0.6584	0.42
	50	0.1	1.5987	0.0471		50	0.2	1.8243	0.0398		50	0.2	3.3064	0.0931		50	0.2	0.6678	0.42
	-5	0.1	1.5988	0.0471		-5	0.1	1.8249	0.0398		-5	0.1	3.3094	0.0931		-5	0.2	0.6544	0.42
	-10	0.1	1.5999	0.0471		-10	0.1	1.8334	0.0398		-10	0.1	3.304	0.0931		-10	0.2	0.6803	0.42
	-20	0.1	1.5986	0.0471		-20	0.1	1.8276	0.0398		-20	0.2	3.3045	0.0931		-20	0.2	0.6929	0.42
	-30	0.1	1.5986	0.0471		-30	0.1	1.8271	0.0398		-30	0.2	3.3061	0.0931		-30	0.2	0.6589	0.42
	-40	0.6	1.5987	0.0471		-40	0.2	1.8268	0.0398		-40	0.5	3.3076	0.0931		-40	0.3	0.6504	0.42
	-50	1.2	1.5987	0.0471		-50	0.4	1.8268	0.0398		-50	0.8	3.3089	0.0931		-50	0.3	0.6505	0.42
A6	0	0	1.3254	0.0486	H6	0	0.1	1.58	0.0373	K6	0	0.1	0.456	0.173	Q5	0	0.1	2.685	0.251
	5	0.1	1.3263	0.0486		5	0.1	1.5879	0.0373		5	0.1	0.4608	0.173		5	0.1	2.6832	0.251
	10	0.1	1.3353	0.0486		10	0.1	1.5779	0.0373		10	0.1	0.4805	0.173		10	0.1	2.6832	0.251
	20	0.2	1.3302	0.0486		20	0.1	1.578	0.0373		20	0.1	0.468	0.173		20	0.1	2.6832	0.251
	30	0.2	1.3233	0.0486		30	0.1	1.5823	0.0373		30	0.1	0.4645	0.173		30	0.1	2.6836	0.251
	40	0.3	1.3301	0.0486		40	0.1	1.5831	0.0373		40	0.1	0.4523	0.173		40	0.1	2.6867	0.251
	50	0.4	1.3234	0.0486		50	0.1	1.5838	0.0373		50	0.2	0.4585	0.173		50	0.1	2.6832	0.251
	-5	0.1	1.3227	0.0486		-5	0.1	1.5818	0.0373		-5	0.1	0.464	0.173		-5	0.1	2.6833	0.251
	-10	0.1	1.3285	0.0486		-10	0.1	1.5883	0.0373		-10	0.1	0.5092	0.173		-10	0.1	2.6867	0.251
	-20	0.3	1.3209	0.0486		-20	0.1	1.5897	0.0373		-20	0.2	0.4765	0.173		-20	0.1	2.6837	0.251
	-30	0.3	1.3209	0.0486		-30	0.1	1.5873	0.0373		-30	0.2	0.4666	0.173		-30	0.1	2.6832	0.251
	-40	0.6	1.3199	0.0486		-40	0.1	1.5825	0.0373		-40	0.3	0.4581	0.173		-40	0.1	2.6835	0.251
	-50	0.9	1.3199	0.0486		-50	0.2	1.5779	0.0373		-50	0.5	0.4532	0.173		-50	0.1	2.6864	0.251
HKH	0	0.1	1.802	0.104	KHA	0	0.1	2.1783	0.0531	K7	0	0.1	4.3958	0.153	Q6	0	0.1	2.1511	0.243
	5	0.1	1.8068	0.104		5	0.1	2.1786	0.0531		5	0.1	4.3968	0.153		5	0.1	2.1509	0.243
	10	0.1	1.8036	0.104		10	0.1	2.1789	0.0531		10	0.1	4.3938	0.153		10	0.1	2.1509	0.243
	20	0.1	1.8088	0.103		20	0.1	2.1797	0.0534		20	0.1	4.3939	0.153		20	0.1	2.151	0.243
	30	0.1	1.8203	0.105		30	0.2	2.1807	0.0536		30	0.1	4.3939	0.153		30	0.1	2.1513	0.243
	40	0.1	1.8153	0.0699		40	0.2	2.1813	0.0546		40	0.1	4.3938	0.153		40	0.1	2.1512	0.243
	50	0.2	1.8172	0.0739		50	0.3	2.1834	0.0556		50	0.1	4.3938	0.153		50	0.1	2.1509	0.243
	-5	0.1	1.7984	0.105		-5	0.1	2.1781	0.053		-5	0.1	4.3938	0.153		-5	0.1	2.1513	0.243
	-10	0.1	1.7972	0.106		-10	0.1	2.1779	0.053		-10	0.1	4.394	0.153		-10	0.1	2.1518	0.243
	-20	0.1	1.7975	0.106		-20	0.1	2.1775	0.0531		-20	0.1	4.3938	0.153		-20	0.1	2.1557	0.243
	-30	0.2	1.7956	0.106		-30	0.2	2.1824	0.053		-30	0.3	4.3951	0.153		-30	0.1	2.1506	0.243
	-40	0.5	1.7961	0.101		-40	0.3	2.1811	0.053		-40	0.6	4.3963	0.153		-40	0.1	2.1508	0.243
	-50	0.9	1.7987	0.101		-50	0.4	2.1772	0.053		-50	1.1	4.3975	0.153		-50	0.1	2.1553	0.243

J. Ind. Geophys. Union (January 2019)
v.23, no.1, pp: 69-84

Runoff estimation using SCS-CN method for degrading lakes/tanks: a case study of Bilikere and Halebidu tanks, Karnataka (India)

Pradeep Raja K.P.[1]*, Suresh Ramaswwamyreddy[2]

[1]Research Scholar, Department of Civil Engineering, BMS College of Engineering, Basavanagudi, Bengaluru, Karnataka, India -560019.

[2]Department of Civil Engineering, BMS College of Engineering, Basavanagudi, Bengaluru, Karnataka, India -560019.

* Corresponding author: kppradeepraja@yahoo.co.in

ABSTRACT

Rainfall and runoff are essential components of water resources in a watershed. Similarly, the rainfall is a principal source of surface water storage in lakes or tanks. Assessment of water availability for storage, in artificial/manmade structures depends upon the rainfall and runoff characteristics in a catchment. Surface water storage in tanks/lakes is also an important factor in tank irrigation and enhancement of ground water level. It is fairly well known that the runoff in a catchment is governed by several factors like land use/land cover, amount of rainfall, intensity of rain, type of soil, soil moisture and other hydro-geomorphological features. In view of this, the present study considers two minor irrigation (MI) tanks, Bilikere and Halebidu, which have dried up completely since 2004. The collective catchment (BKHB) of both the tanks is a mini watershed that covers 46.33 km^2 area, in Lakshman Theertha River basin, which is a sub-basin of the river Cauvery flowing through semi-arid region of Mysore district of Karnataka. Soil Conservation Service Curve Number (SCS-CN) method is integrated with RS and GIS technology to estimate the runoff. Study reveals that the volume of runoff is decreasing in recent times due to the change of land use pattern and significant decrease in intensity of rainfall in the studied region.

Key words: Bilikere and Halebidu tanks, Mean daily intensity (MDI), Antecedent moisture condition (AMC), Surface runoff, Soil conservation service curve number (SCS-CN).

INTRODUCTION

The process of surface runoff is intricate in nature and is governed by several inter-connected physical and morphological factors. There are various methods available for estimating the depth of runoff such as the rational method, empirical equations and watershed simulations. Estimation of surface runoff from a catchment area having the records of rainfall is complicated. For the BKHB catchment, which is the area under study, no specific records of runoff are available. SCS-CN method, one of the watershed simulation methods is best suited for such situations, where runoff records are not available. Hence for the present case study, SCS-CN method is adopted for estimating the runoff. The advantage of SCS-CN method is that it includes several influencing factors governing the runoff such as type of soil, antecedent moisture condition (AMC), land use/land cover (LULC) by integrating them into a single dimensionless factor called curve number (CN).

In fact, several methods based on SCS-CN are being used by researchers worldwide. For example, a methodology described by Morel-Seytoux and Verdin (1981) based on the relationship between CN, hydraulic gradient (K) and corresponding storage suction factor (S_f), has been used in calculating the surface runoff by Silveira et al. (2000). A renewed SCS-CN procedure based on soil moisture accounting (SMA) was established by clearing the confusion between intrinsic parameter and initial condition by Michel et al. (2005). Using the volumetric concept, CN was determined for gauged as well as ungauged watersheds that exhibited a power relation between the potential maximum retention and 5-day AMC. This modified SCS-CN was used and found to give similar results between actual and predicted values of runoff (Mishra and Singh 2006). The accuracy of the modified SCS-CN method by incorporating the observed degree of saturation for the estimation of potential maximum retention parameter (S), coupled with a geomorphological unit hydrograph transfer function, was also tested in simulating catchment response (Brocca et al., 2009). Best performance is however achieved by adopting median, geometric mean and asymptotic fit procedures for the determination of standard CN and monthly CN values to estimate runoff (Gundalia and Dholakia 2014).

Earlier studies carried out by many researchers (Pandey et al., 2003; Rao et al., 2011; Dhawale, 2013; Bansode and Patil, 2014; Tailor and Shrimali, 2016; Satheeshkumar et al., 2017) have shown that the SCS-CN method is best suited for Indian conditions. Therefore, in the present case study, runoff estimation is carried out by using modified SCS-CN model for Indian conditions, coupled with Remote Sensing (RS) and Geographical Information System (GIS) techniques.

Table 1. Details of Satellites and Sensors.

S.No	Name of the Satellite	Sensor	Date of acquisition	Path	Row
1	Land Sat -5	MSS	05/12/1994	144	052
2	Land Sat -5	MSS	06/11/1996	144	052
3	Land Sat -5	MSS	11/09/1999	144	052
4	Land Sat -5	MSS	16/12/2004	144	052
5	Land Sat -5	MSS	31/12/2006	144	052
6	IRS-P6	LISS-III	03/11/2009	099	065

STUDY AREA

Hunsur Taluk of Mysore district has seven MI (Minor irrigation) tanks with overall CCA (Culturable command area or atchkat) of 740 ha (Hectares). Among seven lakes, two major lakes, Bilikere Lake and Halebidu Lake, have dried up completely since 2004. These lakes are situated between 12°21′10.163″N and 12°17′37.353″N latitude and 76°25′46.296″E and 76°31′4.167″E longitude as shown in Figure 1. Both the tanks are rain fed perennial water bodies situated at an altitude of 695 m and 680 m above mean sea level (msl) respectively, towards west of Mysore in a suburban area. The water was usually used for agriculture, horticulture, fish culture and domestic purposes. The combined catchment of BKHB is 46.33 km^2 with a highest elevation of 774 m and lowest elevation of 680 m above msl. Geologically, the area comprises of granites, gneisses and charnockite rock stratum. The catchment is an agricultural terrain, in which major part of the land is a cropland, sparse vegetation and poor soil cover. Inconsistent rainfall lead to recurring drought in the study area. Plate 1 shows the temporal satellite images of the study area and Table 1 shows the details of satellite, sensor, date of acquisition, path and row.

DETAILS OF STUDIED TANKS

There are about 27 water bodies including ponds and lakes ranging from 0.7 ha to 62 ha in the BKHB catchment. This catchment is a part of Lakshman Theertha River which is a sub-basin of Cauvery river. The Bilikere Lake is having a catchment of 23.71 km^2, live capacity of 21 MCft (Million cubic feet) with water spread area of 36.8 ha and a total physiographical area of 62.12 ha. Similarly, the Halebidu Lake has a catchment of 22.62 km^2, live capacity of 18 MCft with a water spread area of 30 ha and a total physiographical area of 58.33 ha. (Minor Irrigation Department, 2014).

DATA

i. Topographic map of 1:50,000 scale from Survey of India (SOI); D43W7 and D43W11; 2005 edition, is used as the base map.
ii. Landsat images from USGS are used to generate the LULC maps by supervised classification.
iii. Stream network is generated using Arc Hydro tools and CARTOSAT-1; (2005-2014) DEM Image-Stereo Data, ISRO, India.
iv. The daily rainfall from 1975-2014 for Hunsur taluk of Mysore district is used for the analysis. The data is collected from Karnataka State Natural Disaster Monitoring Centre (KSNDMC), Bengaluru.
v. Soil map is acquired from National Bureau of Soil Survey and Land Use Planning (NBSS and LUP), Bengaluru is used to generate soil map and hydrological soil group map.
vi. Figure 2 depicts the methodology used for estimation of runoff from BKHB catchment.

METHODOLOGY

Estimating runoff: SCS-CN Method

SCS-CN method developed by soil conservation services of USDA in 1969, 1972, 1986 (USDA-NRCS 1986) is a modest, predictable and stable conceptual method for estimation of direct runoff based on storm rainfall depth. It depends on only one parameter, Curve Number (CN). The CN varies for different soils, land use/land cover and hydrological conditions. The method is based on the basic theory of water balance equation of the rainfall in a known interval of time Δt, which can be expressed as

$$\mathbf{P = I_a + F + Q} \quad (1)$$

where P =total rainfall, I_a =initial abstraction, F=cumulative infiltration excluding I_a and Q =direct surface runoff (all in units of volume expressed as depth in 'mm' occurring in time Δt =1day).

The above equation is modified with two fundamental hypotheses, which are stated as (i) ratio of the actual direct runoff (Q) to the maximum potential runoff (P-I_a) is equal to the ratio of the actual infiltration (F) to the potential infiltration (S) and (ii) the amount of initial abstraction is some fraction of the potential maximum retention (S) and is given by

$$\frac{\mathbf{Q}}{\mathbf{(P-I_a)}} = \frac{\mathbf{F}}{\mathbf{S}} \quad (2)$$

$$\mathbf{I_a = \lambda S} \quad (3)$$

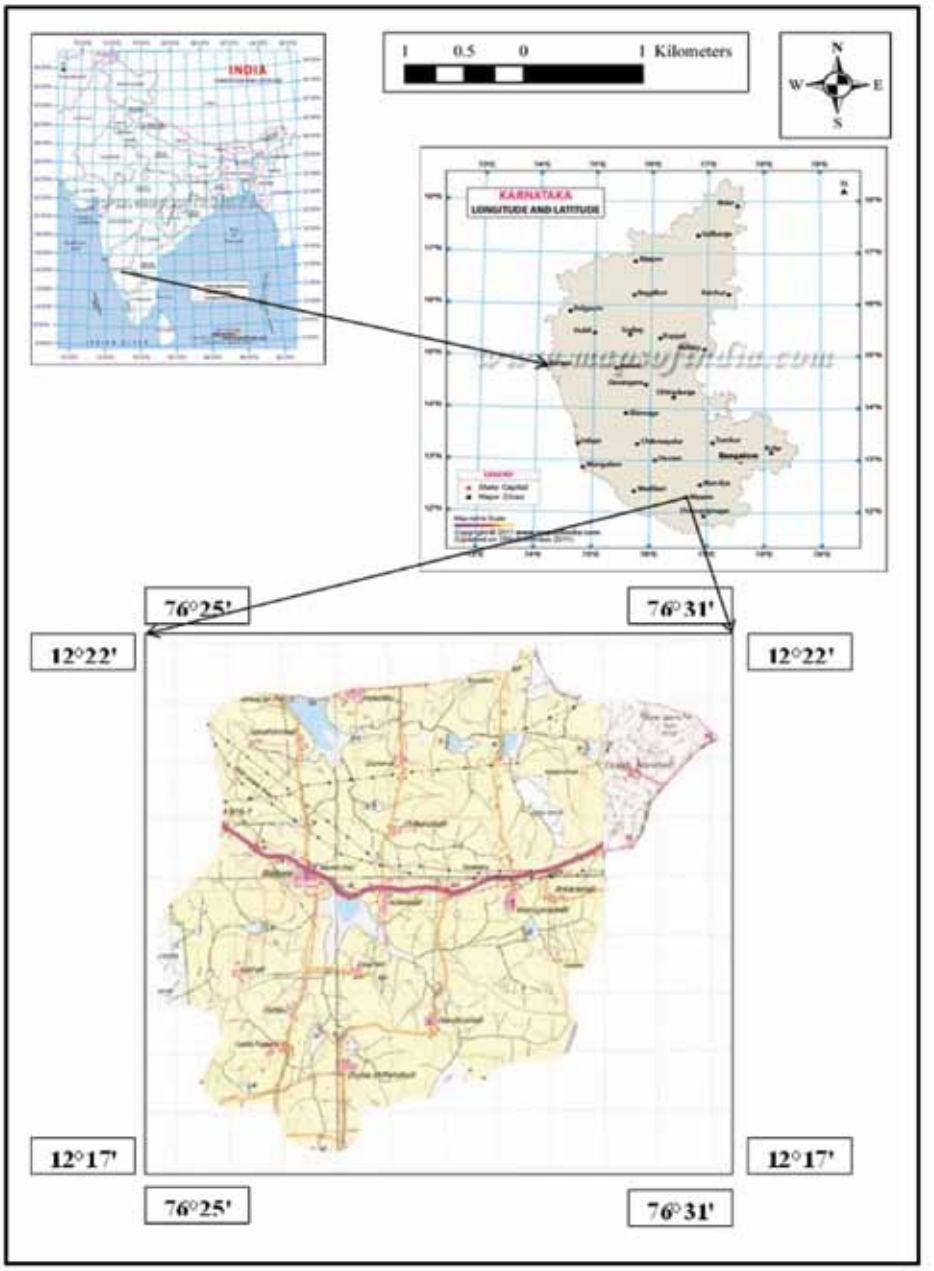

Figure 1. Location map of the study area.

Combining equation 2 and 3 and solving

$$\mathbf{Q} = \frac{(\mathbf{P}-\lambda\mathbf{S})^2}{\mathbf{P}+(1-\lambda)\mathbf{S}} \quad \text{for } P > \lambda S \text{ and } Q = 0 \text{ for } P \leq \lambda S \qquad 4$$

Generally the value of 'λ' varies from 0.1 to 0.3 for Indian conditions. In this study it is considered as 0.2, hence the equation 4 reduces to

$$\mathbf{Q} = \frac{(\mathbf{P}-0.2\mathbf{S})^2}{\mathbf{P}+0.8\mathbf{S}} \quad \text{for } P > 0.2S \text{ and } Q = 0 \text{ for } P \leq 0.2S \qquad 5$$

The parameter 'S' in mm representing the potential maximum retention depends upon the soil-vegetation-land use complex of the catchment and also upon the AMC in the catchment just prior to the commencement of the rainfall event. It is expressed in terms of a dimensionless parameter CN as

$$\mathbf{S} = \frac{25400}{\mathbf{CN}} - 254 \qquad 6$$

The CN (varies from 0 to 100, a value of 100 represents S=0 and a value of '0' represents S=∞) is determined using a data table, based on land cover, hydrological soil groups (HSG) and AMC. CN value is obtained from technical release TR-55 (USDA-NRCS, 1986).

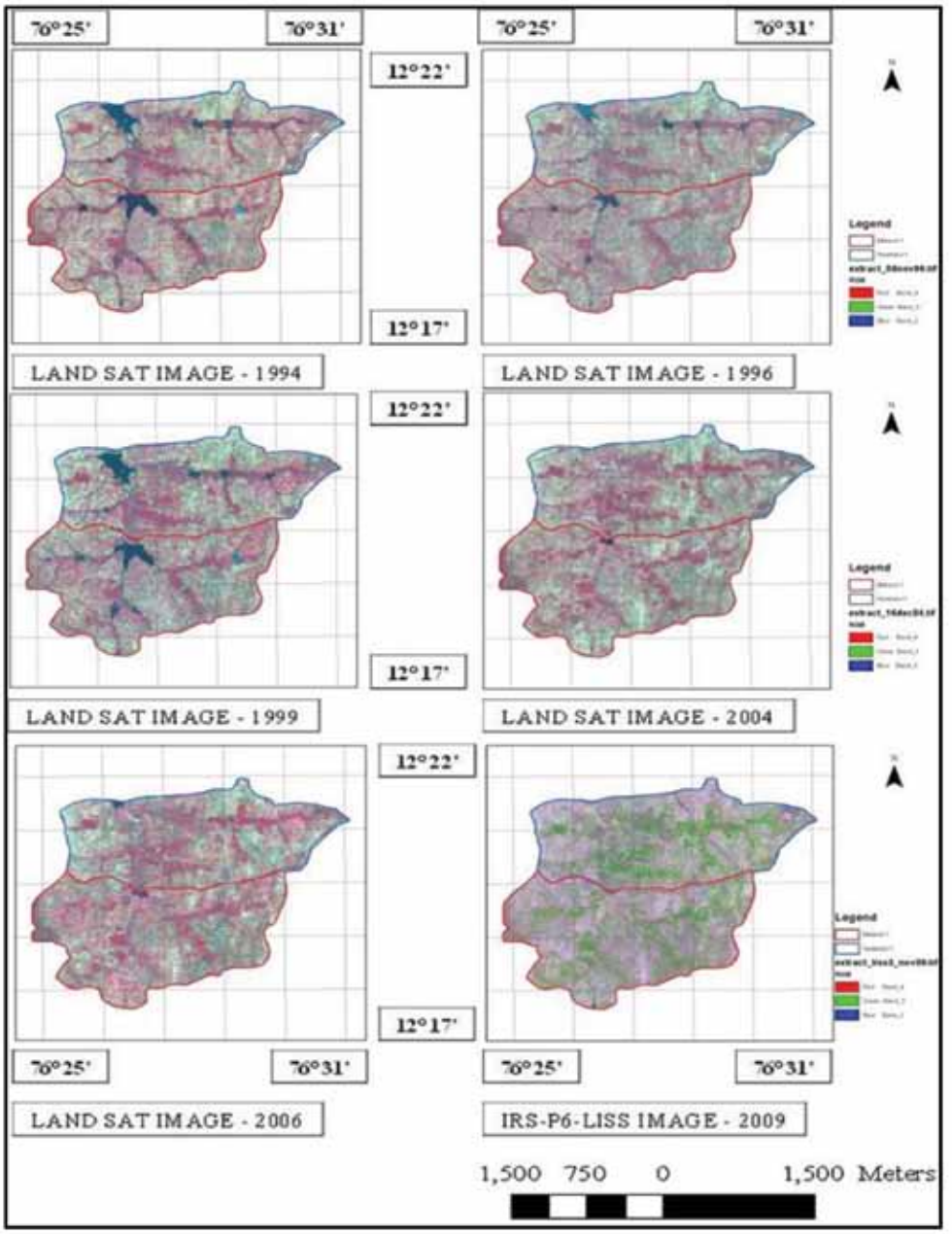

Plate 1. Temporal satellite images of the study area

The modified SCS-CN method for larger watersheds, by weighted curve numbers with respect to watershed/land cover area and is given

$$CN_w = \frac{\sum CN_i A_i}{A} \quad 7$$

where CN_w = weighted curve number, CN_i = curve number from 1 to any number 'i', Ai = area with curve number CN_i and A = total area of the catchment (Subramanya, 2008).

Antecedent soil moisture condition (AMC)

Antecedent moisture condition denotes the moisture content present in the soil at the beginning of the rainfall-runoff event under consideration. It is well known that initial abstraction and infiltration is governed by AMC. For purposes of practical application three levels of AMC are recognized by SCS as shown in Table 2. These values are applied only to AMC-II to get the values CN-II. In turn, the values of CN-I and CN-III for AMC-I and AMC-III is determined using the equation 8 and 9.

$$CN_I = \frac{CN_{II}}{2.281 - 0.01281 CN_{II}} \quad 8$$

$$CN_{III} = \frac{CN_{II}}{0.427 + 0.00573 CN_{II}} \quad 9$$

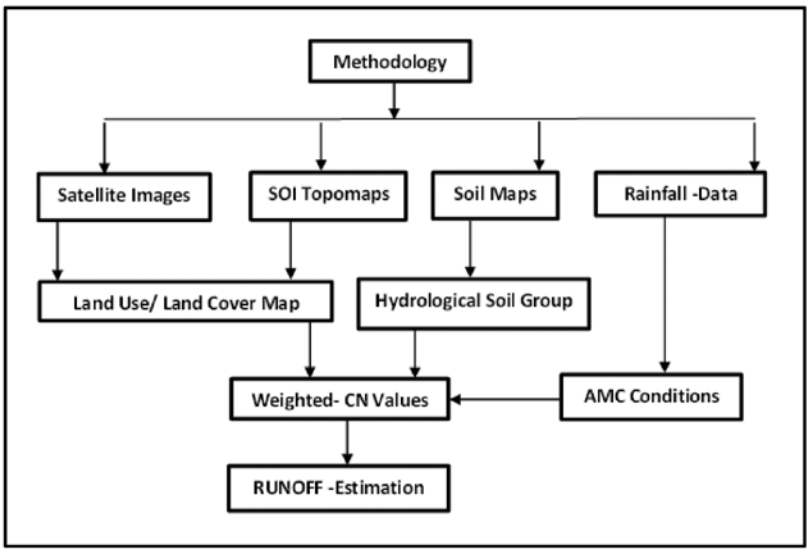

Figure 2. Methodology for the calculation of runoff from BKHB catchment

Table 2. AMC Conditions for calculating CN - as per USDA-NRCS

AMC Type	Condition of soil	Total rain in previous 5 days (mm)	
		Dormant season	Growing season
I	Soils are dry but not to wilting point	<13	<36
II	Average conditions	13 to 28	36 to 53
III	Saturated soil condition prevails	>28	>53

Table 3. Results of LULC classification

S. No	Land use/land cover classification	Area - ha	
		1994	2004
1	Water in lakes and ponds	141.57	8.19
2	Settlement - Rural	195.30	268.20
3	Vegetation – Open forest and wetlands	257.31	574.38
4	Vegetation – Agricultural plantations, Trees Etc.,	586.26	311.58
5	Stony scrub and Rock out crops Etc.,	25.38	40.05
6	Agricultural crop lands – Both kharif and rabi	3427.38	3430.80
	Total	4633.20	4633.20

RESULTS AND DISCUSSION

Land use/land cover classification (LULC)

Loss of vegetation cover and agricultural land, deforestation and destruction of important wet lands is a complex feature of environmental degradation. LULC is a significant process of detecting the historical changes of landforms. The land cover features are classified from the satellite data using supervised classification (Lillesand and Kiefer, 2007) method in conjunction with Google Earth Images and ground truth data. Thematic maps are generated using Arc GIS software (ESRI, 2010). The land cover features identified in the study area are water in lakes and ponds, rural settlement, open forest and wetland vegetation (consisting more of eucalyptus plantations), Agricultural plantations are mainly of coconut plantations, rock outcrops and stony scrub, agricultural crop land includes both Kharif and Rabi seasons with straight row treatment practice. The main crops in the study area are ragi and tobacco (Raithamitra, 2014). Classification is carried for two different years, one for the year 1994 (Figure 3) and other one is for 2004 image (Figure 4). It is observed from LULC maps that, water spread area in tanks and ponds reduced significantly from 2004 onwards. An increase in wet land plantations especially eucalyptus plantations near and surrounding the dry lakes (The units are confirmed by field visits). Simultaneously, there is a reduction in

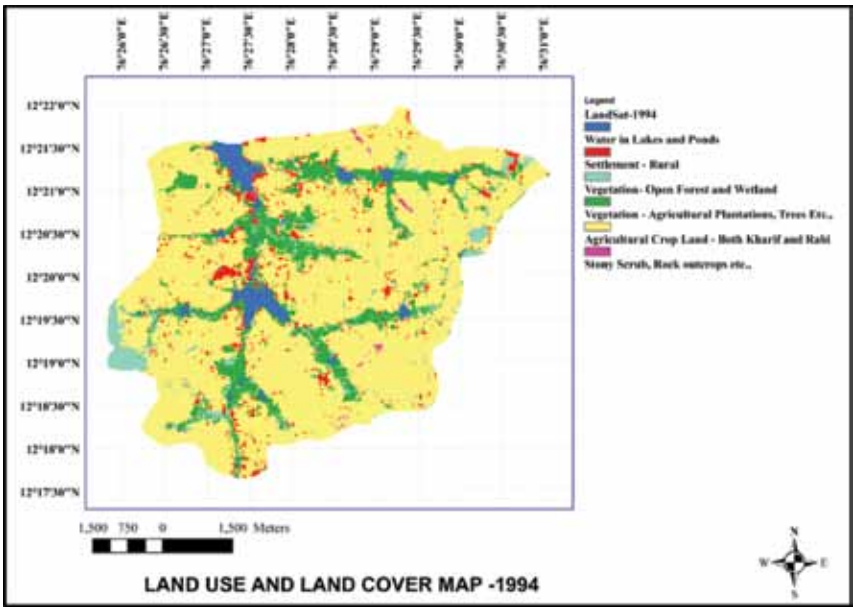

Figure 3. Land Use/Land Cover map of BKHB catchment – 1994 Image

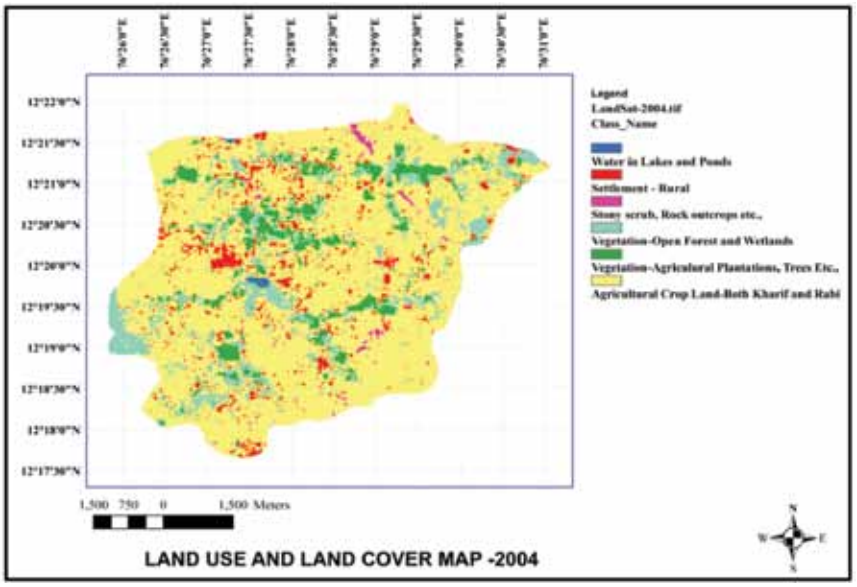

Figure 4. Land Use /Land Cover map of BKHB catchment – 2004 Image.

agricultural plantations. No change in cropland area is observed. Increase of rock out crop is observed and this is caused due to quarry extraction/mining. Results are presented in Table 3 and Figures 5 and 6.

Soil map and hydrological soil map

Soil texture

Six varieties of soil texture have been identified in the study area which are gravelly sandy loam, loamy sand, sandy clay, sandy clay loam, clay and rock outcrops with dyke ridges. The soil map is shown in Figure 7 and is generated using the map from NBSS and LUP. Maximum depth of gravelly sandy loam, loamy sand and sandy clay is 20 m, sandy clay loam varies up to 9 m and clayey soil ranges upto 16 m.

Hydrological soil group (HSG) mapping

Soils are classified by the Natural Resource Conservation Service into four Hydrologic Soil Groups based on the soil's runoff potential. The four Hydrologic Soils Groups are A, B, C and D (USDA-NRCS 1986).

***Group A*:** Sand, loamy sand or sandy loam types of soils. It has low runoff potential and high infiltration rates, even when thoroughly wetted. They consist primarily of

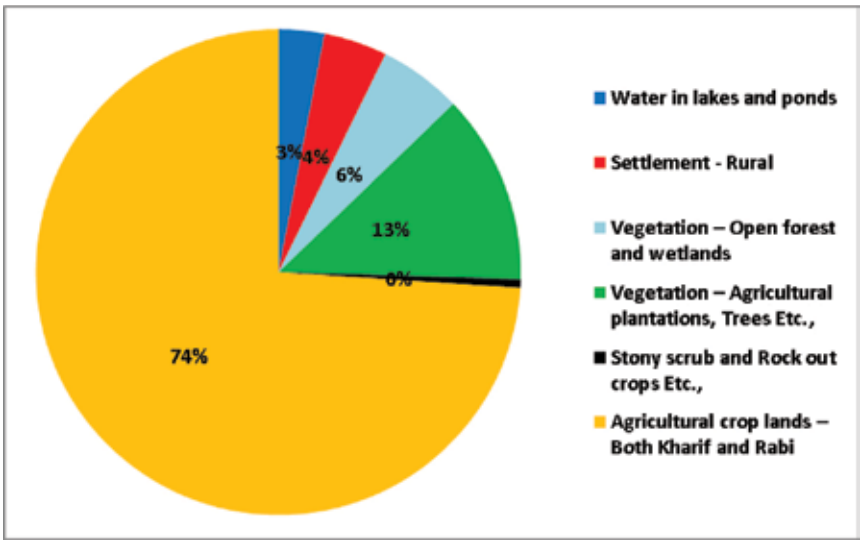

Figure 5. Percentage area distribution of LULC for the year 1994.

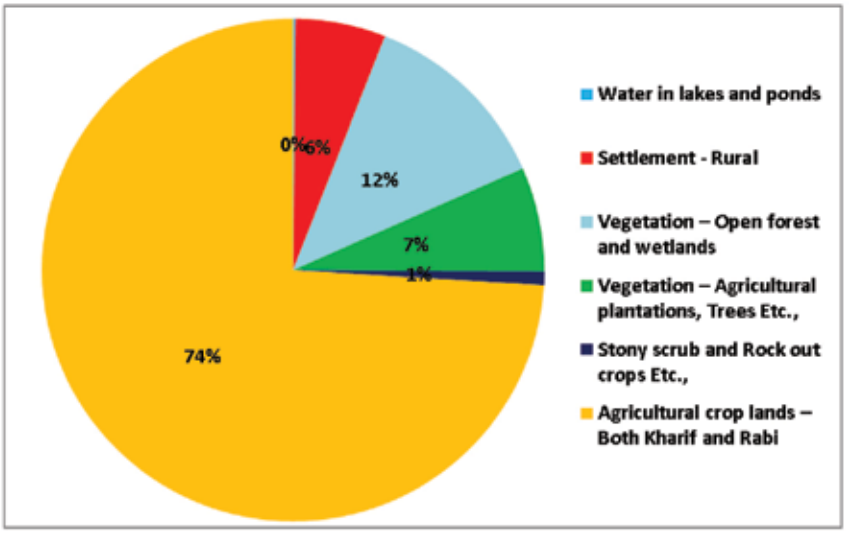

Figure 6. Percentage area distribution of LULC for the year 2004

deep, well to excessively drained sands or gravels and have a high rate of water transmission.

***Group B*: S**ilt loam or loam. It has a moderate infiltration rate when thoroughly wetted and consists predominantly or moderately deep to deep, moderately well to well drained soils with moderately fine to moderately coarse textures.

Group C: Soils are sandy clay loam. They have low infiltration rates when thoroughly wetted and consist essentially of soils with a layer that impedes downward movement of water and soils with moderately fine to fine structure.

***Group D*:** Soils are clay loam, silty clay loam, sandy clay, silty clay or clay. This HSG has the highest runoff potential. They have very low infiltration rates when thoroughly wetted and consist mainly of clay soils with high swelling potential, soils with a permanent high water table, soils with a clay layer at or near the surface and shallow soils over nearly impervious material.

In the present study, the soil texture is classified into three hydrological soil groups A, C and D as shown in Figures 8 and 9. It is seen that, 59% of the soil texture falls in the group 'A' indicating low runoff potential and high infiltration rate when thoroughly wetted, and consists of excessively drained sands or gravels. 16% of soil texture fall in 'C' group suggesting low infiltration and moderate rate of water transmission and remaining 25% of the texture indicate group 'D' suggesting low infiltration rates and high runoff potential. The drainage pattern is dendritic in the BKHB catchment, 1st and 2nd order streams dominate the catchment as shown in the Figure 8 and most of them are formed in group 'A' soil signifying that, very high intensity

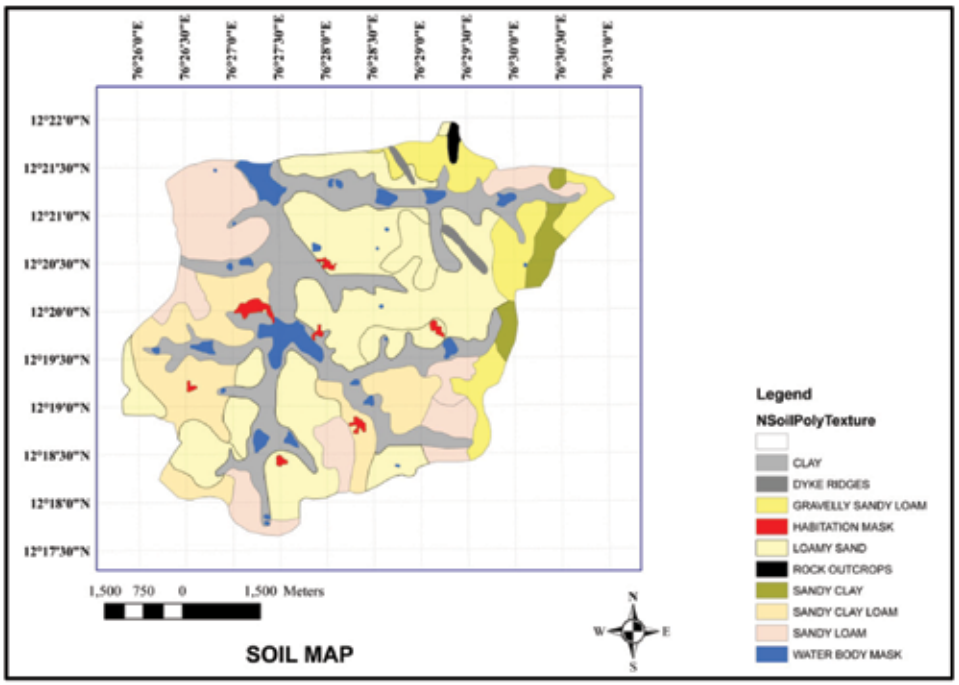

Figure 7. Soil map of the BKHB catchment (Source: NBSS and LUP).

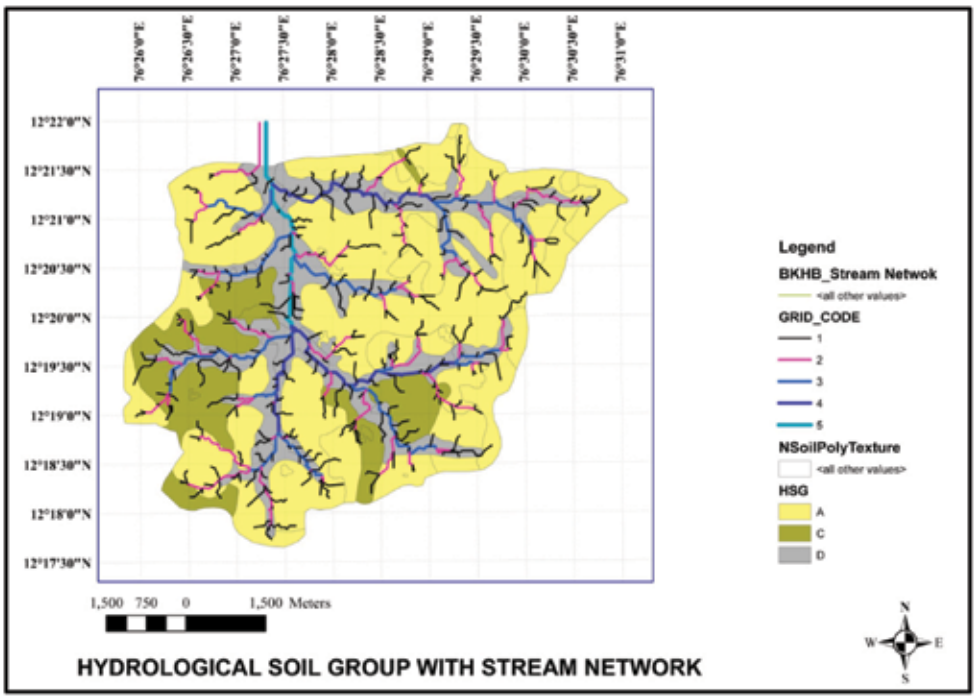

Figure 8. Map of HSG with stream network.

rainfall is required to overcome the rate of infiltration in the catchment and to generate surface runoff.

Curve number (CN) calculation

The CN values for each hydrological soil group and corresponding land use class during years 1994 and 2004 are organized as shown in Table 4. The values are for AMC-II condition. From this CN value, CN-I and CN-III values for AMC-I and AMC-III is calculated using equation (8) and (9). In order to homogenize the curve numbers, weighted curve number is determined for the BKHB catchment. The weighted CN-II values are 77.36 for 1994 and 75.95 for 2004 (Table 5).

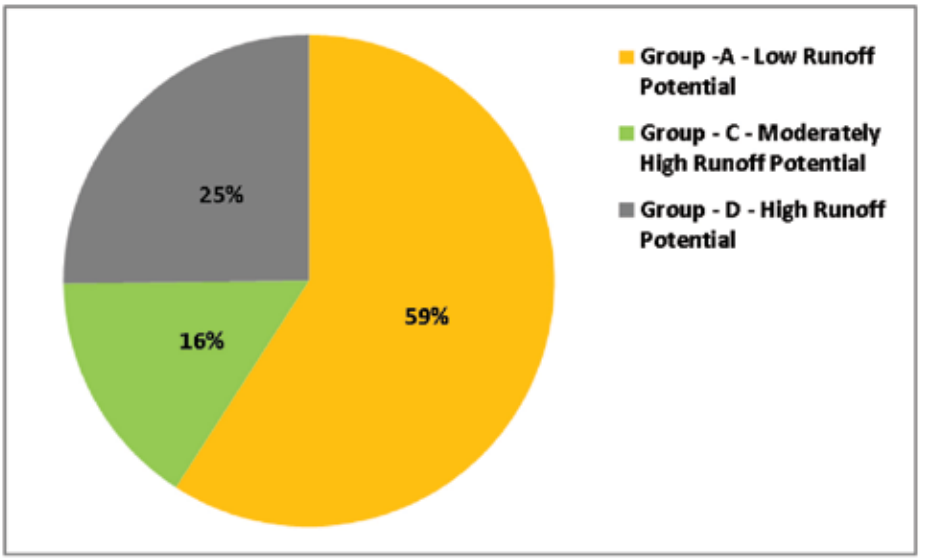

Figure 9. Areal distribution of HSG.

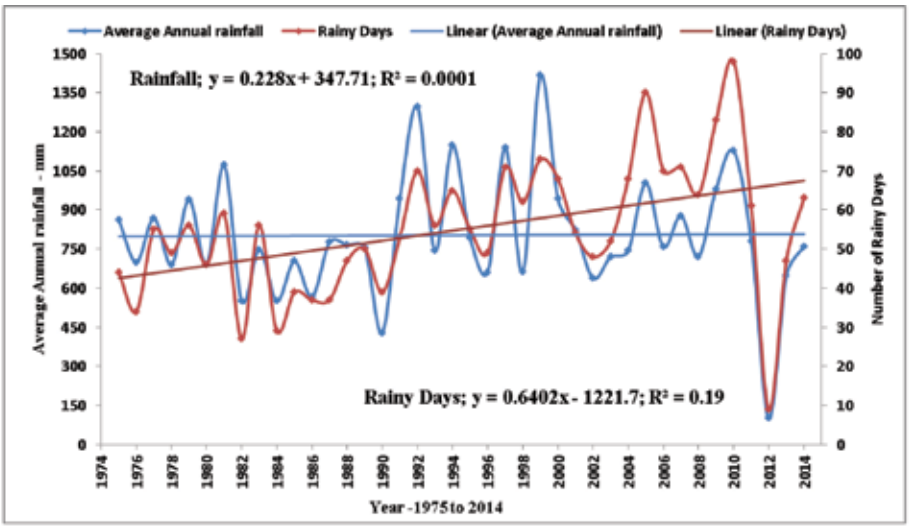

Figure 10. Relationship between rainy days and average annual rainfall.

Rainfall analysis

Average annual rainfall of Hunsur taluk is 802.37 mm, distributed with a coefficient of variation (CV) of 29.34 %, standard variation (SD) of 235.4 mm. The minimum average annual rainfall of 100 mm was in 2012 and a maximum average annual rainfall of 1416 mm in 1999. Excess precipitation (>962.8 mm) occurred in 8 years, Deficient rainfall occurred in 5 years. Scanty rainfall occurred in only one year i.e., in 2012 (-88%) and normal rainfall (range 649.9 mm to 954.82 mm) occurred in 26years among 40 years, indicating that the average annual rainfall is normal in the taluk.

Intensity of rain

The intensity of rainfall is a measure of the amount of rain that falls over time. Forty years daily rainfall data is analyzed and classified as per India Meteorological Department (IMD, 2016); NR: no rain (Intensity of rainfall equal to zero); VLR: very light rain (rainfall between 0.1 mm- 2.4 mm per day); LR: light rain (between 2.5 mm-7.5 mm per day); MR: moderate rain (7.6 mm-35.5 mm per day); RH: rather heavy (35.6 mm-64.4 mm per day); HR: heavy rain (64.5 mm-124.4 mm per day); VHR: very heavy rain (124.5 mm-244.4 mm per day); EHR: extremely heavy rain (greater than 244.5mm per day). Details of various intensities are

Table 4. Calculation of weighted curve number for BKHB catchment

S. No	LU/LC-1994 Image	HSG	CN	Area-km^2	% Area	%Area * CN	Weighted CN
1	Water in Lakes and Ponds	A	90	0.02	0.04	3.85	
		C	98	0.00	0.00	0.19	
		D	100	0.30	0.64	63.91	
		D	100	1.10	2.37	237.18	
2	Settlement - Rural	A	72	0.91	1.96	140.84	
		C	81	0.37	0.80	64.67	
		D	86	0.68	1.46	125.62	
3	Vegetation – Open Forest and Wetlands Etc.,	A	28	1.34	2.89	80.93	
		C	60	0.19	0.40	24.13	
		D	64	1.07	2.30	147.19	77.36
4	Vegetation – Agricultural plantations, Trees Etc.,	A	41	1.22	2.63	107.83	
		C	69	0.14	0.31	21.58	
		D	73	4.54	9.79	714.67	
5	Agricultural Crop Land – Both Kharif and Rabi – Straight row treatment practice.	A	76	23.77	51.29	3898.40	
		C	90	6.49	14.00	1259.92	
		D	93	3.97	8.58	797.57	
6	Stony scrubs and Rock outcrops Etc.,	A	77	0.08	0.16	12.56	
		C	91	0.06	0.12	10.96	
		D	93	0.12	0.25	23.30	
LU/LC-for 2004 Image							
1	Water in Lakes and Ponds	D	100	0.08	0.18	17.87	
2	Settlement - Rural	A	72	1.43	3.09	222.79	
		C	81	0.61	1.33	107.46	
		D	86	0.59	1.27	109.42	
3	Vegetation – Open Forest and Wetlands Etc.,	A	28	2.52	5.44	152.24	
		C	60	0.44	0.95	56.88	
		D	64	2.81	6.06	388.12	
4	Vegetation – Agricultural plantations, Trees Etc.,	A	41	0.72	1.56	64.03	75.95
		C	69	0.07	0.16	11.12	
		D	73	2.34	5.05	368.68	
5	Agricultural Crop Land – Both Kharif and Rabi – Straight Row treatment practice.	A	76	22.44	48.43	3680.50	
		C	90	6.00	12.95	1165.89	
		D	93	5.84	12.61	1172.96	
6	Stony scrubs and Rock outcrops Etc.,	A	77	0.18	0.38	29.61	
		C	91	0.14	0.30	27.58	
		D	93	0.08	0.16	15.17	

(Source: Govt. of India, 1972)

Table 5. Summaries of CN, S and I_a

S. No	AMC	Weighted - CN values		Maximum soil retention (S) - mm		Initial abstraction – I_a=0.2S	
		1994	2004	1994	2004	1994	2004
1		59.97	58.06	169.54	183.47	33.91	36.70
2		77.36	75.95	74.34	80.43	14.87	16.09
3		88.89	88.09	31.75	34.34	6.35	6.87

presented in Table 6, it is noticed that the intensity of VLR and LR has increased considerably since 2005, MR persists uniformly, RH and HR has decreased significantly.

Mean daily intensity (MDI)

It is the ratio of average rainfall to the number of rainy days (as per IMD- a rainy day is described as a day with a rain amount of 2.5 mm or more). Average annual number of rainy days is 55 and average annual MDI is 14.92 mm per rainy day. Figure 10 displays the variation of average annual rainfall and number of rainy days from 1975 to 2014. It is noticed that the rainfall is relatively uniform and the number of rainy days is increasing. Figure 11 shows the relation between average annual rainfall and MDI.

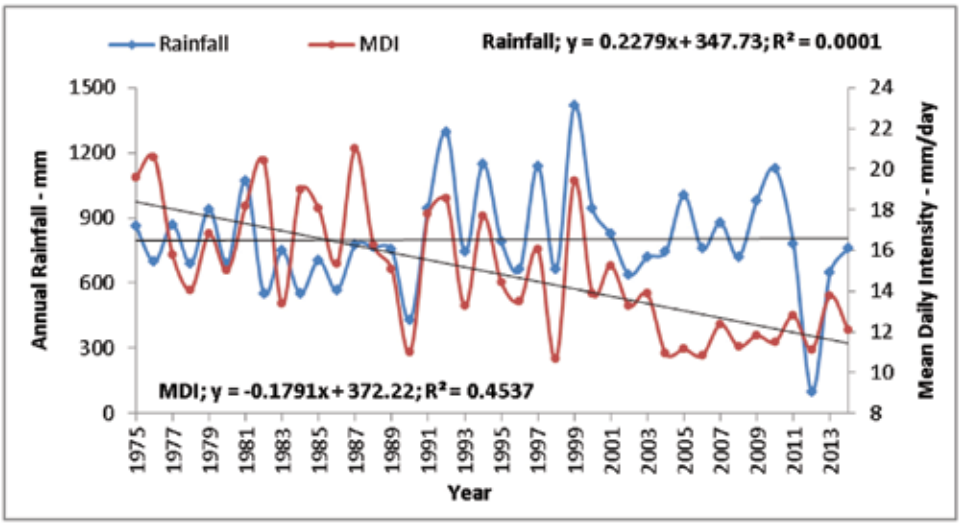

Figure 11. Variation of MDI and annual rainfall (1975 to 2014).

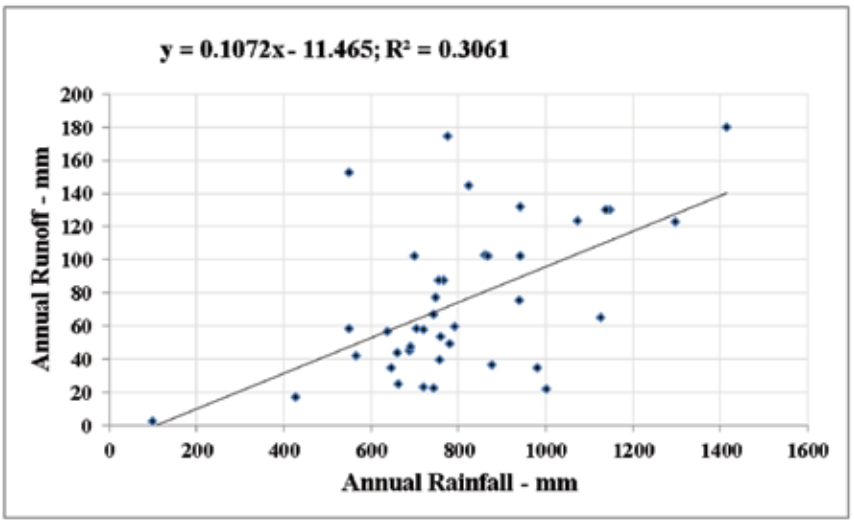

Figure 12. Linear relation between annual rainfall and annual runoff.

Rainfall is more consistent and MDI is in the negative trend. This tendency is due to the increase of more VLR and LR intensities than RH and HR.

Runoff calculation

The daily rainfall data for 40 years from 1975 to 2014 is considered for the runoff calculation. Initial abstraction is calculated at 20% of the maximum potential retention (I_a =0.2S). If the storm event is higher than the initial abstraction, the runoff exists for that rainfall event. From Figures 12 and 13, it is observed that exponential curve fitting is better than linear fit (considering the 'R' Value) between rainfall and runoff. It is seen that a minimum of 508 mm annual rainfall is required to get 43 mm runoff from linear regression and whereas 603 mm is required to get the same runoff in exponential fitting. The equation (10) for linear regression with 'R' value of 0.55 and exponential regression with 'R' equal to 0.74 is given by equation (11).

$$Y = 0.1072x - 11.465 \quad (10)$$

$$Y = 0.0035x^{1.466} \quad (11)$$

From Table 7, it is observed that a minimum rainfall of 14.87 mm/day to 16.09 mm/day is required to start the runoff process in the BKHB catchment for average AMC conditions. Table 6 shows the annual runoff and MDI from 1975 to 2014. From the observation of satellite images from 1975-2014, it is established that both the tanks were getting filled till 2003, except for the years 1990 and 1998. It is also seen that the lakes/tanks are dry since 2004; therefore a scatter plot between MDI and runoff is drawn

Table 6. Intensity of Rainfall, Rainy days and Mean Daily Intensity (MDI)

S.No	Period	Average annual rainfall	NR	VLR	LR	MR	RH	HR	VHR	RND	MDI
1	1975	862.30	320	1	14	25	4	1	0	44	19.60
2	1976	699.20	330	2	7	20	6	1	0	34	20.56
3	1977	868.30	309	1	22	28	3	2	0	55	15.79
4	1978	689.10	316	0	14	32	2	1	0	49	14.06
5	1979	940.90	309	0	16	34	6	0	0	56	16.80
6	1980	691.00	320	0	12	31	2	1	0	46	15.02
7	1981	1073.00	306	0	9	43	4	3	0	59	18.19
8	1982	550.40	333	5	10	14	2	0	1	27	20.39
9	1983	748.50	277	32	32	18	5	1	0	56	13.37
10	1984	550.00	337	0	5	19	4	1	0	29	18.97
11	1985	703.90	325	1	11	25	3	0	0	39	18.05
12	1986	566.90	328	0	8	26	3	0	0	37	15.32
13	1987	776.50	327	1	14	16	5	1	1	37	20.99
14	1988	766.00	292	27	17	26	3	1	0	47	16.30
15	1989	754.90	281	34	22	24	3	1	0	50	15.10
16	1990	428.60	283	43	24	14	1	0	0	39	10.99
17	1991	942.40	291	21	24	20	8	1	0	53	17.78
18	1992	1297.20	275	21	27	30	12	1	0	70	18.53
19	1993	743.00	290	19	28	24	3	1	0	56	13.27
20	1994	1148.20	275	25	25	33	5	2	0	65	17.66
21	1995	792.90	297	13	18	33	3	1	0	55	14.42
22	1996	661.00	311	6	22	25	2	0	0	49	13.49
23	1997	1139.20	259	35	28	36	5	2	0	71	16.05
24	1998	662.00	287	16	33	27	2	0	0	62	10.68
25	1999	1416.00	275	17	20	44	6	3	0	73	19.40
26	2000	942.80	278	20	37	26	2	3	0	68	13.86
27	2001	823.90	281	30	33	14	4	3	0	54	15.26
28	2002	637.40	290	27	28	18	1	1	0	48	13.28
29	2003	720.60	291	22	23	23	6	0	0	52	13.86
30	2004	742.90	282	16	33	34	1	0	0	68	10.93
31	2005	1003.20	238	37	43	45	2	0	0	90	11.15
32	2006	758.20	259	36	40	28	1	1	0	70	10.83
33	2007	877.90	262	32	33	35	3	0	0	71	12.36
34	2008	721.20	265	37	37	25	2	0	0	64	11.27
35	2009	980.50	180	102	47	33	3	0	0	83	11.81
36	2010	1126.40	182	85	52	42	3	1	0	98	11.49
37	2011	780.87	250	54	34	23	4	0	0	61	12.80
38	2012	100.00	354	3	4	5	0	0	0	9	11.11
39	2013	647.50	277	41	21	24	2	0	0	47	13.78
40	2014	760.00	261	41	39	18	6	0	0	63	12.06
	Avg	802.37	288	23	24	27	4	1	0	55	14.92

(Rainfall in mm, NR-No rain, VLR-Very light rain, LR-Light rain, MR-Moderate rain, RH-Rather heavy rain, HR-Heavy rain, VHR-Very heavy rain)

as shown in Figure 14. The equation for linear trend with 'R' value of 0.8 is given by

$$\mathbf{Y = 11.703x - 100.04} \qquad 12$$

where Y= runoff and x = mean daily intensity.

From the equation (12) it is consequent that a least MDI value of 8.6 mm/day is required to have the surface runoff. Assessment of runoff data reveals that, when the runoff is higher than 43 mm (AMC-II) both the lakes/tanks were full with a corresponding MDI value greater than 12.3 mm/rainy day and average annual rainfall greater than 603 mm. Looking at the Table 6 and Figure 15, it is observed that the runoff is significantly in the decreasing trend since 2004 even though the rainfall is more consistent. This is because of the decreasing MDI. Though the value of runoff is greater than 43 mm in the years 2010 and 2014, the tanks are not getting filled due to the lower value of MDI. Whereas in the year 2011, both runoff and MDI are higher than the specified values; smaller ponds and ditches were filled but not Bilikere and Halebidu lakes. This may be due to the increased wetland vegetation cover in the catchment and clogging of stream channels.

Table 7. Annual runoff values with Mean Daily Intensity

Year	Annual-Rainfall (mm)	Annual Runoff (mm)			MDI (mm/rainy day)
		AMC-I	AMC-II	AMC-III	
1975	862.30	15.23	102.85	280.09	19.60
1976	699.20	16.69	101.79	246.64	20.56
1977	868.30	20.49	102.11	255.71	15.79
1978	689.10	6.91	44.68	147.64	14.06
1979	940.90	6.22	74.98	247.66	16.80
1980	691.00	5.06	46.97	160.39	15.02
1981	1073.00	24.11	123.51	316.31	18.19
1982	550.40	83.28	152.72	241.28	20.39
1983	748.50	11.37	77.22	197.37	13.37
1984	550.00	6.95	58.27	164.47	18.97
1985	703.90	3.07	58.14	191.02	18.05
1986	566.90	4.15	41.50	133.08	15.32
1987	776.50	66.77	174.56	321.69	20.99
1988	766.00	17.80	87.19	213.11	16.30
1989	754.90	26.72	87.31	202.88	15.10
1990	428.60	0.42	16.74	67.04	10.99
1991	942.40	20.64	131.96	315.73	17.78
1992	1297.20	14.14	122.53	331.45	18.53
1993	743.00	10.49	66.79	184.16	13.27
1994	1148.20	22.33	129.90	348.05	17.66
1995	792.90	9.60	59.11	178.59	14.42
1996	661.00	2.76	43.59	147.41	13.49
1997	1139.20	26.24	129.86	325.65	16.05
1998	662.00	1.66	24.77	108.39	10.68
1999	1416.00	34.73	179.94	457.35	19.40
2000	942.80	19.79	102.04	260.96	13.86
2001	823.90	44.98	144.40	284.94	15.26
2002	637.40	7.46	56.52	164.04	13.28
2003	720.60	4.59	57.40	170.29	13.86
2004	742.90	0.81	22.14	106.94	10.93
2005	1003.20	0.02	21.97	130.73	11.15
2006	758.20	5.83	39.29	127.39	10.83
2007	877.90	3.41	36.50	147.85	12.36
2008	721.20	0.04	22.77	106.11	11.27
2009	980.50	0.70	34.40	156.35	11.81
2010	1126.40	12.37	65.00	197.41	11.49
2011	780.87	5.08	49.18	155.60	12.80
2012	100.00	0.00	2.33	13.26	11.11
2013	647.50	1.59	34.36	129.23	13.78
2014	760.00	3.86	53.47	171.50	12.06
Average	802.37	14.21	74.52	202.64	14.92

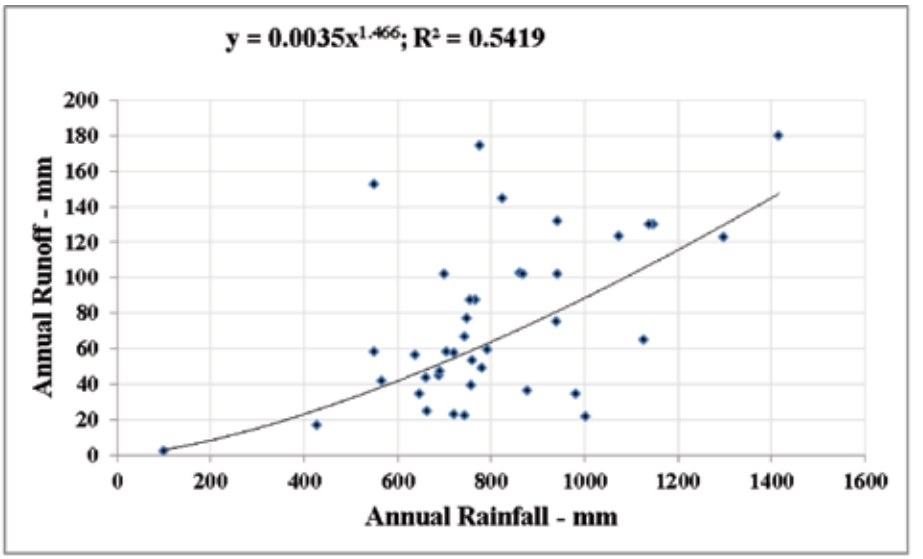

Figure 13. Exponential relationship between annual rainfall and annual runoff.

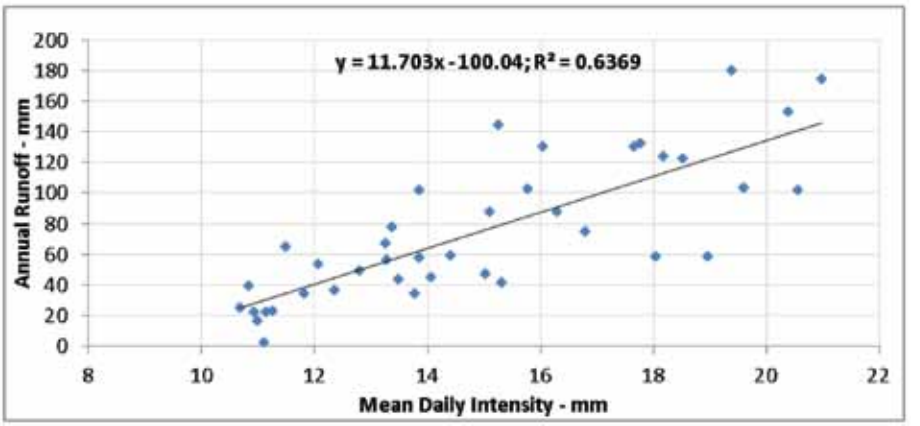

Figure 14. Linear relationship between MDI and annual runoff.

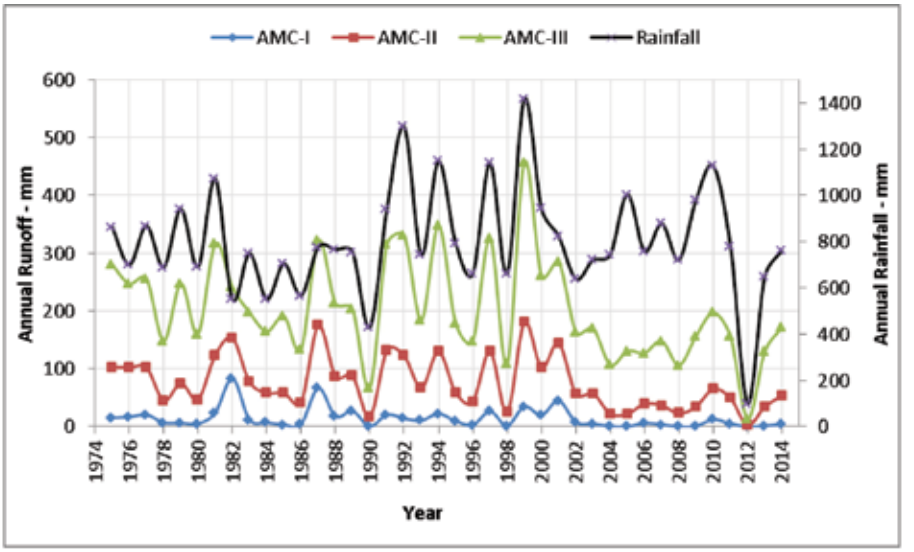

Figure 15. Annual rainfall and annual runoff for all 3-AMC conditions (1975-2014).

CONCLUSIONS

SCS-CN model combined with RS and GIS is used to calculate the surface runoff from BKHB catchment. The following observations are made from the present study

i. Daily rainfall data from 1975 to 2014 reveals that, the Antecedent Moisture Condition (AMC) in the catchment for the Kharif and Rabi season belongs to average conditions, i.e., AMC-II.
ii. Land use/land cover classification of 1994 and 2004 image discloses that, the water bodies have dried up from 3% to 0.1%, vegetation cover in and around the wetlands has increased significantly from 6% to 12%, rural settlement also has increased from 4% to 6%.
iii. Almost sixty percent of the catchment area is occupied under the category of 'A' group of HSG, indicating higher permeable soil texture and low runoff potential. Hence, necessitates a minimum of 15 mm rainfall per day to have the surface runoff.
iv. BKHB Catchment is dominated by first and second order streams and majority of them are formed in group-A soil which leads to higher rate of infiltration.
v. Weighted curve number values of 77.36 and 75.95 suggest that the basin is having low to moderate runoff capability.
vi. Potential maximum retention of soil varies from 75 to 80 mm for the BKHB catchment.
vii. Rainfall analysis shows that, the average annual rainfall is uniform in the region, however intensity of rainfall is decreasing gradually.
viii. Mean Daily intensity is also in the negative drift from the average value.
ix. Number of rainy days is in the positive movement but with low intensity rainfall.
x. Direct runoff has lowered from 2004. This may be due to increase in vegetation cover surrounding the lake and stream bed.
xi. A runoff value higher than 43 mm is essential for both the tanks to get water upto the maximum level.
xii. A minimum of 603 mm average annual rainfall required to have 43mm annual runoff.
xiii. A least MDI value of 12.3 mm/per rainy day is necessary to have minimum runoff.
xiv. Thus, it may be concluded that the surface runoff in the BKHB catchment has decreased since 2004 and hence the lakes/tanks in the catchment have dried up completely.

ACKNOWLEDGEMENT

Authors are grateful for the following organizations and authorities for providing suitable data for the research work:

i. KSNDMC, Bengaluru for providing the daily rainfall data for 40 years
ii. SOI, Bengaluru for providing the topo maps for the study area.
iii. USGS and NRSC, Hyderabad for the satellite images.
iv. NBSS and LUP, Bengaluru for providing the soil map.

Compliance with Ethical Standards

The authors declare that they have no conflict of interest and adhere to copyright norms.

REFERENCES

Bansode, A. and Patil, K.A., 2014. Estimation of runoff by using SCS curve number method and Arc GIS. Int. J. Scientific and Engg. Res., 5, 1283–1287.

Brocca, L., Melone, F., Moramarco, T. and Singh, V.P., 2009. Assimilation of observed soil moisture data in storm rainfall-runoff modeling. J. Hydrologic Engg., 14, 153–165.

Dhawale, A.W., 2013. Runoff estimation for Darewadi watershed using RS and GIS. Int. J. of Recent Technology and Engg., 1, 46–50.

ESRI, 2010, Arc GIS. Environmental Systems Research Institute.

Govt. of India, 1972: Handbook of Hydrology. Ministry of Agriculture. New Delhi.

Gundalia, M. and Dholakia, M., 2014. Impact of monthly curve number on daily runoff estimation for Ozat catchment in India. Open J. Modern Hydrology., 4, 144–155.

India Meteorological Department, 2016. Seasons- Terminologies and Glossary, p-20

Michel, C., Andre, V. and Perrin, C., 2005. Soil conservation service curve number method , How to mend a wrong soil moisture accounting procedure ? Water Resour. Res., 41, 1–6.

Minor Irrigation Department, 2014. PWD, Govt. of Karnataka.

Mishra, S.K. and Singh, V.P., 2006. A relook at NEH-4 curve number data and antecedent moisture condition criteria. Hydrological Processes, 2768, 2755–2768.

Morel Seytoux, H.J. and Verdin, J.P., 1981. Extension of the SCS rainfall runoff methodology for ungauged watersheds. Report FHWA/RD-81/060., U.S. National Technical Information Service, Springfield, Virginia.

Pandey, A., Chowdary, V.M., Mal, B.C. and Dabral, P.P., 2003. Estimation of runoff for agricultural watershed using SCS curve number and geographic information system. Map India conference proceedings, Agriculture India., 307, 1213–1229.

Raithamitra, 2014. Karnataka State Department of Agriculture, http://raitamitra.kar.nic.in

Rao, B.S.P., Amminedu, E., Rao, J., Srinivas, N. and Rao, N.B., 2011. Run-off and flood estimation in Krishna River delta using remote sensing and GIS. J. Ind. Geophys. Union, 15, 101–112.

Satheeshkumar, S., Venkateswaran, S. and Kannan, R., 2017. Rainfall–runoff estimation using SCS–CN and GIS approach in the Pappiredipatti watershed of the Vaniyar sub basin, South India. Modeling Earth Systems and Environment, 3(1), 1-8.

Silveira, L., Charbonnier, F. and Genta, J. L., 2000. The antecedent soil moisture condition of the curve number procedure. Hydrological Sciences J., 45(1), 3–12.

Subramanya. K, 2008. Engineering Hydrology. The McGraw-Hill Companies. 3rd edn. Tata McGraw-Hill, New-Delhi.

Tailor, D. and Shrimali, N.J., 2016. Surface runoff estimation by SCS curve number method using GIS for Rupen-Khan watershed, Mehsana district, Gujarat. J. Indian Water Resour. Soc., 36(4), 2–6.

Lillesand, T.M. and Kiefer, R.W., 2007. Remote Sensing and Image Interpretation 5th edn, John Wiley & sons (Asia) Pte.Ltd., Singapore.

USDA-NRCS., 1986. Urban hydrology for small Watersheds, TR-55, United States Department of Agriculture, 210-VI-TR-55, 2nd edn, June 1986.

Received on: 17.7.18; Revised on: 19.10.18; Revised on: 6.11.18

J. Ind. Geophys. Union (January 2019)
v.23, no.1, pp: 85-100

Sub-watersheds wise slope instability analysis and prioritization of the Balason River Basin of Darjeeling Himalaya, India using compound ranking method

Subrata Mondal[1]* and Sujit Mandal[2]

[1]*Department of Geography, University of Gour Banga, West Bengal-732103, India
[2]Department of Geography, Diamond Harbour Women's University, Sarisha, West Bengal-743368, India
*Corresponding Author: subratapanchagram@gmail.com

ABSTRACT

To balance between the demand and supply and ever increasing demand, it is necessary to conserve natural resources like watersheds, with proper prioritization. In that sense, morphometric analysis of any drainage basin is considered of high importance in hydrological investigation. Morphometric parameters describe the topology, the structure, the platform and the relief of basin, applied for the prioritization of watersheds. Some pre-information such as runoff, stages of its development and soil loss etc. are also provided by the analysis of morphometric parameters. In the present study, an attempt has been made to prioritize sub-watersheds based on morphometric analysis in relation to slope instability. The base map of stream network were digitized from toposheets no. 78A/4, 78A/8, 78B/1, 78B/5 and 78B/6 (Scale 1:50000) and then updated on Google earth. Arc GIS 9.3 software and MS excel-2007 was used to assess 13 morphometric parameters i.e. bifurcation ratio (Rb), length of overland flow (Lof), drainage density (Dd), stream frequency (Fs), texture ratio (Rt), drainage texture (Td), compactness coefficient (Cc), constant of channel maintenance (Ccm), shape factor/ basin shape (Sf), form factor (Ff), circularity ratio (Rc), elongation ratio (Re) and relief ratio (Rr). The results showed that SW 4, SW 5 and SW 8 fall under very high priority class in respect of soil erosion and soil loss or simply instability, having Rb of 3.532 – 4.002, Dd of 5.986 – 6.538, Fs of 14.934 – 29.447, Td of 9.765 – 23.158, Rt of 7.055 – 16.958, Lof of 0.069 – 0.084, Rr of 0.209 – 0.302, Cc of 1.265 – 1.554, Ccm of 0.139 – 0.167, Sb of 2.969 – 5.556, Ff of 0.180 – 0.337, Rc of 0.420 – 0.634 and Re of 0.479 – 0.655. Sub-watershed wise highest priority was obtained by SW 5 followed by SW 8, SW 4, SW3, SW 9, SW 1, SW 6, SW 16, SW 2, SW 17, SW 15, SW 13, SW 7, SW 10, SW 11, SW 12, SW 14, and SW 18.

Keywords: Sub-watersheds, Morphometric parameters, GIS, Compound Ranking Method, Prioritization.

INTRODUCTION

Drainage basin or watershed is the basic or ideal areal unit of the earth surface in geomorphological study of fluvially eroded landscapes (Chorley, 1969), for the management and sustainable development of natural resources (Patel et al. 2013). Keeping in view of the increasing population demand and food security for the future generation, it is realized that the water and land resources need to be developed and used and managed comprehensively in an integrated way (Biswas et al., 1999). Morphometric analysis is very much important in analyzing the changing quality of water and soil of a small hilly micro watershed. In addition, it is very useful in regional flood frequency analysis, hydrological modeling, watershed prioritization, natural resources conservation and management, drainage basin evaluation, etc. For that, it requires measurement of linear, areal and relief aspects of the basin (Nautiyal, 1994). The estimation of morphometric parameters of a hilly catchment gains more importance in spite of the difficulty in collection and measurement of hydrologic data (National Institute of Hydrology 1998). Hence, GIS is an effective tool, not only for collection, storage, management and retrieval of spatial and non-spatial data, but also for the derivation of the useful results and modeling (Gupta and Srivastava, 2010; Srivastava et al., 2011). Pioneering work on the drainage basin morphometry has earlier been carried out by Horton (1932, 1945), Smith (1950), Stahler (1952, 1964), Miller (1953), Schumm (1956), Melton (1958) and Chorley (1969). Prioritization of sub-watersheds based on morphometric analysis were also attempted by Biswas et al. (1999), Chopra et al. (2005), Patel et al. (2013), Rekha et al. (2011), Panhalkar et al. (2011), Vandana (2012), Patil and Mali (2013), Panda and Nagarajan (2013), Tolessa and Rao (2013), Ali and Ali (2014), Amani and Safaviyan (2015) etc. Shrimali et al. (2011) delineated and prioritized of soil erosion areas in Sukhana lake catchment in the Shiwalik hills by using RS and GIS. Nookaratnam et al. (2005) carried out check dam positioning by prioritization of micro-watersheds using Sediment Yield Index (SYI) model and morphometric analysis using GIS. Similarly, Javed et al. (2009) and Javed et al. (2011) studied on prioritization of sub-watersheds of Kanera watershed in Guna district of Madhya Pradesh and Jaggar watershed in the Karauli district of Rajasthan respectively, based on morphometric and land use analysis using RS and GIS techniques.

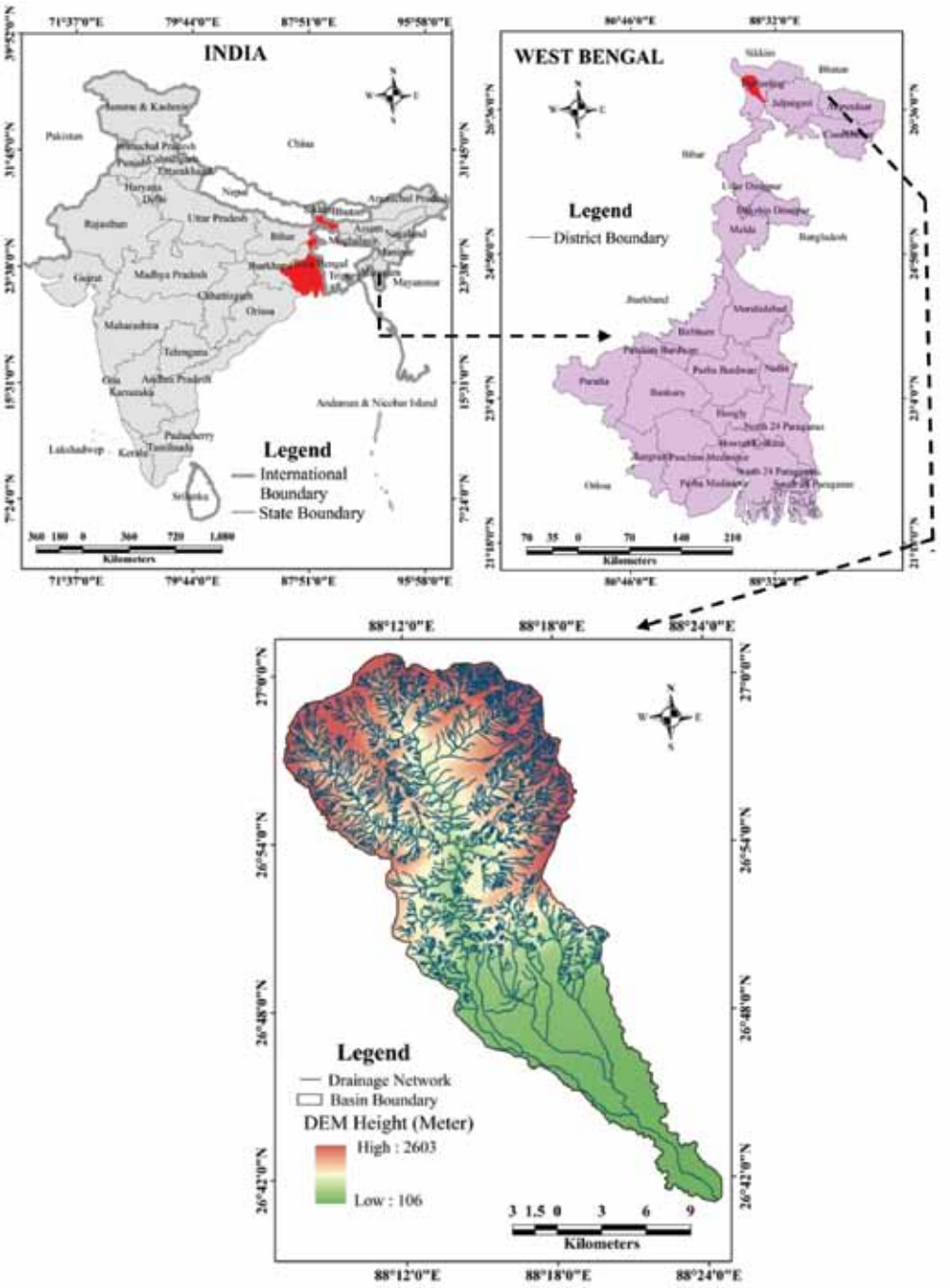

Figure 1. Location map of the study area.

Apart from these studies, Patel et al. (2013) carried out a case study to select suitable sites for water harvesting structures in Varekhadi watershed, a part of Lower Tapi Basin (LTB), Surat district, Gujarat by overlaying of Shuttle Radar Topography Mission DEM, soil map and slope map using RS and GIS approach. Chirala et al. (2015) worked on Meghadrigedda catchment in Visakhapatnam, India for mapping of soil erosion zones using RS and GIS techniques.

The present study focuses on sub-watersheds wise slope instability analysis and prioritization based on the 13 morphometric parameters of the Balason river basin, Darjeeling Himalaya, West Bengal (India), using RS and GIS techniques. Prioritization rating of 18 sub-watersheds is carried out through compound ranking method. The sub-watershed with the lowest rank is given the highest priority in terms of erosion and suggested for conservation measures urgently.

Table 1. Empirical formula for calculating of morphometric parameters

Sl. No.	Morphometric Parameters	Types/ Aspects	Methods/ Formulae	References	Units	Results
1	Bifurcation Ratio (Rb)	Linear aspect	Rb =Nu/Nu+1 Nu= Total number of stream segment of order 'u', Nu+1= Number of stream segment of next higher order	Schumm, 1956	Unit less	1.6-4.103
2	Length of Overland Flow (Lof)	Linear aspect	Lof= 1/2Dd Dd= Drainage density	Horton, 1945	Km/sq.km	0.069-0.857
3	Drainage Density (Dd)	Areal aspect	Dd= L/A L= Total length of streams, A= Area of watershed	Horton, 1945	Km/sq.km	0.583-7.207
4	Stream Frequency (Fs)	Areal aspect	Fs= N/A N= Total number of streams, A= Area of watershed	Horton, 1945	No. of stream/ sq.km	0.069-29.447
5	Texture Ratio (Rt)	Areal aspect	Rt= N1/P N1=Total number of first order streams, P= Perimeter of watershed	Horton, 1945, Schumm, 1956	No. of first order stream/km	0-16.958
6	Drainage Texture (Td)	Areal aspect	Td= Nu/P Nu= Total number of streams, P= Perimeter of watershed	Horton, 1945	No. of stream/km	0.069-23.158
7	Compactness Coefficient (Cc)	Areal aspect	Cc= 0.2841*P/$A^{0.5}$ P= Perimeter of watershed, A= Area of watershed	Gravelius, 1914	Unit less	1.198-2.156
8	Constant of Channel Maintenance (Ccm)	Areal aspect	Ccm= 1/Dd Dd= Drainage density	Horton, 1945	Sq. km/km	0.139-18.714
9	Shape Factor/ Basin Shape (Sf)	Areal aspect	Sf= Lb^2/A Lb= Length of watershed, A= Area of watershed	Horton, 1932	Unit less	1.780-5.804
10	Form factor(Ff)	Areal aspect	Ff= A/ Lb^2 A= Area of watershed, Lb= Length of watershed	Horton, 1932	Unit less	0.172-0.562
11	Circulatory ratio(Rc)	Areal aspect	Rc= 4□A/P^2 A= Area of watershed, □=3.14, P= Perimeter of watershed	Miller, 1953	Unit less	0.218-0.707
12	Elongation ratio (Re)	Areal aspect	2√(A/□)/Lb A= Area of watershed, □=3.14, Lb= Length of watershed	Schumm, 1956	Unit less	0.468-0.846
13	Relief Ratio (Rr)	Relief aspect	Rr= Bh/Lb Bh= Basin relief, Lb= Basin length	Schumm, 1956	Enumer-ative	0.023-0.302

STUDY AREA

The Balason river basin which is located in the western part of Darjeeling district, confronted frequent destructive landslide events, was chosen as a study area (Figure 1). The major right bank tributary of the Mahananda River, the Balason River originates from Lepchajagat (2361 m) located on the Ghum-Simana ridge. Balason river basin coversparts of Rangli Rangliot, Naxalbari, Matigara, Jorebunglow Sukiapokhri, Mirik and Kurseong block of Darjeeling district in West Bengal, having an area of 378.45 km^2. It is located in between 26° 40´ N to 27° 01´ N and 88°7´E to 88°25´ E. The main Balason River flows north to south-east having length of about 51.92 km and joins Mahananda River at 26°41´28´´ N and 88°24´15´´ E . The highest and lowest elevations are 2613 m found in southeastern corner and 105 m in Southern part of the basin respectively. About 83% of basin area falls within the slope 0°-30° revealing the activeness of the total erosional agents in its upper reaches. The area having above 30° slope have mostly been deforested and affected by weathering processes. The average rainfall of the basin is 2300 mm (range 2000-5000 mm) which is primarily dependent on southwest monsoon and occurs mostly in the months of June to September. The mean annual temperature is about 20.94°C. The northern upper hill tract and southern alluvial zone have a mean annual temperature of 12°C and 24.70°C respectively (Lama, 2003).

The study area is predominately represented by very shallow to deep soils. A vast portion of the basin is consisted of wide open gently sloping southern alluvial plain. Just immediately north of this rolling plain, a foothill zone is situated which associated with active exogenetic processes and various geological disturbances. Above this zone, comparatively less dissected and lower relative relief but rugged northern highland is located. The river basin is characterized by complex geological formation. The major portion of the basin is consisting of Darjeeling

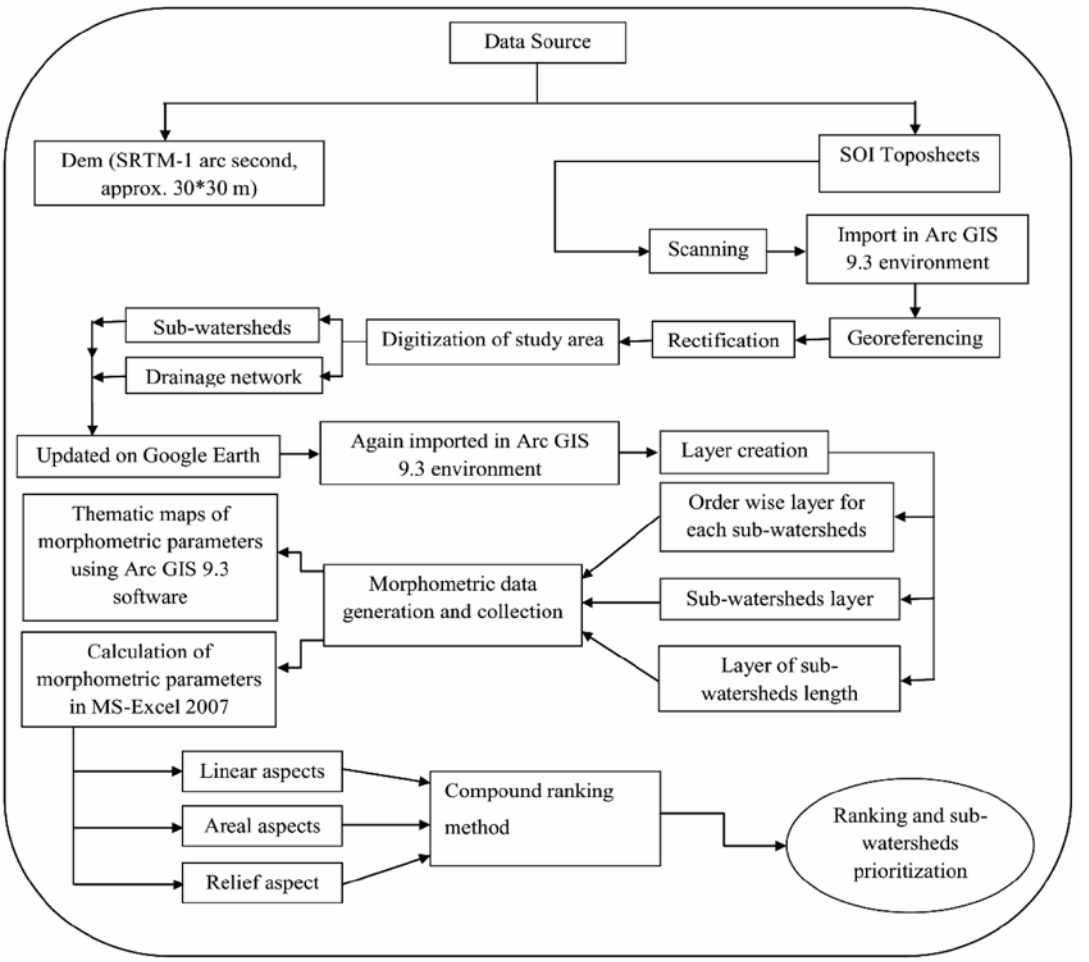

Figure 2. Methodology followed in the present study.

group, Daling series rock type and Permian Damuda series that rests along a thin belt, mostly extending in an E-W direction. The Darjeeling group of metamorphic rocks consists of carbonaceous mica-schists, granetiferous mica-schists, golden-silvery mica schists and coarse grained gneiss of various resistances. These rocks are deeply weathered and having high density of fractures. During rainy season water percolates through the exposed fractures which reduce the cohesive strength of the soil.

METHODOLOGY

The present study is basically based on morphometric analysis of Balason river basin. To assess the morphometric conditions, SRTM Dem (30m resolution), Survey of India (SOI) toposheets and geological maps were used. The drainage network was initially derived from SOI toposheets78A/4, 78A/8, 78B/1, 78B/5 and 78B/6 (Scale 1:50000) and later updated using Google Earth. The sub-watersheds boundaries were demarcated on the basis of slope, elevation, 3D view and drainage flow directions and then the basin was divided into 18 sub-watersheds. To find out the sub-watersheds which are more unstable on the basis of slope instability, two major steps have been considered i.e. morphometric parameters calculation and preparation of spatial data layers and sub-watersheds wise slope instability analysis and prioritization using compound ranking method (Figure 2).

Morphometric parameters calculation and preparation of spatial data layers

The morphometric parameters, such as bifurcation ratio (Rb), length of overland flow (Lof), drainage density (Dd), stream frequency (Fs), texture ratio (Rt), drainage texture (Td), compactness coefficient (Cc), constant of channel maintenance (Ccm), shape factor/ basin shape (Sf), form factor (Ff), circularity ratio (Rc), elongation ratio (Re) and relief ratio (Rr), were computed using standard methods and formulae and prepared data layers in GIS (Table 1).

Table 2. Results of some of the morphometric parameters.

Watershed no.	Basin area(A) in km^2	Basin Perimeter (P) in km	No. of first order stream	Total stream length	Total number of stream	Drainage density in km/ km^2	Drainage frequency in no. of stream/ km^2	Texture ratio in no. of first order stream/km	Drainage texture in no. of stream/km	Constant channel maintenance	Length of overland flow
SW 1	54.21	36.40	442	264.95	592	4.887	10.920	12.143	16.264	0.205	0.102
SW 2	13.28	16.55	82	52.88	110	3.982	8.283	4.955	6.647	0.251	0.126
SW 3	10.47	14.19	117	52.27	155	4.992	14.804	8.245	10.923	0.200	0.100
SW 4	5.69	10.62	94	37.20	131	6.538	23.023	8.851	12.335	0.153	0.076
SW 5	14.84	18.87	320	106.95	437	7.207	29.447	16.958	23.158	0.139	0.069
SW 6	28.96	24.17	264	143.06	373	4.940	12.880	10.923	15.432	0.202	0.101
SW 7	24.44	37.52	138	93.23	186	3.815	7.610	3.678	4.957	0.262	0.131
SW 8	12.79	19.56	138	76.56	191	5.986	14.934	7.055	9.765	0.167	0.084
SW 9	29.86	27.00	431	188.60	597	6.316	19.993	15.963	22.111	0.158	0.079
SW 10	11.25	16.77	60	39.31	84	3.494	7.467	3.578	5.009	0.286	0.143
SW 11	20.50	25.63	109	74.34	152	3.626	7.415	4.253	5.931	0.276	0.138
SW 12	7.69	11.69	43	28.04	59	3.646	7.672	3.678	5.047	0.274	0.137
SW 13	18.67	29.18	129	64.93	183	3.478	9.802	4.421	6.271	0.288	0.144
SW 14	19.31	18.60	32	37.04	44	1.918	2.279	1.720	2.366	0.521	0.261
SW 15	27.57	29.96	185	100.93	258	3.661	9.358	6.175	8.611	0.273	0.137
SW 16	14.00	19.70	101	53.93	151	3.852	10.786	5.127	7.665	0.260	0.130
SW 17	6.74	12.35	59	28.59	83	4.242	12.315	4.777	6.721	0.236	0.118
SW 18	58.18	57.65	0	33.94	4	0.583	0.069	0.000	0.069	1.714	0.857

Bifurcation ratio (Rb)

Rb is an index of reliefs and dissections (Horton, 1945). It is a dimensionless property that expresses the ratio of the number of streams of a given order to the number of streams of the next higher order (Horton, 1932, 1945; Schumm, 1956). In different environmental condition, as well as different regions, Rb values shows only a little variation, except where very strong geological control dominates (Stahler, 1957) and morphometric control of the basin itself (Singh et al., 1984). Lower Rb values are the results of structurally less disturbed watershed without any distortion in drainage pattern (Javed et al., 2009; Magesh et al., 2012) and are the attributed to the relatively gentle slope (Panda and Nagarajan 2013). In this study, Weighted Mean Bifurcation Ratio (Rbwm) was considered which obtained by multiplying the bifurcation ratio for each successive pair of orders by the total numbers of streams involved in the ratio and taking the mean of the sum of these values.

Length of overland flow (Lof)

Lof is one of the most independent variables affecting both the hydrologic and physiographic development of drainage basin (Sharma and Padmaja, 1982). It refers to the length of the run-of the rainwater on the ground surface, before it localized into definite channels and considered length of overland flow to be about half the distance between stream channels and taken it to be roughly half the reciprocal of the drainage density (Horton, 1945). Length of overland flow is inversely relates with the average channel slope (Patel et al., 2013).

Drainage density (Dd)

It indicates the closeness of spacing between channels (Javed et al., 2009) and is a measure of the stream length per unit area in a region of watershed (Horton, 1932 and 1945; Stahler 1952; Melton, 1958); thus 'Dd' has units of the reciprocal of length (Patel et al., 2013). Structures, relief history (Pareta and Pareta, 2012), resistance to weathering, permeability of rock formation, climate, and vegetation etc. are the important controlling factors of drainage density (Javed et al., 2009). 'Dd' is helpful to study hydrologic response to rainfall events (Melton, 1957; Gupta and Srivastava, 2010), landscape dissection, runoff potential, infiltration capacity, climatic condition and vegetation cover of the basin (Patil and Mali, 2013). Singh (2010) divided drainage density into five categories i.e. (i) very low (ii) low (iii) moderate (iv) high (v) very high.

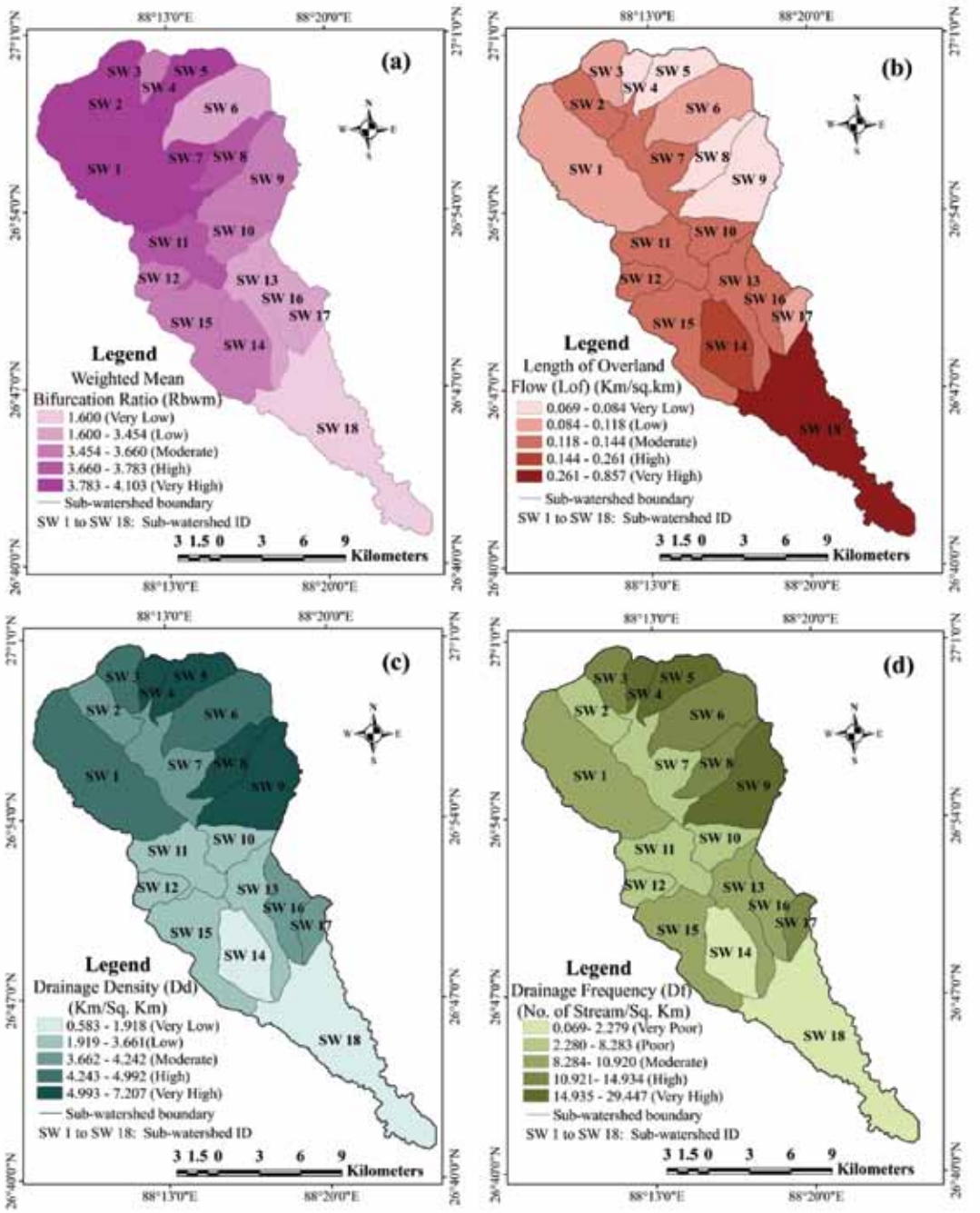

Figure 3. Sub-watershed-wise data layers of (a) weighted mean bifurcation ratio. (b) length of overland flow, (c) drainage density, and (d) drainage frequency.

Stream frequency (Fs)

The word 'stream frequency' introduced by Horton refers to the total number of stream segments of all orders per unit area (Horton, 1932, 1945). It has the positive correlation with 'Dd', indicating the increase in stream frequency with respect to increase density (Javed et al., 2009; Patel et al., 2013; Parveen, 2012). 'Fs' too can be classified into five categories i.e. very poor, poor, moderate, high and very high (Singh 2010).

Texture ratio (Rt)

Texture ratio is an important factor in the drainage morphometric analysis, which depends on the underlying lithology, infiltration capacity and relief aspects of the

Table 3. Calculation table for relative relief and relief ratio

Compactness Coefficient (Cc)	Basin Shape (Sb)	Longest Axis in km	Highest Elevation (m)	Lowest Elevation (m)	Relative Relief (rr)	Relief Ratio (Rr)
1.40	3.28	13.33	2300	580	1720	0.129
1.29	2.83	6.13	2300	1020	1280	0.209
1.25	2.31	4.92	2300	1080	1220	0.248
1.26	2.97	4.11	2320	1080	1240	0.302
1.39	3.47	7.18	2460	940	1520	0.212
1.28	2.94	9.22	2613	820	1793	0.194
2.16	3.43	9.16	1720	540	1180	0.129
1.55	5.56	8.43	2420	660	1760	0.209
1.40	2.84	9.21	2420	540	1880	0.204
1.42	2.95	5.76	2000	520	1480	0.257
1.61	1.78	6.04	1680	400	1280	0.212
1.20	2.55	4.43	1400	420	980	0.221
1.92	5.80	10.41	1920	200	1720	0.165
1.20	3.00	7.61	980	200	780	0.102
1.62	4.01	10.52	1240	200	1040	0.099
1.50	4.94	8.32	1820	220	1600	0.192
1.35	3.97	5.17	1120	220	900	0.174
2.15	5.03	17.10	500	105	395	0.023

terrain and can be defined as the ratio between first order stream streams and perimeter of the basin (Schumm, 1956).

Drainage texture (Td)

Drainage texture is an important geomorphic concept which means that the relative spacing of drainage lines (Smith, 1950). Horton (1945) defined drainage texture as the total number of stream segments of all orders per perimeter of the area. The drainage density and drainage frequency have been collectively defined as drainage texture (Tolessa and Rao, 2013). According to Singh (2010), drainage texture refers to the relative spacing of streams per unit length in grid squares. It depends on the underlying lithology, infiltration capacity and relief aspects of the terrain. Smith (1950) and Singh (2010) classified drainage texture into five different textures i.e. very coarse (<2), coarse (2-4), moderate (4-6), fine (6-8) and very fine (>8).

Compactness coefficient (Cc)

Cc can be defined as the ratio of perimeter of watershed to circumference of circular area, which equals the area of the watershed (Gravelius, 1914) and also known as Gravelius Index (GI). A circular basin will yield the shortest time of concentration before peak flow occurs in the basin, thus it is most hazardous from a drainage point of view (Javed et al., 2009; NookaRatnam et al., 2005). It is dependent only on slope. This parameter is inversely related with the elongation ratio.

Constant of channel maintenance (Ccm)

Constant of channel maintenance is an important property of landforms and it can be defined as the inverse of drainage density (Schumm, 1956). It means that the number of square km or kms of basin surface required developing and sustaining of a channel of 1 km long. According to Strahler (1957) it indicates the relative size of landforms units in a drainage basin and has a specific genetic connotation. The values of Ccm are divided into five classes i.e. very high, high, moderate, low and very low.

Shape factor/ basin shape (Sf)

Sf is the ratio of the square of the basin length to area of the basin (Horton, 1945) and inversely related with form factor. Lower value of Sf reveals peaked flood discharge, while higher value indicates weaker flood discharge periods.

Form factor (Ff)

According to Horton (1932, 1945) form factor may be defined as the ratio of basin area to square of the basin length. For a perfectly circular watershed, the value of form factor would always be less than .754 (Chopra et al., 2005; Javed et al., 2009). Smaller the value of form factor, more elongated will be the basin.

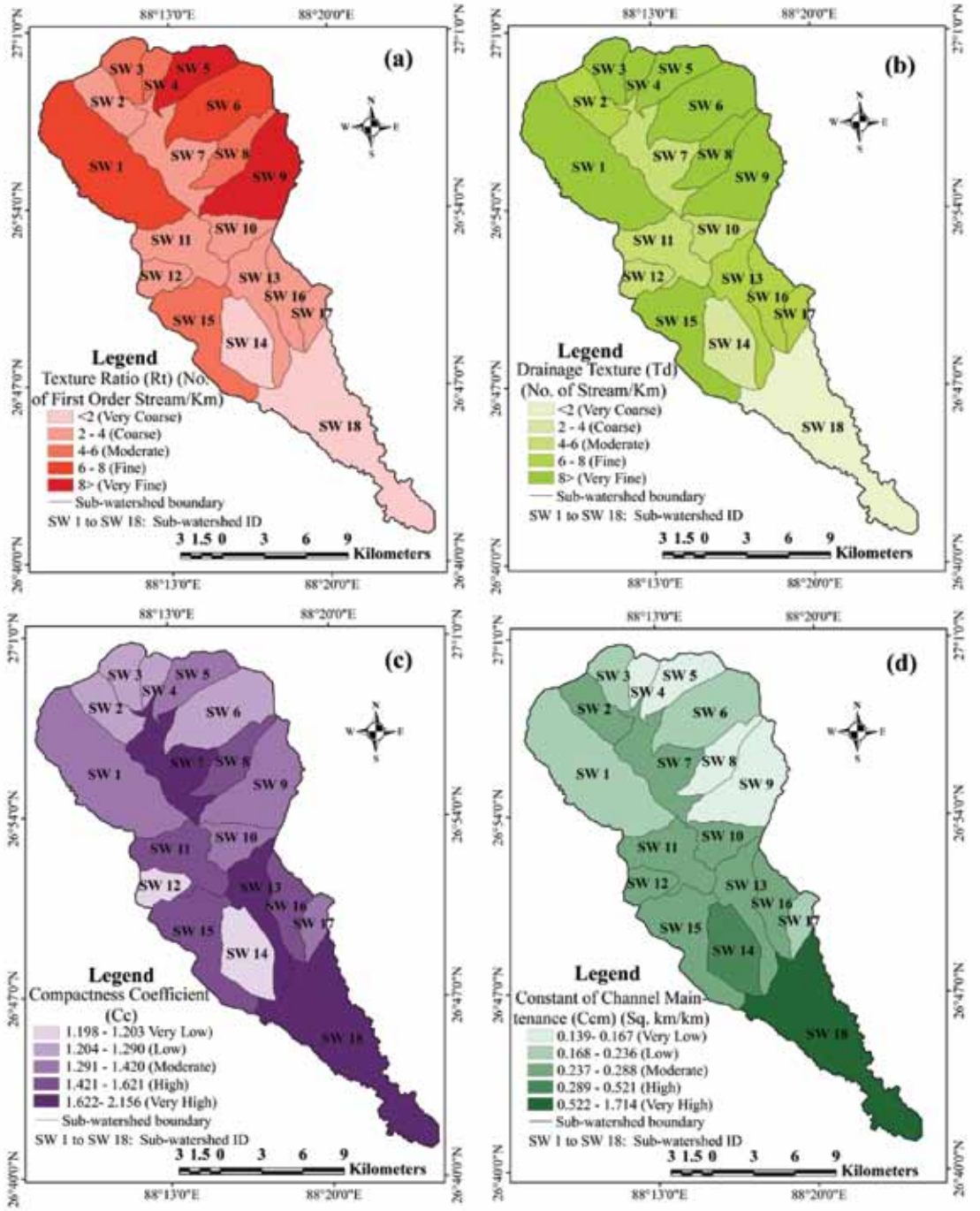

Figure 4. Sub-watershed wise data layers of (a) texture ratio, (b) drainage texture, (c) compactness coefficient, and (d) constant of channel maintenance.

Circularity ratio (Rc)

Quantitative dimensionless circularity ratio is used for the outline form of a watershed (Miller, 1953; Stahler, 1964). It can be defined as the ratio of the area of a basin to the area of a circle, having the same circumference as the perimeter of the basin (Miller, 1953). It depends on the length and frequency of streams, geological structures, land use/land cover, climate and slope of the basin. Rc varies from 0 (a line) to 1 (a circle).

Elongation ratio (Re)

Elongation ratio is defined as the ratio of diameter of a circle of the same area as the basin to the maximum basin length (Schumm, 1956). This ratio runs between 0.6 and

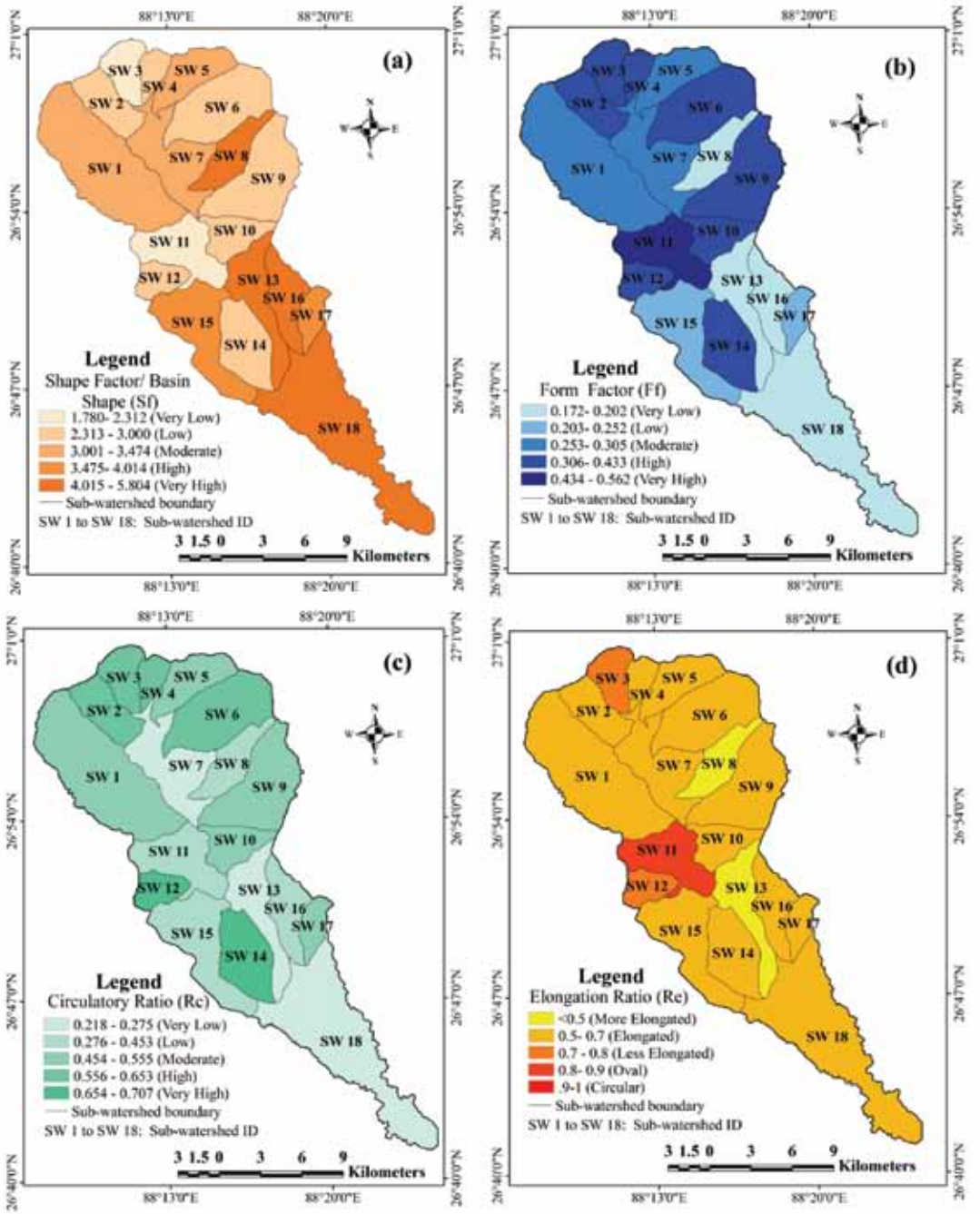

Figure 5. Sub-watershed wise data layers of (a) shape factor, (b) form factor, (c) circulatory ratio, and (d) elongation ratio.

1.0 over a wide variety of climatic and geologic types and it can be classified into five categories i.e. circular (0.9-1.0), oval (0.8-0.9), less elongated (0.7-0.8), elongated (0.5-0.7) and more elongated (<0.5) (Strahler, 1964). The value of Re varies from 0 (highly elongated shape) to 1 (circular shape).

Relief ratio (Rr)

The relief ratio may be defined as the ratio between the total relief of a basin and the longest dimension of the basin parallel to the main drainage line (Schumm, 1956). Total relief is the difference in the elevation between the highest point of a watershed and the lowest point on the valley floor (Pareta and Pareta, 2012).

Sub-watersheds wise slope instability analysis and prioritization using compound ranking method

The morphometric parameters i.e. bifurcation ratio (Rb), drainage density (Dd), stream frequency (Fs), texture ratio

Table 4. Calculation table for form factor, circulatory ratio and elongation ratio

Watershed no.	Area(A) in km^2	Length in km (Lb)	Perimeter (P) in km	Form factor(A/Lb^2)	Circulatory ratio($4\pi A/P^2$)	Elongation ratio $2\sqrt{(A/\pi)}/Lb$
1	54.21	13.33	36.40	0.305	0.514	0.623
2	13.28	6.13	16.55	0.353	0.609	0.671
3	10.47	4.92	14.19	0.433	0.653	0.742
4	5.69	4.11	10.62	0.337	0.634	0.655
5	14.84	7.18	18.87	0.288	0.523	0.605
6	28.96	9.22	24.17	0.341	0.623	0.659
7	24.44	9.16	37.52	0.291	0.218	0.609
8	12.79	8.43	19.56	0.180	0.420	0.479
9	29.86	9.21	27.00	0.352	0.514	0.669
10	11.25	5.76	16.77	0.339	0.502	0.657
11	20.50	6.04	25.63	0.562	0.392	0.846
12	7.69	4.43	11.69	0.392	0.707	0.706
13	18.67	10.41	29.18	0.172	0.275	0.468
14	19.31	7.61	18.60	0.333	0.701	0.652
15	27.57	10.52	29.96	0.249	0.386	0.563
16	14.00	8.32	19.70	0.202	0.453	0.507
17	6.74	5.17	12.35	0.252	0.555	0.567
18	58.18	17.10	57.65	0.199	0.220	0.503

(Rt), drainage texture (Td), length of overland flow (Lof), compactness coefficient (Cc), basin shape/shape factor (Sb), form factor (Ff), circularity ratio (Rc) and elongation ratio (Re) are termed as erosion risk assessment parameters (Biswas et al., 1999). In this study, two extra parameters were added for prioritization of sub-watersheds, i.e. constant of channel maintenance (Ccm) and relief ratio (Rr). The linear aspects like bifurcation ratio and length of overland flow, areal aspects like drainage density, stream frequency, texture ratio, drainage texture and relief aspects like relief ratio, have a direct correlation with erodibility that means higher the value, more is the erodibility or simply instability. Thus for prioritization of 18 sub-watersheds, the highest value was rated as 1, second highest value was rated as 2 and so on, and the lowest value was rated as 18 (Table 5). On the other hand, the areal aspects such as compactness coefficient, constant of channel maintenance, basin shape, form factor, circularity ratio, elongation ratio have an inverse relationship with erodibility, lower the value, more is the erodibility (Nooka Ratnam et al., 2005). Hence the lowest value was rated as 1, next lower value was rated as 2 and so on, and the highest value was rated as 18 (Table 5). After assigning the rank to every single parameter in relation to slope instability, the ranking values of each sub-watershed were summed up for each of the 18 sub-watersheds to arrive at compound score. Based on the compound score, the sub-watersheds having least value was assigned highest priority, next higher value was assigned second highest priority and so on.

RESULT AND DISCUSSION

Linear aspects

The detailed results of linear aspects like weighted mean bifurcatin ratio (Rbwm) and length of overland flow (Lof) is shown in Table 6. The values of Rbwm was used to classify the watershed into five categories i.e. very low, low, moderate, high and very high. SW 1, SW 2, SW 3, SW 5, and SW 7, are dominated by very high Rbwm value ranging from 3.78-4.10 due to low permeability and the presence of joints/fractures, observed in the exposed rocks helping first order streams, while SW 18 registered with very low Rbwm of 1.60, indicating less disturbed watersheds (Figure 3a). Low value of Lof indicates the basin was structurally complex and vice versa (Table 2). The calculated values of Lof are classified into five classes i.e. very high, high, moderate, low and very low. Very high (0.262 - 0.857) and very low (0.069 - 0.084) Lof were found for SW 18 and SW 4, SW 5, SW 8, SW9 respectively (Figure 3b).

Areal aspects

The results of areal aspects like drainage density (Dd), drainage frequency (Fs), texture ratio (Rt), drainage texture (Td), compactness coefficient (Cc), constant of channel maintenance (Ccm), shape factor (Sf), form factor (Ff), circularity ratio (Rc) and elongation ratio (Re) were given in Table 6. Dd in all the sub-watersheds range from 0.58

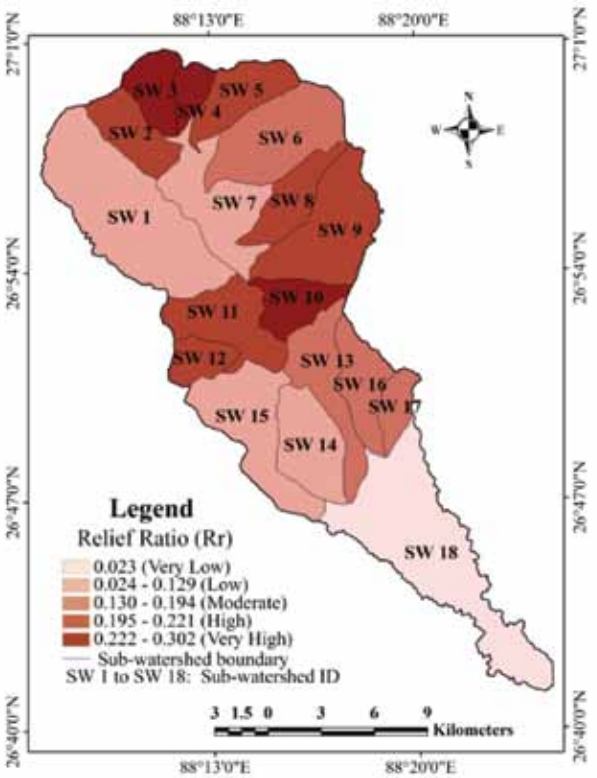

Figure 6. Sub-watershed-wise data layer of relief ratio.

Table 5. Logic behind ranking of 18 sub-watersheds in relation to slope instability, based on morphometric parameters

Morphometric parameters	Rank at 18 point scale	Logic applied
Bifurcation Ratio (Rb)	1 rank to sub-watershed which has the highest Bifurcation Ratio	Higher the Bifurcation Ratio value greater the slope instability
Length of Overland Flow (Lof)	1 rank at the highest Length of Overland Flow	Higher the Length of Overland value, the sub-watershed become more instable
Drainage Density (Dd)	1 rank at the sub-watershed having highest Drainage Density	The sub-watershed become more instable where the Drainage Density value is maximum
Stream Frequency (Fs)	1 rank at the highest Stream Frequency	Higher Stream Frequency value leads more instability
Texture Ratio (Rt)	1 rank at the maximum Texture Ratio	Texture Ratio value directly related to slope instability
Drainage Texture (Td)	1 rank at the largest drainage texture	Slope become More instable where Drainage Texture value is higher
Compactness Coefficient (Cc)	1 rank at the lowest Compactness Coefficient	Slope instability is negatively correlated with Compactness Coefficient value
Constant of Channel Maintenance (Ccm)	1 rank at the lowest Constant of Channel Maintenance	Higher the Constant of Channel Maintenance value lower the slope instability
Shape Factor/ Basin Shape (Sf)	1 rank at the lowest Shape Factor	Higher Shape Factor value represents lesser slope instability
Form Factor (Ff)	1 rank at the lowest Form Factor	Slope instability is more in lesser Form Factor value area.
Circularity Ratio (Rc)	1 rank at the lowest Circularity Ratio	Basin Circularity Ratio value negatively related to slope instability
Elongation Ratio (Re)	1 rank at the lowest elongation ratio	Lower the value of elongation ratio indicates greater slope instability
Relief Ratio (Rr)	1 rank at the highest Relief Ratio	Higher value indicates more slope instability

Table 6. Morphometric parameter wise sub-watersheds that fall in different categories

Parameters	Sub-Watersheds fall in different category				
	Very Low	Low	Moderate	High	Very High
Drainage Density	SW 14, SW 18	SW 10, SW 11, SW 12, SW 15	SW 2, SW 7, SW 16, SW 17	SW 1, SW 3, SW 6	SW 4, SW5, SW8, SW 9
Stream Frequency	SW 14, SW 18	SW 2, SW 7, SW 10, SW 11, SW 12	SW 1, SW 13, SW 15, SW 16	SW 3, SW6, SW8, SW17	SW 4, SW 5, SW 9
Bifurcation Ratio	SW 18	SW 6, SW 13, SW 16, SW 17	SW 4, SW 9, SW 10, SW 12, SW14, SW 15	SW 8, SW 11	SW 1, SW 2, SW 3, SW 5, SW 7
Length of Overland Flow	SW 4, SW 5, SW 8, SW 9	SW 1, SW 3, SW 6, SW 17	SW 2, SW 7, SW 10, SW 11, SW 12, SW 13, SW 15, SW 16	SW 14	SW 18
Constant of Channel Maintenance	SW 4, SW 5, SW 8, SW 9	SW 1, SW 3, SW 6, SW 17	SW 2, SW 7, SW 10, SW 11, SW 12, SW 15, SW 16	SW 14	SW 18
Form Factor	SW 8, SW 13, SW 16, SW 18	SW 15, SW 17	SW 1, SW 5, SW 7	SW 2, SW 3, SW 4, SW 6, SW 9, SW 10, SW 12, SW 14	SW 11
Circularity Ratio	SW 7, SW 13, SW 18	SW 8, SW 11, SW 15, SW 16	SW 1, SW 5, SW 9, SW 10, SW 17	SW 2, SW 3, SW 4, SW 6	SW 12, SW 14
Shape Factor	SW 3, SW 11	SW 2, SW 4, SW 6, SW 9, SW 10, SW 12, SW 14	SW 1, SW 5, SW 7	SW 15, SW 17	SW 8, SW 13, SW 16, SW 18
Compactness Coefficient	SW 12, SW 14	SW 2, SW 3, SW 4, SW 6	SW 1, SW 5, SW 9, SW 10, SW 12, SW 14, SW 17	SW 8, SW 11, SW 15, SW 16	SW 7, SW 13, SW 18
Relief Ratio	SW 18	SW 1, SW 7, SW 14, SW 15	SW 6, SW 13, SW 16, SW 17	SW 2, SW 5, SW 8, SW 9, SW 11, SW 12	SW 3, SW 4, SW 10
	Very Coarse	Coarse	Moderate	Fine	Very Fine
Texture Ratio	SW 14, SW 18	-	SW 7, SW 10, SW 11, SW 12	SW 2, SW 13, SW 15, SW 16	SW 1, SW 3, SW4, SW 5, SW 6, SW 8, SW 9, SW 17
Drainage Texture	SW 18	SW 14	SW 7, SW 10, SW 11, SW 12	SW 2, SW 13, SW 16, SW 17	SW 1, SW 3, SW4, SW 5, SW 6, SW 8, SW 9, SW 15
	More Elongated	Elongated	Less Elongated	Oval	Circular
Elongation Ratio	SW 8, SW 13	SW 1, SW 2, SW 4, SW 5, SW 6, SW 7, SW 9, SW 10, SW 15, SW 16, SW 17, SW 18	SW 3, SW 12	SW 11	-

to 7.21 Km/Sq. km. (Table 2). The low values of Dd are associated with regions, having highly permeable sub-soil materials under dense vegetation cover and low relief while high values of Dd indicate regions of weak or impermeable subsurface materials, sparse vegetation and mountainous relief. In the Balason river basin, very low Dd were found in SW14 and SW18 (0.583 - 1.918) and on the other hand, very high Dd regions were found in SW 4, SW 5, SW 8 and SW 9 (4.993 - 7.207), because of impermeable subsurface materials and high relief (Figure 3c). SW 4, SW 5 and SW 9 (14.935 - 29.447) have very high Fs, because of the presence of ridges on both sides of the valley, high relief resistant/ low conducting sub surface material and indicate large number of stream availability, high runoff value, low infiltration capacity while, very poor was found in SW 14, SW 18 (0.069- 2.279), indicating low relief, highly permeable subsurface material, low runoff value and small number of stream availability (Table 2 and Figure 3d). The Rt were calculated for the 18 sub-watersheds (Table 2) and classified into five classes i.e. very coarse, coarse, moderate, fine and very fine (Figure 4a).Very coarse texture ratio was found in SW 14and SW 18 (<2) indicating permeable subsurface while very fine was in SW 1, SW 3, SW 4, SW 5, SW 6 and SW 9 (>8), representing impermeable subsurface. In the same way, the Td was very coarse in SW 18(<2) revealing permeable surface, while very fine in SW 1, SW 3, SW 4, SW 5, SW 6, SW 8, SW 9 and SW15 (>8), indicating impermeable subsurface material (Table 2 and Figure 4b). Lower value of Cc reveals less erosion while higher value indicates high erosion (Table 3). SW12 and SW 14 are associated with very low Cc (1.198 - 1.203), and on the other hand, SW 7, SW 13, SW 18 were depicted with high

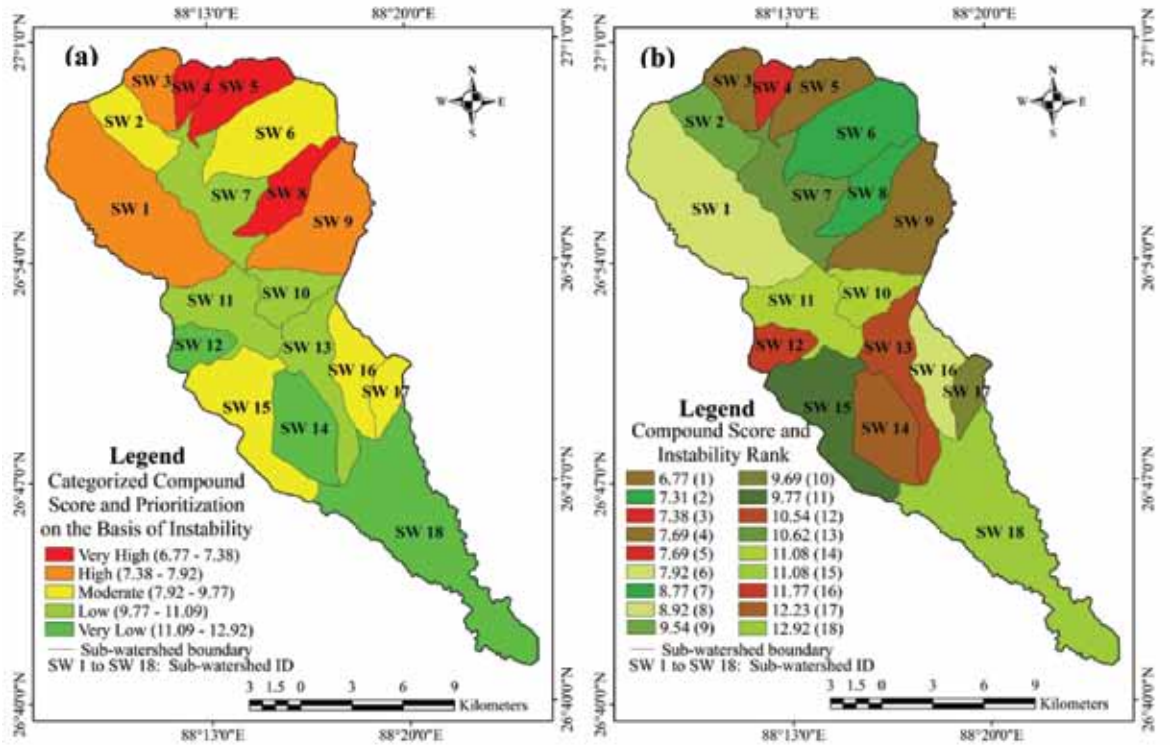

Figure 7. Sub-watershed prioritization. (a) Categorized compound score and prioritization, (b) Individual sub-watershed prioritization.

Table 7. Details of prioritized zones of Balason river basin

Prioritized zone	Sub-basins fall in this category
Very high	SW 4, SW 5, SW 8
High	SW 1, SW 3, SW 9
Moderate	SW 2, SW 6, SW 15, SW 16, SW 17
Low	SW 7, SW 10, SW 11, SW 13
Very low	SW 12, SW 14, SW 18

Cc (1.622- 2.156) (Figure 4c).The lower value of Ccm indicates that the area is under the influence of structural disturbances, having high runoff and low permeability. In this study, the value of Ccm was very high in SW 18 (0.522 - 1.714) and very low in SW4, SW 5, SW 8 and SW 9 (0.139- 0.167) (Table 2 and Figure 4d). SW 3, SW 11 fall in the category of very low Sf (1.780- 2.312) that would indicate peaked flood discharge, while SW 8, SW 13, SW 16 and SW 18 have the very high shape factor (4.015 - 5.804), revealing weaker flood discharge periods (Table 3 and Figure 5a).The watershed with high Ff has high peak flows of shorter duration and vice versa (Table 4). In present study, the Basin was classified into five parts based on form factors i.e. very high, high, moderate, low and very low. Value of form factor obtained very low for watershed SW 8, SW13, SW 16 and SW 18 (0.172- 0.202) while very high for watershed SW 11 (0.434 - 0.562) (Figure 5b).

Based on Rc value, the Balason River basin can be classified into five category i.e. very high, high, moderate, low and very low. If the value was low then the discharge will be slow as compared to the others and so the possibility of erosion will be less. Very high value of Rc was found in SW 12 and SW 14 (0.654 - 0.707), while very low value observed in SW 7, SW 13 and SW 18 (0.218 - 0.275) (Table 4 and Figure 5c). The oval shape sub-watershed was found in SW 11(0.8- 0.9) and more elongated shape in SW8 and SW13 (<0.5) (Table 4 and Figure 5d).

Relief aspects

It measures the overall steepness of the watershed. Low values of Rr indicates lower slope and minimum intensity of erosion process while high value reveals high slope, hilly region and maximum intensity of erosion process (Table 3).

Table 8. Instability rank of Balason river basin, based on composite ranking coefficient value

Watershed Id.	Rbwm	Dd	Fs	Td	Rt	Lof	Rr	Cc	Ccm	Sb	Ff	Rc	Re	Composite score	Compound score	Instability rank
SW 1	4.016 (2)	4.887 (7)	10.92 (8)	16.264 (3)	12.143 (3)	0.102 (12)	0.129 (14)	1.405 (10)	0.205 (7)	3.278 (10)	0.305 (9)	0.514 (9)	0.623 (9)	103	7.92	6
SW 2	4.012 (3)	3.982 (9)	8.283 (12)	6.647 (11)	4.955 (10)	0.126 (10)	0.209 (7)	1.290 (6)	0.251 (9)	2.830 (4)	0.353 (15)	0.609 (13)	0.671 (15)	124	9.54	9
SW 3	4.103 (1)	4.992 (5)	14.804 (5)	10.923 (6)	8.245 (6)	0.100 (14)	0.248 (3)	1.246 (3)	0.200 (5)	2.312 (2)	0.433 (17)	0.653 (16)	0.742 (17)	100	7.69	4
SW 4	3.532 (13)	6.538 (2)	23.023 (2)	12.335 (5)	8.851 (5)	0.076 (17)	0.302 (1)	1.265 (4)	0.153 (2)	2.969 (8)	0.337 (11)	0.634 (15)	0.655 (11)	96	7.38	3
SW 5	4.002 (4)	7.207 (1)	29.447 (1)	23.158 (1)	16.958 (1)	0.069 (18)	0.212 (15)	1.392 (8)	0.139 (1)	3.474 (12)	0.288 (7)	0.523 (11)	0.605 (7)	88	6.77	1
SW 6	3.454 (14)	4.94 (6)	12.88 (6)	15.432 (4)	10.923 (4)	0.101 (13)	0.194 (10)	1.276 (5)	0.202 (6)	2.935 (6)	0.341 (13)	0.623 (14)	0.659 (13)	114	8.77	7
SW 7	3.969 (5)	3.815 (11)	7.61 (14)	4.957 (16)	3.678 (14)	0.131 (8)	0.129 (15)	2.156 (18)	0.262 (11)	3.433 (11)	0.291 (8)	0.218 (1)	0.609 (8)	138	10.62	13
SW 8	3.783 (6)	5.986 (4)	14.934 (4)	9.765 (7)	7.055 (7)	0.084 (15)	0.209 (8)	1.554 (13)	0.167 (4)	5.556 (17)	0.180 (2)	0.420 (6)	0.479 (2)	95	7.31	2
SW 9	3.639 (10)	6.316 (3)	19.993 (3)	22.111 (2)	15.963 (2)	0.079 (16)	0.204 (9)	1.404 (9)	0.158 (3)	2.841 (5)	0.352 (14)	0.514 (10)	0.669 (14)	100	7.69	5
SW 10	3.539 (12)	3.494 (15)	7.467 (15)	5.009 (15)	3.578 (16)	0.143 (4)	0.257 (2)	1.420 (11)	0.286 (15)	2.949 (7)	0.339 (12)	0.502 (8)	0.657 (12)	144	11.08	14
SW 11	3.771 (7)	3.626 (14)	7.415 (16)	5.931 (13)	4.253 (13)	0.138 (5)	0.212 (6)	1.608 (14)	0.276 (14)	1.780 (1)	0.562 (18)	0.392 (5)	0.846 (18)	144	11.08	15
SW 12	3.636 (11)	3.646 (13)	7.672 (13)	5.047 (14)	3.678 (15)	0.137 (6)	0.221 (4)	1.198 (1)	0.274 (13)	2.552 (13)	0.392 (16)	0.707 (18)	0.706 (16)	153	11.77	16
SW 13	3.432 (16)	3.478 (16)	9.802 (10)	6.271 (12)	4.421 (12)	0.144 (3)	0.165 (13)	1.919 (16)	0.288 (16)	5.804 (18)	0.172 (1)	0.275 (3)	0.468 (1)	137	10.54	12
SW 14	3.66 (8)	1.918 (17)	2.279 (17)	2.366 (17)	1.72 (17)	0.261 (2)	0.102 (16)	1.203 (2)	0.521 (17)	2.999 (9)	0.333 (10)	0.701 (17)	0.652 (10)	159	12.23	17
SW 15	3.647 (9)	3.661 (12)	9.358 (11)	8.611 (8)	6.175 (8)	0.137 (7)	0.099 (17)	1.621 (15)	0.273 (12)	4.014 (14)	0.249 (5)	0.386 (4)	0.563 (5)	127	9.77	11
SW 16	3.011 (17)	3.852 (10)	10.786 (9)	7.665 (9)	5.127 (9)	0.130 (9)	0.192 (11)	1.496 (12)	0.260 (10)	4.944 (15)	0.202 (4)	0.453 (7)	0.507 (4)	116	8.92	8
SW 17	3.445 (15)	4.242 (8)	12.315 (7)	6.721 (10)	4.777 (11)	0.118 (11)	0.174 (12)	1.351 (7)	0.236 (8)	3.966 (13)	0.252 (6)	0.555 (12)	0.567 (6)	126	9.69	10
SW 18	1.6 (18)	0.583 (18)	0.069 (18)	0.069 (18)	0 (18)	0.857 (1)	0.023 (18)	2.147 (17)	1.714 (18)	5.026 (16)	0.199 (3)	0.220 (2)	0.503 (3)	168	12.92	18

The Rr for watersheds varies from 0.023-0.302. Very low Rr was found in SW 18 and very high Rr for SW 3, SW 4 and SW 10 (Table 6 and Figure 6).

Prioritization of sub-watersheds

On the basis of morphometric analysis, SW 4, SW 5 and SW 8 fall in the high priority zone, while SW 12, SW 14 and SW 18 fall in the very low category (Table 7 and Figure 7a). Sub-watershed wise highest priority obtained by SW 5 followed by SW 8, SW 4, SW3, SW 9, SW 1, SW 6, SW 16, SW 2, SW 17, SW 15, SW 13, SW 7, SW 10, SW 11, SW 12, SW 14, and SW 18 (Table 8 and Figure 7b).

CONCLUSION

Watershed prioritization is considered as one of the most important aspects of planning, development and management programmes for the developing countries like India. The morphometric parameters, evaluated using GIS, have helped to understand the existing geomorphic process, operating within the framework of drainage basin which helps prioritization of watershed development. Balason is a seventh order basin. The 13 morphometric were used for this study. It can realistically be assumed that watersheds which attained low priority for soil conservation, are likely to have a high level of environment quality and hence,

the high priority watersheds should be considered for protection. Therefore, immediate attention towards soil conservation measures is required in these sub-watersheds, to conserve land for future erosion. These sub-watersheds may also be applicable in land use planning, in conservation of biodiversity, natural resources and locating water harvesting structure.

ACKNOWLEDGEMENTS

The authors would like to express their sincere thanks to Survey of India (SOI), Geological Survey of India (GSI) and National Bureau of Soil Survey and Land Use Planning (NBSS& LUP) for providing necessary data, facilities and support during the study period.

Compliance with Ethical Standards

The authors declare that they have no conflict of interest and adhere to copyright norms.

REFERENCES

Ali, U. and Ali, S.A., 2014. Analysis of drainage morphometry and watershed prioritization of Romushi-Sasar catchment, Kashmir Valley, India using Remote Sensing and GIS technology. International Journal of Advance Research 2, 5-23.

Amani, M. and,Safaviyan, A., 2015. Sub-basins prioritization using morphometric analysis- remote sensing technique and GIS-Golestan-Iran. International Letters of Natural Sciences 38, 56-65.

Biswas, S., Sudhakar, S. and Desai, V.R., 1999. Prioritization of sub-watersheds based on morphometric analysis of drainage basin: a remote sensing and GIS approach. Journal of the Indian Society of Remote Sensing 27, 155-166.

Chirala, U., Gurram, M.K. and Nookaratnam, K., 2015. Mapping of soil erosion zones of Meghadrigedda catchment, Visakhapatnam, India for conservation- a geospatial approach. International Journal of Geosciences 6, 326-338.

Chopra, R., Dhiman, R.D. and Sharma, P., 2005. Morphometric analysis of sub-watersheds in Gurdaspur district, Punjab using remote sensing and GIS techniques. J Indian Soc Remote Sens 33, 531-539.

Chorley, R.J., 1969. The drainage basin as the fundamental geomorphic unit. In: Chorley, R.J., (ed) Water, earth and man, Methuen, Londo, pp 77-100.

Gravelius, H., 1914. Grundrifi der gesamtangewcisserkunde; Band I: Flufikunde (compendium of hydrology, Vol. I. Rivers, in German), Goschen, Berlin, Germany.

Gupta, M. and Srivastava, P.K., 2010. Integrating GIS and Remote Sensing for identification of ground water potential zones in the hilly terrain of Pavagarh, Gujrat, India. Water International 35, 233-245.

Horton, R.E., 1932. Drainage basin characteristics. American Geophysical Union 13, 350-361.

Horton, R.E., 1945. Erosional development of streams and their drainage basins, a hydrophysical approach to quantitative morphology. Geological Society of American Bulletin 56, 275-370.

Javed, A., Khanday, M.Y. and Ahmed, R., 2009. Prioritization of sub-watersheds based on morphometric and land use analysis using RS and GIS technology. J. Indian Soc. Remote Sensing 37, 261-274.

Javed, A., Khanday, M.Y. and Rais, S., 2011. Watersheds prioritization using morphometric and land use/land cover parameters: a remote sensing and GIS based approach. Journal Geological Society of India 78, 63-75.

Lama, I. L., 2003. Study of the Environmental Geomorphology in the Balason Basin. Unpublished Ph. D Thesis, North Bengal University, pp 24-28.

Magesh, N.S., Jitheshlal, K.V., Chandrasekar, N. and Jini, K.V., 2012. GIS based morphometric evaluation of Chimmini and Mupily watersheds, parts of Western Ghats, Thrissur District, Kerala, India. Earth Sci Inform, 5(2), 111–121.

Melton, M.A., 1957. An analysis of the relations among the elements of climate, surface properties and geomorphology. Technical report 11, New York: Department of Geology, Columbia University.

Melton, M.A., 1958. Correlations structure of morphometric properties of drainage systems and their controlling agents. Journal of Geology 66, 442-460.

Miller, V.C., 1953. A quantitative geomorphic study of drainage basin characteristics in the Clinch mountain area, Virginia and Tennessee. Deptt.of Geology, Columbia University, contract N6 ONR 271-30, technical report 3 1-30.

Nautiyal, M.D., 1994. Morphometric analysis of a drainage basin, district Dehradun, Uttar Pradesh. J Indian Soc Remote Sens. 22(4), 251–261.

NookaRatnam, K., Srivastava, Y.K., VenkateshwaraRao, V., Amminedu, E. and Murthy, K.S.R., 2005, Check dam positioning by prioritization of micro-watersheds using SYI model and morphometric analysis- Remote sensing and GIS perspective. Jour. Indian Soc. Remote Sensing 33, 25-38.

Panda, R.K, and Nagarajan, R., 2013. Prioritization of sub-basins of Ghataprabhariver using morphometric parameters. International Journal of Geomatics and Geosciences 3, 605-617.

Panhalkar, S.S. and Pawar, C.T., 2011. Watershed development prioritization by applying WERM model and GIS technique in Vedganga basin (India). ARPN Journal of Agriculture and Biological Science, 38-44.

Pareta, K. and Pareta, U., 2012. Quantitative morphometric analysis of a watershed of Yamuna basin, India using ASTER (DEM) data and GIS. International Journal of Geomatics and Geosciences 2, 248-269.

Parveen, R., Kumar, U. and Singh, V.K., 2012. Geomorphic characterization of upper south Koel basin, Jharkhand: a

remote sensing and GIS approach. Journal of Water Resource and Protection 4, 1042-1050.

Patel, D.P., Gajjar, C.A. and Srivastava, P.K., 2013. Prioritization of Malesari mini-watersheds through morphometric analysis: a remote sensing and GIS perspective. Environ Earth Sci. 69, 2643-2656.

Patil, V.S.P. and Mali, S.P., 2013. Watershed characterization and prioritization of Tulsi sub-watershed: a geospatial approach. International Journal of Innovative Research in Science, engineering and Technology 2, 2182-2189.

Rekha, V.B., George, A.V. and Rita, M., 2011. Morphometric analysis and micro-watersheds prioritization of Peruvanthanam sub-watershed, the Manimala river basin, Kerala, South India. Environmental Research, Engineering and Management 3, 6-14.

Schumm, S.A., 1956. Evaluation of Drainage System and Slopes in Badlands at Perth Amboy, New Jersey. Geological Society of America Bulletin 67, 597-646, http://dx.doi.org/10.1130/0016-7606(1956)67[597:EODSAS]2.0.CO;2).

Sharma, H. and Padmaja, G., 1982. Quantitative fluvial characteristics of streams of the Mej basin (Rajasthan). In: Sharma, H.S., (ed) Perspectives in geomorphology, quantitative fluvial geomorphology, Concept, New Delhi, pp 143-190.

Shrimali, S.S., Agarwal, S.P. and Samra, J.S., 2011. Prioritization erosion prone areas in hills using remote sensing and GIS: a case study of Sukhna lake catchment, North India. Journal of Applied geology 3, 54-60.

Singh, S., Ojha, S.S. and Agnihotri, S.P., 1984. On the regional variations in bifurcations ratios. In: Mukhopadhayay, S.C., (ed) Geographical Mosaic, Calcutta University, pp 203-210.

Singh, S., 2010. Geomorphology. Prayag Pustak Bhawan, Allahabad, pp 371-374.

Smith, K. G., 1950. Standards of grading texture of erosional topography. Am. Jour. Sci. 248, 655-668.

Srivastava, P.K., Mukherjee, S., Gupta, S. and Singh, S.K., 2011. Characterizing monsoonal variation on water quality index of river Mahi in India using geographical information system. Water Quality: Exposure and Health 2, 193-203.

Strahler, A.N., 1952. Hypsometric (area-altitude) analysis of erosional topography. Geological Society of American Bulletin 63, 117-142.

Stahler, A.N., 1957. Quantitative analysis of watershed geomorphology. Trans. Am.Geophys. Union 38, 913-920.

Strahler, A.N., 1964. Quantitative geomorphology of drainage basins and channel networks. In: Chow, V.T., (ed) Handbook of Applied Hydrology, Section 4-11, McGraw Hill Book Company, New York.

Tolessa, G.A. and Rao, P.J., 2013. Watershed development prioritization of Tandava river basin, Andhra Pradesh, India-GIS approach. International Journal of Engineering Science Invention 2, 12-20.

Vandana, M., 2012. Morphometric analysis and watershed prioritization: a case study of Kabani river basin, Wayanad district, Kerala, India. Indian Journal of Geo-Marine Sciences 42, 211-222.

Received on: 28.7.18; Revised on: 22.10.18; Accepted on: 1.11.18

J. Ind. Geophys. Union (January 2019)
v.23, no.1, pp: 101-105

TECHNICAL NOTE

OMNI (Ocean Moored buoy Network for northern Indian Ocean) Buoy System—a critical component of ocean observational programme of ESSO (Earth System Science Organization), Ministry of Earth Sciences, Government of India

Raja Acharya* and Suman Chattopadhyay

India Meteorological Department, Regional Meteorological Centre, Ministry of Earth Sciences, 4, Duel Avenue, Alipore, Kolkata-700027

*Corresponding Author: raja.acharya2011@gmail.com

ABSTRACT

The NIOT (National Institute of Ocean Technology) Chennai deployed moored bouys attached with sensors to collect subsurface oceanographic parameters on real time basis at selected locations in Eastern Arabian Sea and Bay of Bengal and named it as the OMNI (Ocean Moored Bouy Network for Northern Indian Ocean) bouy system. This paper presents the usefulness of OMNI Bouy programme, in terms of technical advancements and met-ocean data quality and future strategies related to the programme.

Keywords: OMNI Bouy, Ocean Observational programme, ESSO

INTRODUCTION

The National Institute of Ocean Technology (NIOT), Chennai, the nodal agency for ocean technology, deployed instrumented moored buoys in Eastern Arabian Sea and selected locations of the Bay of Bengal since 1997, to provide continuous time-series measurements of surface meteorological and oceanographic parameters at such locations. In the recent years, several studies have shown the important role of variability of heat storage in the near-surface layers on the intra-seasonal and inter-annual evolution of monsoons and cyclones. Hence, a strong need was felt to augment some of these buoys with subsurface temperature, salinity and current sensors to continuously record the temporal evolution of their vertical structures. Under a new initiative, NIOT has deployed six moored buoys, attached with sensors, to collect subsurface oceanographic parameters on real-time basis in at selected locations. These are coded as the OMNI (Ocean Moored buoy Network for Northern Indian Ocean) buoy system. The OMNI buoys are Moored Buoy Network in Northern Indian Ocean having the capability to Measure Ocean current, conductivity and temperature up to 500 m depth and transmit hourly data through satellite. Moreover, these buoys are also equipped with radiation sensors and rain gauges too (Venkatesan et al., 2013).

SIGNIFICANCE

The primary objective of this mooring is to understand the complex near surface thermohaline structure in the northern Bay of Bengal and understand the phenomenon of the mean seasonal cycle of the Indian monsoon, the intra-seasonal to intra-decadal oscillations of air–sea interactions, trends that are related to tropical cyclones and the annual cycle balance in the exchange of waters between the two limbs of North Indian Ocean, i.e. the Arabian Sea and the Bay of Bengal.

SYSTEM DESCRIPTION

The moored bouys are floating platforms, which consist of discuss shaped bouys, 3 m in diameter, with an aluminium instrument vessel to which sensors are attached for measuring meteorological parameters. These bouys are equipped with GPS, beacon light and satellite transceiver. The OMNI bouys are powered by lithium batteries and equipped with data acquisition and processing unit. The sensors are programmed to acquire data samples of specific duration of time and frequency. The performance of the data bouy depends upon the type of bouy, location and the water depth. The data bouy carries out sampling process for 30 minutes and at the end of sampling, the averaged data are transmitted to NIOT (National Institute of Ocean Technology) Chennai, every 3 hours, via IMMARSAT satellite telemetry (Venkatesan et al., 2013). The data is placed in the global telecommunication system for weather and forecasting purposes. The data are disseminated to ESSO INCOIS (Indian National Centre for Ocean Information Services) after necessary quality control checks.

Table 1. Details of sensors used for measuring the aforesaid parameters in OMNI bouy system.

Parameter	Sensor Type	Resolution	Accuracy	Range	Data Recorded
Wind Speed	Cup Anaemometer	01.m/s	±2%	0–35 m/s	1 h
Wind Direction	Vane+flux gate compass	0.1°	1.5– 4° ±	0–359° –30–	1 h
Air temperature	Pt/100 RTD	0.0015°C	0.3°C	70°C	1 h
Relative humidity	Capacitance	0.47	± 1%	0–100% RH	1 h
Air pressure	Pressure transducer	0.01 hPa	± 0.15 hPa	500–1100 hPa	1 h
Rainfall	Capacitance	0.058		0–50 mm	2min
Downwelling long-Wave radiation	Pyrgeometer	1.27 W/m2	± 1 mm 5%	0–700 W/m2	1h
Downwelling Short wave radiation	Pyranometer	0.488 W/m2	3%	0–2800 W/m2	1h
Water temperature	Thermistor	T: 0.0001°C	0.002°C	–5–35°C	1h
Conductivity	Conductivity cell	C: 0.0001mS/cm	0.002°C	0–70 mS/cm	1h
Water pressure	Strain gauge	P: 0.002%	0.003mS/cm	0–70 mS/cm	1h
Directional wave Spectra	Accelerometer, angular ratesensor, magnetometer	Pitch and roll: < 0.001°	Heave: 5 cm pitch and roll: 0.05° Heading: 1.2°	Heave: ± 50 m Heading: ± 180°	1h
Ocean current Profile	Accoustic Doppler Current Profiler	Velocity: 0.1 cm/s Dir: 0.01°	Velocity :± 5 mm/s Dir: ± 2°	0–256 cm/s	1h
Single point	Doppler Volume Sampler	Velocity: 0.1 cm/s Dir: 0.01°	Velocity 1% Dir: ± 2°	0–600 cm/s	1h

(Source: Venkatesan et al., 2013)

The meteorological sensors

They are assembled and fitted on the top of the bouy assembly. The meteorological sensors fixed on the sensor arm include air temperature, relative humidity, wind speed and direction at 3 m amsl. The Radiation and rainfall sensors are placed on the sensor arm at 2 m and 1m amsl respectively. The surface temperature and conductivity (to yield salinity) are measured from the bouy at a nominal depth of 1m. Subsurface CT (conductivity temperature) sensors are mounted on the inductive cable of the mooring system to measure temperature and conductivity at 10 different levels. The Accoustic Doppler Current Profiler (ADCP) is attached to the inline mooring for measuring subsurface currents. The depth at which the moorings are anchored to the seabed is 5000 m. (http://www.incois.gov.in/documents/ITCOocean/Suprit_MBD.pdf).The bouy system rely on lithium battery, using compact low power satellite communication system.

Parameters measured by OMNI Bouy system

The OMNI Bouys (Figure 1) measure the following meteorological and oceanographic parameters:

***Surface meteorological*:** Wind speed and direction, air temperature, air pressure, humidity, short wave radiation, incoming long wave radiation and precipitation.

Surface Ocean parameters: Sea surface temperature, conductivity, wave, current speed and direction

Sub surface parameters: Temperature and salinity at depths starting from 5 m, 10 m, 15 m, 20 m, 30 m, 50 m, 75 m, 100 m, 200 m and 500 m. Currents at the depth levels of 10 m, 20 m, 30 m, 50 m and 100 m. Details of sensors and measuring parameters are given in Table 1**.**

OMNI BOUY SYSTEM STRUCTURE

The OMNI Bouy consists of the upper mast fitted with to the top of the bouy assembly, to which various meteorological sensors are attached and the antennas are mounted. A keel with counterweight is mounted under the hull to prevent capsizing of the buoy. The instrumentation cylinder is attached in the middle of the buoy hull which contains all electronic modules, the power package and the wave sensors. There are 3 sections of the OMNI Bouy Structure (https://www.niot.res.in/uploads/Mooring%20 Design.pdf):

Figure 1. OMNI (Ocean Moored buoy Network for northern Indian Ocean) Buoy System (https://www.niot.res.in/index.php/node/index/129/

Upper section

The Upper section has an alloy long link chain and an induction cable of about 16 mm diameter and 500 m length and the sub – surface sensors are attached in it. The link chain of 5 m in length is connected at the keel frame. Diameter of the chain is about 19 mm. It also has to absorb the rotational energy of the mooring, induced by the buoy rotating around its axis. The link chain ends at the Accoustic Doppler Current Profiler (ADCP) frame and the inductive cable is attached to the ADCP frame and extends up to the nylone rope below.The inductive cable has a diameter of 16 mm and has a maximum breaking load of 9000 kg. This section is designed to protect the mooring from fish bite and to enable the safe deployment and retrieval of the buoys.

Middle Section

The Middle section has a nylon rope, having diameter 18 mm, Length 500 m, depths below 2500 m , 750 m and above 2500 m. This section gives S–shape to the mooring. During high current, the nylon rope stretches and keeps the buoy always surfaced. The length of the nylon rope is chosen carefully to provide sufficient stretch to the mooring line. The maximum breaking load of the nylon rope is 5500 kg and it can stretch to about 20% of its initial length, when stretched to its working load limit. The nylone rope is fitted to the trawl floats, which help to keep the mooring in position.

Lower Section

This section consists of a polypropylene rope of 18 mm diameter and 4000 m in length, besides an anchor chain of 16 mm diameter and 1m in length .The polypropylene rope has a working load limit of 5500 kg. The polypropylene rope can stretch upto 15% of its original length. The ground chain connects the polypropylene rope with the sinker having weight of 1900 kg. In order to avoid the rubbing of chain with the sinker weight, subsurface floats consisting of 3 glass spheres with net buoyancy 25.4 kg, are mounted on the link chain with shackles that keeps the chain in upright position. The sinker weight and the drag anchor of the mooring, keeps the buoy in its position. The acoustic release is used for the recovery of bouy system. The release will hold onto the anchor of a buoy system until it is commanded to release it by signal from ships etc. An acoustic release has the ability to both receive and transmit signals to a surface instrument.

TECHNICAL ADVANCEMENTS AND DATA UTILITY

The sensors used in the OMNI Bouys have been selected based on performance history of similar systems at sea and due recommendations of an national expert committee comprising of eminent meteorologists and ocean scientists. The sensor is chosen on the basis of its withstanding hostile weather conditions and data stability. High correlation has been observed during inter-comparsion of conductivity and temperature data of OMNI Bouy with insitu, ship based measurement (**Mathew et al., 2016**).The analysis of OMNI bouy data have contributed in better prediction of monsoons and cyclones in the Bay of Bengal (**Venkatesan et al., 2014**). Moreover, data collected from the OMNI Bouy system are utilized in the validation of remote sensing data. Validation of retrieved and corrected SST(K-SST) from Kalpana satellite has been carried out, using near simultaneous observations of NIOT moored bouy data in E. Arabian sea and Bay of Bengal regions. A significant improvement in Root Mean Square Deviation (RMSD) of K-SST with respect to buoy (1.50–1.02 K),

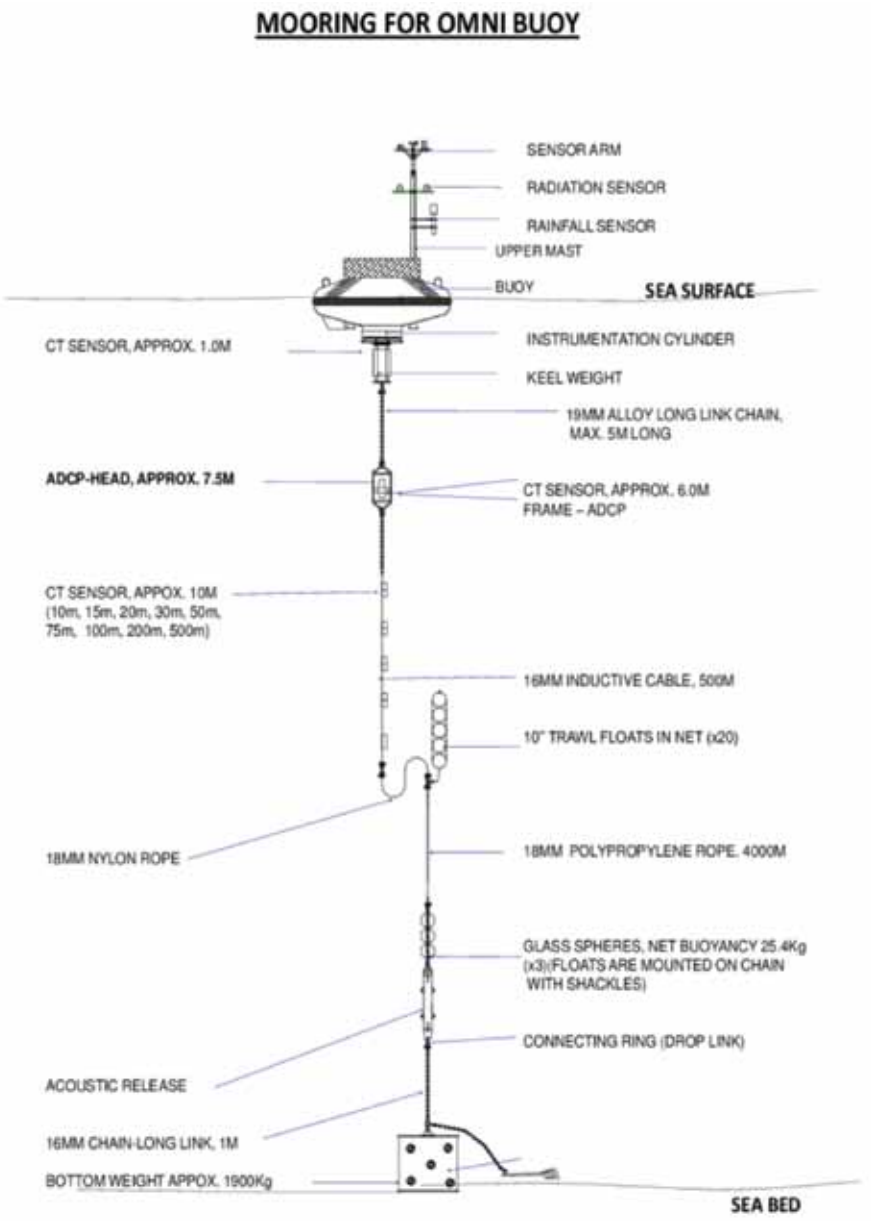

Figure 2. Mooring Configuration of the OMNI Bouy System (**Venkatesan et al., 2013**).

has been observed with the use of near real-time water vapour fields of TMI (**Shahi et al., 2011**).Data from NIOT moored data bouy are also used in the validation of Ocean Generation Circulation Model (OGCM) and Coupled Ocean Atmospheric Model (Thompson et al., 2008). The bouy data available on surface waves and currents can be effectively used for optimum ship routing to save time and fuel costs. Specially designed mooring system with induction mooring cable, acoustic release and anchors are used to keep the system in position in deep sea bed, as mentioned before. The huge voluminous data generated through OMNI Bouy network require proper data management and to overcome the manual mode of data management quality control, Advanced Data Reception and Analysis System(ADDRESS), has further been been developed, specially for data inventory, cruise and operations management(Venkatesan et al., 2015a).

LIMITATIONS

Maintenance of the OMNI bouy system is expensive, specially in view of the challenges posed by increase in vandalism and piracy in Arabian Sea and Bay of Bengal. The availability of ship time according to planned schedule, is another challenge to maintain the bouy network for its optimum performance. Uninterrupted data transmission

through satellites is another challenge. To overcome the problems of data reliability caused due to sensor fouling, anti fouling paint/anti foulant device is applied to bouycomponent (Venkatesan et al., 2015b).

FUTURE STRATEGIES

Permanent maritime security arrangements to be considered on prority basis to address the problem of vandalism and privacy. Specialised ships with deep sea mooring capabilities are required for retrieval and deployment operations to ensure high standard of bouy data quality (Venkatesan et al., 2016). There is a growing interest in continous multidisciplinary observations of oceans from regional scale to global scale and thus, bio-geochemical sensors and bio-optical sensors are highly needed. Bio-geochemical sensors are needed to monitor causes and effects of global climate change and ocean's capabaility to act as a sink for CO_2 and other green house gases and heat. Bio-optical sensors are required for measuring parameters to indicate occurrence of water turbidity, harmful algal booms and near surface trapping of heat. The O-SCOPE (Ocean Systems for Chemical, Optical and Physical Experiment) project sponsored by the NOPP (National Oceanographic Partnership Program), USA have taken a leading role in development and testing of advanced interdisciplinary ocean sensors (Dickey and Moore, 2003).The Ocean Obseving System (OOS) is presently collaborating with ESSO-NCAOR (National Centre for Antarctic and Ocean Research) in the design and deployment of surface and subsurface mooring systems in the southern Indian ocean, to collect data on various parameters such as ocean currents, temperature, partial pressure of CO_2 gas dissolved in water, dissolved oxygen etc to measure the quantity of sinking particulate organic material (Venkatesan et al., 2016).

CONCLUSIONS

The longstanding need for comprehensive and continous measurements on surface met. Ocean parameters along with subsurface ocean measurements have been fulfilled with the deployment of OMNI Bouy Network. These bouy data are assimilated into models by various operational forecasting agencies all over the world, leading to improved forecasts. Moreover, the moored bouy data are used to validate the performance of ocean atmospheric and coupled models and provide various measurement of ocean surface parameters viz SST, wave height etc. to validate satellite measurements and numerical model outputs.

ACKNOWLEDGEMENTS

This technical note has been compiled using internet and other sources basically to propagate the importance of OMNI Bouy network systems. We unequivocally state that the technical details given above have not been developed by us either directly or indirectly. We are grateful to the Ministry of Earth Sciences, Govt of India and NIOT for introducing this state of art Bouy technology and placing various resources relating to the same online. We are thankful to the Dy. Director General of Meteorology, Regional Meteorological Centre, and Kolkata for encouragement for preparing this note. We are also grateful to the Chief Editor of JIGU, for editing and publishing this technical note. The views expressed in the article are solely the views of ours and not our employing organisation and our employing organisation has no financial liability in the matter.

Compliance with Ethical Standards

The authors declare that they have no conflict of interest and adhere to copyright norms.

REFERENCES

Dickey, T. and Moore, C., 2003. New sensors monitor bio-optical/ bio geochemical ocean changes. Sea Tech, 44, 17-24.

Mathew, S., Shamji, V.R., Vengatesan, G., ArulMuthiah, M. and Venkatesan, R., 2016. Systematic Validation of conductivity and Temperature from Ocean Moored Bouy data in northern India Ocean with *insitu* ship based measurement. Indian .J.Geo-marine Sci., 45(2), 224-229.

Shahi, N.R., Agarwal, N., Mathur, A.K. and Abhijit Sarkar, A., 2011.Atmospheric correction from sea surface temperature retrieval from single thermal channel radiometer data onboard Kalpana satellite.J.Earth Sys.Sci., 120, 337-345

Thompson, B.,Gnanaseelan, C., Parekh, A. and Slavekar, P.S., 2008. North Indian Ocean warming and sea level rise in an OGCM. J.Earth Syst. Sci., 117,169-178.

Venkatesan,R., Shamji, V. R., Latha, G. and Mathew, S., 2013. Insitu ocean subsurface time series measurement from OMNI bouy network in the Bay of Bengal. Current Sci., 104, 1166-1177

Venkatesan, R.,Mathew, S., Vimala, J., Latha. G., et al., 2014. Significance of bouy observatories for accurate prediction of Phalin Cyclone in the Bay of Bengalduring Oct. Current Sci., 107, 589-595

Venkatesan, R., Ramasundaram, R., Ranganathan, S., Vedachalam, N., et al., 2015a.Reliability assessment of state- of – the- art reat time data reception and analysis system for the Indian seas. Marine Techno. Soc. J., 49, 127-134

Venkatesan, R., Muthiah, M.A., Kesavakumar, B., 2015b. Study of performance of sensors in Indian Moored Bouys, Data Bouy Cooperation Panel (DBCP), JCOMM 31st Scientific and Technical Workshop, WMO Geneva, 19th Oct 2015.

Venkatesan, R., Lix, J.K., Phanindra Reddy, A., Arul Muthiah, M. and Atmanand, M.A., 2016. Two decades of operating the Indian moored bouy network: significance and impact, J. Operational Oceanography, 9, 45-54.

Received on: 17.10.18; Revised on: 22.10.18; Accepted on: 29.10.18

GUIDE FOR AUTHORS

The Journal of Indian Geophysical Union (J-IGU), published bimonthly by the Indian Geophysical Union (IGU), is an interdisciplinary journal from India that publishes high-quality research in earth sciences with special emphasis on the topics pertaining to the Indian subcontinent and the surrounding Indian Ocean region. The journal covers several scientific disciplines related to the Earth sciences such as solid Earth geophysics, geology and geochemistry, apart from marine, atmosphere, space and planetary sciences. J-IGU welcomes contributions under the following categories:

- Research papers and short notes reporting new findings.
- Review articles providing comprehensive overview of a significant research field.

In addition, J-IGU also welcomes short communications, after communications and report on scientific activity, book reviews, news and views, etc.

The manuscript should be submitted electronically as a single word format (.doc file) including the main text, figures, tables, and any other supplementary information along with the signed "Declaration Letter". The manuscript should be submitted by email (jigu1963@gmail.com) to the Chief Editor.

After acceptance of the manuscript the corresponding author would be required to submit all source files (text and Tables in word format) and figures in high resolution standard (*.jpg, *.tiff, *.bmp) format. These files may be submitted to J-IGU as a single *.zip file along with the "Copyright Transfer Statement".

IMPORTANT INFORMATION

Ethics in publishing
J-IGU is committed to ensuring ethics in publication and takes a serious view of plagiarism including self-plagiarism in manuscripts submitted to the journal. Authors are advised to ensure ethical values by submitting only their original work and due acknowledgement to the work of others used in the manuscript. Authors must also refrain from submitting the same manuscript to more than one journal concurrently, or publish the same piece of research work in more than one journal, which is unethical and unacceptable. Editor of J-IGU is committed to make every reasonable effort to investigate any allegations of plagiarism brought to his attention, as well as instances that come up during the peer review process and has full authority to retract any plagiarized publication from the journal and take appropriate action against such authors if it is proven that such a misconduct was intentional.

Similarly, Editor and Reviewers are also expected to follow ethical norms of publishing by ensuring that they don't use any unpublished information, communicated to them for editorial or review purpose, in their own research without the explicit written consent of the author. They are also expected to keep manuscript/ data/ observations/ any other information related to the peer review confidential to protect the interest of the authors. Reviewers should refrain from reviewing the manuscripts in which they have conflicts of interest resulting from competitive, collaborative, or other relationships or connections with any of the authors, companies, or institutions connected to the manuscript.

Conflict of interest
All authors are requested to disclose any actual or potential conflict of interest including any financial, personal or other relationships with other people or organizations within three years of beginning the submitted work that could inappropriately influence, or be perceived to influence, their work.

Submission declaration
Submission of a manuscript implies that the work has not been published previously and it is not under consideration for publication elsewhere, and that if accepted it will not be published elsewhere in the same or any other form, in English or in any other language, without the written consent of the publisher. It also implies that the authors have taken necessary approval from the competent authority of the institute/organization where the work was carried out.

Copyright
After acceptance of the manuscript the corresponding author would be required to sign and submit the "Copyright Transfer Statement".

MANUSCRIPT PREPARATION

The corresponding author should be identified (include E-mail address, Phone/Mobile number). Full affiliation and postal address must be given for all co-authors.

Abstract:
An abstract of not more than 300 words must be included.

Text:
The manuscript should be structured to include a front page containing the title, Author(s) name, affiliation and address of the institute, where the work was carried out, a short title, and 5-to-6 Key words. Author(s) present address, if different from the above mentioned address, may be given in the footnote. The corresponding author should be identified with an asterisk and his/her email ID should be provided. This page should be followed by the main text consisting of Abstract, Introduction, Methods/ Techniques/ Area description, Results, Discussion, Conclusions, Acknowledgements, and References. Tables and Figures with captions should be inserted at the end of main text. It should not be inserted in the body of the text.

Figures/ Illustrations:
All figures should be provided in camera-ready form, suitable for reproduction (which may include reduction) without retouching. Figures in high-resolution (at least 300 dpi) standard formats (*.jpg, *.tiff, *.bmp) are acceptable. Figures should be numbered according to their sequence in the text. References should be made in the text to each figure. Each figure should have a suitable caption.

Tables:
Authors should take note of the limitations set by the size and layout of the journal. Table should not exceed the printed area of the page. They should be typed on separate sheets and details about the tables should be given in the text. Heading should be brief. Large tables should be avoided and may be provided as supplementary information, if required.

Equations:
Equations should be numbered sequentially with Arabic numerals and cited in the text. Subscripts and Superscripts should be set off clearly. Equation writing software that presents each equation as an object in MS Word will be accepted. Style and convention adopted for the equations should be uniform throughout the paper.

References:
All references to publications cited in the main text should be presented as a list of references in order following the text and all references in the list must be cited in the text. References should be arranged chronologically, in the text. The list of references should be arranged alphabetically at the end of the paper.

References should be given in the following form:
Kaila, K.L., Reddy P.R., Mall D.M., Venkateswarlu, N., Krishna V.G. and Prasad, A.S.S.S.R.S., 1992. Crustal structure of the west Bengal Basin from deep seismic sounding investigations. Geophys. J. Int., 111,45-66.

REVIEW PROCESS:

All manuscripts submitted to the journal are peer-reviewed. It is advisable to send the contact details of 4 potential reviewers along with the manuscript to expedite the review process. Editor has the option to select reviewers from the list or choose different reviewers. The review process usually takes about 3 months. All enquiries regarding the manuscript may be addressed to the Editor.

GALLEY PROOF:

Technical editing of manuscripts is performed by the editorial board. The author is asked to check the galley proof for typographical errors and to answer queries from the editor. Authors are requested to return the corrected proof within two days of its receipt to ensure uninterrupted processing. The editor will not accept new material in proof unless permission from the editorial board has been obtained for the addition of a "note added in proof". Authors are liable for the cost of excessive alterations to galley proof.

PUBLICATION CHARGES:

There are no page charges for publication and printing charges for b/w figures. However, in view of substantial cost involved in printing of color figures, author will be charged for printing of pages containing color figures @ Rs. 2,500/- per page. The charges may be revised at any time based on cost of printing and production. Author will receive an estimate/ invoice of the color figures reproduction cost along with the galley proof. It is the responsibility of the author to remit the color figures reproduction cost within one month of the receipt of the estimate/invoice.

The corresponding author will receive a soft copy (pdf format) of his/her published article. Should the author desire to purchase reprints of his/her publication, he/she must send the duly signed Reprint Order Form (accompanies the galley proof and contains price details) along with the corrected galley proof to the Editor. The reprint charges must be paid within one month of sending the Reprint Order Form.

Any payment related to printing of color figures and/or purchase of reprints should be made in the form of a Demand Draft in the name of Treasurer, Indian Geophysical Union, payable at Hyderabad.

You may download the pdf file from: http://www.j-igu.in/IGU-Guide-forAuthors.pdf